Fault Representation in Reservoir-Scale Hydro-Mechanical Finite Element Models

Fachbereich Material- und Geowissenschaften der Technischen Universität Darmstadt

Dissertation
Zur Erlangung des akademischen Grades
Doktor-Ingenieur (Dr.-Ing.)

Von Torben Treffeisen

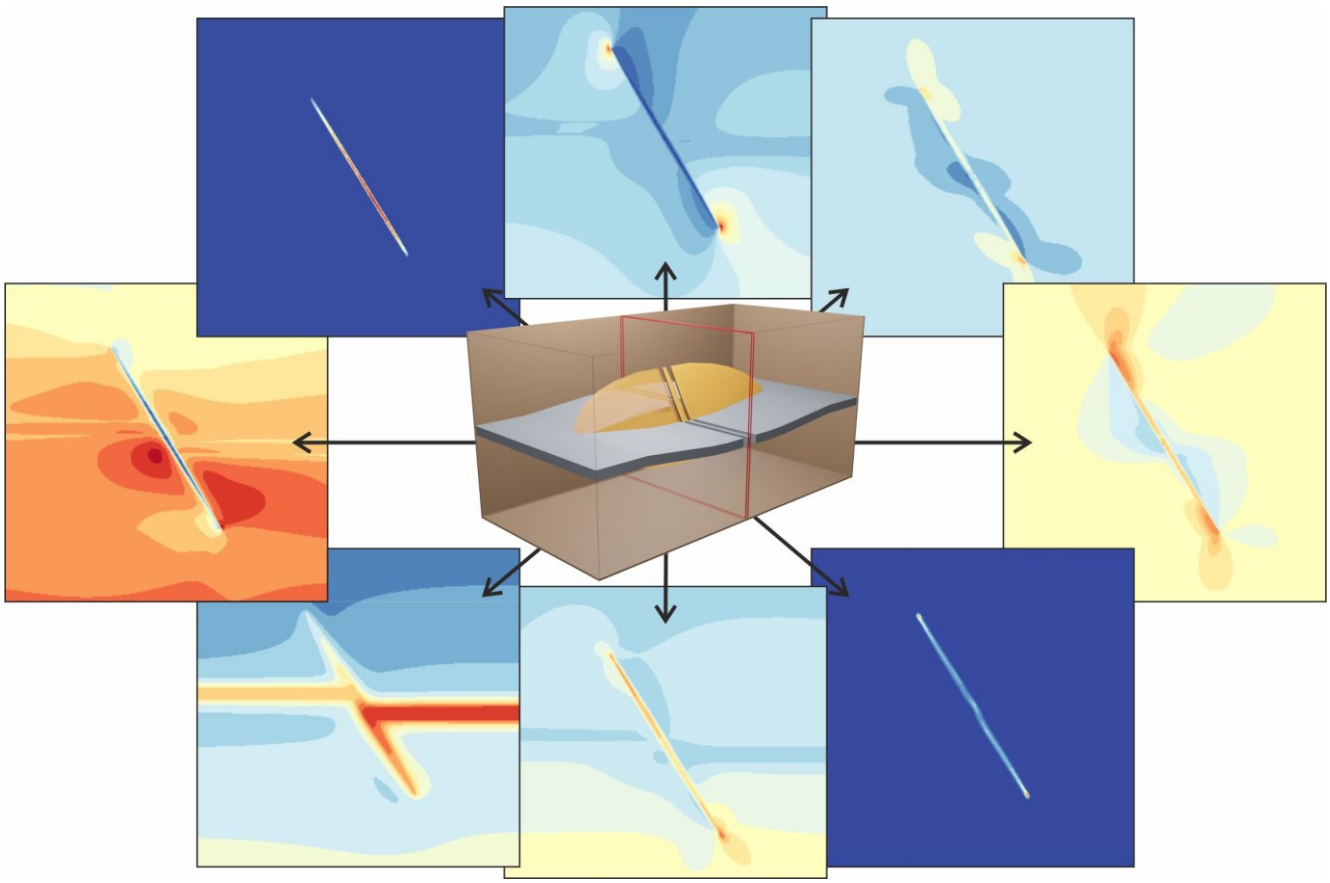

Referent: **Prof. Dr. Andreas Henk**
Korreferent: **Prof. Dr. Tobias Backers**

Darmstadt, 2020

M.Sc. Torben Treffeisen

geboren am 24. Januar 1991 in Marburg, Hessen / Deutschland

Einreichung: 04.11.2020

Disputation: 17.12.2020

Vorsitzender der Prüfungskommision:	Prof. Dr. Stephan Weinbruch
Referent:	Prof. Dr. Andreas Henk
Koreferent:	Prof. Dr. Tobias Backers
Prüfer:	Prof. Dr. Christoph Schüth
Prüfer:	Prof. Dr.-Ing. Uwe Rüppel

Year of publication of dissertation in TUprints: 2021

URI: https://tuprints.ulb.tu-darmstadt.de/id/eprint/17419

URN: urn:nbn:de:tuda-tuprints-174196

Statement of Authorship

I hereby certify that this thesis has been composed by myself and describes my own work unless otherwise acknowledged in the text. All references and verbatim extracts have been quoted and all sources of information have been specifically acknowledged. This thesis has not been accepted in any previous application for a degree.

Hiermit versichere ich, dass ich die vorliegende Arbeit selbstständig und ohne Benutzung anderer als der angegebenen Hilfsmittel angefertigt habe. Stellen, die wörtlich oder sinngemäß aus anderen Schriften entnommen sind, sind als solche kenntlich gemacht. Die Arbeit ist in gleicher oder ähnlicher Form noch nicht als Prüfungsarbeit eingereicht worden.

Darmstadt 04.11.2020. Signature , Treffeisen

Acknowledgements

Throughout the writing of this dissertation I have received a great deal of support and assistance.

First and foremost, I would like to thank Prof. Dr. Andreas Henk for the initial idea behind this research project and for giving me the great opportunity to partake in and accomplish these studies. I am truly grateful that he gave me the freedom to develop my own concepts, particularly in programming with Python, and to find my own solutions while always giving insightful feedback that pushed me to sharpen my thinking and brought my work to a higher level. I am also thankful for the overall outstanding supervision and the countless inspiring discussions, not only on this thesis.

I also want to thank Prof. Dr. Tobias Backers for the co-supervision of this work. Meeting him at the STC 2019 in Aachen and discussing my work provided me with invaluable feedback. His interest in my work and passion for Geomechanics encouraged as well as inspired me for which I am deeply grateful.

In Darmstadt, I was very happy to have Dr. Clairet Guerra and Dominik Gottron as office roommates, great colleagues - and friends. Thanks for all the serious scientific discussions, constructive comments and also loads of fun we shared in our room. I count myself lucky to enjoy your support – not limited to work - and friendship.

Moreover, I want to thank the engineering geology group of the Institute of Applied Geosciences in Darmstadt for the fantastic work environment and cooperation: Dr. Tobias Hergert, Dr. Karsten Reiter, Muhammad Zain-Ul-Abedin, Steffen Ahlers, Dennis Fehre, Reimund Rosmann and Stefanie Kollmann. The pleasant atmosphere made things so much easier for me. I would particularly like to single out Dr. Karsten Reiter and Dr. Tobias Hergert for their valuable input that helped me further my research.

Special thanks also have to go to Reimund Rosmann for his help and advice during several field trips and Stefanie Kollmann for her support in all organizational matters.

I also wish to express my sincere appreciation for the support given by Dr. Karsten Fischer, from Schlumberger Inc. and Dr. Oliver Heidbach, from the GFZ Helmholtz-Zentrum Potsdam, in particular for thoroughly reviewing research articles, providing detailed feedback and giving honest advice.

Aside from work, I want to thank all my friends for their unwavering support in these last years. Thank you for giving warm encouragement, sharing whole-hearted laughs - and sometimes just for lending a listening ear. I am looking very much forward to all that is yet to come.

My deepest appreciation goes to Cord-Gerrit Peters for accompanying me on this journey – not only for having been – and being!- my best man and all of the great time we had during learning, studying and field trips at the TU Darmstadt but also for his patience in listening to new ideas.

Furthermore, I would like to thank my parents and my sister for giving me the opportunities and experiences that have made me who I am. I would also like to thank my parents- & sister-in-law for their role in supporting me and always providing some lightheartedness when it was needed.

Above all I would like to thank my wife Lisa, the love of my life, for her constant support, her understanding when working endless hours and for our life and our future. I am truly grateful to have you by my side.

Preface

The work presented in this thesis is part of the project 'Hydro-Mechanical Fault Zone Modeling' carried out in the Engineering Geology group at the Institute for Applied Geoscience at the Technical University Darmstadt. This cumulative PhD thesis covers the fault representations in reservoir-scale finite element models and includes three published and peer-reviewed research articles. Each article presents a sensitivity study of numerical approaches a modeler can choose and simplifications regarding the representation of faults in hydro-mechanical simulations.

Chapter 1 is an introductory chapter into the overall topic of the thesis. A brief description about the general motivation behind this work and the importance of faults in hydro-mechanical simulations is given. Afterwards, challenges regarding fault representation, a simplified workflow of fault incorporation in reservoir-scale models as well as the aim and objective of this thesis are presented.

Chapter 2 briefly reviews general literature about faults in nature and the faulting regime. Furthermore, different scales of faults occurring in nature, especially reservoir-scale faults, as well as implications for hydro-mechanical finite element modeling are discussed in this chapter.

Chapter 3 introduces the specific workflow used in this thesis to carry out the sensitivity studies published in peer-review journals. It also describes the Python scripts and the geometrical methods used to automate model generation in Ansys.

Chapter 4 (first article):

Treffeisen, T., Henk, A. 2020. Representation of faults in reservoir-scale geomechanical finite element models – A comparison of different modeling approaches. Journal of Structural Geology 131, 1-12.

Two different numerical approaches – discontinuum and continuum approach – to incorporate faults in geomechanical models are studied in this article. Moreover, two different grid geometries – rectangular and curvilinear – are observed. The results show differences between all three approaches and also provide a solid background for the following studies.

Chapter 5 (second article):

Treffeisen, T., Henk, A. 2020. Faults as Volumetric Weak Zones in Reservoir-Scale Hydro-Mechanical Finite Element Models - A Comparison Based on Grid Geometry, Mesh Resolution and Fault Dip. Energies 13, (10), 1-28.

Based on the findings of the first article, the grid geometry – rectangular or curvilinear – as well as the associated mesh resolution of a fault representation as volumetric weak zone are investigated in this study. Aside from these two simplifications concerning the mesh of the finite element simulation, the influence of different fault dips on the modeling results are considered as well. General recommendations are achieved, helping to accurately include faults into hydro-mechanical models regarding the aim of the study.

Chapter 6 (third article):

Treffeisen, T., Henk, A. 2020. Elastic and Frictional Properties of Fault Zones in Reservoir-Scale Hydro-Mechanical Models-A Sensitivity Study. Energies 13, (18), 1-27.

This sensitivity study uses a generic finite element (FE) model with a volumetric fault zone description to examine what effect the corresponding upscaled material parameters have on pore pressures, stresses, and deformation within and surrounding the fault zone. Finally, some general recommendations concerning the choice of mechanical fault zone properties for reservoir-scale hydro-mechanical models are given.

Chapter 7 is a synthesis of the three research articles and the results and conclusions as well as their limitations. Furthermore, an integration of the findings into the workflow a modeler normally faces when incorporating faults in reservoir simulations is discussed. Lastly, implications for models of larger or smaller than reservoir-scale are given.

Chapter 8 contains the outlook of this thesis and thereby introduces three possible directions future research may take based on this study. Input and calibration data for verification of each numerical approach with hydro-mechanical fault behavior in nature are illustrated. Also a modeling concept to implement further details usually observed in fault zones in nature and a possible upscaling concept from such detailed fault models to reservoir-scale models containing multiple faults are introduced.

Abstract

Hydro-mechanical reservoir models are used to obtain quantitative insights into the spatial distribution of stress, strain and pore pressure. Recent studies have shown that different approaches to incorporate faults into such reservoir simulations have a profound impact on the modeling results. Since faults are a key feature in the subsurface affecting both the hydraulic and mechanical behavior of a reservoir, their proper implementation in the numerical model is crucial. Fault representation has to accurately model the effect faults have on (1) fluid flow and (2) the local stress field. However, a fault is not just a discrete geological feature but rather a fault zone with a complex geometry and various rock units with distinct material properties. This small-scale heterogeneity can hardly be represented in reservoir scale finite element models considering the typical grid size used in these simulations. Thus, fault representation in reservoir-scale hydro-mechanical simulations has to be based on simplifications and upscaling techniques.

To improve decision making and help in choosing the right fault representation, knowledge about the different effects each simplification and each approach used to incorporate faults has on the modeling results is necessary. This thesis focuses on different approaches of fault representation with a single upscaled set of material properties in reservoir-scale hydro-mechanical finite element models. The main objectives are

(1) Implementing the fault geometry with respect to the finite element grid properly

(2) Addressing the scale differences between the internal heterogeneity of the fault zone (centimeters to meters) and the typical size of the calculation cells of the numerical grid (meters to tens of meters) accurately

(3) Assigning fault material properties to the numerical models, which stem – if available at all – from rock mechanical testing on core samples with a diameter of a few centimeters and therefore require upscaling and merging techniques

In order to meet these challenges three research articles were published, each based on simple generic fault zone models. The approaches analyzed to represent faults in reservoir-scale hydro-mechanical include a regular rectangular grid, a grid geometry adapted to the fault geometry as well as fault representation by contact elements. Fault representation as volumetric weak zones is investigated for different grid geometries, fault dip angles as well as different mesh resolutions inside the fault zone. In addition, the impact of different elastic and frictional fault zone properties is assessed.

Differences and similarities in the calculated stress and strain patterns as well as the pore pressure field obtained from different fault implementation strategies are discussed and general recommendations concerning the implementation of faults in hydro-mechanical reservoir models are given. Fault representation as either volumetric weak zones or contact elements leads to significant differences in the stress and strain patterns in the vicinity of the fault zone (< 50 m). While fault dip is not of critical importance for fluid flow, it has a significant impact on the stress perturbation induced by the fault. Another important finding is that the mesh resolution has to be considered very carefully as – particularly in combination with a rectangular grid – interlocking effects and serious errors can occur. If, however, the focus of a modeling study is not in the vicinity of the fault zone, a rectangular grid with the appropriate mesh resolution allows for faster and easier model generation in comparison to a curvilinear grid adapted to the fault geometry. Regarding material parameters, Young's modulus and cohesion assigned to the fault zone have the most significant impact on the modeling results, while the internal friction angle and Poisson's ratio play a subordinate role.

Overall, this thesis provides recommendations and guidelines to improve fault representation in reservoir simulations. The goal is to gain more realistic simulations and thus, more reliable modeling results to improve forecasts, lower costs and reduce risks during subsurface operations.

Zusammenfassung

Hydromechanische Reservoir-Modelle werden erstellt um quantitative Einblicke in die räumliche Verteilung von Spannungen, Verformungen und Porendruck zu erhalten. Aktuelle Studien haben jedoch gezeigt, dass die verschiedene Ansätze Störungen in solche Reservoir-Simulationen zu integrieren eine nicht zu unterschätzende Auswirkung auf die Modellierungsergebnisse haben. Störungszonen stellen ein wichtiges Merkmal des Untergrunds dar. Diese beeinflussen sowohl das hydraulische als auch das mechanische Verhalten eines Reservoirs. Deshalb ist es von immenser Bedeutung, Störungen möglichst akkurat in derartigen numerische Modelle zu implementieren. Die Darstellung von Störungszonen sollte präzise die Effekte abbilden, die Störungszonen in Bezug auf (1) Fluid-Fluss und (2) das lokale Spannungsfeld haben. Eine Störung ist allerdings nicht nur ein einzelnes geologisches Merkmal, sondern vielmehr eine Störungszone mit internen, komplexer Geometrie und verschiedenen Gesteinseinheiten mit ihrerseits unterschiedlichen Materialeigenschaften. Aufgrund der typischen Netzgröße Reservoir-maßstäblicher Finite Element Modelle kann diese kleinmaßstäbliche Heterogenität nur schwer in diesen Modellen repräsentiert werden. Daher basiert die Darstellung von Störungszonen notwendigerweise auf Vereinfachung und Aufskalierungsmethoden.

Um die Entscheidungsfindung zu vereinfachen und zur Unterstützung in der Auswahl der besten Repräsentation, sind Kenntnisse hinsichtlich der verschiedenen Auswirkungen jeder Vereinfachung und jedes zum Einbau von Störungen verwendeten Ansatzes auf die Modellierungsergebnisse nötig. Diese Thesis konzentriert sich folglich auf die verschiedenen Ansätze der Darstellung von Störungszonen mit einem einzigen aufskalierten Set von Materialeigenschaften in Reservoir-maßstäbliche hydromechanischen Finite Elemente Modellen.

Hauptziele sind hierbei:

(1) Korrekte Implementierung der Störungsgeometrie innerhalb des Finite Elemente Netz

(2) Akkurates Adressieren der Skalenunterschiede zwischen der internen Heterogenität der Störungszone (Zentimeter bis Meter) und der üblichen Größe der Berechnungszellen des numerischen Netzes (Meter bis Zehnermeter)

(3) Zuweisen der Materialeigenschaften des Störungsgesteins in das numerische Model, welche – wenn überhaupt verfügbar – von gesteinsmechanischen Tests von Kernproben mit einem Durchmesser von wenigen Zentimetern stammen und deshalb Upscaling und Merging Techniken benötigen

Um diese Herausforderungen anzugehen wurden drei wissenschaftliche Paper veröffentlicht, basierend auf simplen generischen Störungszonen-Modellen. Die untersuchten Ansätze im Hinblick auf die Darstellung von Störungszonen in Reservoir-maßstäbliche hydromechanischen Modellen beinhalten ein rechtwinkliges Netz, eine Netzgeometrie, die sich an die Störungsgeometrie anpasst sowie die Störungsrepresentation durch Kontaktelemente. Die Darstellung von Störungszonen als volumetrische Schwächezonen wird weiterhin untersucht bezüglich verschiedener Netzgeometrie, Einfallswinkel der Störung sowie verschiedenen Netz-Auflösungen innerhalb der Störungszone. Weiterhin wird der Einfluss von verschiedenen elastischen und Reibungs-Eigenschaften der Störungszonen bewertet.

Unterschiede und Gemeinsamkeiten in den berechneten Spannungs- und Verformungsmustern als auch dem Porendruck-Bereich, die durch verschiedene Störungszonen-Integrations-Strategien erzielt wurden, werden diskutiert und grundsätzliche Empfehlungen hinsichtlich der Implemetierung von Störungszonen in hydromechanischen Reservoir Modellen gegeben. Die Darstellung von Störungszonen als volumetrische Schwächezone oder Kontaktelemente führt zu signifikanten Unterschieden in den Spannungs- und Verformungsmustern im Nahfeld der Störung (< 50 m).

Während der Einfallswinkel der Störung grundsätzlich nicht von großer Bedeutung für den Fluid-Fluss ist, hat er einen erheblichen Einfluss auf die Spannungs-Perturbation, die von der Störungszone ausgelöst wird. Eine weitere wichtige Entdeckung ist die, dass die Netz-Auflösung sehr sorgfältig ausgewählt werden muss - insbesondere in Kombination mit rechtwinkliger Vernetzung – da andernfalls blockierende Effekte und ernste Fehler zu befürchten sind.

Falls jedoch der Fokus der Studie nicht in der direkten Umgebung der Störungszone liegt, erlaubt ein rechtwinkliges Netz mit angemessener Netz-Auflösung schnellere und einfachere Modell-Generierung im direkten Vergleich zu einem gekrümmten Netz, dass angepasst an die Störungszonengeometrie ist. Bezüglich der Material Parameter hat das der Störungszone zugewiesene Elastizitätsmodul und die Kohäsion den größten Einfluss auf die Resultate, während der interne Reibungswinkel und die Poissonzahl nur eine untergeordnete Rolle spielen.

Insgesamt bietet dieses Thesis Empfehlungen und Richtlinien um die Darstellung von Störungszonen in Reservoir Simulationen zu verbessern. Das Ziel ist es hierbei, realistischere Simulationen zu erzeugen und daraus folgend verlässlichere Modellierungsergebnisse zu liefern, die wiederum Vorhersagen verbessern, Kosten verringern und Risiken während Arbeiten im Untergrund reduzieren.

Table of Content

List of Figures

List of Tables

List of Symbols and Abbreviations

c	Cohesion
c'	Effective cohesion
CW	Clockwise
CCW	Counterclockwise
d	Depth
E	Young's modulus
FE	Finite Elements
g	Gravitational acceleration
HM	Hydro-mechanic
k	Permeability
n	Fluid viscosity
p_f; p	Pore fluid pressure
p_i	Pressure increment
p_r	Surcharge
Q^*	compressibility parameter
q; q_f	Darcy Fluid flow
S	Specific storage
S_1, S_2, S_3	Principle stresses
$S_{1,eff}$, $S_{2,eff}$, $S_{3,eff}$	Effective principle stresses
S_f	fluid saturation
S_H	Horizontal stress, maximum/minnium
S_{Hmax}	Maximum horizontal stress,
S_{hmin}	Minimum horizontal stress,
S_v	Vertical stress
t	Time step; Time
τ	Shear stress

T_0; TS	Tensile strength
τ_{crit}	critical shear stress at failure
α	Biot coefficient
δ_{ij}	Kronecker's delta
ε	Strain
ε_{ij}	Total strain tensor
ε_v	volumetric strain
ϱ_f	Fluid density
ϱ_r	Rock density
σ'_{ij}	Total effective stress tensor
σ'_{kk}	Sum of the effective principal stresses
σ_{ij}	Total stress tensor
σ_n	Normal stress
υ	Poisson's ratio
φ	angle of internal friction
ϕ, p	porosity
φ'	effective angle of internal friction
ρ_f	fluid viscosity

1. Introduction

1.1. Motivation - The Importance of Faults in Hydro-Mechanical Simulations

Faults are a common feature in the subsurface and often have a high impact on a variety of geotechnical engineering and engineering geology tasks like tunneling (Schubert & Riedmüller, 1997; Schubert & Riedmüller, 2000; Jeon et al., 2004; Schubert et al., 2006; Zhang et al., 2006; Schubert, 2009; Kun & Onargan, 2013; Paltrinieri et al., 2015), mining (Brady & Brown, 1993; Burtan et al., 2014; Sainoki & Mitri, 2015; Kushwaha et al., 2016; Wang et al., 2016), nuclear waste storage sites (Martin & Lanyon, 2003; Guglielmi et al., 2017; Jaeggi et al., 2017; Park et al., 2020) or reservoir related projects like hydrocarbon production (Wiprut & Zoback, 2002; Cuisiat et al., 2010; Backers, 2015), geothermal energy (Moeck et al., 2009a; Moek et al., 2009b; Gan & Elsworth, 2014; Loveless et al., 2014; Duwiquet et al., 2019; Anyim & Gan, 2020) and more recently the storage of CO2 in the underground (Carbon Capture and Storage - CCS; (Nagelhout & Roest, 1997; Vidal-Gilbert et al., 2009; Vidal-Gilbert et al., 2010; Morris et al., 2011; Orlic et al., 2011; Rinaldi et al., 2014). In order to visualize the geology and the associated faults, structural models of the subsurface are a customary tool. These structural models are usually based on the interpretation of 3D seismic and well data and typically contain plenty of faults (Zoback, 2007; Faulkner et al., 2010). As a classic example of such structural models, the Gullfaks hydrocarbon reservoir, which is located in the North Sea, is shown in Figure 1-1.

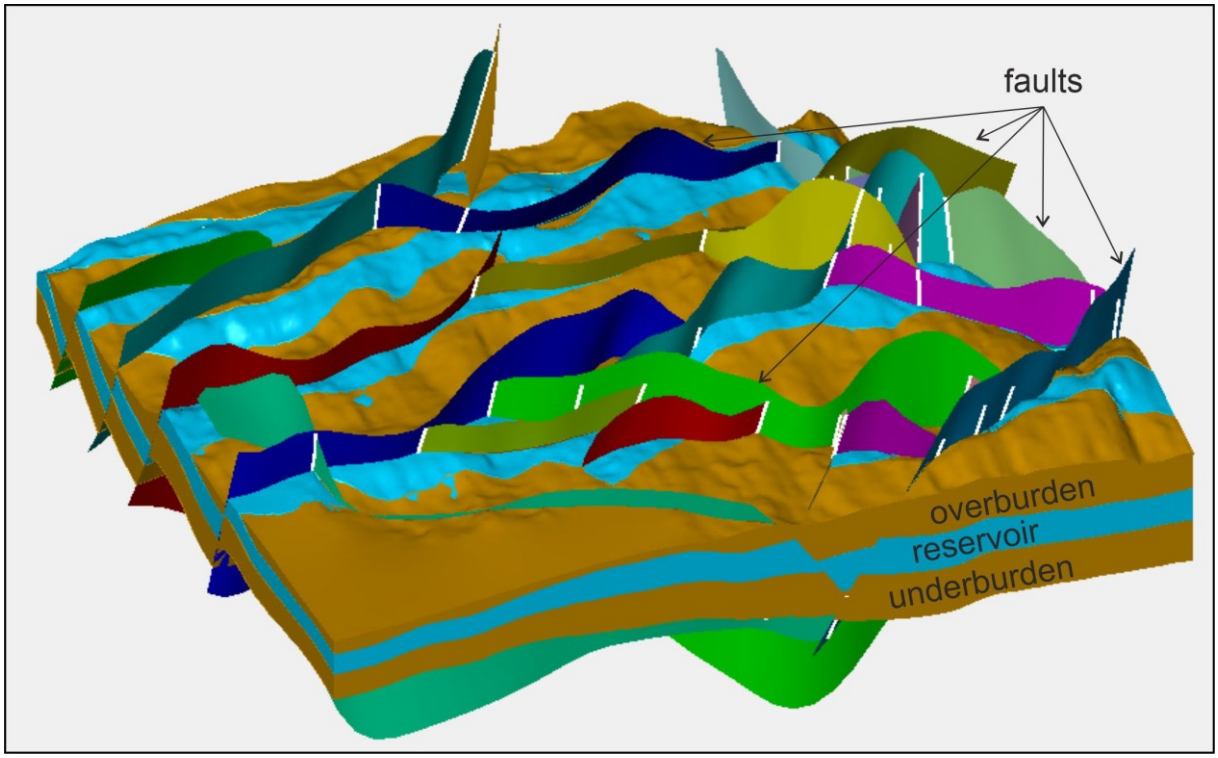

Figure 1-1: Structural model of the Gulfaks reservoir located in the North Sea (Modeldata according to Schlumberger, 2019). The model contains a reservoir horizon embedded in over- and underburden sections and the slightly horizontal orientated horizons are intersected and offsetted by more than 15 faults.

Since the beginning of the 21st century, the hydrocarbon industry has shifted towards structurally even more complex conventional or unconventional reservoirs (Pereira et al., 2014; Rueda et al., 2014; Fachri et al., 2016). Within a reservoir, faults not only have a profound control on the hydraulic regime as they can act as conduits or barriers for fluid flow (Fredman et al., 2008; Faulkner et al., 2010) but also affect the reservoir mechanically, since faults alter the tectonic stress field which results in local

changes in stress orientation and magnitude (Yale, 2003; Faulkner et al., 2006; Prevost & Sukumar, 2015). During construction or mining projects, faults, due to their generally weaker mechanical properties as compared to the undeformed host rock, often cause stability problems (Brady & Brown, 1993; Schubert & Riedmüller, 2000; Jeon et al., 2004; Burtan et al., 2014; Wang et al., 2016). Within reservoir related applications, those weaker mechanical properties make faults more sensitive to pore pressure changes resulting from fluid injection into or fluid withdrawal from the reservoir. In the worst case scenario, those pore pressure changes can reactivate preexisting faults (Pereira et al., 2014; Rueda et al., 2014; Sanchez et al., 2015; Haug et al., 2018) leading to induced seismicity which in turn potentially causes critical situations like fault seal breach, land subsidence and well collapse (Segall et al., 1994; Wiprut & Zoback, 2000; Morton et al., 2006; Chan & Zoback, 2007; Faulkner et al., 2010; Cuisiat et al., 2010; Vilarrasa et al., 2017). Thus, a thorough understanding of both the hydraulic and the mechanical behavior of faults in subsurface applications is absolutely essential.

Routinely used in reservoir engineering, numerical modeling has proven to be a valuable tool to support field management decisions by gaining quantitative insights into both the hydraulic and the mechanical compartment of a reservoir (Qu & Tveranger, 2016; Azarfar et al., 2018). On the hydraulic part, fluid flow simulations are a well-established tool in the industry (Manzocchi et al., 2008; Qu et al., 2015) and geomechanical modeling has also turned out to be of tremendous help when trying to gain quantitative insights into the spatial distribution of stress and strain on the reservoir-scale (Geertsma, 1973; Segall et al., 1994; Fisher & Jolley, 2007; Ferronato et al., 2008; Orlic & Wassing, 2012). Due to the interaction of fluid flow and mechanical behavior, fully-coupled hydro-mechanical simulations are developing into a standard tool for various subsurface applications, ranging from hydrocarbon and geothermal reservoirs to underground storage sites for CO2 (Cappa & Rutqvist, 2011; Fachri et al., 2016; Serajian et al., 2016; Schuite et al., 2017). Different numerical modeling techniques have been applied, e.g., finite difference (FD), boundary element (BE), discrete element (DE) and hybrid methods (Jing & Hudson, 2002; Hilley et al., 2010; Cappa & Rutqvist, 2011; Fournier & Morgan, 2012; Zhang et al., 2015), but the most commonly used approach is the finite element (FE) method which is also the focus of the present thesis. The aim of the hydro-mechanical modeling work is closely related to the scale of the study and the utilized model size. Hence (hydro-)mechanical simulations can be large-scale models comprising areas of several thousand kilometers edge length in order to examine plate tectonic processes and large-scale stress patterns (Buchmann & Connolly, 2007; Hergert et al., 2011). At the reservoir scale, the lateral size of such FE reservoir models is typically in the range of kilometres to tens of kilometres and applications vary from hydrocarbon and geothermal reservoirs to sites for underground gas storage (Croucher & O'Sullivan, 2008; Jayakumar et al., 2011; Orlic et al., 2011; Backers, 2015). These models typically concentrate on the prediction of local perturbations in stress orientation and magnitude which is important for the optimal orientation of horizontal well trajectories and hydraulic fracture planning (Will & Eckardt, 2015). Other applications are related to pore pressure changes leading to surface subsidence or induced seismicity resulting from fault reactivation (Rueda et al., 2014; Sanchez et al., 2015; Meier & Backers, 2017). Even smaller-scale (hydro-)mechanical models can be used to study topics like wellbore integrity (Fontoura et al., 2013; Feng & Grey, 2018).

Since faults are a common feature in the subsurface, they have to be considered in reservoir models in order to provide a realistic subsurface representation for reliable stress and fracture predictions as well as fluid flow path analysis. Consequently, an appropriate representation of faults in a hydro-mechanical reservoir simulation is of critical importance for the reliability of the numerical model predictions.

In contrast, several authors (Rueda et al., 2014; Sanchez et al., 2015; Azarfar et al., 2018) discovered that the numerical simulation results, i.e. deformation, stress and strain, differ depending on the method applied to incorporate faults. In this thesis I focus on testing different methods to represent faults in reservoir-scale models in order to analyze the different results between the different techniques qualitatively. This thesis shall provide a framework for reservoir modelers to better

understand the influence different fault representations have and thereby to gain more realistic simulations regarding the aim of the specific study.

1.2. Challenges regarding fault representation in reservoir-scale models & aim of study

Challenges for the proper implementation of faults into reservoir-scale numerical models have been addressed in various studies over the past years (Chan & Zoback, 2007; Fredman et al., 2007; Faulkner et al., 2010; Orlic & Wassing, 2012).

The simulation grid is normally based on the typically horizontally layered geometry of the reservoir stratigraphy and therefore favors a relative rectangular element geometry. Hence the often complex geometry and steep fault dip of faults poses the challenge of (1) properly representing the fault geometry within the geometry of the FE grid. Likewise, the difference in (2) scale between the internal heterogeneity of the fault zone (centimeters to meters) and the typical size of the calculation cells of the numerical grid (meters to tens of meters) remains as another challenge. This topic will be addressed in chapter 2, where faults in nature and the implications for reservoir-scale models are introduced. Apart from these two numerical challenges, (3) determining fault material properties at all is already challenging, since faults are usually not a target for drilling operations. As a consequence, fault-specific material parameters often have to be estimated from literature sources to populate the hydro-mechanical model. Even if coring of a fault zone is attempted in order to receive samples for testing intense fracturing and poor consolidation of fault zone rocks frequently lead to very limited core recovery. Concurrently, the properties stem from rock mechanical testing on core samples with a diameter of a few centimeters of the meters to hundreds of meters long highly heterogonous fault zone.

To overcome the aforementioned challenges, simplifications and upscaling techniques have been developed (Manzocchi et al., 2008; Olden et al., 2012; Zhang et al., 2015; Qu & Tveranger, 2016) in order to reflect the fault zone geometry properly and assign reasonable material properties to the fault zone elements of a reservoir-(kilometer)- scale hydro-mechanical model. However, all simplifications regarding fault implementation in reservoir models add limitations and uncertainties, which affect the results of the simulations. Thus, it is of utmost importance to know the sensitivity of the modeling results for each method to improve decision making – economically and result-oriented - regarding the aim of the study.

For example, implementing fault zones in detail in reservoir models is computationally more expensive (Syversveen et al., 2006; Qu & Tveranger, 2016), particularly on field-scale, but on the reservoir-scale the resulting difference to a more practical representation might be insignificant. For studies targeting the fault zone itself or the nearby surrounding rock units, different results may significantly change the informative value of the study.

In order to tackle these questions, three peer-review articles resulting from the modeling work are the main part of this thesis (Chapter 4-6). Each of them is a standalone research article with its own introduction, methodology, results, discussion and conclusion, but somehow follow a path of decisions a modeler will have to make during the incorporation of faults in reservoir-scale models (Figure 1-2). Following this structure Chapter 4 analyses differences between the two main numerical implementation techniques of faults: discontinuum, i.e. contact surface, approach or continuum, i.e. volumetric weak zone, approach. For the continuum approach differences between fault implementation into (a) a curvilinear, adaptive grid and (b) a rectangular grid are also investigated. Since the volumetric representation offers the possibility to later explicitly model complex internal fault material heterogeneity, Chapter 5 dives deeper into this method. The effect of the different representation of the fault geometry – curvilinear or rectangular – on the modeling results by varying mesh resolution inside the fault zone or simplification of the fault dip are examined in the related article.

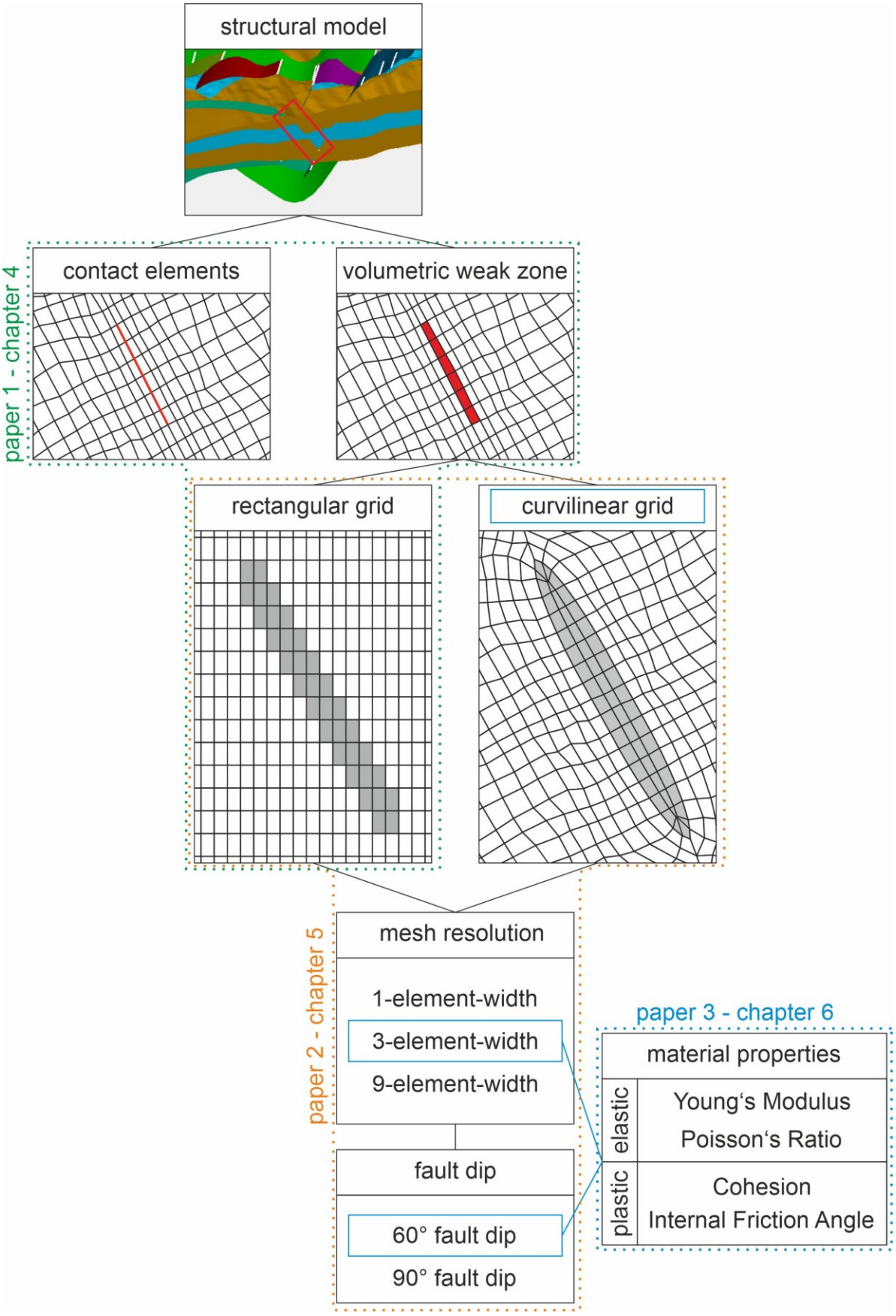

Figure 1-2: Common approaches and simplifications done during fault implementation into reservoir-scale hydro-mechanical simulations and the associated peer-review article, where each technique is investigated in this thesis.

These two articles mainly address topics regarding the challenges of (1) proper fault geometry and (2) scale difference. The challenges of (2) scale difference and (3) the lack of fault specific material properties as well as improvement of related upscaling/merging techniques are topics addressed in Chapter 6 by investigating the effect elastic and frictional material properties of fault zones have on hydro-mechanical reservoir modeling results.

The main part of this thesis is prepended by a brief description of fault zones in nature (Chapter 2) as well as a short introduction of methods and techniques used in this thesis, which are not already mentioned in the methods section of one of the research articles (Chapter 3). Following the research articles, their conclusions are compared and the advantages and disadvantages of the different approaches are discussed in Chapter 7. The primary goal is to provide guidelines for appropriate fault representations and a framework to understand qualitatively the effect each technique has on numerical reservoir models regarding the aim of the study. Such guidelines may assist in building more realistic hydro-mechanical simulations of faulted reservoirs.

However, this thesis can only address several topics of the challenges raised by the incorporation of faults in reservoir models and future research is needed in order to further improve the knowledge regarding faults in numerical models. The modeling techniques developed and experiences gained can only be considered as a starting point for future studies investigating e.g. the effect of faults zone heterogeneities and to develop refined upscaling techniques for hydro-mechanical fault zone properties. Chapter 8 gives an outlook on this possible future research important for the further improvement of fault modeling in hydro-mechanical reservoir models.

2. Faults in Nature

Faults in nature are structural elements within the lithosphere where deformation under brittle conditions occurs. Normally, they are defined as structural discontinuity combined with movement that takes place inside a rock mass and thereby associated with a surface (Anderson, 1951; Jaeger et al., 2007; Faulkner et al., 2010; Gudmundsson, 2011; Brandes & Tanner, 2019). However, simple geometrical models are insufficient to describe the complex structures of natural faults observed in outcrop studies. Faults show three-dimensional features varying extremely in terms of spatial extent (length, width and thickness) as well as internal content and structure on a small scale (e.g. Childs et al., 1996; Foxford et al., 1998; Syversveen et al., 2006; Bonson et al., 2007). Faults are usually weaker than the surrounding host rock (Childs et al., 2009) and thus act as elastic inclusions or inhomogeneity which concentrate stresses and modify the local stress field (Eshelby, 1957; Savin, 1961; Gudmundsson, 2011; Gudmundsson et al., 2013). Faults also alter the hydraulic behavior in their vicinity. Faults can act as barriers to fluid-flow and separate previously connected or equal rock units hydraulically. Likewise, faults can act as conduits to fluid-flow and connect previously hydrologically separated rock masses (Antonellini & Aydin, 1994; Caine et al., 1996; Fisher & Knipe, 2001; Fisher et al., 2001; Odling et al., 2004; Manzocchi et al., 2008). The mechanical and fluid flow properties are inextricably coupled and both modify fault behavior in the subsurface. Hence, many recent studies concentrate on describing and understanding the importance of hydro-mechanical properties of fault zones and how they affect the surrounding rock (e.g. Rawling et al., 2001; Faulkner et al., 2006; Fjær et al., 2008; Cuisiat et al., 2010; Faulkner et al., 2010; Gudmundsson, 2011; Olden et al., 2012; De Souza et al., 2014; Bauer et al., 2015).

2.1. Faulting Regime

Based on the direction of movement along a fault, faults are classified into three faulting regimes (Figure 2-1). Normal faults show downward movement of the hanging-wall, relative to the footwall and thereby maintain the superposition by placing younger rocks over older ones (Figure 2-1 A; Engelder, 1993; Ferrill et al., 1999; Peacock et al., 2000; Rotevatn et al., 2018). Reverse faults move in the opposite sense and for reverse faults with low angle of dip (<45°) the term thrust fault is used. The superposition is reversed by placing older beds over younger ones (Figure 2-1 B, Odonne et al., 1999; Gudmundsson et al., 2008; Chenglong et al., 2018).

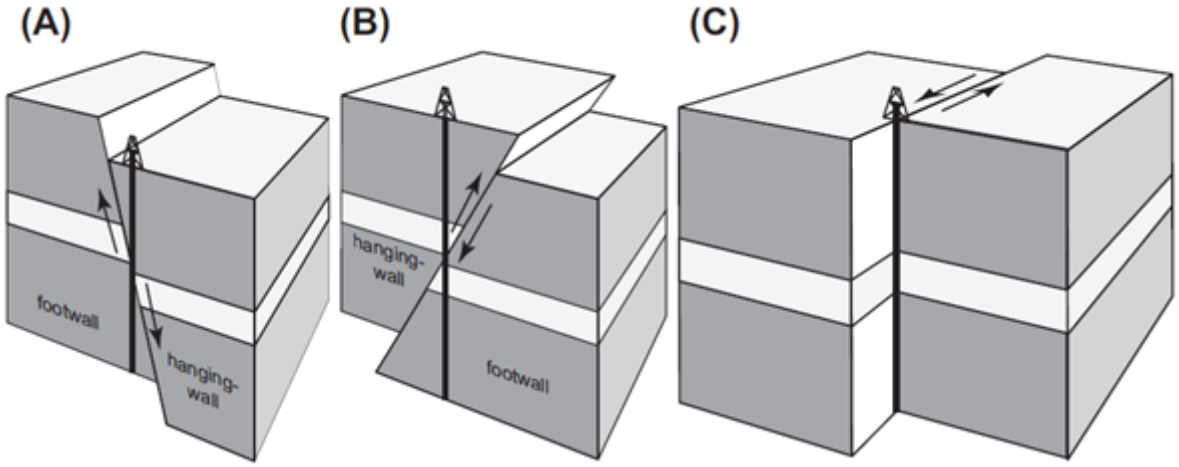

Figure 2-1: Different classification of faults depending on the sense of movement. (A) a normal fault, (B) a reverse fault, (C) a left-lateral strike-slip fault. Note that in (A) the borehole misses part of the stratigraphy, whereas in (B) the stratum is doubled, and in (C) the borehole sees no change (Tanner & Brandes, 2019)

Faults with lateral movement of rock units relative to each other are named strike-slip faults and have no effect on the stratigraphy (Figure 2-1 C, Walsh, 1968; Achenbach & Abo-Zena, 1973; Merzer & Freund, 2007; Stefanov & Bakeev, 2014; Rohr et al., 2018). However, these three fault regimes are simplified end members and faults occurring in nature often feature two directions, horizontal and lateral, movement and the classification results from the dominant direction (Tanner & Brandes, 2019).

2.2. Faults at Different Scale

In the Earth's upper crust, faults vary widely in scale, but all faults are subject to the same basic mechanical laws. These fault mechanics control the formation, development and the long-term behavior of centimeter- to kilometer-scale faults (e.g. Anderson, 1951; Caine et al., 1996; Faulkner et al., 2010). Tectonic forces initialize the development of a fault by cracking the rock mass. The resulting fissures are called fractures and mechanical discontinuities in rocks. The accumulation of multiple fractures in a certain area of the subsurface can generate a fault, which – in addition to the deformed rock mass inside the fault zone - also has a distinct offset (Jaeger et al., 2007; Brandes & Tanner, 2019). Examples of faults on different scales are shown in Figure 2-2. Figure 2-2 A shows a small-scale fault zone in the visitor mine in Neubulach, Germany. This fault strikes NNW-SSE and thereby is perpendicular to the NNE-SSW striking Upper Rhein Graben (Bauer et al., 2015). The width of the fault zone is around 5-10 cm and the offset is around 20 cm in the underground outcrop. Contrary to this small-scale fault Figure 2-2 B exhibits a seismic section through the Parihaka Fault, which is located along the western margin of the Taranaki Basin. The Basin is west of the North Island of New Zealand and shows backarc rifting to the Hikurangi Through, where subduction of the Pacific Plate under the Australian Plate occurs (Walcott, 1987; Stern & Davey, 1989; Nicol et al., 2005; Stagpoole & Nicol, 2008; Stern & Nicol, 2008).

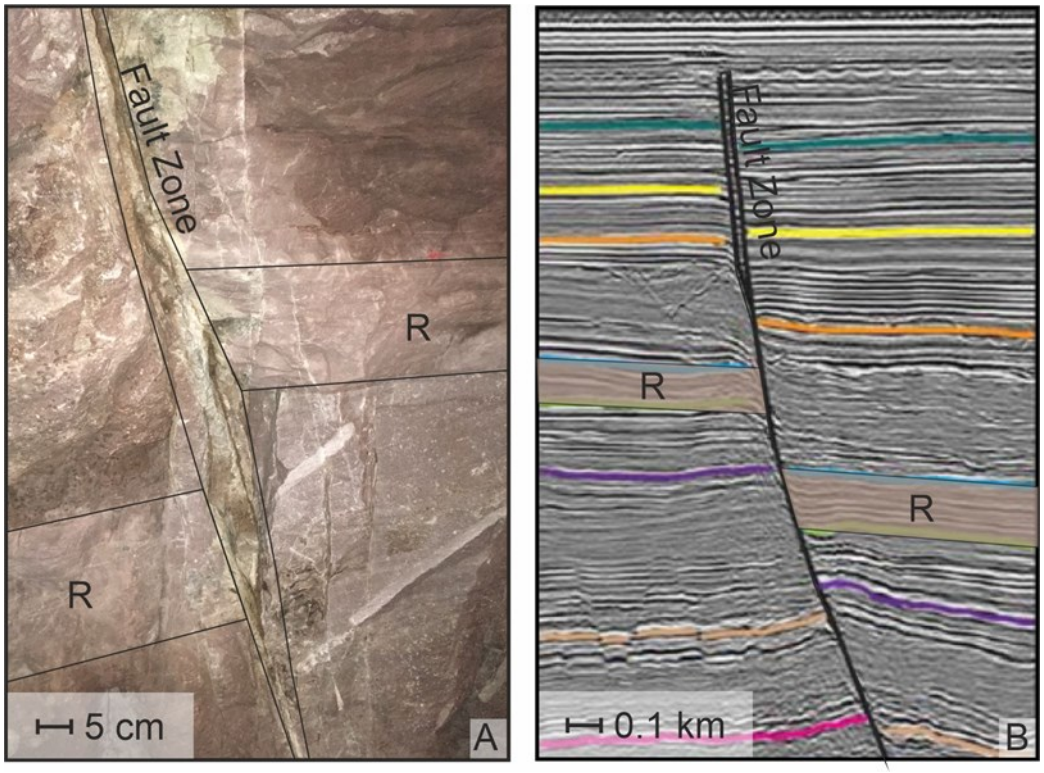

Figure 2-2: Examples of fault in the subsurface offsetting a horizon (R) on different scale. (A) represents a small-scale reverse fault pictured in visitor mine Neubulach, Germany. (B) shows seismic section through the upper part of the Parihaka Fault from the Taranaki Basin, New Zealand (modified from Giba et al., 2012).

The backarc rifting reactivates large north-south striking normal faults in the Taranaki Basin leading to displacements of up to 3 km. The Parihaka Fault shows a multiphase deformation history including

extension during the Late Cretaceous to Early Eocene (ca 84–50 Ma) and contraction from the Late Eocene to Recent (ca 40–0 Ma) as well as the backarc extension ongoing since the Late Miocene (12–0 Ma, Ballance, 1976; King & Thrasher, 1992; Holt & Stern, 1994).

While small-scale faults show relatively short offset and therefore movement and deformation along the fault plane, large fault zones, especially plate boundary faults such as the San Andreas fault or the North Anatolian fault, can offer displacements of hundreds to thousands of meters. Ongoing with the deformation along fault zones, earthquakes occur and can, depending on their strength, lead to important global geological hazards like landslides, tsunami, and the destruction of infrastructure (Anderson, 1951; Wiprut & Zoback, 2002; Jaeger et al., 2007; Zoback, 2007; Faulkner et al., 2010; Gudmundsson, 2011; Serajian et al., 2016; Tanner & Brandes, 2019). While earthquakes mostly related to plate boundary fault zones on average have cost 27000 lives per year since 1990 (Guha-Sapir et al., 2011), induced seismicity related to fluid withdraw or injection to oil and gas reservoirs caused less lethal but partially still dramatic economical damage. Faults on a reservoir-scale, which are the focus of this thesis, are responsible for such induced seismicity observed for example in Strachan gas field, Alberta, Canada (Baranova et al., 2011), the Groningen gas field (De Waal et al., 2015; Buijze et al., 2017; Vlek, 2019) and producing areas of the Permian basin, Texas, USA (Frohlich et al., 2016; Lund Snee & Zoback, 2018; Skoumal et al., 2020).

2.3. Reservoir-Scale Faults and Implications for Modeling

Considering reservoir-scale faults, the relative displacement is typically in the range of tens to hundreds of meters. Such faults are frequently rather complex fault zones, i.e. volumetric features, which can be described relative to the intact host rock. Such reservoir-scale fault zones normally consist of two main hydro-mechanical units: a fault core and two accompanying damage zones on either side (e.g. Caine et al., 1996; Faulkner et al., 2003; Berg & Skar, 2005; Cappa et al., 2007; Childs et al., 2009; Gudmundsson, 2011; Johri et al., 2014).

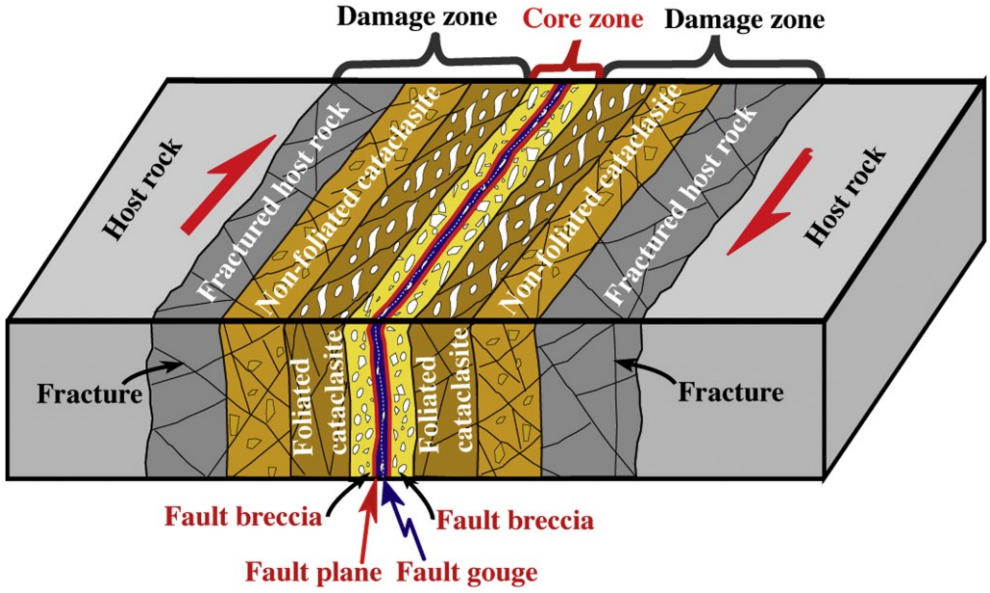

Figure 2-3: Schematic model of a fault zone containing fault core and damage zone in context of strike slip regime. Different rock units, with different material properties, are included in both the fault core and the damage zones (Aiming & Kazuhiko, 2013).

Most displacement and deformation is accommodated in the fault core and the previous host rock is transformed to fault gouge or breccia (Caine et al., 1996; Rawling et al., 2001; Billi et al., 2003). The

surrounding damage zones undergo less deformation. Hence, the undeformed host rock stays identifiable while still being typically highly fractured, especially towards the fault core, which can be continued until cataclasites are formed (Vermilye & Scholz, 1998; Gudmundsson, 1999; Guglielmi et al., 2008; Mitchell & Faulkner, 2009). Besides these two main components, various sub-zones with quite variable hydraulic and mechanical properties exist in reservoir-scale fault zones (e.g. Myers & Aydin, 2004; Braathen et al., 2009; Fasching & Vanek, 2011). Figure 2-3 schematically shows a fault zone located in southwest Japan like that, containing different rock units for the fault core as well as the damage zone for active fault zones.

The internal heterogeneity and geometrical complexity can already vary on a small scale (centimetres and less), with e.g. anastomosing slip surfaces and intervening, lenticular shear bodies in the fault core or e.g. fracture connectivity and hydrothermal overprint in the damage zone (e.g. Walsh et al., 2003; Collettini & Holdsworth, 2004). These variations highly depend on host rock lithology, pore pressure and deformation history and therefore vary from fault to fault (e.g. Wibberley et al., 2008; Faulkner et al., 2010).

This richness of detail of a fault zone cannot be captured in a reservoir-scale FE simulation considering the size of the entire model (km to tens of km) and of individual elements (typically tens to hundreds of meters), respectively, thus upscaling techniques are necessary for fault representation in reservoir-scale simulations.

However, some recent studies conclude that in order to honor the architecture and internal heterogeneity of faults, they should be treated as volumetric features in the numerical simulations, even if the fault zone thickness seems to be negligible in contrast to the overall model and element size, respectively (Braathen et al., 2009; Fachri et al., 2013). This is considered of particular relevance for complex, intensively faulted reservoirs (Manzocchi et al., 2008; Qu & Tveranger, 2016) and could improve projects where faults are part of the full-scale reservoir model (e.g. Braathen et al., 2009; De Souza et al., 2012; Fischer & Henk, 2013).

3. Special Methods Used in this PhD

The geological rational used in this thesis is a permeable reservoir horizon embedded in impermeable over- and underburden sections and intersected by an elliptical shaped fault zone (Figure 3-1 A). For reasons of simplification, the model domain of the finite element model is limited to a slice through the center of the geological rational model, perpendicular to the fault.

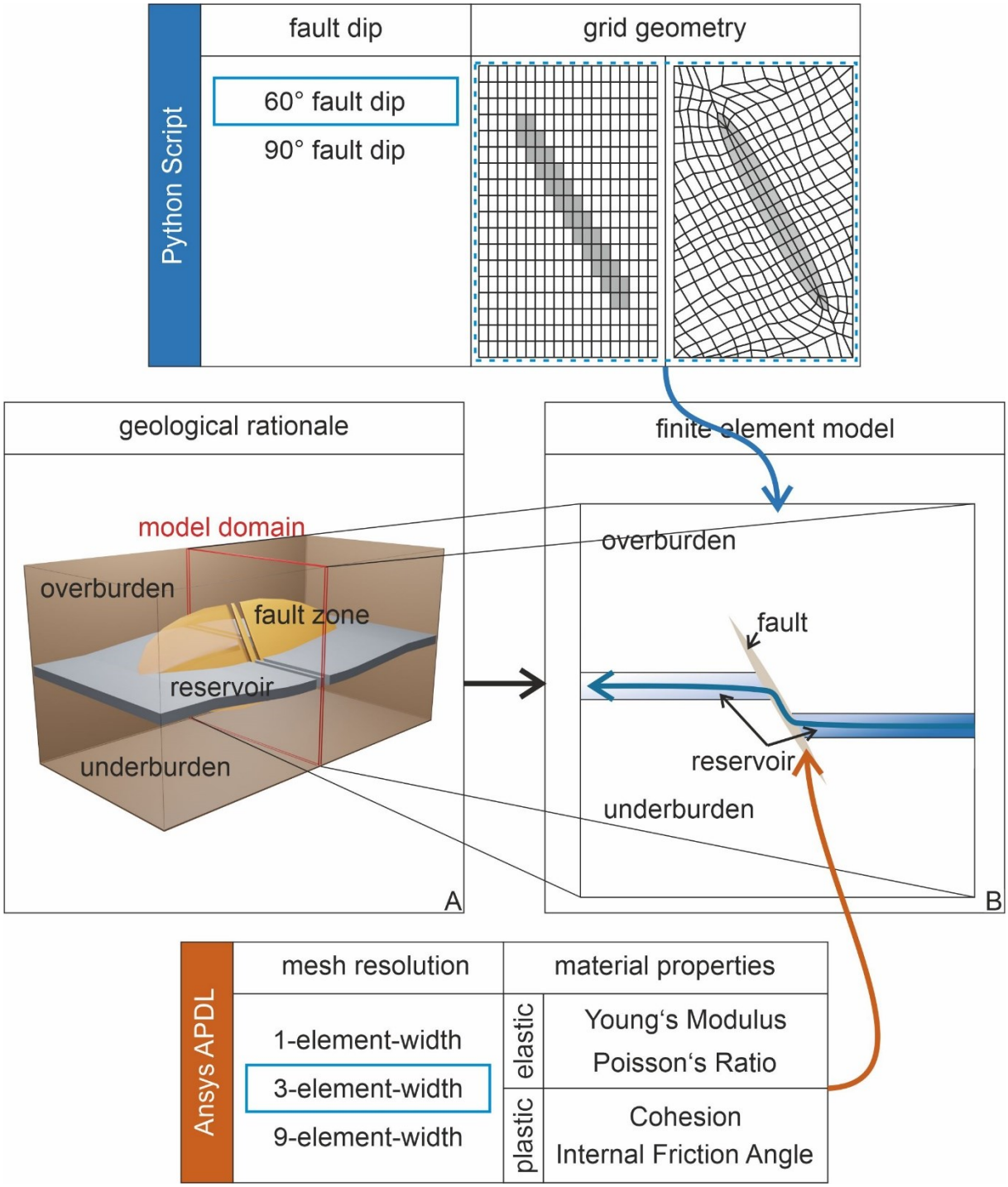

Figure 3-1: Schematic workflow done in this thesis and classification based on the implementation technique used for different parameters investigated in this thesis. Geological rational (A) is transferred to a finite element model (B) by applying a Python script which uses different fault dips and grid geometries to generate the overall model geometry. This model geometry is then meshed with a specific mesh resolution and populated with material properties in Ansys APDL

While the research presented in chapter 4 uses a 2D-plane-stress geomechanical model, not including the hydraulic part, chapter 5 & 6 utilize the fully coupled hydro-mechanical model (Figure 3-1 B). In this case, injection into the lower part of the reservoir horizon increasing constantly over a timeframe of 5 years is simulated. The fluid migrates through the semipermeable fault zone up to the higher part of the reservoir and thereby initializes plastic deformation along the fault plane. The Finite Element Analyses is carried out with the commercial software Ansys (Ansys, 2019). The exact model geometry, dimensions and boundary conditions as well as the specific material properties assigned are introduced in the methods section (Chapter 4.4., 5.4., 6.3.) for each study as part of the related research article. The section in the review articles also contains the constitutive laws relevant for each study. For this reason, these methods are not repeated here and this chapter focuses on methods and techniques used to simplify the workflow done during the numerical studies.

Since this thesis and the related sensitivity studies required many models, automation and fastening of the workflow was a key issue. Generating different model geometries in Ansys (Ansys, 2019) can be very time consuming. To overcome this obstacle, different scripts using Python 3.6 (Van Rossum & Drake, 2009) are programmed. These scripts can generate a geometrical model, based on different input values described in the following sections 3.1. & 3.2. The main purpose for this thesis is to enable the modeler to quickly generate different fault zone geometries based on the fault dip and the grid geometry of the numerical model (Figure 3-1). The script is based on the assumption of point symmetry throughout the whole model area. In order to achieve this, the midpoint of the fault is simultaneously the origin of the coordinate system used to calculate the model points. This thesis uses two grid geometries, namely the rectangular and curvilinear grid for the volumetric weak zone approach. The main difference between both is whether the grid is adapting to the fault zone – curvilinear grid – or the fault zone properties are assigned to a preexisting rectangular grid and are described in detail in chapter 4.3.1. – 4.3.3. & 5.2.2.

The Python scripts provide an Ansys command file including all needed geometry commands i.e. model keypoints, areas and volumes of each material domain. Based on this file, the element size and thereby the mesh resolution inside the fault zone is defined in Ansys APDL (Ansys, 2019) and the finite element model is generated. Also, the material properties for every material domain are defined through Ansys APDL. This workflow allows the fast and easy generation of a multitude of model set ups needed to carry out the different sensitivity studies done in this thesis. The boundary conditions and the pore pressure increase remain the same for all models computed in one study. They are assigned through Ansys before finally running each simulation.

3.1. Python Script to Generate a Curvilinear Fault Zone Geometry

The length, width and dip of the fault, the top and thickness of the upper and lower reservoir section as well as the model dimensions in x- and y-direction are only input values needed for the curvilinear grid. Going out from the midpoint of the fault (Figure 3-2 A), the endpoints of the fault model, i.e. the fault tips (FT-1 & FT-2) and the points with the largest distance parallel to the middle of the fault (FW-1 & FW-2) are calculated by using the congruence theorem ASA (Cox et al., 2005; Pickover, 2009). Based on these four points, two circles, on for each side of the fault zone, are computed using three-points-on-the-circle-Mehod (Figure 3-2 B). The circles contain both fault tips and one of the FW-1 or FW-2 and the output variable received from this function are the radius and the center of auxiliary arc. In the next step, the law of cosines (Cox et al., 2005; Pickover, 2009) which is:

$$c^2 = a^2 + b^2 - 2 \cdot a \cdot b \cdot \cos\alpha \tag{3-1}$$

can be reorganized to calculate the angle between FT-1 & FT-2 by using the fault length (fl) and the radius (r) as following:

$$\alpha = \cos^{-1}\left(\frac{2 \cdot r^2 - fl^2}{2 \cdot r^2}\right) \quad (3\text{-}2)$$

The angle between FT-1 and FT-2 is then divided equally and associated points on the circle are calculated, all having the same distance to their neighbours (Figure 3-2 D). This workflow is necessary since Ansys has difficulties in representing a curve in its finite element grid. In order to overcome this difficulty and still model a curvilinear fault zone, the curvilinear fault surface is divided into small parts, i.e. straight lines between the equally separated points on the surface. The points are generated in Ansys by the input of their coordinates (x/y/z). During this generation process, a number to identify each point is also assigned to the points. These numbers are later used to generate an area or volume of the model in Ansys. To automate this process with Python, it is necessary that sequential identification number are also assigned to sequential points on the curvilinear surface. Due to the geometric technique used, it is relatively easy to get the points generated to model the curvilinear surface in order. However, it remains a problem to get the intersection between the reservoir sections and the fault zone at the right position in this sequence (Figure 3-2 E). The reservoir dimensions are input parameters and hence can vary, so the exact position in this sequence of points representing the curvilinear fault surface also varies. Consequently, this position has to be estimated every time the script is used to generate a model geometry. This is done by a three step process with first calculating all possible intersections between the reservoir boundary and the straight line between two consecutive points on the curvilinear suface (Figure 3-2 F). Second, the Python script evaluates which intersect is located between two points on the curvilinear surface as well as the identification number of these two points (Figure 3-2 F). Lastly, the script assigns the higher identification number to the intersect and raises the following numbers in the sequence by one. With the curvilinear fault zone defined by points on its curvilinear surface and the reservoir section by their intersect, the only missing points are the edges (Figure 3-2 G) which are calculated from model dimensions in x- and y-direction.

Aside from those points which are called 'Keypoints' in Ansys, the Python script also defines the Ansys-'areas'-command for every material domain – host rock, reservoir and fault zone - later used in Ansys to define areas by these keypoints.

Thus, the 2D model geometry for the curvilinear fault representation is defined by the Python script only by the variables length, width and dip of the fault, the top and thickness of the upper and lower reservoir section as well as the model dimensions in x- and y-direction. Since the curvilinear fault models simulated in Ansys are 3D slices, the 2D model geometry is then extended into the third dimension by the edge length of one element.

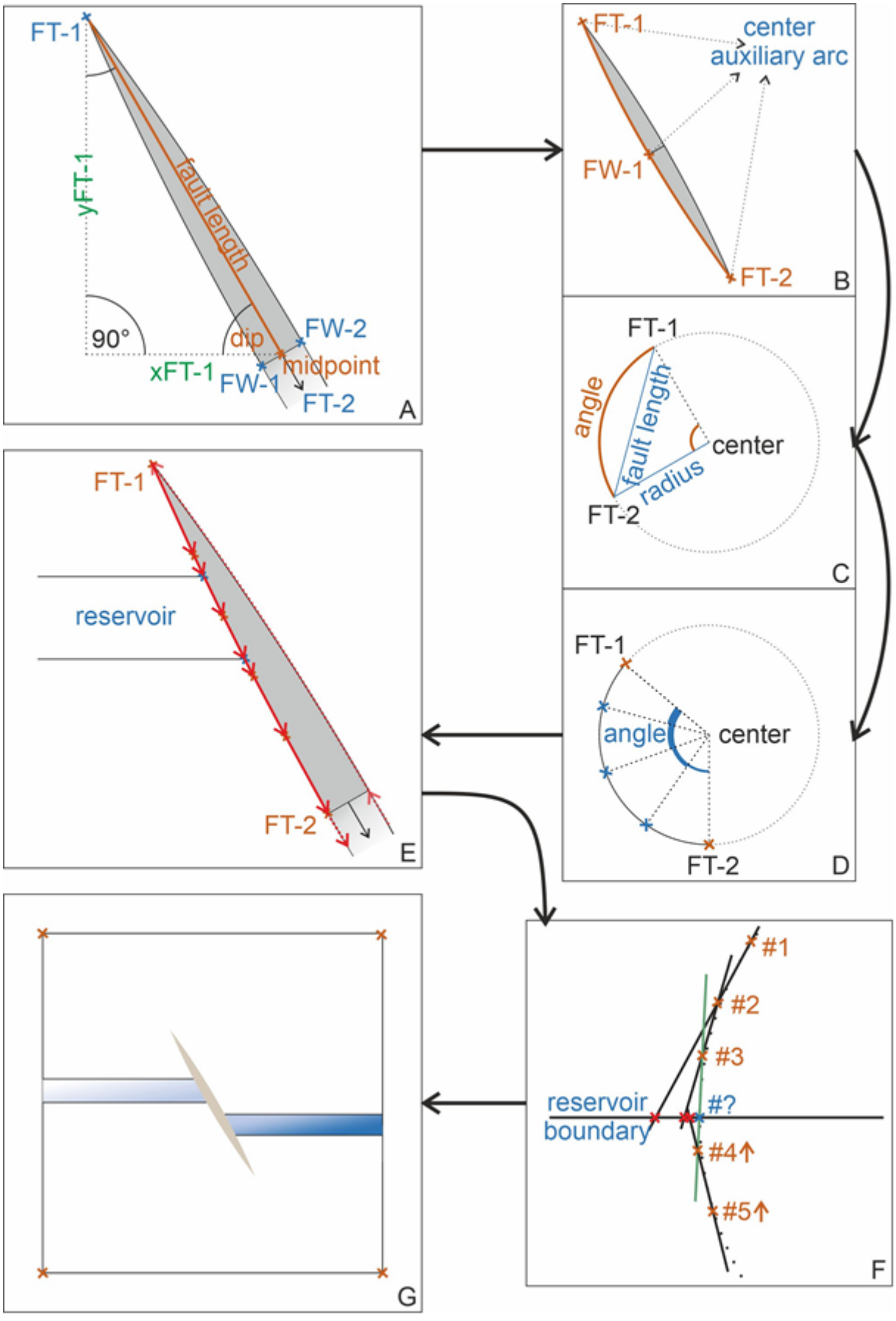

Figure 3-2: Shematic workflow and mathematic operations done by the Python script to generate a curvilinear fault zone model.

3.2. Python Script to Generate a Rectangular Fault Zone Geometry

Generating a model containing a rectangular fault zone in Ansys is the other way around. In this case the fault zone and model geometry is not generated as a starting point to then mesh this geometry in order to get the finite element model. For the rectangular representation the first step is to generate a rectangular mesh and then assign the volumetric weak zone material properties to the cells cut by the fault plane.

Again, the fault length and dip as well as the extend in x- and y- direction are used as input values. Generation of this grid, which later contains the fault zone, starts similarly to the curvilinear approach by using congruence theorem ASA (Cox et al., 2005; Pickover, 2009) to find the fault tips (FT-1 &FT-2; Figure 3-3 A). Next, fault help points (FH-1 & FH-2) are gained by combining the y-coordinate of FT-1 with the x-coordinate of FT-2 to get FH-1 and vice versa the x-coordinate of FT-1 and the y-coordinate of FT-2 for FH-2. These four points span the rectangle in which the fault zone is later assigned. Based on the dedicated element size and fault width, the number of divisions between FT-1 and FH1 as well as FH-1 and FT-2, respectively, is defined (Figure 3-3 B) and the x- and y-edge length of the elements are calculated. This concludes all calculations necessary to generate a rectangular grid with the right dimensions to incorporate a rectangular fault zone in Ansys.

To assign the volumetric weak zone properties to the associated elements of the rectangular grid, the elements have to be selected correctly in Ansys first. This is done by using so called 'paths' in Ansys, which are defined by a starting- and endpoint. To get exactly the desired elements and no additional elements, it has turned out to be efficient to choose the midpoint of the first and last element of the desired path as starting- and endpoint, respectively. In order to do so, the points are defined by using the x- and y-edge length of the elements as a measurement. For example, to get the coordinates of the starting point of the middle path, 0.5 of the x- element edge length and 0.5 of the y-element edge length are subtracted from the same coordinates of FT-1 (Figure 3-3 C). For the upper path, the same subtraction is done with 1.5 of the x-edge length and 0.5 of the y-edge length and for the lower path with 0.5 of the x-edge length and 1.5 of the y-edge length to get the associated starting point. With the starting- and endpoints for all three paths Ansys can select all fault elements and assign the fault zone material properties to create a volumetric weak zone.

The last step in the generation of the rectangular fault zone model is to get the areas of the reservoir sections. Again the calculated element edge lengths are used to define the coordinates of the intersections of the reservoir and the fault zone to be exactly the corner of a fault zone element (Figure 3-3 D). This is necessary to ensure that Ansys creates a rectangular grid for the whole model domain, since the software otherwise tends to use different element shapes for a smooth transition between the reservoir and fault zone grid. The number of x- and y-element edge length subtracted from the respective coordinates of the midpoint are chosen by the offset of the reservoir sections and the thickness of the reservoir.

With the rectangular fault zone defined by the starting and endpoints of the paths intersecting the rectangular grid and the intersection of the fault zone and the reservoir section by the coordinates of the corner of the dedicated fault zone element, the only missing points are the model edges (Figure 3-3 E) which are calculated from model dimensions in x- and y-direction.

Please note that generating a rectangular grid in Ansys is not the common way to model a fault zone and the shown method does not allow to choose every parameter one would normally choose freely. The elements x- and y-edge length used to create the rectangular grid are somewhat increments limiting the variation of the fault width, reservoir top and bottom as well as offset. The comparison of the rectangular and curvilinear fault zone representation done in chapter 5 therefore requires very precise considerations and calculations to get a similar model geometry for both models. Despite these

difficulties Ansys is chosen to be the only software used in this thesis in order to eliminate any effects the different software code may has on the simulation results.

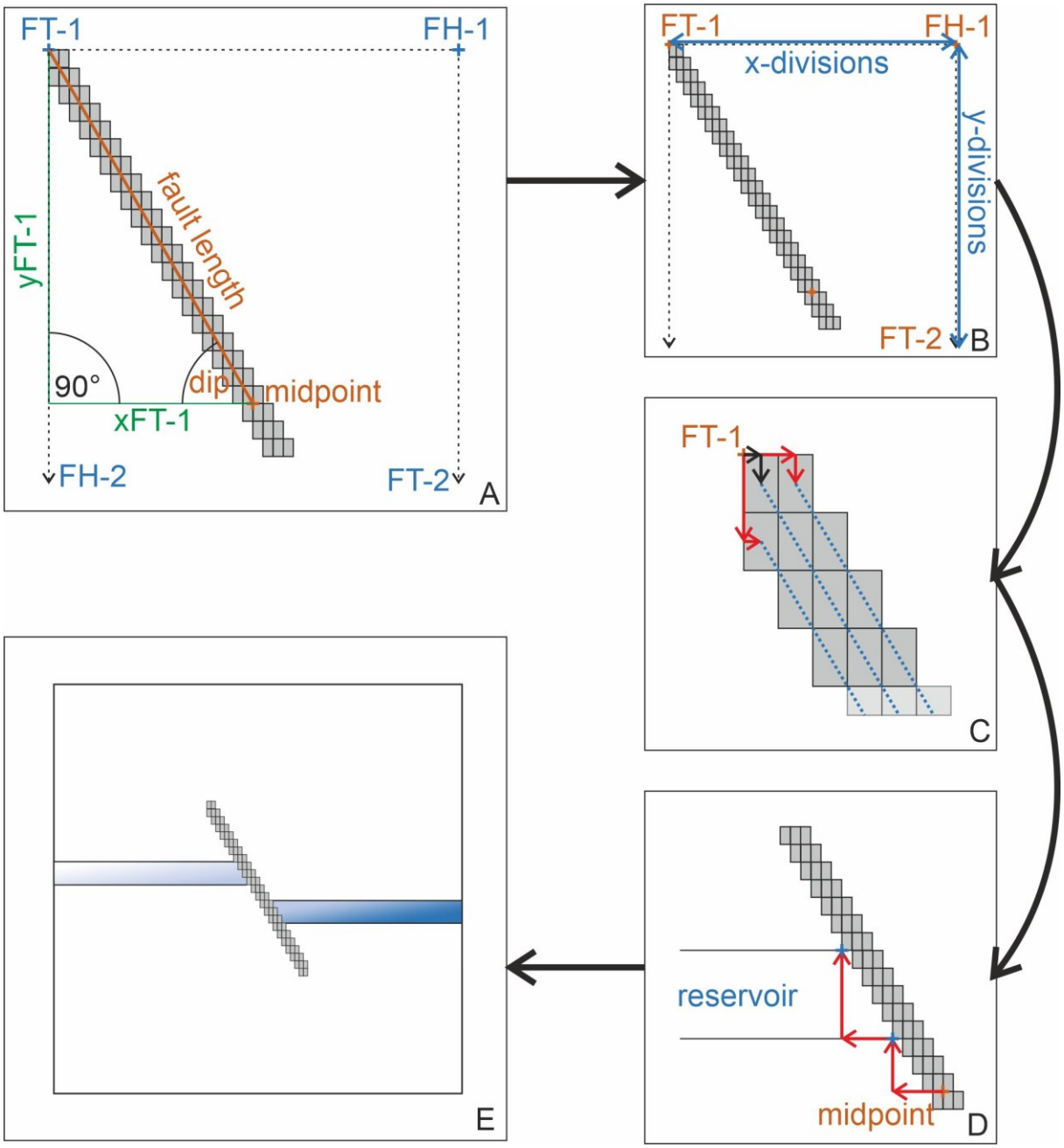

Figure 3-3: Shematic workflow and mathematic operations done by the Python script to generate a rectangular fault zone model.

4. Representation of Faults in Reservoir-Scale Geomechanical Finite Element Models – a Comparison of Different Modeling Approaches

Torben Treffeisen & Andreas Henk

TU Darmstadt, Institut für Angewandte Geowissenschaften, Schnittspahnstraße 9, 64287 Darmstadt, Germany

Published in: Structural Geology 131 (2020): 1-12, (https://doi.org/10.1016/j.jsg.2019.103931)

Abstract

Different approaches exist to incorporate faults in reservoir-scale geomechanical models. Challenges are the proper representation of the fault geometry as well as the small-scale variations in the internal architecture and the mechanical properties of the fault zone regarding the typical size of such models, i.e., kilometres to tens of kilometres. The present study utilizes a simple generic fault zone model to compare three different possibilities commonly used to represent faults in finite element reservoir models. Two differ in the basic grid geometry and the arrangement of mechanically weak fault zone elements, respectively. The third uses a discontinuous grid and contact elements to represent the fault. Modeling results show remarkable differences in the calculated stress and strain patterns. The relatively strongest perturbations result for a continuous curvilinear grid adapted to the fault geometry. In contrast, the fault implementation has the least impact on local stresses and strains if it is represented as a stair-step structure contained in a rectangular grid. The use of contact elements has an intermediate effect. Modeling results are used to infer some general recommendations concerning the appropriate approach of representing faults in a numerical-geomechanical reservoir models depending on fault geometry, model scale and scope of interest.

4.1. Introduction

Over the past two decades, geomechanical modeling has proven to be a valuable tool to gain quantitative insights into the spatial distribution of stress and strain on the reservoir scale (e.g. Fisher & Jolley, 2007; Ferronato et al., 2008; Orlic & Wassing, 2012). Different numerical modeling techniques have been applied, e.g., finite difference (FD), boundary element (BE), discrete element (DE) and hybrid methods (e.g. Jing & Hudson, 2002; Hilley et al., 2010; Fournier & Morgan, 2012; Cappa & Rutqvist, 2011; Zhang et al., 2015), but the most commonly used approach is the finite element (FE) method which is also in the focus of the present study. The lateral size of such FE reservoir models is typically in the range of kilometers to tens of kilometers and applications vary from hydrocarbon and geothermal reservoirs to sites for underground gas storage (e.g. Croucher & O'Sullivan, 2008; Jayakumar et al., 2011; Nasir et al., 2015). In order to provide a realistic subsurface representation for robust stress and fracture predictions, the reservoir models frequently have to consider faults in addition to lithostratigraphic horizons, i.e., discontinuities offsetting the strata. Such faults are not only sites of discrete deformation but they can also cause stress perturbations, i.e., local changes in stress magnitude and orientation differing significantly from the regional trend (e.g. Yale, 2003). Thus, an appropriate representation of the faults in a geomechanical reservoir simulation is of critical importance for the reliability of the numerical model predictions. In addition, it also depends on the aim of the geomechanical modeling work, which is closely related to the scale of the study. Geomechanical simulations can be large-scale models comprising areas of several thousand kilometers edge length in order to examine plate tectonic processes and large-scale stress patterns (Buchmann & Connolly, 2007; Hergert et al., 2011). At the reservoir scale, models typically concentrate on the prediction of local perturbations in stress orientation and magnitude which is important for the optimal orientation of horizontal well trajectories and hydraulic fracture planning. Other applications are related to pore pressure changes leading to surface subsidence or induced seismicity resulting from

fault reactivation (Rueda et al., 2014; Sanchez et al., 2015). Even smaller-scale geomechanical models can be used to study topics like wellbore integrity (Fontoura et al., 2013; Feng & Grey, 2018).

Two main challenges arise from the need to incorporate faults into geomechanical FE models: (1) How can the small-scale heterogeneity of faults and fault zones be adequately described regarding the typical cell size of FE reservoir models of tens to hundreds of meters and (2) how can the geometry of the FE grid properly honor the fault geometry? In order to tackle these questions, we start with a brief description of how faults look like in reality and review some concepts to incorporate their geometrical and petrophysical characteristics in reservoir-scale numerical simulations. Various approaches have been used hitherto which differ fundamentally regarding the basic grid geometry, the element types and the mechanical fault characterization. In this study, we use a simple generic approach to implement three different fault descriptions in a FE model and compare the impact on the modeling results, in particular, regarding the amount of strain and the extent of the stress perturbations predicted. Finally, we discuss the advantages and disadvantages of the different approaches regarding their use in geomechanical models of faulted reservoirs.

4.2. Geometrical and Petrophysical Characteristics of Reservoir-Scale Faults

Reservoir-scale faults having relative displacements typically in the range of tens to hundreds of metres, are frequently rather complex fault zones, i.e. volumetric features, which can be described relative to the intact host rock in terms of a fault core and two accompanying damage zones on either side (Figure 3-1; e.g. Caine et al., 1996; Berg & Skar, 2005; Childs et al., 2009). Thereby, the size, thickness, shape and internal structure as well as the hydraulic and mechanical properties of the various sub-zones can be quite variable (e.g. Myers & Aydin, 2004; Braathen et al., 2009; Fasching & Vanek, 2011). Even the fault core proper can already be heterogeneous on a small scale (centimetres and less) and geometrically complex with anastomosing slip surfaces and intervening, lenticular shear bodies (e.g. Walsh et al., 2003; Collettini & Holdsworth, 2004). The damage zones are characterized by abundant fracturing, but depending on host rock lithology, pore pressure and deformation history, very different dimensions have been observed (e.g. Wibberley et al., 2008; Faulkner et al., 2010). Connectivity of the fractures in this zone and a possible later hydrothermal overprint will mainly determine if the fault zone acts as barrier or conduit for fluid flow at present.

Upscaling techniques are necessary as this richness of detail of a fault zone cannot be captured in a reservoir-scale FE simulation considering the size of the entire model (km to tens of km) and of individual elements (typically tens to hundreds of meters), respectively. For hydraulic simulations the use of fault transmissibility multipliers is common practice to account for the bulk permeability of faults (e.g. Walsh et al., 1998; Manzocchi et al., 1999; Jolley et al., 2007; Myers et al., 2007). Calculation of fault transmissibility multipliers is typically based on two parameters: One is the fault permeability, which is usually estimated from empirical correlations of the fault rock shale content. The other is the fault rock thickness derived from correlations based on fault throw (Manzocchi et al., 2008). These transmissibility multipliers are then assigned to the appropriate cells separating different fault blocks of the hydraulic reservoir model to act either as barrier or pathway for fluid flow. For the description of the bulk mechanical behaviour of a fault, various concepts have been used hitherto. One option is a refinement of the FE grid near the fault (e.g., adjusted meshes of Qu et al., 2015; Fachri et al., 2016) to incorporate the different properties of the fault zone subunits (e.g., fault facies models of Fredman et al., 2008; Braathen et al., 2009). Although this reduces the difference in scale between model and reality, the basic problem remains, i.e., that the combined mechanical effect of rock and fractures has to be assigned to the various fault zone elements. Different constitutive laws ranging from simple isotropic linear-elastic to more complex elasto-plastic and strain rate-dependent visco-plastic material behaviour can be considered for the mechanics of a fault zone (Cappa & Rutqvist, 2011).

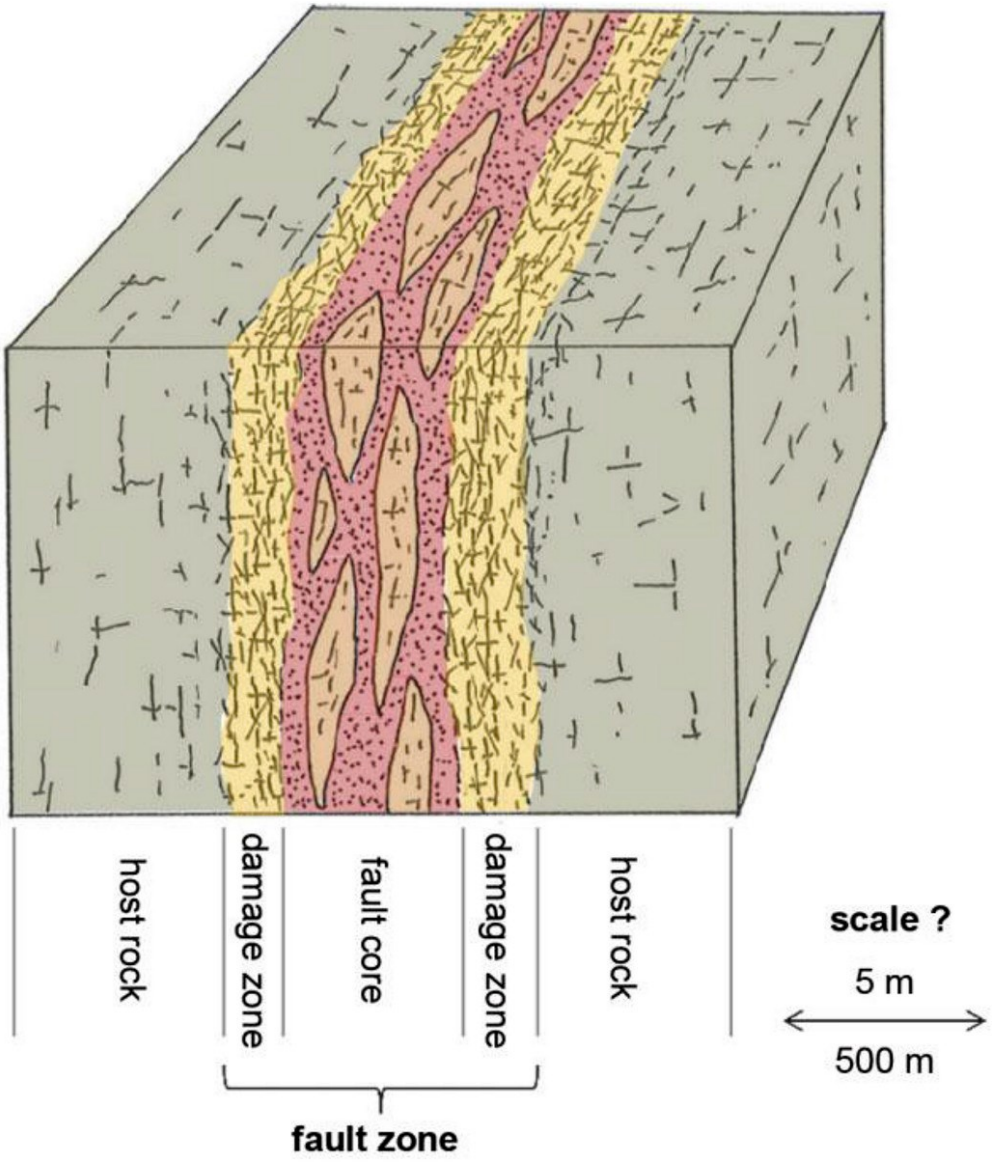

Figure 4-1: Conceptual model of the internal architecture of a fault zone consisting of host rock, two damage zones and a fault core (Fasching & Vanek, 2011).

However, the basic mechanical properties required to simulate stresses and deformation in the elastic domain are normal and shear stiffness in case of a surface representation of the fault and Young's modulus and Poisson's ratio of the fault zone rocks in case of a volumetric description. They latter parameters can be anisotropic, i.e., different in directions parallel and perpendicular to the fault zone. As a failure criterion limiting the elastic domain, the Mohr Coulomb model describing rock strength in terms of cohesion and friction angle is widely used (Barton, 2013). Thus, an approach to describe the bulk mechanical effect of a fault zone can already be the consideration of a lower Young's modulus and a lower friction angle in comparison to the undeformed host rock (De Souza et al., 2014). More advanced constitutive laws attempt to take into account the multiple joint sets and fractures that often characterize larger faults and damage zones, respectively. For example, the jointed rock model of (Will et al., 2015) incorporates up to four fracture systems with different orientations and material properties resulting in a highly anisotropic rock mass behaviour. Thus, it is a homogenized continuum approach to capture the mechanical behaviour of a fractured rock mass combining rock and fracture properties rather than the individual response of its components (Will & Eckardt, 2015).

4.3. Characteristics of Commonly Used Approaches to Represent Faults in Reservoir-Scale Models

We compare three different basic approaches used in previous studies to implement faults in FE geomechanical models (Figure 3-2). These approaches differ regarding the basic mesh geometry and whether the fault is represented as a volumetric feature with upscaled mechanical properties or as a discrete surface with zero thickness. Thereby, the appropriate representation may also differ regarding the scale and aim of the geomechanical study, e.g., it may have to be adapted depending on if reservoir- or wellbore-scale topics are addressed. Please note that this study concentrates on the appropriate representation of existing faults in geomechanical simulations rather than on modeling of fault formation, rupturing and fault propagation processes.

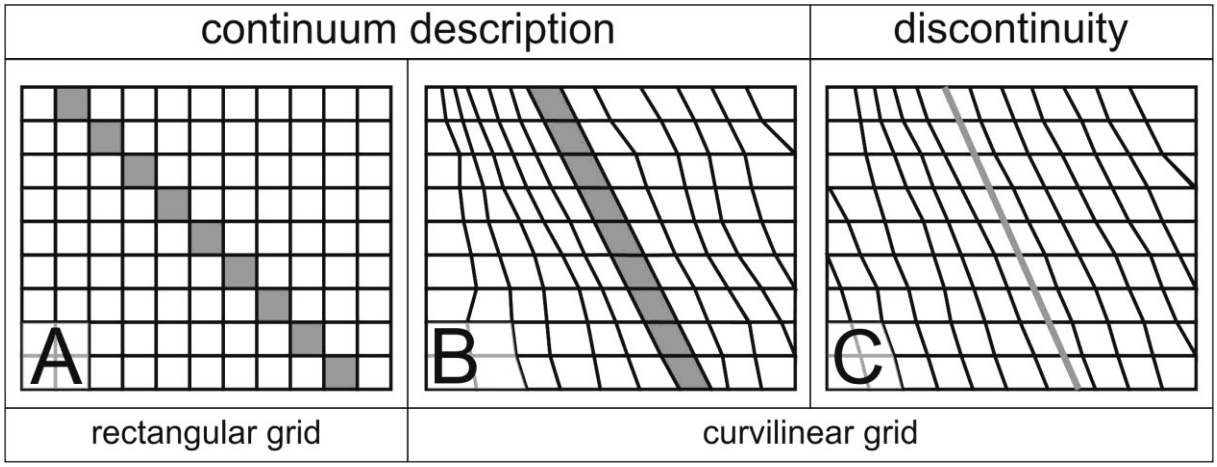

Figure 4-2: Cartoon showing the main characteristics of the different fault modeling approaches. Approach A (left) uses a continuous rectangular grid. Fault rock properties are assigned to those grid cells intersected by the fault plane. This results in a stair-step fault representation. Approach B (middle) also uses a continuous grid but in this case the grid geometry is adapted to the fault geometry. Fault rock properties hold for a continuous row of grid cells. Both approaches A and B result in a volumetric fault description. Finally, modeling approach C (right) uses contact elements with frictional properties to represent the fault as a discrete surface in the FE model. Thus, this fault zone description implies a zero thickness, but allows for discrete slip between the two independently meshed parts of the model.

4.3.1. Approach A: Continuous Rectangular FE Grid with Fault Zone Represented by a Homogenized Continuum

A commonly used approach for the representation of faults in FE reservoir models is based on a rectangular element grid (A in Fig. 2; e.g. Prevost & Sukumar, 2015; Deb & Jenny, 2017). Such a rectangular grid geometry is frequently already available from preceding property modeling and flow simulations, respectively. As it is characteristic for a classical FE analysis (Olden et al., 2012; De Souza et al., 2014), the grid is continuous and consists of numerous elements connected at common corner points called nodes. This grid is then intersected with a structural model, e.g., a fault interpretation derived from 3D seismic interpretation, and fault rock properties are assigned to those cells cut by the fault planes. Neighboring cells maintain the intact rock properties. This results in a stair-like fault geometry with a width of one element size. As the cell size is typically much larger than the thickness of the fault zone and its subunits no details of the fault architecture can be considered explicitly. Instead, the mechanical properties assigned to the fault cells have to represent the joint effects of fractured damage zone and fault core, i.e., as a homogenized continuum (Manzocchi et al., 2008; Schlegel, 2016) optionally with anisotropic properties.

4.3.2. Approach B: Continuous Curvilinear FE Grid with Fault Zone Represented by a Homogenized Continuum

In an alternative approach to represent faults in geomechanical models, the FE grid geometry is adapted to the fault geometry (B in Fig. 2; e.g. Rinaldi et al., 2013). This results in a curvilinear grid following the shape of the fault surface. The approach allows to represent the fault zone as a continuous volumetric feature rather than the stair-stepped geometry used in approach A. Studies applying this technique recommend that the fault should have a thickness of one element (e.g. Will & Eckardt, 2015; Zhang et al., 2015; Vilarrasa et al., 2017), which implies that its actual width depends on the spatial resolution of the FE mesh used. Again, the fault zone width in the model will in most cases be larger than in reality and no details of the internal fault zone structure can be depicted. As is the case for approach A, a homogenized continuum approach (optionally with anisotropic properties) has to be applied to upscale the actual heterogeneity of the fault zone to the size of the FE grid cells representing the fault.

4.3.3. Approach C: Discontinuous Curvilinear FE Grid with Fault Zone Represented by a Discrete Surface

As a third option, contact elements have been used in FE reservoir models to represent faults as a discrete discontinuity (C in Fig. 2; e.g. Buchmann & Connolly, 2007; Hergert et al., 2011; Fischer & Henk, 2013; Franceschini et al., 2016). The approach is similar to the interface elements used, for example, by Ye et al. (2018). This is an important expansion of the classical continuum approach characteristic for FE analysis, which allows for differential movements between individually meshed parts of the model. Contact and the corresponding target elements are defined at opposing sides of the pre-assigned faults. The contact elements can transmit shear and normal stresses and are capable of describing frictional sliding, usually defined by cohesion and a friction coefficient. Thus, relative displacement between corresponding nodal points occurs once the stress state at the contact elements violates the failure criterion defined (Franceschini et al., 2016). In contrast to the two previous approaches, the fault is not represented as a volumetric feature but by a line in 2D and a surface in 3D models, respectively. However, a true zero-thickness would imply infinitely high normal stiffness values to enforce compatibility between adjacent fault surfaces, which results in numerical instabilities. In practice, stiffness values similar to the Young's moduli of the rocks in contact are used which results in a certain mesh penetration at the interface.

The use of contact elements for fault representation has two important implications: (1) like in approach B, the FE grid has to be fitted to the fault geometry (otherwise the definition of discrete planes of weakness would not be possible) and (2) dual grid nodes (belonging either to the contact or to the target element) are required along the fault plane. These requirements imply the generation of a specific FE mesh with curvilinear geometry and locally duplicate nodes. This can be – depending on the complexity of the fault network – a very time-consuming and labour-intensive task, if insertion of duplicate notes cannot be completely automated.

4.4. Modeling Concept for Comparison

In order to compare the differences in calculated stresses and strains between the approaches outlined above, we set up three FE models which use the same overall geometry, the same mechanical properties of intact and fault rocks as well as the same boundary conditions. They only differ regarding the basic mesh geometry (rectangular vs. curvilinear) and the fault representation (volumetric feature with properties derived from a homogenized continuum approach vs. discrete contact surface with frictional properties). Modeling utilizes the FE software Ansys 19.1.

4.4.1. Model Geometry

For ease of result visualization, we use a 2D plane stress approach describing a vertical (strike-slip) fault and the surrounding intact rock mass in top view (Figure 3-3). The model covers an area of 3 x 3 km² and the fault length is 1150 m. Orientation of the pre-defined fault is 30° relative to the maximum displacement applied to the model side. For approach A, the total number of elements is 91,975 and the size of the elements describing the fault is 12.12 m x 7 m, respectively. For approaches B and C, the corresponding numbers are 45,840 elements and 12 m x 7 m. The difference in the element number results from a higher resolution at the grid boundaries for approach A. In the area of interest, i.e., in the vicinity of the fault, all three FE grids comprise about 20,000 elements.

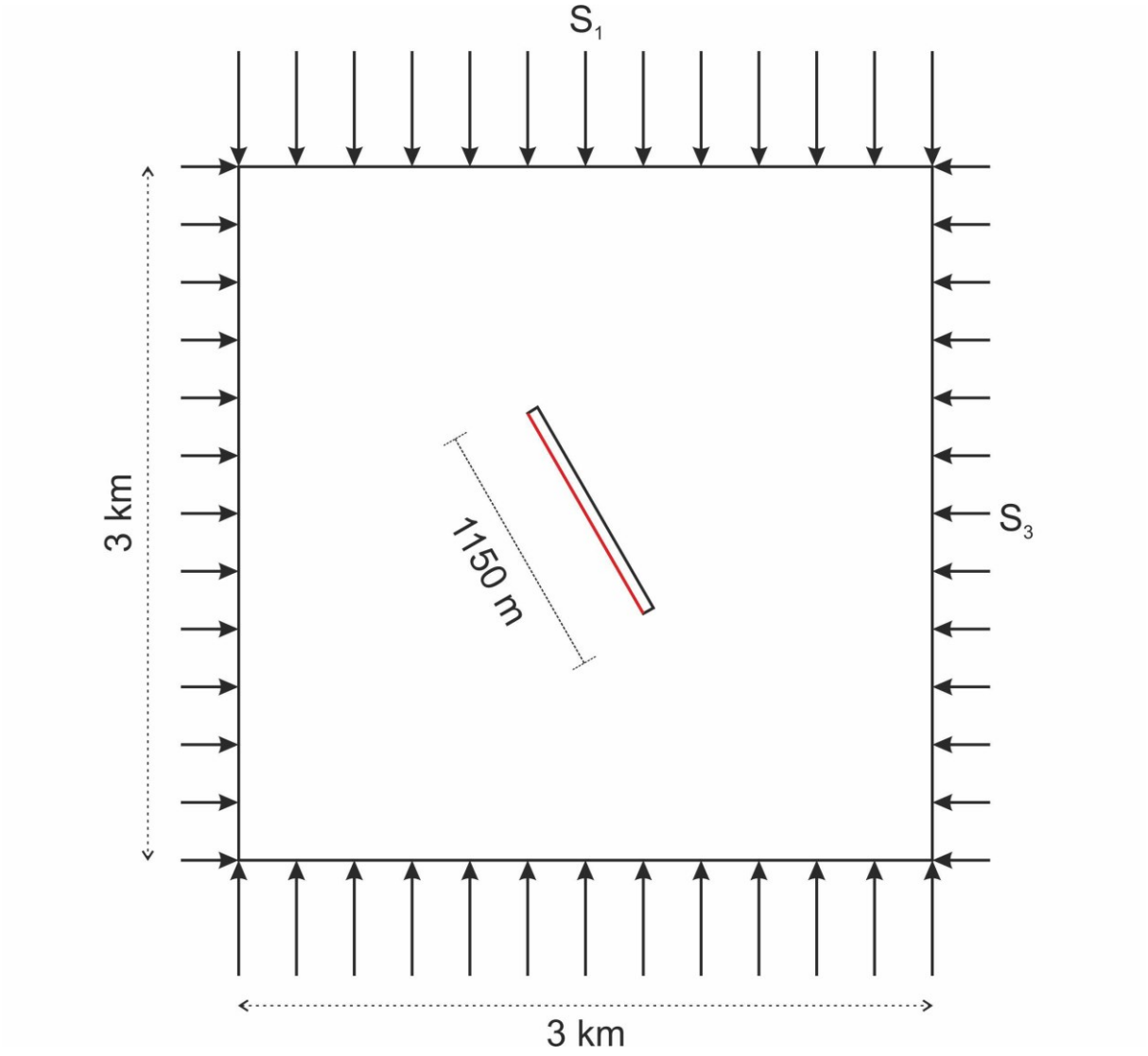

Figure 4-3: Cartoon showing the model set-up. Model dimensions are 3 km x 3 km in top view centered around a 1150 m long fault. Displacement boundary conditions are assigned to the sides of the model to generate a regional stress field with S_1 oriented in N–S and S_3 in W-E direction. The angle between the fault and S_1 is 30°.

4.4.2. Boundary Conditions

The displacement boundary conditions applied to the model are shown in Fig 3. In order to generate a strike-slip tectonic regime, 1 m of inward directed displacement is assigned to the upper (N) and lower (S) model side, whereas 0.1 m of displacement act on the left (W) and right (E) side. Thus, the regional undisturbed direction of the maximum principal stress S_1 is directed N-S.

4.4.3. Constitutive Laws and Material Parameters

An elastic – perfectly plastic constitutive law with specific parameters for undeformed and fault rocks is assumed for modeling. Material behaviour in the elastic domain is described by Hooke's Law according to

$$\varepsilon_{xx} = \frac{1}{E} \cdot \left(\sigma_{xx} + \nu \cdot \sigma_{yy}\right) \tag{4-1}$$

$$\varepsilon_{yy} = \frac{1}{E} \cdot \left(\sigma_{yy} + \nu \cdot \sigma_{xx}\right) \tag{4-2}$$

is assumed where E is the Young's Modulus, ν is the Poisson's ratio, σ is the stress (in xx- and yy-direction) and ϵ is the resulting strain (Jaeger et al., 2007). The shear failure criterion delimiting the elastic range is defined according to the Mohr-Coulomb law as

$$\tau = \sigma_n \cdot \tan\varphi + c \tag{4-3}$$

where τ is the shear stress, σ_n is the normal stress, φ is the angle of internal friction and c is the cohesion (Jaeger et al., 2007). Tensile failure is incorporated via a tension cut-off delimiting the Mohr-Coulomb failure line for tensile stresses (Figure 3-4).

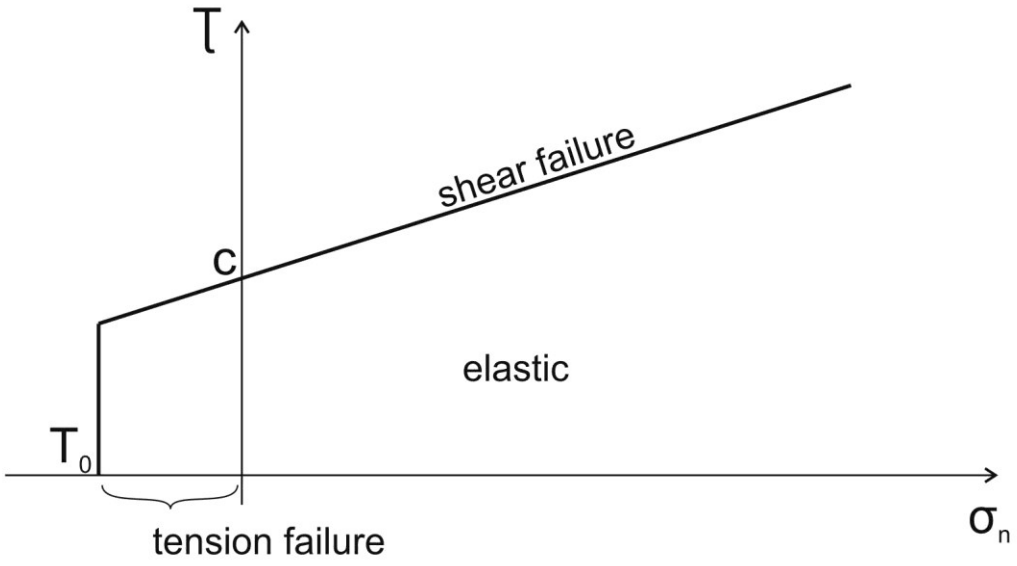

Figure 4-4: Shear stress vs. normal stress diagram showing the Mohr-Coulomb failure criterion with tension cut-off delimiting the elastic domain.

The material properties assigned to the intact rock and to the fault rock are listed in Table 3-1. For simplicity, only Young's modulus and the frictional properties are varied between the two rock types, whereas density, Poisson's ratio and tensile strength are kept the same. For approaches A and B the properties assigned to the elements representing the fault are based on a homogenized continuum describing the mechanical behaviour of fractured rock whereas the frictional properties of the contact elements in approach C use the same frictional properties which also delimit the elastic range of the fault rock in the other two approaches. A low friction angle resulting in a weak fault strength was chosen to account for the observation, that already small amounts of phyllosilicates (e.g., fault gouge, clay smearing), cataclasis and/or the presence of fluids (Faulkner, 2004; Holdsworth, 2004; Collettini et al., 2009) strongly reduces the friction angle of fault zone rocks with respect to the values suggested by Byerlee's frictional relationship (Byerlee, 1978).

Table 4-1: Mechanical parameters used for comparison of the different fault representation approaches.

	Host rock	Fault zone rock
Density [kg/m³]	2300	2300
Young's modulus [GPa]	30	20
Poisson's' ratio [–]	0.23	0.23
Friction angle [°]	40	10
Cohesion [MPa]	2	0.01
Tensile strength [MPa]	10	2

4.5. Results

In the following, the stress and strain patterns both in the surrounding of the faults as well as the fault zone itself are compared for the different approaches. Numerical simulation results are visualized by means of contour and vector plots as well as sections through the model.

4.5.1. Stress Magnitudes

The prescribed boundary conditions result in dextral displacement along the fault and a stress distribution, which is point-symmetric with respect to the centre of the model (Figure 3-5). In general, an increase in the magnitude of the maximum principal stress S_1 is observed at the upper left and lower right end of the fault while S_1 decreases at the opposite sides (Figure 3-5). However, the spatial range of this stress perturbation and the minima/maxima of S_1 differ significantly between the three approaches. The largest range of S_1 magnitudes is encountered for approach B, for which minima and maxima are 7 MPa and 81 MPa compared to the regional undisturbed S_1 of 23 MPa. For approach C using the contact elements, differential slip has occurred and a similar but less pronounced stress pattern is found for which S_1 magnitudes range between 6 and 70 MPa. The least changes in S_1 magnitudes result for approach A which is based on a regular rectangular grid. There S_1 differs only by ± 5 MPa from the regional background value. Due to the softer mechanical properties assigned to the fault elements, stresses within the fault zone are lower than in the host rock. This also holds for approach B.

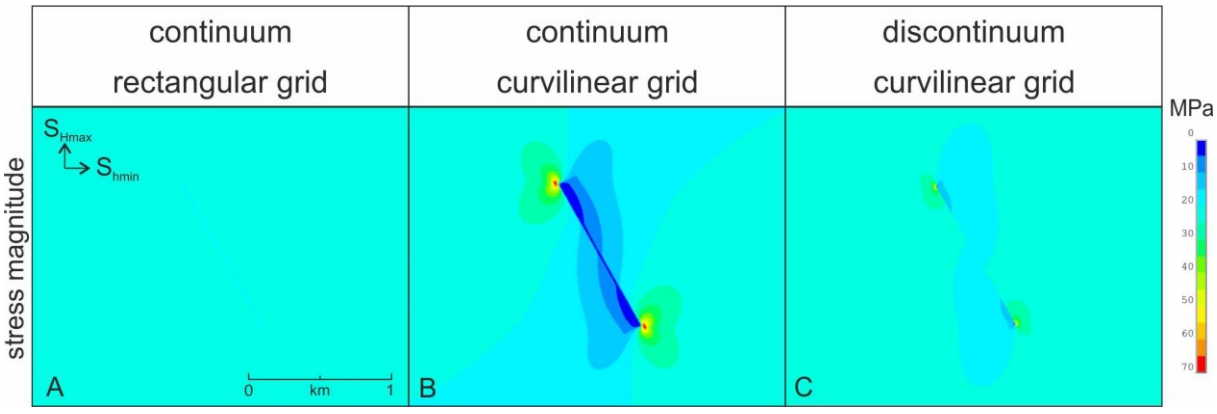

Figure 4-5: Spatial variations in the magnitude of the maximum principal stress S_1 induced by the different fault representations. Mechanical properties and boundary conditions are the same for all three scenarios studied. The same color legend is used for ease of comparison.

Sections through the midpoint of the fault zone and its immediate vicinity (Figure 3-6 left) show the small-scale variations in S_1 magnitudes for all three approaches. A rather uniform distribution can be observed for approach C, i.e., the contact element model. S_1 values decrease less than 1 MPa towards the fault zone. Approach A with the continuous rectangular grid displays an increase towards the fault cells to about 24 MPa, whereas S_1 magnitudes within the fault zone drop to about 17 MPa. The lowest stress values both in the vicinity as well as within the fault zone result for approach B. At a distance

of 50 m from the fault, S_1 magnitudes have already dropped from the regional background value to about 11 MPa and very low stress levels are achieved within the fault itself.

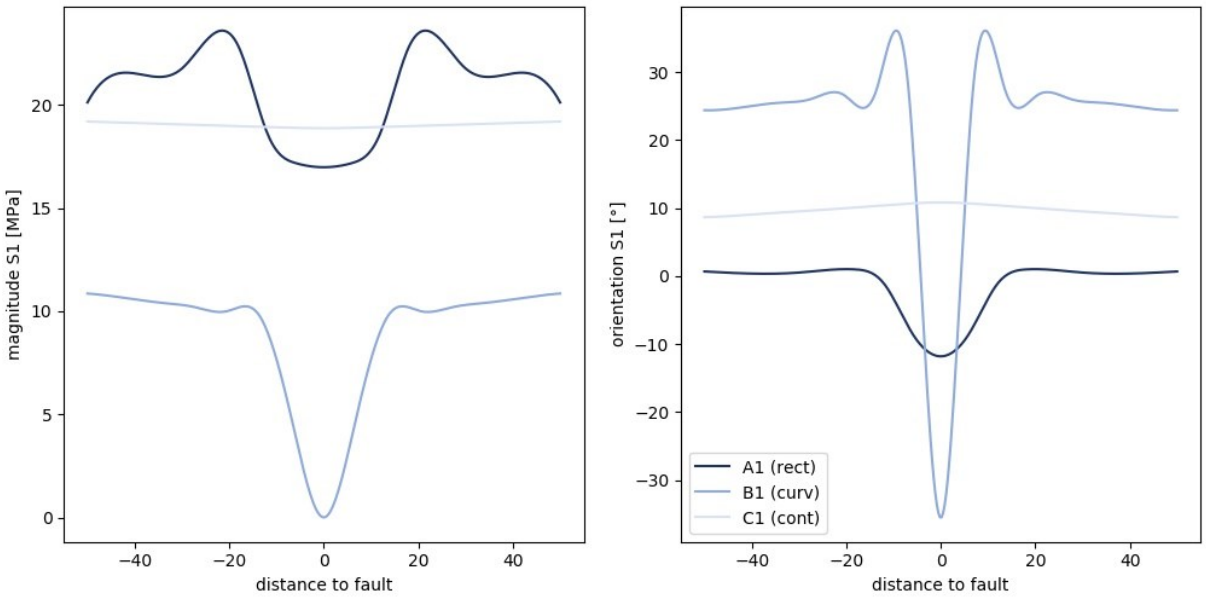

Figure 4-6: Magnitude (left) and orientation (right) of the maximum principal stress S_1 along a profile through the fault zone and its immediate vicinity. The section is drawn through the midpoint of the fault and is oriented perpendicular to the strike of the fault. For the orientation changes, negative values indicate counterclockwise rotation whereas positive values correspond to clockwise rotation. 0° corresponds to a N–S orientation of S_1 (= S_{Hmax}) and reflects the undisturbed state resulting from the imposed boundary conditions.

4.5.2. Stress Orientations

The model fault does not only lead to stress magnitude perturbations but also to significant local reorientations of the stress field. In general, the largest variability of S_1 orientations is observed for approach B which already showed the largest range of S_1 magnitudes. Local orientations differing by up to 90° from the regional trend occur especially near the fault tips (Figure 3-7). In case of approach C using contact elements these deviations are smaller and confined to a smaller region close to the fault tip. They progressively diminish towards the midpoint of the fault. The least impact of the fault is again found for approach A, where reorientations are restricted to single fault zone elements.

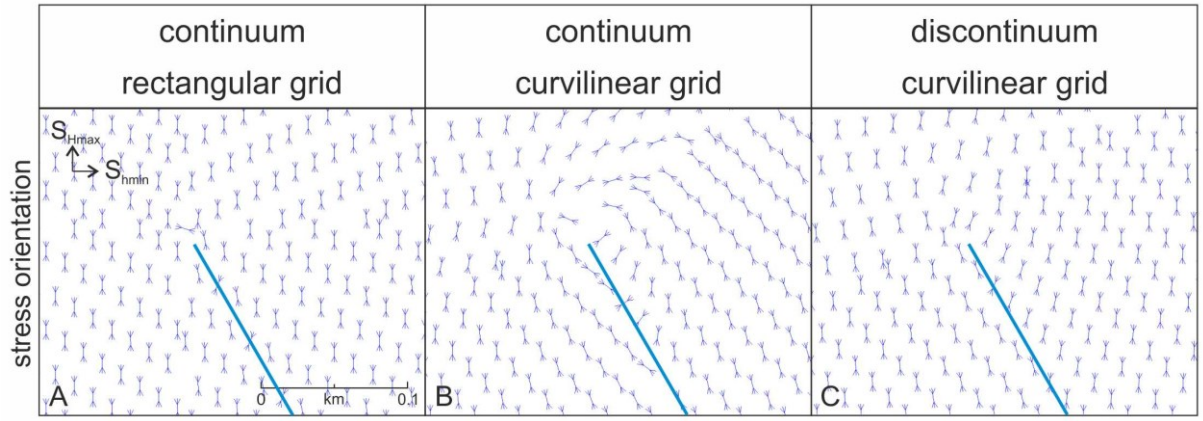

Figure 4-7: Detailed view of the orientation of S_1 (= S_{Hmax}) near the fault tip for the three different approaches.

Profiles across the midpoint of the fault zone (Figure 3-6 right) also show these differences in the orientation of S_1 (= S_{Hmax}). For approach C, only a very minor deviation from the clockwise rotation of

the stress field in the surrounding of the fault is observed at the fault itself. For approach A, counter-clockwise rotation up to 10° is restricted exclusively to the fault zone and already in the immediate vicinity of the fault no stress perturbations can be observed. The most striking changes across the fault were found for approach B: While stress orientations in the vicinity of the fault (up to 30 m distance) show up to 10° clockwise rotations on top of the regional distribution (i.e., 25° – 35° in total), stress orientation within the fault zone are rotated 30° counter-clockwise with respect to the state undisturbed by a fault.

4.5.3. Spatial Extent of Stress Magnitude Perturbations

The spatial extent of stress magnitude changes induced by the fault also differs between the three approaches. For approach B substantial variations (i.e. 10 MPa and +- 30° difference to the undisturbed stress field) occur at distances of up to 300 m from the fault. For approach C the effected region extends about 100 m around the fault. This contrasts significantly with approach A for which the stress perturbations are confined to the fault zone elements and their immediate vicinity.

4.5.4. Strain

The strain resulting from the different fault descriptions is analyzed by comparing not only the von Mises total strain but also its elastic and plastic strain components. For ease of comparison, Figure 3-8 uses a uniform color legend, whereas Figure 3-9 uses different color coding schemes to depict also the small-scale differences. The calculation results, however, are the same for both figures.

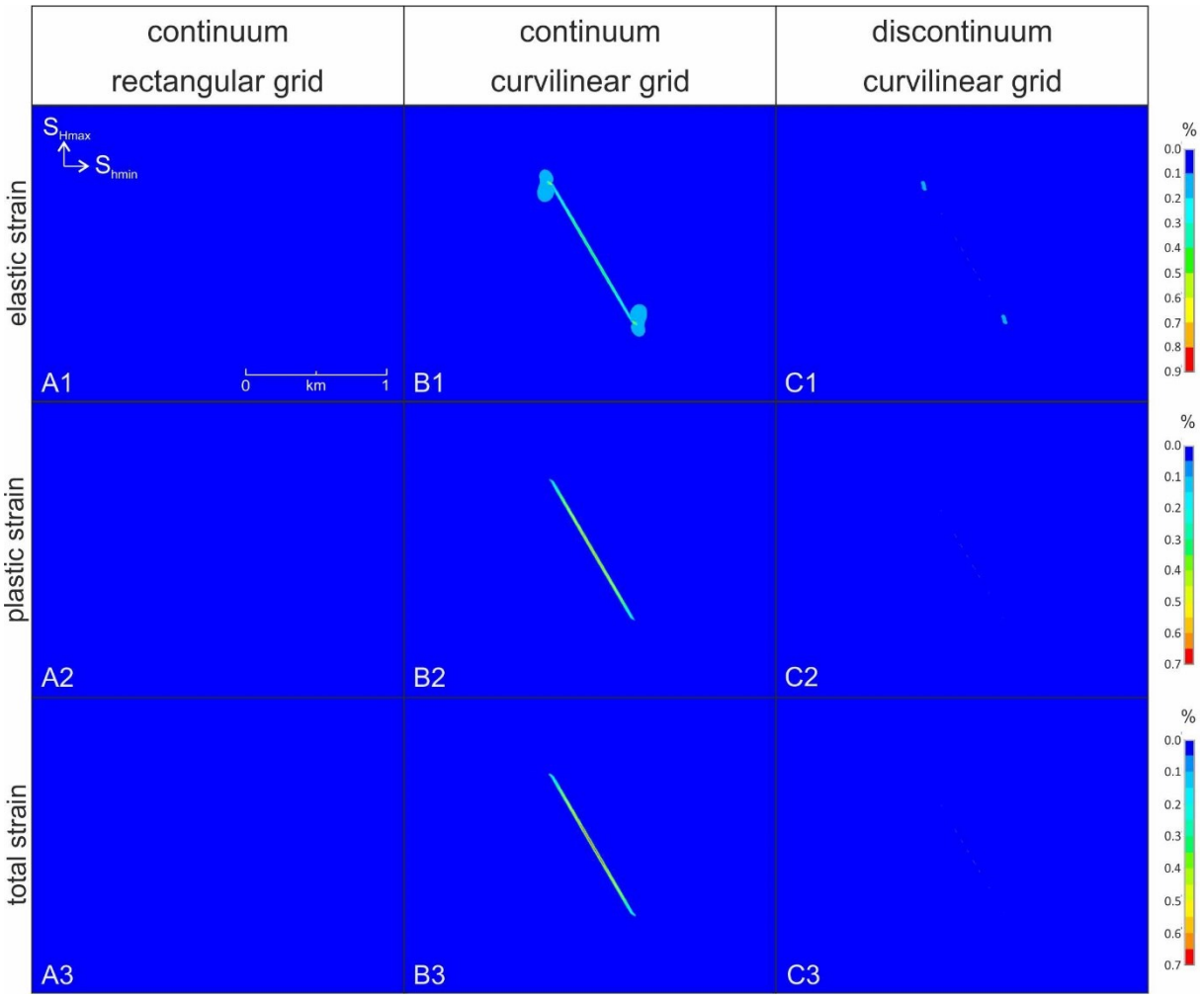

Figure 4-8: Elastic, plastic and total von Mises strain. The same color legend is used for all three simulations for ease of comparison.

Of all three simulations the elastic strain achieved in approach B using the curvilinear mesh geometry is the largest. Peak values are 0.009 and 0.9 %, respectively (Figures 3-8 and 3-9). The other two approaches exhibit much smaller elastic strains, i.e., maximal 0.0025 for approach C and 0.0014 for approach A. The plastic strain component is substantially larger, e.g., it amounts to 0.062 for approach B. This results in a total strain of 0.07 and 7 %, respectively. Much lower plastic and total strains of 0.0004 and 0.0032 are observed for approach A. Figure 3-9 shows that all fault zone elements in approaches A and B have reached the plastic limit. For approach C, differential slip along the contact elements leads to plastic straining at the fault tips only.

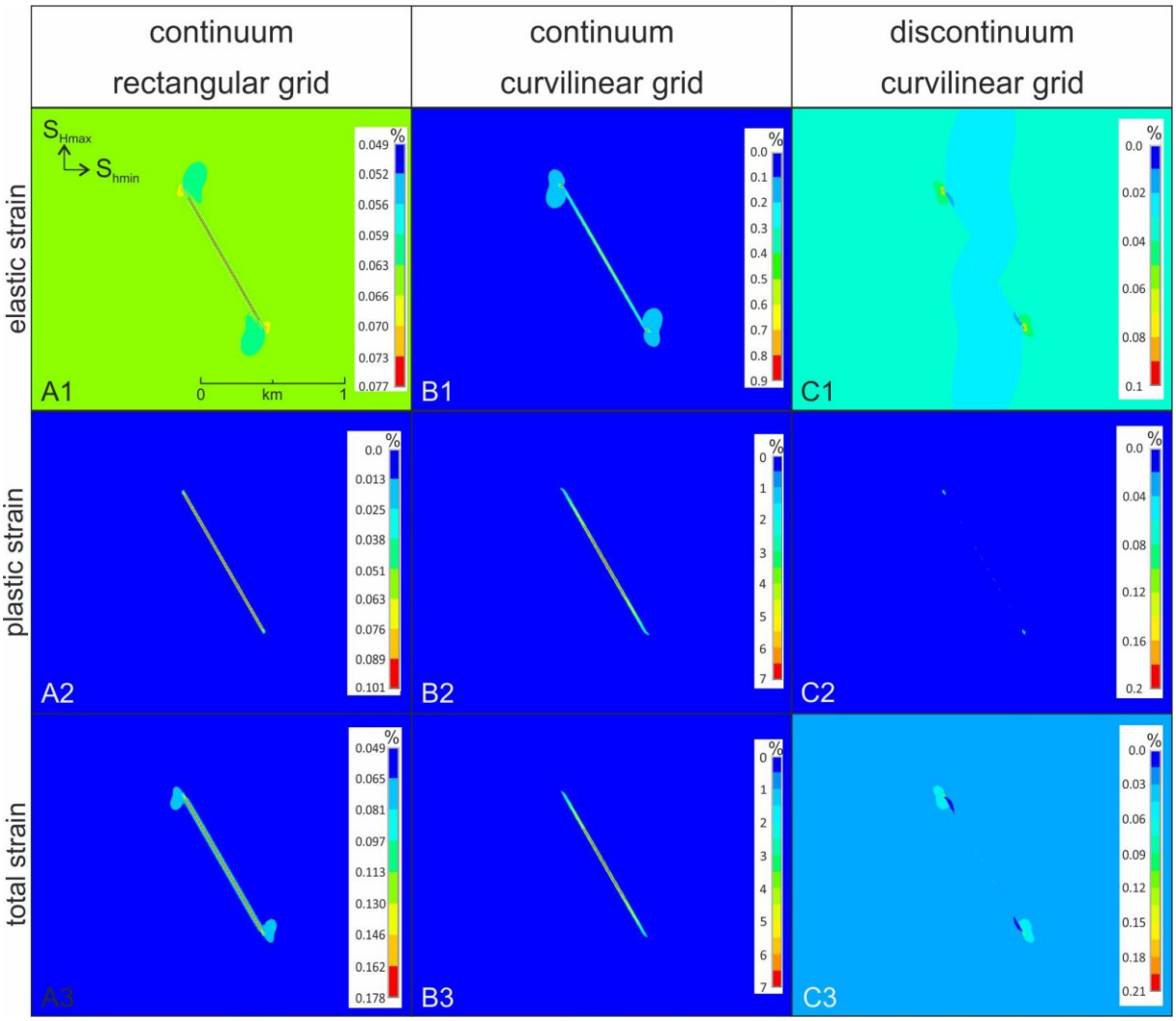

Figure 4-9: Elastic, plastic and total von Mises strain. Modeling results are the same as in Figure 3-8 but now different color legends are used to show details of the three simulations.

Details of the strain distribution in the fault zone and its immediate vicinity are shown in Figure 3-10. For approaches A and C, elastic strain is less than 0.07 % throughout the cross-section and only minor plastic straining occurs in the fault zone elements of approach A, respectively. In contrast, deformation in the connected fault zone elements of approach B accumulates to about 0.5 % elastic strain, 6.5 % plastic strain and, hence, almost 7 % total strain.

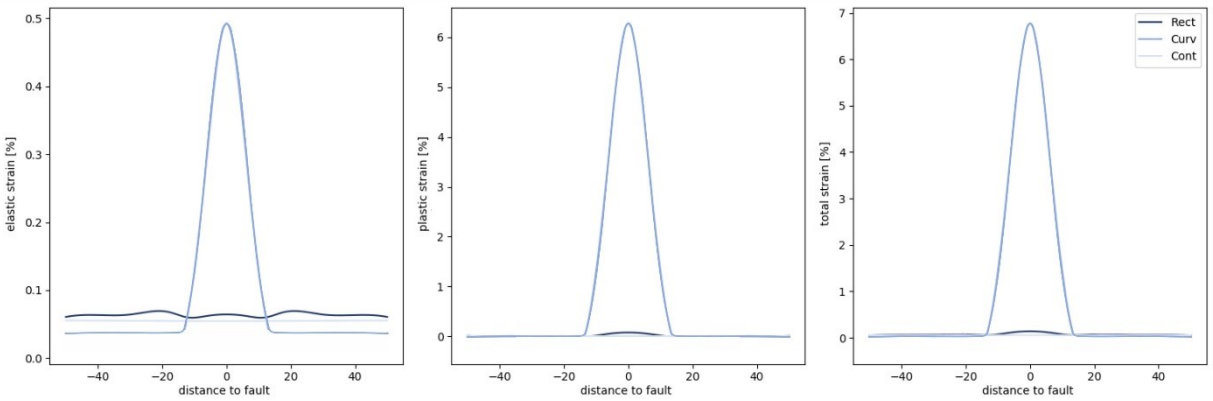

Figure 4-10: Elastic, plastic and total von Mises strain for cross-sections across the midpoint and perpendicular to the fault zone.

4.5.5. Mesh Resolution

In order to test the influence of cell size and mesh resolution, the three modeling approaches were also run with fault zone elements having twice and half the size of the reference model. No substantial differences regarding the magnitude of the stress and strain perturbations as well as their spatial extent were found.

4.5.6. Anisotropic Jointed Rock Model

The Mohr-Coulomb friction model describes plastic behaviour as isotropic. In nature, fault zones may have anisotropic properties, i.e. different parameters parallel and perpendicular to the fault. We investigate such an anisotropy by using the jointed rock model of (Will et al., 2015) with one fracture set trending parallel to the fault. The friction angle of the pre-existing fractures was set to 10°, whereas 30° were assumed for the fault rock. This results in higher stiffnesses perpendicular than parallel to the fault. For the anisotropy ratio selected only very subtle differences in the modeling results are observed.

4.5.7. Number of Fault Cells in Approach A

The stair-stepped grid of approach A assuming one element width of the fault zone cannot lead to large displacements because the intact rock elements in the surrounding interlock. In order to investigate if a band of fault cells in a stair-stepped rectangular grid can achieve similar results as a single row of interconnected fault elements like in approach B, the width of the fault zone was varied (Figure 3-11). It shows, that for the rectangular grid – for the given fault orientation and shape – already a width of the fault zone of two cells results in rather similar stress and strain patterns as the single row in the curvilinear approach. This holds for the resulting perturbations in stress magnitude (Figure 3-12) as well as stress orientation (Figure 3-13). Likewise, there are only minor differences in elastic, plastic and total strain between the two approaches, i.e., A2 with two and B with one element fault zone width.

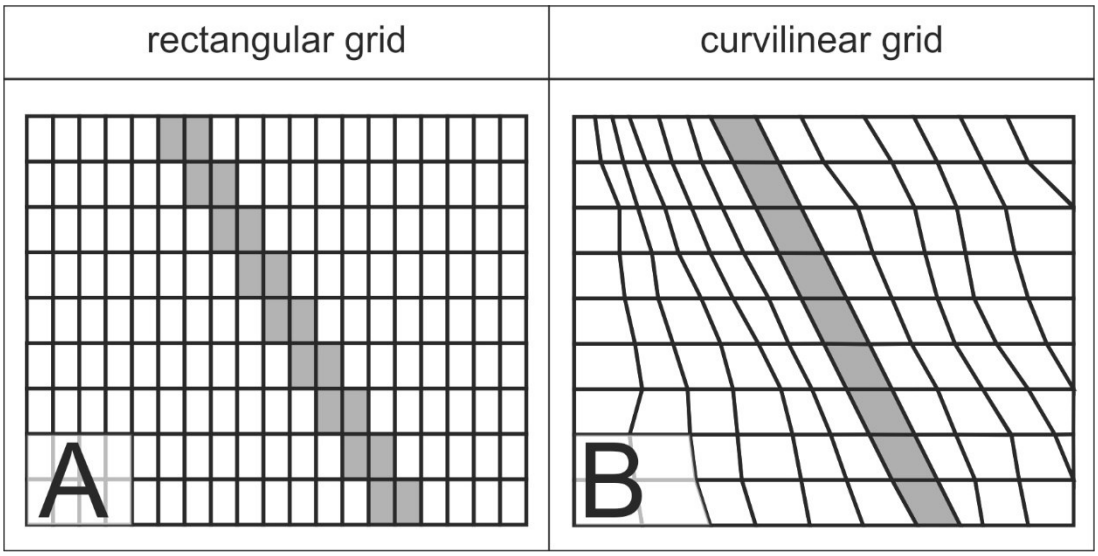

Figure 4-11: Implementation of the fault zone as a band of two cells width in a regular rectangular grid (A) in comparison to representation as a single row of connected elements in a curvilinear grid (B).

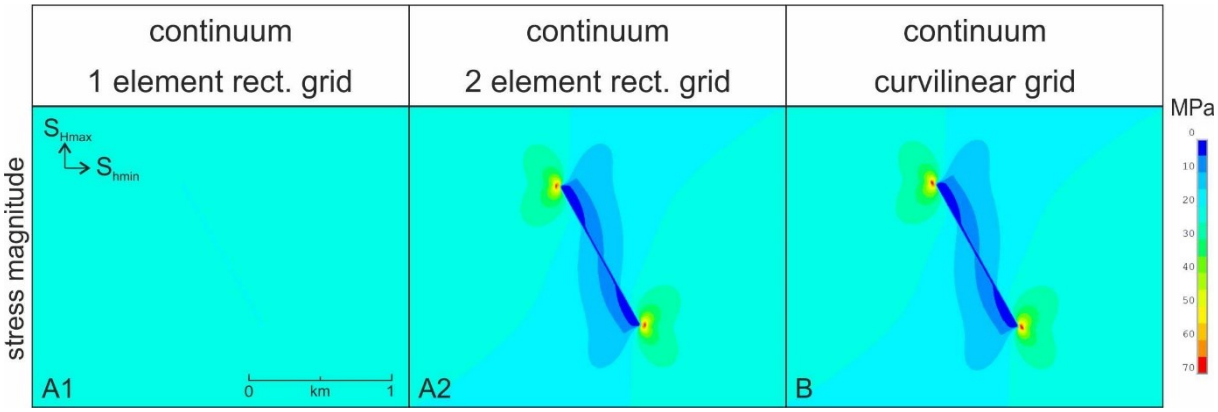

Figure 4-12: Magnitude of S_1 calculated for approach A with one (A1) and two (A2) cells width of the fault zone in comparison to the single row of connected fault elements of approach B (B).

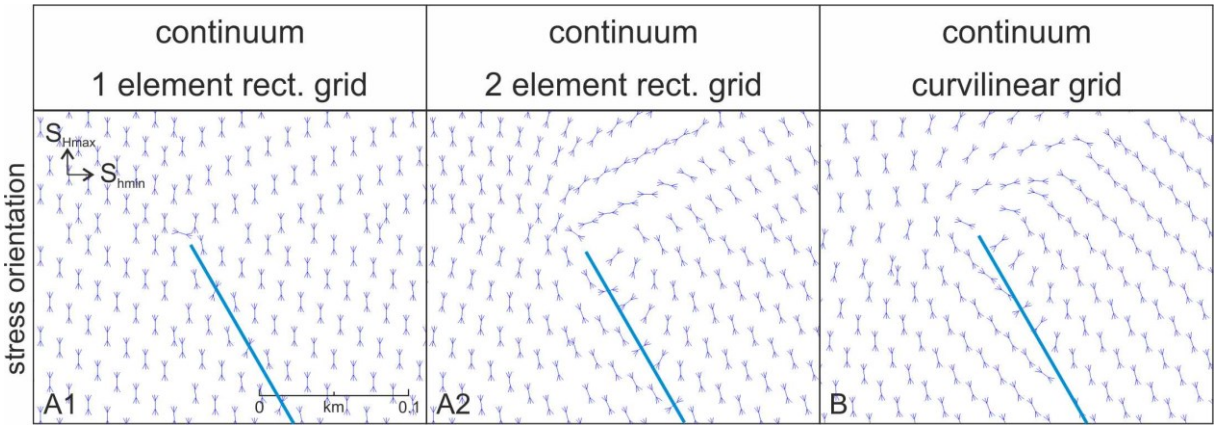

Figure 4-13: Orientation of S_1 (= S_{Hmax}) in the vicinity of the fault tip calculated for approach A with one (A1) and two (A2) cells width of the fault zone in comparison to the single row of connected fault elements of approach B (B).

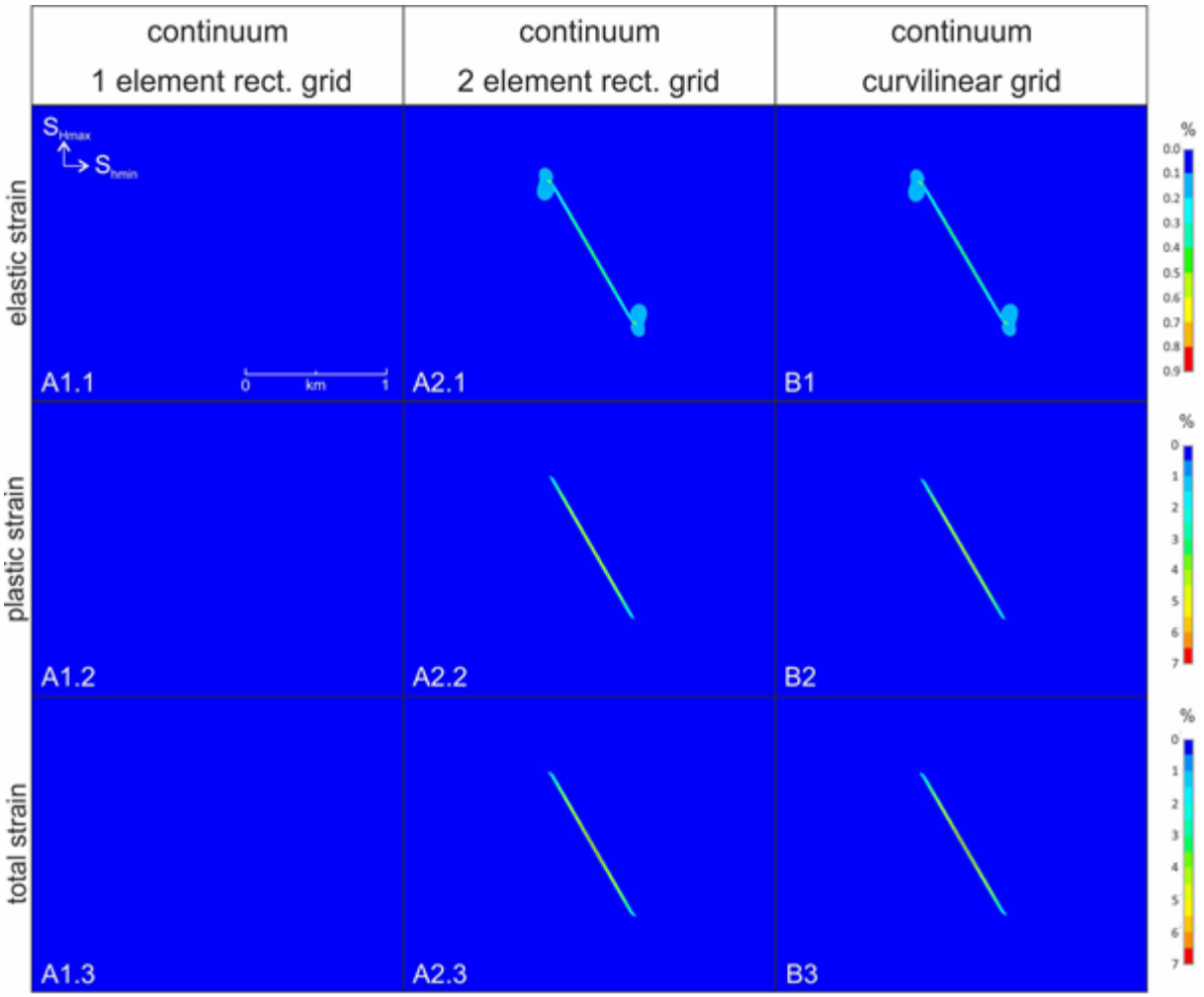

Figure 4-14: Elastic, plastic and total von Mises strain calculated for approach A with one (A1) and two (A2) cells width of the fault zone in comparison to the single row of connected fault elements of approach B (B).

4.6. Discussion

The modeling results indicate substantial differences in the stress and strain patterns as well as magnitudes induced by a fault depending on how it is incorporated in the FE model. The most pronounced effects regarding deviations from the regional trend are encountered for a fault representation which uses a continuous curvilinear grid adapted to the fault geometry and a fault representation by a continuous row of weak elements, i.e., for approach B. The fault has the least impact on stress magnitudes and orientation as well as on strain magnitudes if it is represented as a stair-stepped sequence of weak elements embedded within a rectangular grid like in approach A. A somewhat intermediate effect was found for a fault representation via contact elements embedded in a curvilinear grid which was used for approach C.

The differences between approaches A and B result from the arrangement of the elements to which fault zone properties have been assigned. In case of approach A, the stair-step grid geometry implies that fault zone elements are connected by only one common node (cp. Figure 2A), i.e. all neighbouring elements which share joint edges exhibit the stronger host rock properties. This suppresses the formation of a through-going deformation zone and delimits the strain that can be achieved within each single element. In contrast, the fault zone elements in approach B have common element faces (cp. Figure 2B) and, thus, strain can accumulate and form a continuous zone of deformation. This results in larger magnitudes of stress and strain as well as more pronounced stress orientation changes. However, it should be noted that the fault geometry selected for this comparison maximises the

difference between approaches A and B. It will progressively diminish the closer the fault geometry to be modelled is parallel to the grid orientation as more elements intersected by the fault plane will have joint edges (Figure 3-15).

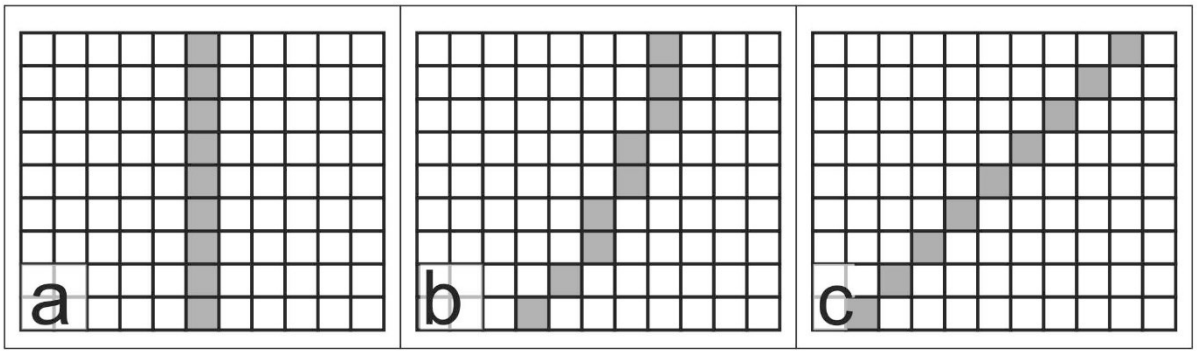

Figure 4-15: Representation of fault planes with different angles relative to the rectangular FE grid as is used in approach A. The more the fault is parallel to the grid geometry the more its effect on stress and strain approaches scenario B as more elements intersected by the fault plane have joint edges rather than only a single joint node.

Using the discontinuum approach in C, the contact element definition allows for localized differential displacements. The fault surfaces, represented by the boundaries of two independently meshed model parts and only connected with contact algorithms, are sliding past each other. Thus, initially coincident nodes of the contact and target surfaces are offset now. In contrast, the grid in approaches A and B maintains its continuity. Figure 3-16 shows the deformed grids of approaches B and C for comparison. While the element grid of the continuum model is distorted across the fault zone, the elements in the discontinuum approach are offset along the contact elements by up to 0.4 m.

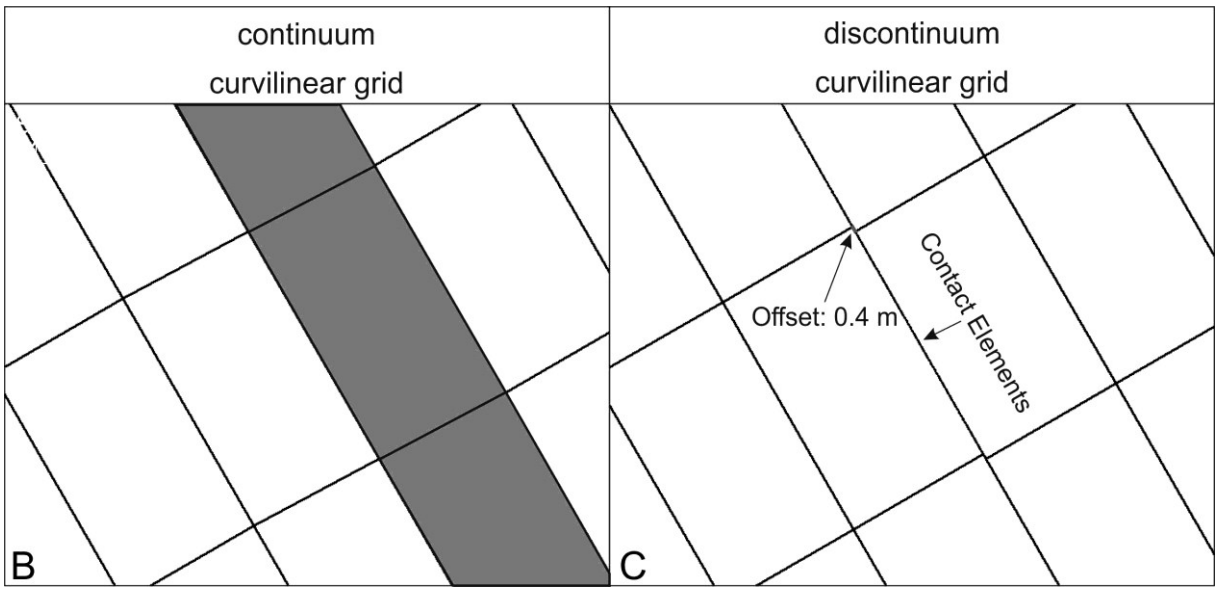

Figure 4-16: Deformed grid across the fault of the continuum approach (B) and sliding along the contact surfaces in the discontinuum model (C).

Comparing the results of approach B and approach C it is evident that within approach B nearly all the elastic strain is accommodated in one element row. In contrast, the elastic strain in approach C shows a wider spatial distribution. It affects the surrounding rock up to several hundreds of meters distance to the fault. Since both approaches have the same load and the same forces acting on the model boundaries, the same amount of energy acts on them. According to the law of conservation of energy no energy can be lost. Yet in approach B the whole energy only acts in one element row and therefore

more energy is released in one element. In contrast to that, in approach C the energy is spread out over a large space and less energy acts on each individual element. Due to that, all elements of the fault row in approach B reach the plastic limit. In approach C plastic strain only occurs at the fault tips. Reaching material failure throughout the whole fault length leads to movement within the fault elements and thus leads to the higher stress magnitudes and the higher orientation changes.

An assessment of how close the three numerical simulations actually reproduce the stress and strain perturbations induced by a real reservoir-scale fault is difficult. At present, no systematic in situ measurements mapping the changes in stress magnitude and orientation in the vicinity of such a fault are available. However, numerical modeling results can be compared phenomenologically to physical (analogue) models using photoelastic experiments (Soliva et al., 2010). Photoelasticity describes that certain transparent materials change their optical properties, i.e. birefringence, under mechanical loading. This can be used to visualize stresses within the material as isochromatic fringe patterns (Duda, 1965). Photoelastic experiments have been used to study the stress patterns about discontinuities intended to represent faults (e.g., Duda, 1965; De Joussineau et al., 2003). The corresponding stress perturbations derived from such physical models resemble more the results of the numerical simulations using approaches B and C regarding spatial extent and magnitude of the stress changes induced by the fault. Field observations suggest that the extent of stress perturbations in the vicinity of reservoir-scale faults can be very variable, i.e., between a few meters and more than a kilometre (e.g. Hickman & Zoback, 2004; Wu et al., 2007). This variability may reflect the large range in fault rock properties, fluid pressure as well as fault shape and internal fault geometry encountered in nature.

Major differences also exist between the three approaches with respect to the amount of time and work required to incorporate faults into a geomechanical reservoir model. By far the most rapid is approach A, as building a regular rectangular model (even if it is not already available from preceding property modeling or a flow simulation) and intersecting it with the fault interpretation is quite straightforward. Approaches B and C require a special grid adapted to the fault geometry and, in case of C, splitting of the grid and generation of dual nodes along the fault surfaces to be represented by the contact elements. This step can be – depending of the geometrical complexity of the fault network to be modelled – a rather time-consuming and labour-intensive task. In addition, the use of contact elements will increase the computing time.

4.7. Conclusions

Using a simple model setup, three different approaches of incorporating faults into reservoir-scale geomechanical models are analysed. The various scenarios differ regarding the basic grid geometry (rectangular vs. curvilinear) and the fault zone representation (volume elements with upscaled mechanical parameters vs. contact elements with frictional properties). The modeling results indicate substantial differences in the stress and strain patterns induced by the fault depending on how it was incorporated in the numerical model. The most pronounced effect regarding spatial extent and changes in stress magnitudes and orientation as well as in strain magnitudes is observed for a fault representation which uses a continuous curvilinear grid adapted to the fault geometry and a fault representation by a continuous row of weak elements (approach B). A fault representation as a stair-step sequence of weak elements embedded within a rectangular grid (approach A) has the least impact. A somewhat intermediate stress and strain effect was found for the fault representation via contact element within a curvilinear grid (approach C). These differences are also apparent for sections through the fault zone and its immediate vicinity. The perturbations regarding stress magnitude, stress orientation and strain are always the largest for approach B, while the least impact results for approach A.

The main advantage of approach A is the rapid model generation through intersection of a rectangular grid with the fault interpretation whereas the generation of a specific FE grid adapted to the fault

geometry as in approaches B and C is much more labour-intensive and time-consuming. This holds especially if fault zones with subvertical geometries are considered, as the differences in modeling results between A and B diminish. The particular benefits of approaches B and C emerge if stress and strain perturbations near faults, i.e., within a few tens to hundreds of meters distance, are of interest and if the faults have a non-vertical geometry. In order to utilize a regular rectangular grid and avoid the interlocking of the host rock elements, a band of fault cells of at least two cells width can be used to achieve similar stress and strain results as in the grid adapted to the fault geometry, i.e., approach B.

Challenges remain regarding upscaling of the complex fault zone architecture and material heterogeneity to homogenized continuum properties and the width of the fault zone. The use of contact elements, i.e. the simplifying assumption of zero thickness, may be a reasonable basis for larger, field-scale reservoir models as the real fault zone width will be small compared to the overall size of the model. For a more detailed analysis, especially of the near-fault stress and strain patterns, a volumetric fault zone description with a grid adapted to the fault zone geometry seems more appropriate. In general, it offers also the possibility of incorporating further details of the fault zone through local mesh refinement rather than upscaling them to the size of one element.

Perspectives for future modeling work include comparison to approaches using local grid refinements near faults and submodeling techniques as well as the proper implementation of contact elements in coupled hydromechanical simulations. However, already the existing approach can be easily modified to study more complex fault geometries and variable fault rock properties in order to gain further insights into the stress and strain perturbations induced by faults.

Acknowledgements

Special thanks to Oliver Heidbach (GFZ Potsdam) for the encouraging discussions about fault representations in numerical-geomechanical models. We would also like to thank Tobias Hergert, Karsten Reiter (both from TU Darmstadt) and Karsten Fischer (Schlumberger) for discussions and their feedback on an earlier version of the manuscript.

5. Faults as Volumetric Weak Zones in Reservoir-Scale Hydro-Mechanical Finite Element Models—A Comparison Based on Grid Geometry, Mesh Resolution and Fault Dip

Torben Treffeisen & Andreas Henk

TU Darmstadt, Institut für Angewandte Geowissenschaften, Schnittspahnstraße 9, 64287 Darmstadt, Germany

Published in: Energies 13, Special Issue "Applied Geomechanics in Petroleum Engineering" (2020): 1-27, (https://doi:10.3390/en13102673)

Abstract

An appropriate representation of faults is fundamental for hydro-mechanical reservoir models to obtain robust quantitative insights into the spatial distribution of stress, strain and pore pressure. Using a generic model containing a reservoir layer displaced by a fault, we examine three issues which are typically encountered if faults have to be incorporated in reservoir-scale finite element simulations. These are (1) mesh resolution aspects honoring the scale difference between the typical cell size of the finite element (FE) reservoir model and the heterogeneity of a fault zone, (2) grid geometry relative to the fault geometry and (3) fault dip. Different fault representations were implemented and compared regarding those on the modeling results. Remarkable differences in the calculated stress and strain patterns as well as the pore pressure field are observed. The modeling results are used to infer some general recommendations concerning the implementation of faults in hydro-mechanical reservoir models regarding mesh resolution and grid geometry, taking into account model-scale and scope of interest. The goal is to gain more realistic simulations and, hence, more reliable results regarding fault representation in reservoir models to improve production, lower cost and reduce risk during subsurface operations.

5.1. Introduction

Since the beginning of the 21st century, the hydrocarbon industry has shifted towards faulted and structurally more complex conventional or unconventional reservoirs, which require a thorough understanding of both the hydraulic and the mechanical reservoir behavior (Pereira et al., 2014; Rueda et al., 2014; Fachri et al., 2016). Fluid flow simulations are a well-established tool in the industry (Manzocchi et al., 2008; Qu et al., 2015) and geomechanical modeling has also turned out to be of tremendous help when trying to gain quantitative insights into the spatial distribution of stress and strain on the reservoir-scale (Geertsma, 1973; Segall et al., 1994; Fisher & Jolley, 2007; Ferronato et al., 2008; Orlic & Wassing, 2012). Due to the interaction of fluid flow and mechanical behavior, fully-coupled hydro-mechanical simulations gain more and more importance.

Various numerical modeling techniques have been tried and tested, e.g., finite difference (FD), boundary element (BE), discrete element (DE) and hybrid methods (Jing & Hudson, 2002; Hilley et al., 2010; Cappa & Rutqvist, 2011; Fournier & Morgan, 2012; Zhang et al., 2015) , but the most commonly used approach for hydro-mechanical reservoir simulations is the finite element (FE) method which the present study focuses on. Such FE reservoir models typically have a lateral size between kilometers to tens of kilometers and applications can range from hydrocarbon and geothermal reservoirs to sites for underground gas storage (Croucher & O'Sullivan, 2008; Jayakumar et al., 2011; Nasir et al., 2015). In order to obtain a realistic subsurface representation for reliable stress and fracture predictions as well as fluid flow path analysis, the reservoir models have to take into accounts faults, i.e., discontinuities offsetting the strata, in addition to the lithostratigraphic horizons.

However, faults are not only characterized by local discrete deformation. Faults can also induce stress perturbations, i.e. local changes in stress orientation and stress magnitude, which differ distinctly from

the regional trends (Yale, 2003). Hydraulically, faults can either act as barriers or conduits for fluid flow between different reservoir compartments (Fredman et al., 2008; Faulkner et al., 2010). Considering the usually weaker mechanical properties of fault zones, if compared to the undeformed rock, they are more sensitive to pore pressure changes resulting from fluid injection into or fluid withdrawal from the reservoir. Those pore pressure changes can reactivate preexisting faults, leading to induced seismicity potentially causing critical situations like, fault seal breach, land subsidence and well collapse (Segall et al., 1994; Morton et al., 2006; Faulkner et al., 2010). Consequently, a realistic representation of faults in a hydro-mechanical reservoir simulation proves to be invaluable for the reliability of the numerical model predictions. This has been an issue in various studies over the past years (Chan & Zoback, 2007; Fisher & Jolley, 2007; Fredman et al., 2007; Faulkner et al., 2010; Orlic & Wassing, 2012). Several authors suggest that in order to honor the architecture and internal heterogeneity of faults, they should be treated as volumetric features in the numerical simulations, even if the fault zone thickness seems to be negligible in contrast to the overall model and element size, respectively (Braathen et al., 2009; Fachri et al., 2013). This is considered of particular relevance for complex, intensively faulted reservoirs (Manzocchi et al., 2008; Qu & Tveranger, 2016) and could improve projects where faults are part of the full-scale reservoir model (e.g. Braathen et al., 2009; De Souza et al., 2012; Fischer & Henk, 2013).

In this paper, we analyze the representation of fault zones as volumetric weak zones in hydro-mechanical simulations regarding three commonly used assumptions in FE reservoir modeling. These are (1) mesh resolution aspects honoring the scale difference between the typical cell size of the FE reservoir model and the heterogeneity of a fault zone, (2) grid geometry relative to the fault geometry and (3) fault dip. Different combinations of these three parameters were investigated and compared regarding their impact on the modeling results. The primary goal is to provide guidelines for appropriate fault representations in numerical reservoir models regarding mesh resolution, grid geometry and scope of interest. Such guidelines will assist in building more realistic hydro-mechanical simulations of faulted reservoirs. Furthermore, the modeling techniques developed and experiences gained are also considered as a starting point for further studies to investigate the effect of fault zone heterogeneities and to develop refined upscaling techniques for hydro-mechanical fault zone properties.

General information about the state of the art of fault modeling in FE reservoir models can be found in Section 4.2 for both fluid flow and geomechanical simulations as well as coupled hydro-mechanical simulations. The third section describes the three commonly used assumptions to incorporate faults in reservoir models which we investigate in this study. The model setup as well as the constitutive laws for the simulation can be found in Section 4.4. Section 4.5 provides the modeling results, which are discussed in Section 6 and lead to the conclusions given in Section 4.7.

5.2. State-of-the-Art: Fault Modeling in Finite Element Reservoir Models

5.2.1. Faults in Fluid Flow Simulations

For fluid flow simulations, the use of transmissibility multipliers is widely used in reservoir engineering (Knai & Knipe, 1998; Walsh et al., 1998; Hollund et al., 2002; Jolley et al., 2007). Transmissibility multipliers are assigned to the cells of the calculation grid intersected by the fault plane. Depending on the selected hydraulic properties which are averaged over the entire fault zone and adjacent rock, these cells then act as barriers or conduits for fluid flow. Different concepts have been suggested over the past years to estimate fault transmissibility multipliers (Manzocchi et al., 1999; Crawford et al., 2002; Myers et al., 2007). More recently, a fault facies concept was developed to improve fault representation in reservoir-scale fluid flow simulations by representing faults as 3D structures with variable material properties for different parts of the fault zone. The fault facies concept tries to include the internal complexity of fault zones and their permeability structure by assigning

various (hydraulic) material properties to the rock bodies influenced by faulting. It is assumed that the fault volume can be populated with a fault facies similar to how geological models are populated with a sedimentary facies concept (Tveranger et al., 2004; Fredman et al., 2007; Fredman et al., 2008; Braathen et al., 2009; Qu et al., 2015; Fachri et al., 2016). However, the basic challenge remains how to properly upscale the complex internal structure and the heterogeneous permeability distribution which exist in real fault zones.

5.2.2. Faults in Geomechanical Simulations

In addition to hydraulic properties, fault zones are also highly heterogeneous with respect to mechanical properties. This heterogeneity together with the complex fault geometry and internal architecture will strongly control the mechanical behavior of a fault zone and how it affects the stress field in its vicinity (Byerlee, 1978; Wibberley et al., 2008; Barton, 2013). There are different approaches to implement faults in geomechanical models, but for FE modeling, which is the most commonly used approach in hydro-mechanical reservoir simulations, there are: (1) Contact or interface elements (Cappa & Rutqvist, 2011; Hergert et al., 2011; Franceschini et al., 2016) and (2) volumetric weak zones (Rinaldi et al., 2013; Vilarrasa et al., 2017; Treffeisen & Henk, 2020a).

Contact or interface elements represent faults as discrete discontinuities (Buchmann & Connolly, 2007; Ye et al., 2018), which is an expansion of the classical continuum approach used in FE simulations. Those elements enable differential movements between separate and individually meshed model parts. A contact surface consists of contact and their correspondent target elements located at opposing sides of the predefined fault. However, a contact- and target-element pair has the same coordinates. Hence, the fault is represented as a line in 2D and a surface in 3D models, respectively (Ferronato et al., 2008; Ye et al., 2018), instead of a volumetric feature.

Infinitely high normal stiffness values would be needed to enforce compatibility between adjacent fault surfaces and to create a zero thickness of the contact elements. In order to prevent numerical instabilities, a certain mesh penetration at the interface has to be accepted. Thus, stiffness values close to Young's moduli of the adjacent rocks are commonly used for the contact elements. Shear and normal stress can be transmitted through the contact elements and material properties like cohesion and a friction coefficient can be used to describe frictional sliding. Therefore, once the stress state at the contact elements violates the defined failure criterion (Franceschini et al., 2016), relative displacement between corresponding nodal points will occur.

In contrast, the concept of volumetric weak zones describes faults in a FE model by assigning (usually weaker) fault rock material properties to the grid cells intersected by faults. This concept can be applied to a rectangular grid, resulting in a stair-stepped fault representation (Figure 4-1, left; Prevost & Sukumar, 2015; Deb & Jenny, 2017). Alternatively, the FE mesh can be adapted to the fault zone geometry, resulting in a curvilinear grid (Figure 4-1, right; Will & Eckardt, 2015; Zhang et al., 2015; Vilarrasa et al., 2017). Both grid geometries are further explained in Section 3.2.

For reservoir models with a typical cell size distinctly larger than the thickness of the fault zone and its subunits, no details of the fault architecture and material heterogeneity can hardly be considered explicitly. Instead, mechanical properties, which represent the joint effects of host rock, damage zone and fault core, i.e., following a homogenized continuum approach, are used. Optionally, anisotropic properties can be assigned to the fault cells (Manzocchi et al., 2008; Schlegel, 2016). However, at least to a certain extent, local grid refinement techniques or detailed submodeling of specific faults in reservoir models allow for incorporation of further details in the fault zone architecture and mechanical property distribution (Syversveen et al., 2006; Fachri et al., 2016).

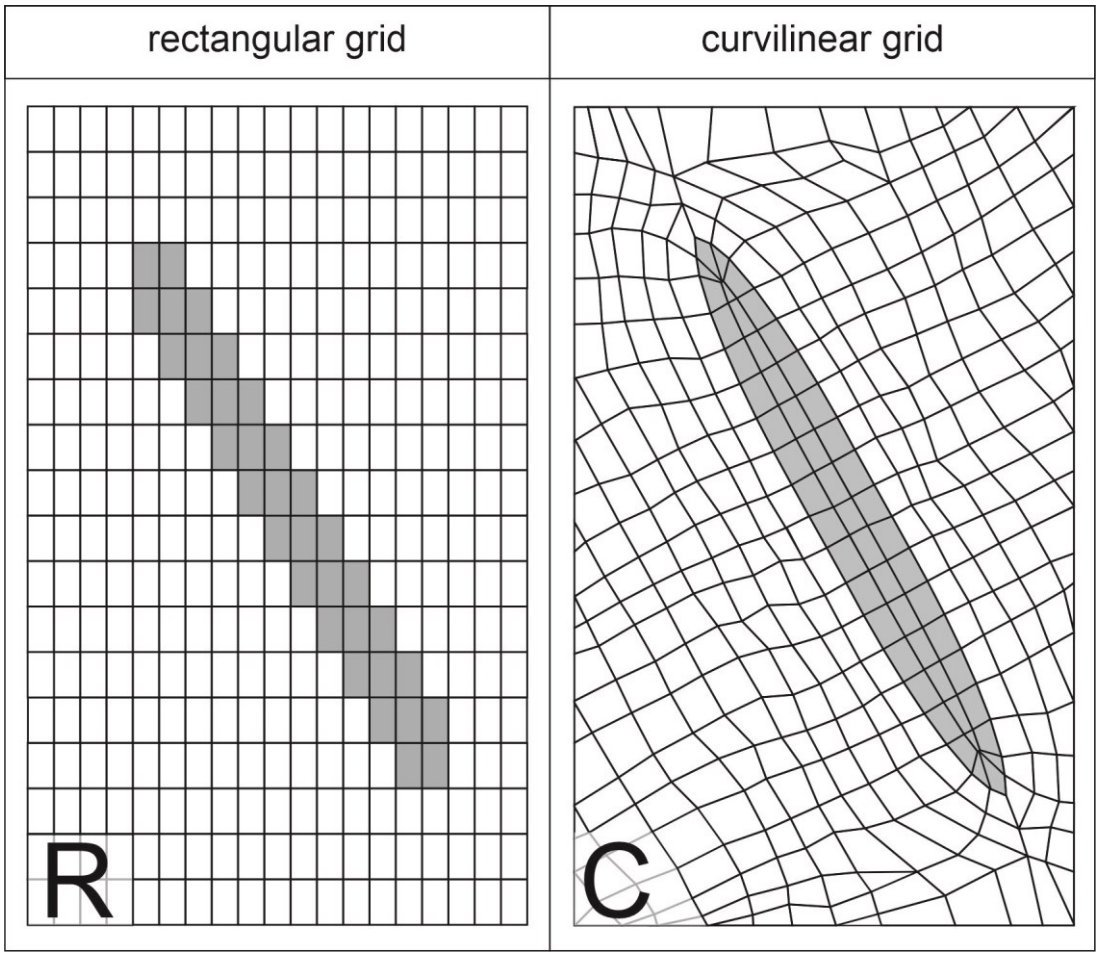

Figure 5-1. Images (not to scale) showing the basic differences between the different grid geometries applied. Left: The rectangular approach (R) uses a regular, rectangular grid in which fault zone properties are assigned to those cells intersected by the fault plane. Due to the underlying grid geometry, a staircase-shaped fault representation results. Right: The curvilinear approach (C) uses an irregular grid geometry which is adapted to the fault geometry. This allows the representation of the true shape of the fault zone in the FE model.

5.2.3. Faults in Coupled Hydro-Mechanical (HM) Simulations

Hydraulic and mechanical processes are closely related (Byerlee, 1978; Yale, 2003; Faulkner et al., 2010). Hence, pore pressure changes can lead to mechanical reactivation of a fault zone and fault reactivation can lead to increasing permeability, fluid flow and fault seal break (Pereira et al., 2014; Sanchez et al., 2015). Coupled hydro-mechanical simulations can reproduce those relationships. It is the volumetric representations of faults that can map both weaker mechanical properties and fault-specific hydraulic parameters onto fault-intersecting elements (Pereira et al., 2014; Schuite et al., 2017).

5.3. Some General Aspects of Representing Faults in Finite Element Reservoir Models

The goal of this study is to show the sensitivity of the fault representation as a volumetric weak zone regarding three common assumptions used to incorporate fault zones into coupled hydro-mechanical reservoir simulations.

5.3.1. Mesh Resolution

FE analysis is affected by both the mesh quality and element quantity (Ghavidel et al., 2017; Azarfar et al., 2018), so meshing is a key issue in FE modeling. While it is established that a finer grid

resolution leads to better modeling results, the grid size used in FE reservoir models is often several orders of magnitude larger than the internal architecture of a fault zone and its material heterogeneities (Knupp, 2006; Henk, 2019). Next to upscaling techniques for both hydraulic and mechanical properties, which include the internal features and material heterogeneity of the fault zone (Manzocchi et al., 2008), detailed rendering of the fault zone architecture through high-resolution local grid refinements around fault zones can lead to simulation results closer to reality (Qu & Tveranger, 2016). However, more elements result in an exponential increase in the computing time for the simulations (Ghavidel et al., 2017; Azarfar et al., 2018). Since longer run-times of simulations mean higher costs, it is of importance to find a proper mesh resolution and simultaneously minimize the computational costs. Consequently, a thorough understanding of the influence the mesh resolution has on numerical fault simulations is crucial.

5.3.2. Grid Geometry

We apply two different basic approaches used in previous studies to implement faults as volumetric weak zones in FE hydro-mechanical models (Figure 4-1). These approaches differ regarding the basic grid geometry and whether the grid is adapted to the fault geometry or not.

4.3.2.1 Rectangular Approach

Rectangular grid geometry is a frequently used approach for the representation of faults in FE reservoir models (Figure 4-1, left; Prevost & Sukumar, 2015; Deb & Jenny, 2017). Such a rectangular element grid often is already available from preceding flow simulations or property modeling. A volumetric weak zone is generated by intersecting this grid with a structural model, e.g., a fault interpretation derived from 3D seismic interpretation and assigning fault rock properties to those cells cut by the fault planes (Olden et al., 2012; De Souza et al., 2014; Prevost & Sukumar, 2015; Deb & Jenny, 2017).

The fault rock properties assigned to the corresponding grid cells normally use a homogenized continuum, optionally with anisotropic properties, to incorporate the joint effects of fault core and fractured damage zone (Manzocchi et al., 2008; Schlegel, 2016) since the cell size is typically much larger than the material heterogeneities inside a fault zone. Neighboring cells maintain the intact rock properties. Such a rectangular grid is fast and easy to generate, and therefore, saves time in model generation. However, the staircase-shaped fault geometry can suppress deformation within the fault zone (Treffeisen & Henk, 2020a).

4.3.2.2. Curvilinear Approach

Compared to the rectangular grid with a staircase-shaped fault geometry, a mesh adapted to the fault zone geometry allows a representation of the fault which is closer to reality, e.g., a lenticular or elliptical fault shape, which is common for normal faults in sedimentary environments (Rippon, 1985; Cowie & Scholz, 1992). If the FE grid geometry is adjusted to the fault geometry (Figure 4-1, right; Rinaldi et al., 2013), an irregular, curvilinear grid following the shape of the fault zone results. The approach permits to represent the fault zone as a continuous feature in contrast to the stair-stepped geometry inevitably connected to the rectangular approach. In most cases, the cell size representing the fault zone will be too large to reproduce details of the internal fault zone architecture. Thus, similar to the rectangular grid, the actual heterogeneity of the fault zone has to be upscaled to the size of the elements representing the fault, e.g., by using a homogenized continuum approach (optionally with anisotropic properties). Adjusting the grid to the fault geometry takes significantly more time to generate, especially for large reservoir models including multiple fault zones. Thus, understanding the influence the fault shape has on the modeling results can allow to decide how accurate the shape has to be regarding to the aim of the hydro-mechanical study.

5.3.3. Fault Dip

Faults, besides other subsurface structures, are commonly detected through geophysical methods. Due to the ability of elastic waves to sense a fault in the subsurface, active seismic is the tool mostly used to detect faults (Cowie & Scholz, 1992; Chopra & Marfurt, 2007; Couples et al., 2007; Tanner et al., 2019). However, there are certain limitations and dependencies, like e.g., the wavelength of the seismic source or the rock density (Geldart & Sheri, 1995; Buske et al., 2009), influencing the seismic resolution and, hence, the ability to detect details of the fault zone. The vertical seismic resolution is dependent on the wavelength and depth, but for reservoirs, it is usually in the range of tens of meters. Further difficulties exist when trying to detect small structures, such as small-scale faults or particular fault zone features, like fault core, fault throw or damage zone (Liu & Martinez, 2012). Identification of steeply inclined fault zones is complex (Moser & Howard, 2008; Ghose et al., 2013; Tanner et al., 2019) and although different migration techniques exist (Baysal et al., 1983; Jones et al., 1998; Buske et al., 2009), finding the correct fault dip remains difficult for the seismic interpreter. Thus, a frequently used simplification in reservoir modeling is to assume vertical faults, i.e., a fault dip of 90°. We compare this value with the typical dip angle of 60° for normal faulting (Anderson, 1951). The aim is to show the impact that improper fault dip estimations can have on the mechanical response of the fault zone.

5.4. Model Setup

In order to compare the different options for volumetric fault representations in the FE models outlined above, we use as the basic model setup a high-permeability reservoir layer embedded in low permeability over-/underburden and offset by a normal fault. The various scenarios studied differ regarding (1) the basic grid geometry (rectangular vs. curvilinear), (2) the mesh resolution of the fault zone (1, 3 and 9-elements width) and (3) the fault dip (60° vs. 90°). The material properties for each of the three model units (fault zone, reservoir rock and over-/underburden) remain the same in all scenarios. Table 4-1 and Figure 4-2 give an overview of the characteristics of the seven cases studied.

The geological rationale for the model setup, i.e., a lenticular fault zone displacing a reservoir horizon, is presented in Figure 4-3a. The resulting model domain, the dimensions as well as all initial and boundary conditions are shown Figure 3b. For the fully coupled hydro-mechanical simulations, the FE software Ansys 19.2 is used (Ansys, 2019).

Table 5-1: Overview of the seven scenarios studied and the corresponding model names. The scenarios differ regarding the basic grid geometry, the mesh resolution of the fault zone and the fault dip.

Model name	Grid geometry	Fault zone width [Number of Elements]	Fault dip [°]
R1-60	rectangular	1	60
R3-60	rectangular	3	60
R3-90	rectangular	3	90
R9-60	rectangular	9	60
C3-60	curvilinear	3	60
C3-90	curvilinear	3	90
C9-60	curvilinear	9	60

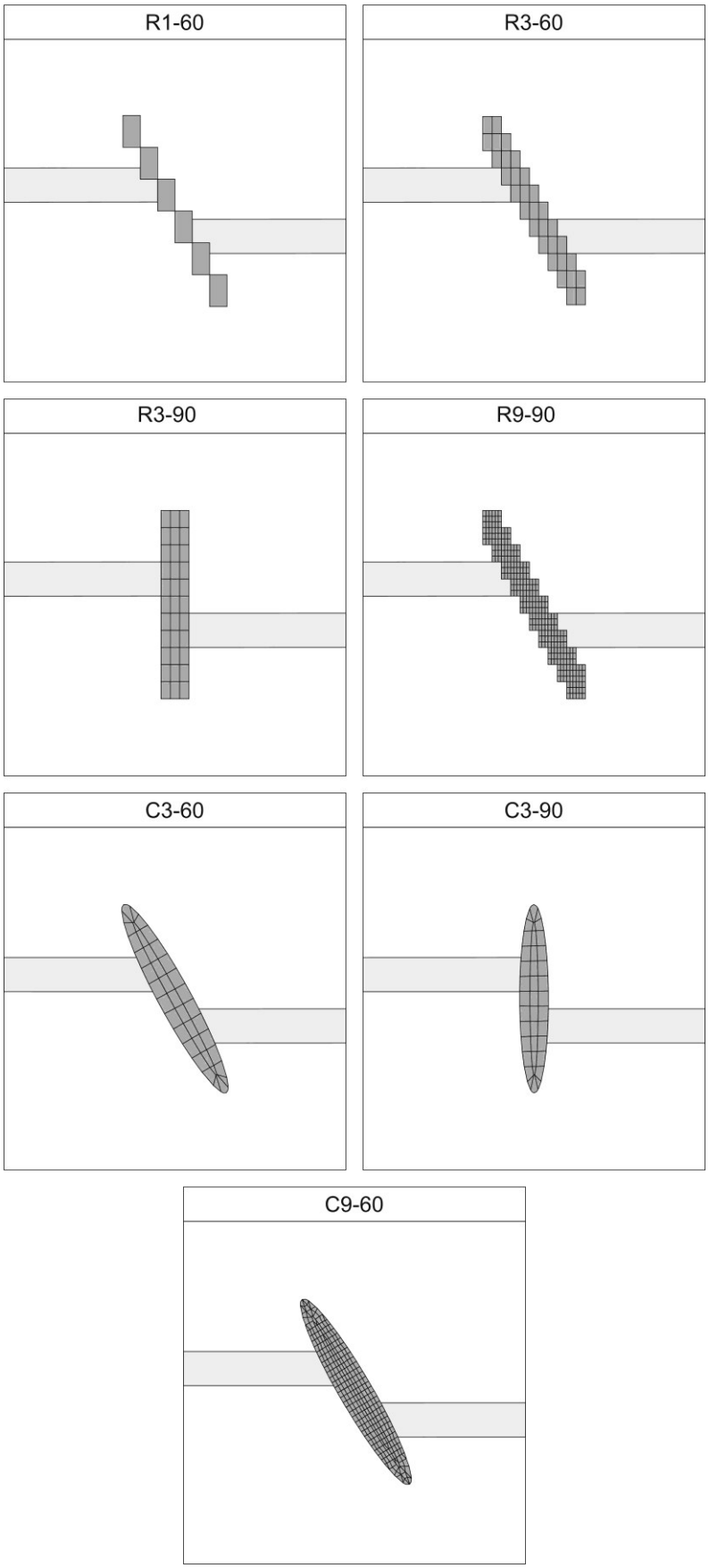

Figure 5-2: Images (not to scale) showing the basic differences between the seven scenarios studied regarding grid geometry, mesh resolution of the fault zone and fault dip.

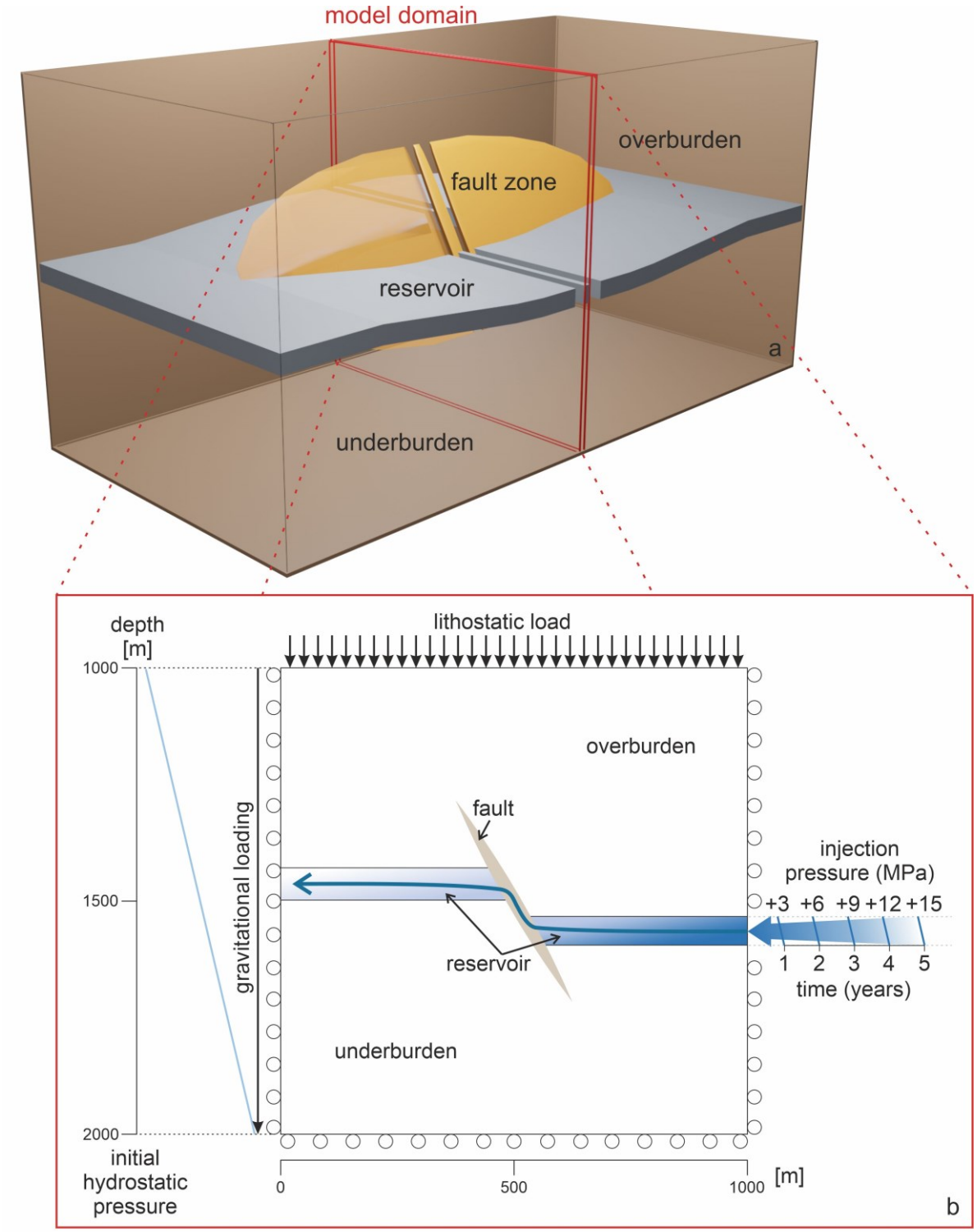

Figure 5-3: (a) The 3D model represents a slice of one-element width through the central section of a fault zone displacing a reservoir horizon (not to scale). (b) General model set-up (in side view) as well as initial and boundary conditions for the hydro-mechanical simulation. Model dimensions are 1 × 1 × 0.001 km centered around a 500 m long fault displacing a reservoir horizon. The model is located between 1 and 2 km depth. No displacements orthogonal to the model boundary are allowed at the base and vertical sides of the model ('roller boundary condition'), whereas a pressure equivalent to the weight of the overburden acts on the model top. Initially, a hydrostatic pore pressure field is assumed. Subsequently, the pore pressure at the nodes on the right side of the downthrown reservoir section is increased at a rate of 0.75 MPa every 3 months until after 5 years a final increase of 15 MPa is reached.

5.4.1. Model Geometry

The 3D model represents a slice through the center of a normal fault offsetting a reservoir horizon (Figure 3a). The overall geological setting is a normal faulting regime, including an elliptically shaped fault zone offsetting a reservoir horizon into upper and lower compartments. The model dimensions of the 3D-slice are 1 × 1 km² and 1-element thickness (Figure 4-3b). The total height of the fault is 500 m, whereas the offset of the 25 m thick reservoir horizon is 47 m. Since the fault zone is represented as one material rather than explicitly subdividing it into fault core and damage zone, scaling relationships (Johri et al., 2014) for both features are combined and the total width of the fault zone is assumed to be 12 m. The fault dip is either 60° or 90°, depending on the scenario studied.

Depending on the mesh resolution inside the fault zone (1-, 3- or 9-element width) the whole model has between 126,000 and 1,134,000 elements for the rectangular and between 45,684 and 312,164 elements for the curvilinear approach. The differences arise from the different mesh resolution towards the model boundaries. The fault zone itself is represented by 119 (1-element width), 358 (3-element width) or 3226 (9-element width) elements for the rectangular and 564 (3-element width) or 4004 (9-element width) elements for the curvilinear models. The actual size of the elements describing the fault geometry are 12 × 12 × 9 m (1-element width), 4 × 4 × 3 m (3-element width) and 1.3 × 1.3 × 1 m (9-element width).

5.4.2. Boundary Conditions

The initial as well as the mechanical and hydraulic boundary conditions used for the simulations are shown in Figure 4-3b. No displacements orthogonal to model boundaries ('roller boundary conditions') are allowed at the basal, left, right, front and back side of the model. A lithostatic pressure boundary condition equivalent to the weight of the overburden holds for the model top. As the top of the model is assumed to be 1000 m beneath the earth's surface, the corresponding pressure acting on the model can be calculated according to (Jaeger et al., 2007):

$$p_r = \varrho_r \cdot g \cdot d \tag{5-1}$$

where ϱr is the average density of the overburden rock (assumed to be 2300 kg/m³; Faulkner et al., 2010), g is gravitational acceleration (9.8 m/s²) and d is depth (1000 m). Since no further tectonic (horizontal) stress components are considered in the simulations, the initial stress field results entirely from gravitational loading. Consequently, the model is located in a normal faulting regime, i.e., outside the area affected by the fault the vertical stress S_v corresponds to the maximum principal stress S_1.

Hydraulic boundary conditions assume impermeable boundaries at the top and base of the model as well as no horizontal flow through the vertical model sides. Initially, hydrostatic pore pressure conditions are assumed throughout the model. The corresponding pore fluid pressures p_f can be calculated according to:

$$p_f = \varrho_f \cdot g \cdot d_n \tag{5-2}$$

where ϱ_f is the fluid density (1000 kg/m³; assumed average density of the pore fill in the overburden) and d_n is the depth of the corresponding element node, i.e., between 1000 m (model top) and 2000 m (model base).

After the initial load step, i.e., after mechanical and hydraulic equilibrium in response to the boundary conditions has been achieved, successively higher pore pressures are applied to the boundary nodes of the reservoir layer in the hanging wall of the fault (lower right in Figure 4-3b). This represents fluid injection in the downthrown block and is continued for 5 years at a rate of 0.75 MPa every 3 months,

i.e., in 20 time steps, until the maximum injection pressure of 15 MPa is reached. Therefore, pore pressure (p_f) for the nodes at the boundary of the reservoir layer is increased according to:

$$p_f = \varrho_f \cdot g \cdot d_n + p_i \cdot t \tag{5-3}$$

where p_i is the pressure increment (0.75 MPa) and t is the time step (1 to 20).

5.4.3. Constitutive Laws

Poroelasto-plastic material behavior and fluid flow through a porous medium is assumed for this hydro-mechanical simulation. In a saturated porous medium, stresses are split between the solid phase and the fluid phase, so the total stresses are reduced by the pore pressure in the rock volume. This relationship can be described by:

$$\sigma'_{ij} = \sigma_{ij} - \alpha \cdot p \cdot \delta_{ij} \tag{5-4}$$

where the effective stresses (σ'_{ij}) are derived from the total stress tensor (σ_{ij}) by subtracting the pore pressure (p), weighted by the Biot coefficient (α) and Kronecker's delta (δ_{ij}) (Johri et al., 2014; Jaeger et al., 2007; Ansys, 2019).

The mechanical material behavior in the poroelastic domain is described by the following stress–strain relationship:

$$\varepsilon_{ij} = \frac{1+\upsilon}{E} \cdot \sigma'_{ij} - \frac{\upsilon}{E} \cdot \sigma'_{kk} \cdot \delta_{ij} \tag{5-5}$$

It links strain (ε_{ij}) and effective stress (σ'_{ij}) through the material properties of Young's modulus (E) and Poisson's ratio (υ) and the sum of the effective principal stresses (σ'_{kk}) (Wang, 2000; Shapiro, 2015; Cheng, 2016). The failure criterion delimiting the poroelastic range and initiating plastic material behavior in a hydro-mechanical analysis can be defined by a variant of the Mohr–Coulomb law according to:

$$\tau_{crit} = (\sigma_n - p_f) \cdot \tan \varphi' + c' \tag{5-6}$$

where τ_{crit} is the critical shear stress at failure, σ_n is the normal stress, φ' is the effective angle of internal friction and c' is the effective cohesion (Jaeger et al., 2007). Injection leads to an increase in pore pressure, which reduces the effective stresses and the effective normal stress. In the σ_n—τ diagram, this pore pressure increase shifts the Mohr Circle towards the left until it ultimately reaches the failure line and shear failure occurs. Tensile failure is incorporated via a tension cut-off delimiting the Mohr–Coulomb failure line for tensile stresses (Figure 4-4).

Besides the hydrostatic pressure, also the injection pressure affects the model and the increase in pore pressure propagates through the model. This is described by Darcy's law as fluid flow (q) is determined according to:

$$\nabla \left[\frac{k}{n} \cdot (\nabla p - \rho_f \cdot g) \right] = S \cdot \frac{\partial p}{\partial t} \tag{5-7}$$

where k is the intrinsic permeability of the porous medium, n the fluid viscosity, p the pore pressure, ρ_f the fluid viscosity, S the specific storage (as a function of porosity) and t the time (Wang, 2000).

The fully coupled hydro-mechanical simulation accounts for the interaction of the hydraulic and mechanical behavior as changes in pore pressure result in effective stress changes and related volumetric strain. This in turn alters porosity and permeability, which again affect the pore pressure field (Jaeger et al., 2007; Streit & Hillis, 2004; Cappa & Rutqvist, 2011).

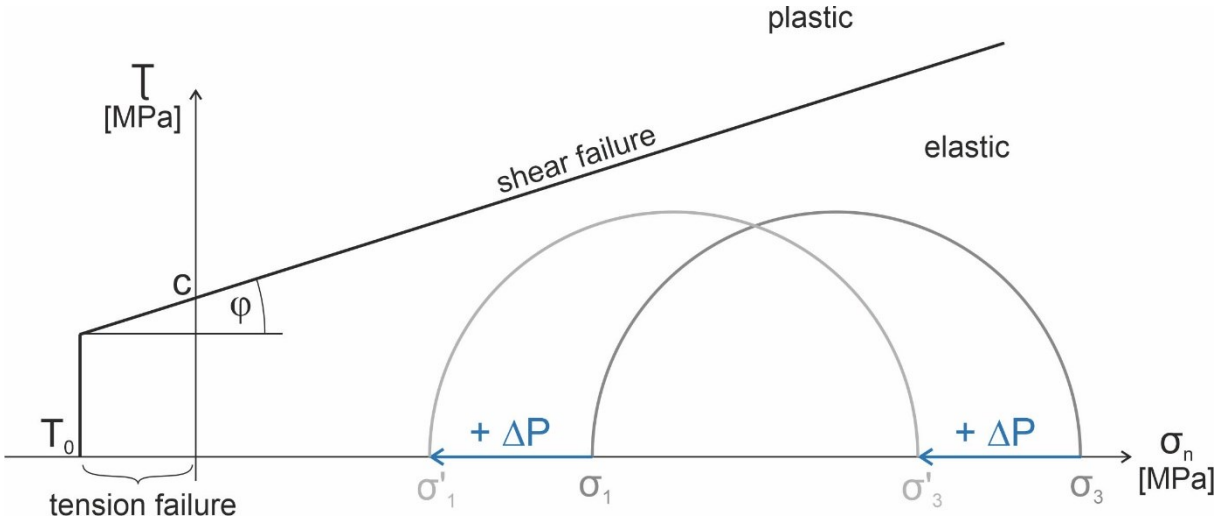

Figure 5-4: Shear stress τ vs. normal stress σn diagram showing the Mohr–Coulomb failure criterion with a tension cut-off delimiting the elastic domain. An increase in pore pressure leads to a decrease in the effective stresses. Thus, the corresponding Mohr circle is shifted to the left towards the shear failure line. If the failure line is ultimately touched, plastic straining and—in case of a fault zone—fault reactivation occurs.

5.4.4. Material Input Parameters

The hydraulic and mechanical material properties assigned to the various model units are listed in Table 2. For the mechanical properties, only Young's modulus and the frictional properties are varied between the fault zone on one side and the reservoir rock and over-/underburden on the other. For ease of comparison, Poisson's ratio and density are kept the same for all three units. A friction angle of 10° was used for the fault zone, which is substantially lower than the typical values for most intact rocks (Byerlee, 1978). However, various studies have pointed out that processes like cataclasis and formation of clay minerals, among others, lower the friction angle and reduce the strength of fault rocks, thus leading to mechanically weak fault zones (Holdsworth, 2004; Faulkner, 2004; Collettini et al., 2009). In this study, we focus on mechanical weak fault zones, where plastic deformation and therefore fault reactivation are most likely to occur.

In order to study fluid flow along the fault zone and how it alters its mechanical strength by changes in effective stress, we decided to choose a permeable fault zone. However, impermeable faults frequently also occur in sandstone-shale regimes (Caine et al., 1996; Faulkner, 2004; Agosta et al., 2006).

Table 5-2: Hydraulic and mechanical parameters used for the three model units.

Mechanical	Symbol	Fault Zone	Reservoir	Over-/Underburden
Young's modulus [GPa]	E	10	30	30
Poisson's' ratio [–]	ν	0.23	0.23	0.23
Friction angle [°]	φ	10	40	40
Cohesion [MPa]	c	4	20	20
Tensile strength [MPa]	TS	5	20	20
Density [kg/m³]	ρ	2400	2400	2400
Hydraulic				
Biot coefficient [–]	α	0.9	0.5	0.5
Permeability [m²]	k	10^{-14}	5^{-12}	10^{-17}
Porosity [–]	ϕ	0.15	0.15	0.025

5.5. Results

The following section presents the simulation results for the various scenarios. First, the stress and strain patterns as well as the pore pressure distribution of a reference model are shown, which provides a baseline for the following comparison between different model setups. The modeling results are visualized by means of contour and vector plots as well as detailed sections of the fault zone. Please refer to Table 1 for relating the model name to the details of the different model setups.

5.5.1. Reference Model (C3-60)

The model setup C3-60 describing the fault zone as a 3-element wide unit embedded in a curvilinear grid is used as a reference model. Applying the material properties and boundary conditions outlined in Section 4.4.2 and 4.4.4 (see also Figure 4-3) leads to the initial model state, i.e., before fluid injection into the reservoir horizon starts, shown in Figure 5a–c. As was defined, the hydrostatic pore pressure increases linearly from 9.81 MPa at the model top (1000 m depth) to 19.62 MPa at the base (2000 m depth) (Figure 4-5 a). The effective maximum principal stress ($S_{1,eff}$) ranges from 15 MPa at the top to 37 MPa at the bottom of the model (Figure 4-5 b). Due to its higher Biot coefficient, the fault zone exhibits lower effective stress magnitudes than the surrounding rock. Some minor perturbations in the stress pattern occur in the immediate vicinity of the fault. For the initial and boundary conditions selected, the fault zone is entirely in an elastic state prior to fluid injection. This ensures, that initial loading does not already cause plastic deformation and fault reactivation (Figure 4-5 c).

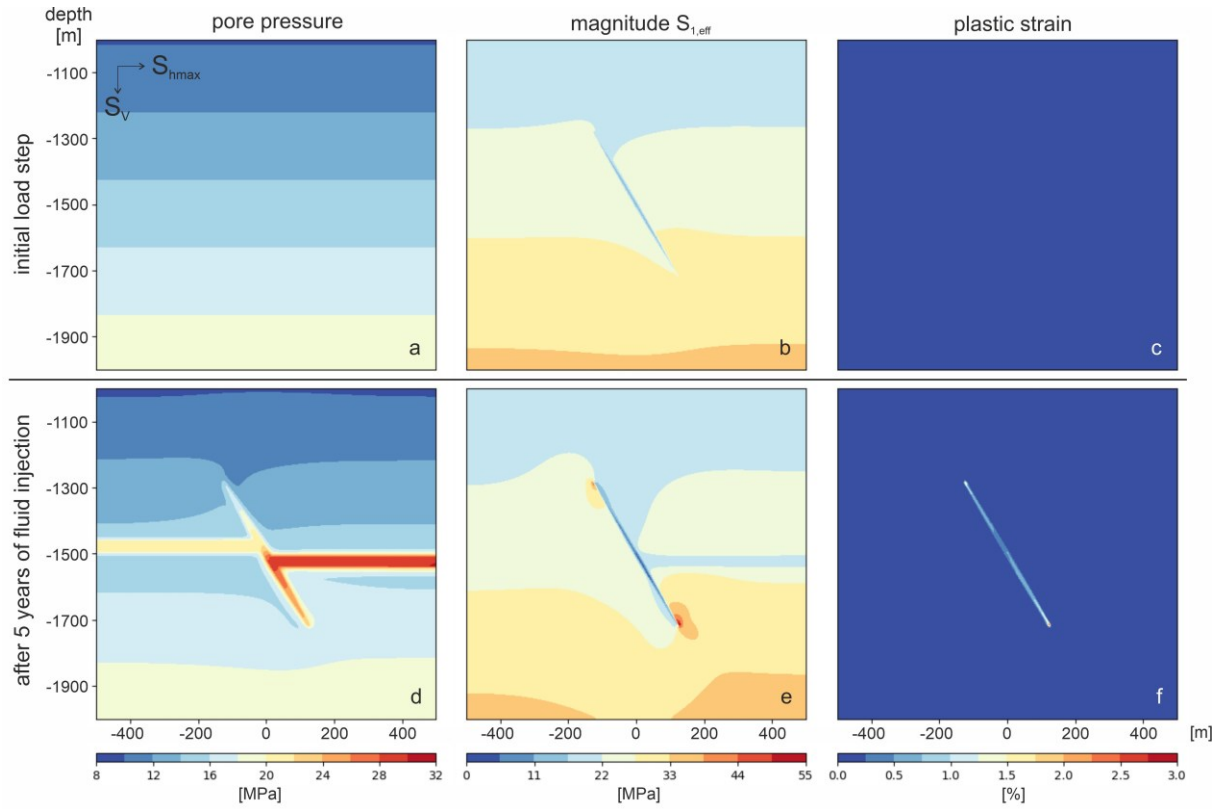

Figure 5-5: Some simulation results for the reference model (C3-60) with a curvilinear grid adapted to a fault with 60° dip and 3-element width. (a–c) show the spatial variation in pore pressure (a), magnitude of the effective maximum principal stress ($S_{1,eff}$; b) and total von Mises plastic strain (c) for the initial state, i.e., prior to fluid injection. (d–f) show the corresponding simulation results after 5 years of injection and a pore pressure increase in the lower reservoir horizon of 15 MPa, respectively.

Figure 5d–f shows the modeling results after 5 years of injection at a rate of 0.75 MPa every 3 months, increasing the pore pressure in the downthrown reservoir section to 30 MPa, i.e., 15 MPa above

hydrostatic. This pore pressure increase has propagated from the injection point through the fault zone all the way up to the upper reservoir section. There, the increase is still about 8 MPa, which results in a pore pressure of about 22 MPa (Figure 4-5 d). The pore pressure increase in the reservoir as well as in the fault zone is also indicated in the $S_{1,eff}$ pattern, as these model parts show 5 to 10 MPa lower stress magnitudes than the surrounding rock mass and for the initial state (Figure 4-5 e). While the reservoir rock as well as the over-/underburden remain in an elastic state, pore pressure increase results in plastic straining of the fault zone elements. The corresponding maximum effective stress pattern shows an increase at the upper left and lower right end of the fault and a decrease over the entire fault zone. Plastic straining occurs in the whole fault zone with deformation ranging between 0.5% within the fault zone and about 3% at the fault tips (Figure 4-5 f).

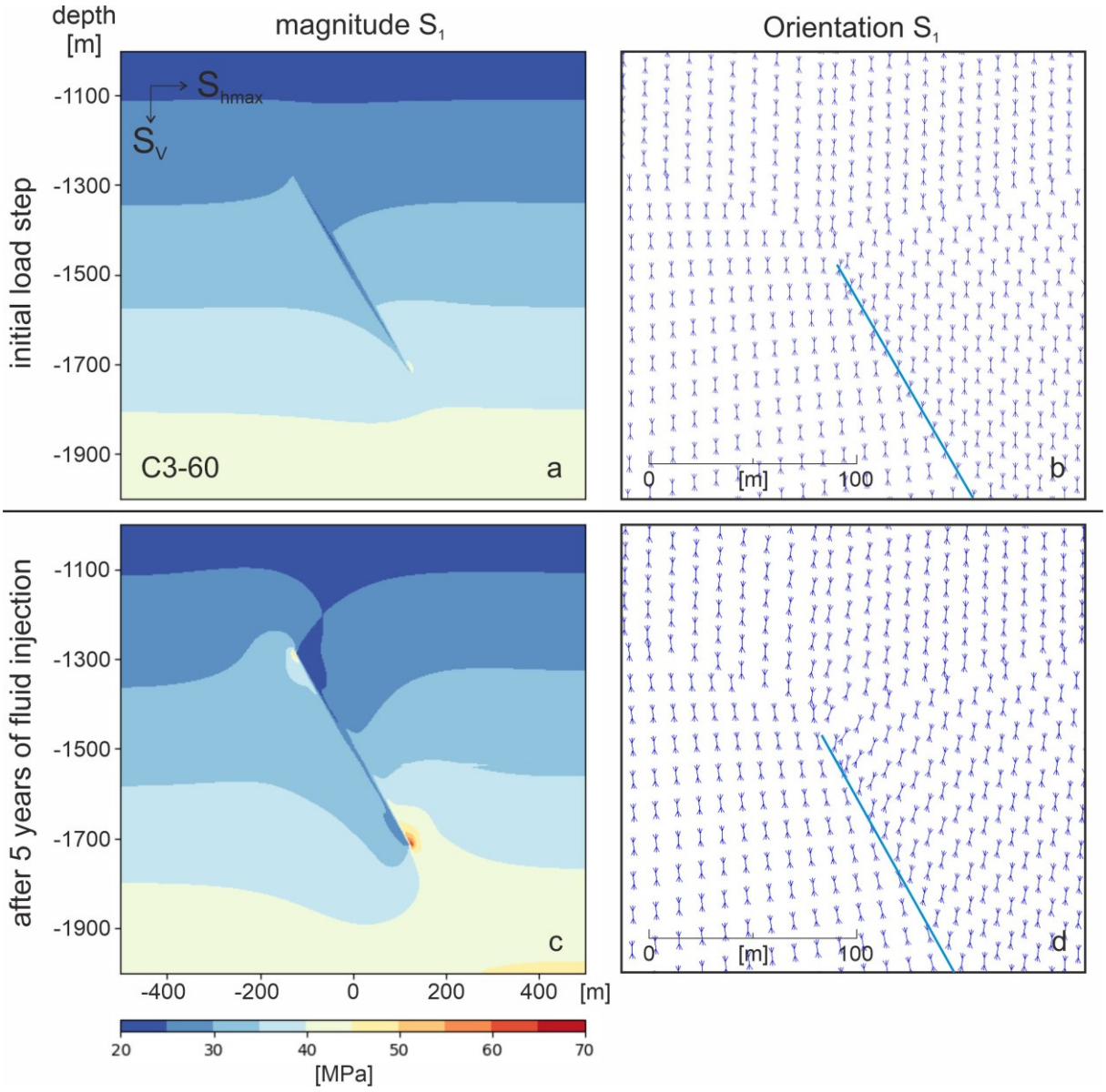

Figure 5-6: Results of the base model (C3-60). Initial state: (a) magnitude of the maximum principal stress (S_1) for the whole model domain. (b) detailed view of the orientation S_1 in the vicinity of the upper fault tip. After 5 years of injection: (c) magnitude S_1 for the whole model domain. (d) detailed view of the orientation S_1 in the vicinity of the upper fault tip.

Examining the model state after 5 years of injection, both the minimum and maximum peaks at the upper fault tip in the close surrounding of the fault zone are around 15 to 20 MPa higher than the

magnitudes for $S_{1,eff}$ (Figure 4-6c). The orientation of S_1 near the fault tip has rotated up to 30° clockwise at the downthrown side. The rotation decreases towards the right until it reaches vertical again. On the left side of the fault tip, the rotation is lower, i.e., about 5° counterclockwise near the fault (Figure 4-6 d).

In Figure 6, the magnitude of the maximum total principal stress (S_1) is displayed together with a detailed view of the orientation of S_1 at the fault tips for both the initial (Figure 4-6 a,b) and the final calculation step (Figure 4-6 c,d) of the base model approach (C3-60). The basic pattern is similar to the magnitudes for $S_{1,eff}$, albeit at higher values as pore pressure effects are not considered (Figure 4-6 a). Due to the assumed normal faulting regime, the regional maximum principal stress orientation is vertical. Only the fault cells properly exhibit a slight rotation of about 5° relative to regional (Figure 4-6 b).

5.5.2. Mesh Resolution

The impact of the mesh resolution of the fault zone is compared by implementing different element sizes for the same total width of the fault zone, i.e., the number of elements used to resolve the fault zone varies. Figures 4-7 and 4-8 display the results after the last load step, i.e., after 5 years of injection, for the magnitude of $S_{1,eff}$ and the orientation of S_1 for different mesh resolutions. Thereby, the fault is represented either as 1-, 3- or 9-element wide zone in a rectangular grid. In general, significant differences between the 1-element (R1-60) on one side and the 3- (R3-60) and 9-element (R9-60) width on the other can be observed.

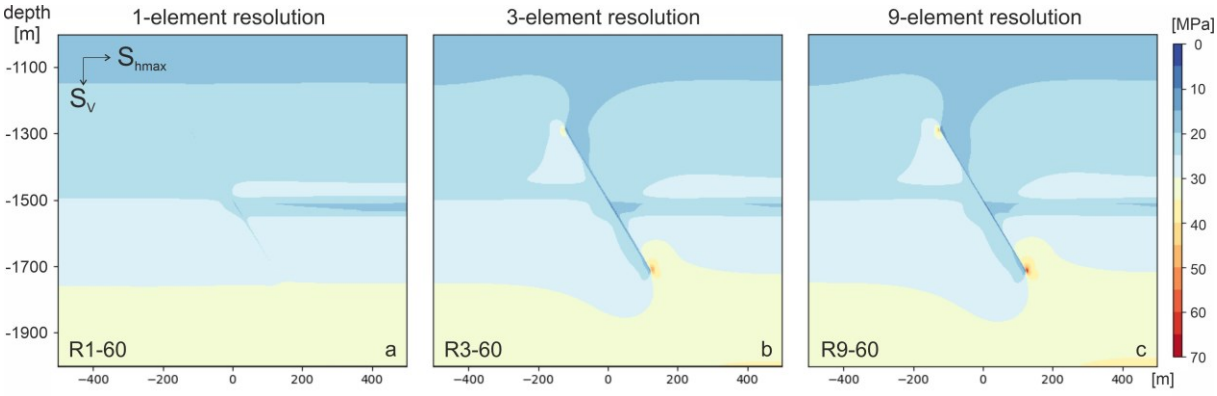

Figure 5-7: Spatial variations in the magnitude of the effective maximum principal stress ($S_{1,eff}$) after the last load step for 1-element- (a), 3-element- (b) and 9-element- (c) wide fault zones dipping at 60° and using a rectangular grid.

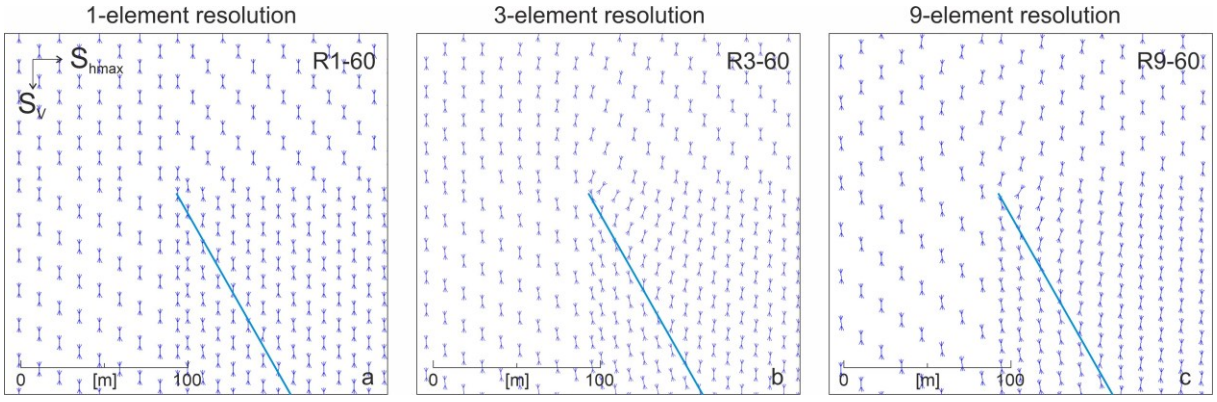

Figure 5-8: Detailed view of the orientation of the maximum principal stress (S_1) after the last load step for 1-element- (a), 3-element- (b) and 9-element- (c) wide fault zones dipping at 60° and using a rectangular grid.

After the last load step, approach R1-60 displays a similar stress pattern, with subhorizontal contour lines like the initial step of the base model. Only the reservoir horizon in the downthrown block shows a reduction of the effective stress because of injection and the resulting increase in pore pressure. The upper left reservoir horizon, however, has not experienced any pore pressure increase (Figure 4-7 a).

In contrast to the 1-element wide fault models, both, the 3- and 9-element wide fault zones clearly undergo a pore pressure increase inside the fault zone. In both models, the entire fault zone is precisely visible by the corresponding decrease in the magnitude of the effective maximum principal stress ($S_{1,eff}$). Peaks of $S_{1,eff}$ occur at the upper and lower fault tips after 5 years of injection (Figure 4-7 b,c). Those peaks are missing in the results for the 1-element width fault zone.

Comparing both higher mesh density models R3-60 and R9-60, only minor differences are found for the $S_{1,eff}$ values. Somewhat higher and, respectively, lower values are produced at the fault tips for the higher mesh resolution. Mesh resolution R3-60 has maximum values of 30 MPa for the upper and 50 MPa for the lower fault tip, while for mesh resolution R9-60 the corresponding values are 40 and 60 MPa. Although these small areas up to 10 m around the fault tips have different maximum values for $S_{1,eff}$, the overall appearance of the $S_{1,eff}$-pattern is the same for the multiple element row approaches (Figure 4-7 b,c).

Likewise, approach R1-60 does not show rotation of the vertical orientation of S_1 except a very slight one (less than 5°) for the actual fault cells for the last load step (Figure 4-8a). The R3-60 and R9-60 approaches exhibit rotations of S_1 similar to the base model. Both display up to 30° clockwise rotations on the right side of the upper fault tip and between 5° and 10° counter clockwise rotation on the left side, respectively. The orientation rotates back to the vertical orientation with increasing distance from the fault (Figure 4-8 b,c).

Figure 9 shows the results for the von Mises plastic strain after the last load step for the three mesh resolutions examined. The 1-element wide fault zone of model R1-60 does not show any plastic straining at all and, hence, is not reactivated (Figure 4-9 a). This contrasts significantly with the strain patterns calculated for the 3- and 9-element fault zone models. Thereby, the finer meshed fault zone shows a larger spatial extent of higher plastic strain values reaching up to 1.3% inside the fault zone (Figure 4-9 c). Apart from this difference, the overall results for the plastic strain are rather similar, i.e., both approaches show larger plastic straining in the fault center, which is reducing towards the fault tips (Figure 4-9 b,c).

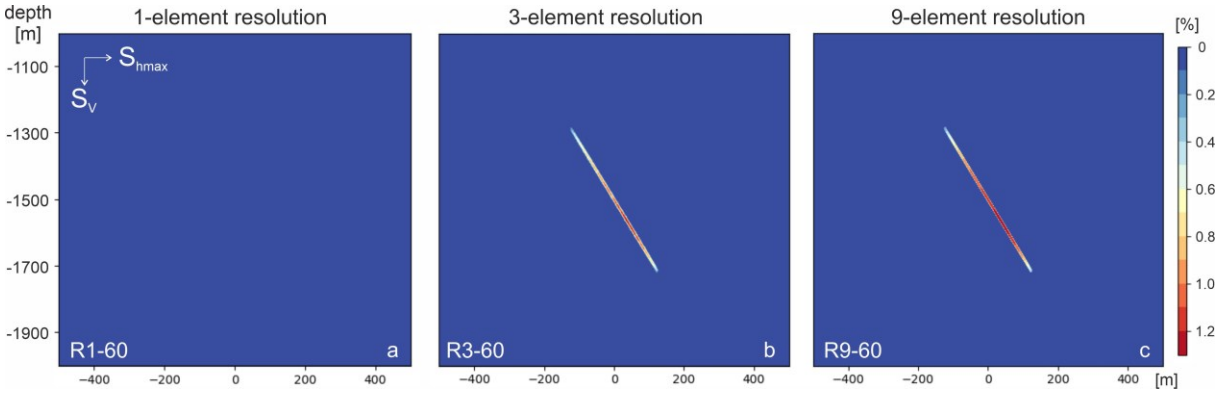

Figure 5-9: Spatial variations in the von Mises plastic strain after the last load step for 1-element- (a), 3-element- (b) and 9-element- (c) wide fault zones dipping at 60° and using a rectangular grid.

5.5.3. Grid Geometry

The modeling results for different gird geometries, rectangular (here, R9-60) and curvilinear (C9-60) are illustrated for 9-element rows fault zone.

4.5.3.1. Pore Pressure and Effective Stress Magnitude

In general, the increase in pore pressure by injection into the downthrown reservoir section propagates through the fault zone in both models. However, there is a slight difference between the rectangular and curvilinear approach in the absolute value reached in the upper reservoir section. While approach C9-60 shows pore pressures up to 25 MPa in this part of the reservoir, they remain below 20 MPa in approach R9-60 stays. Within the fault zone proper, the pore pressure increase expands more towards the fault tips in model C9-60 e.g., the pore pressure for C9-60 is between 27.5 to 32.5 MPa from the spot where the lower reservoir and the fault meet about 100 m towards the fault tip. The remaining distance of the pressure is still between 22.5 and 25 MPa. R9-60 has values of 25 to 30 MPa and 20 to 22.5 MPa, respectively. (Figure 4-10 a,c).

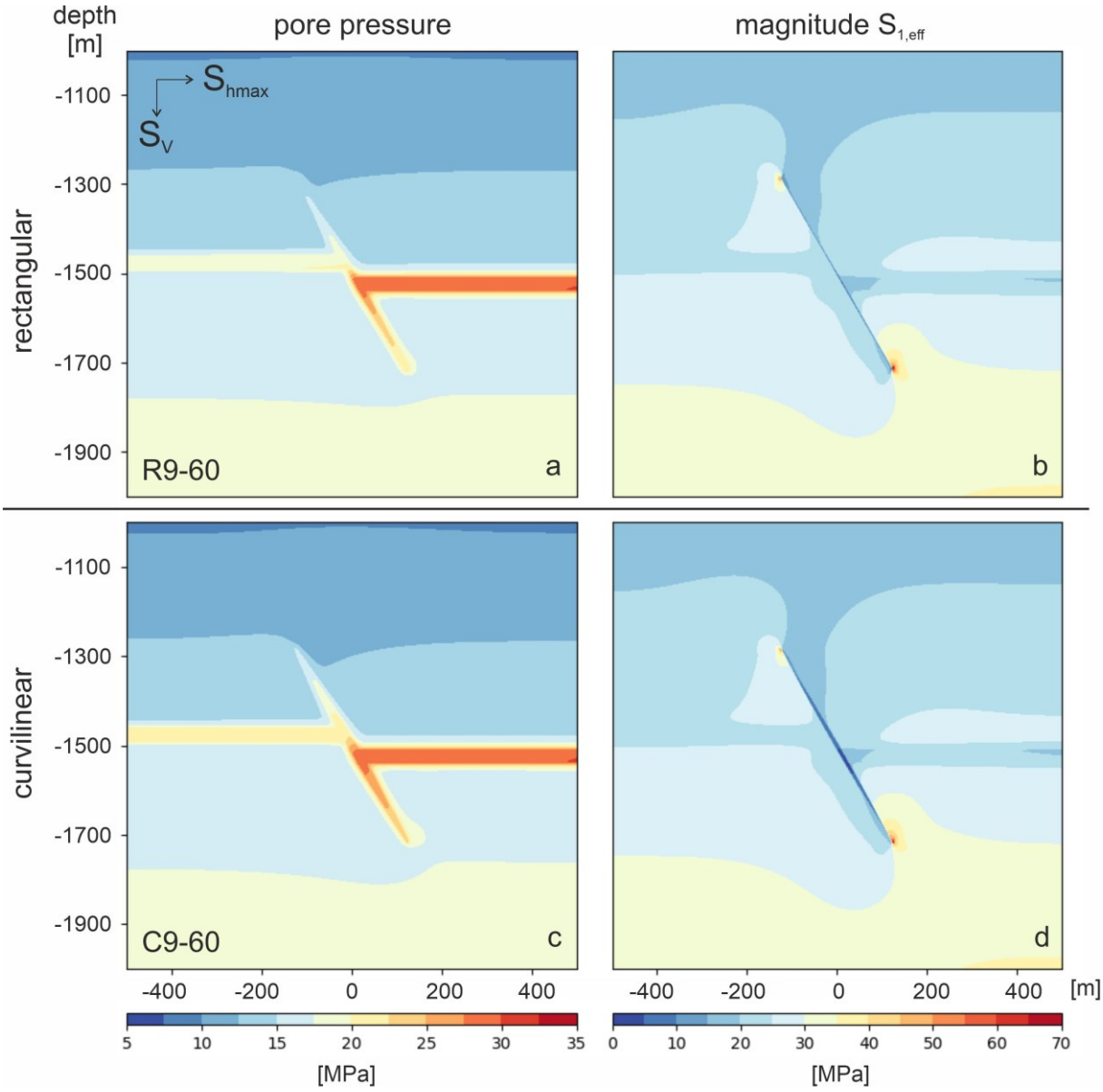

Figure 5-10: Results after the last load step for a 9-element wide fault zone with 60° dip embedded with different grids. Rectangular grid: (a) spatial variations in the pore pressure (b) magnitude of the effective maximum principal stress ($S_{1,eff}$). Curvilinear grid: (c) spatial variations in the pore pressure (d) magnitude of $S_{1,eff}$.

The stress magnitudes for $S_{1,eff}$ display the same overall behavior, but due to the higher pore pressures, $S_{1,eff}$ is lower in the central part of the fault zone for the curvilinear approach (C9-60). There, magnitudes of less than 10 MPa are observed and the spatial extent is up to 12 m wide to both sides

of the fault. The magnitudes achieved with the rectangular approach (R9-60) only gain around 10 to 15 MPa in the middle of the fault and the spatial extent is only about 8 m. Considering the magnitudes of $S_{1,eff}$ at the fault tips for both grid geometries, the approach C9-60 exhibits higher peaks with 68 MPa for the lower and 47 MPa for the upper fault tip. The values observed for the rectangular approach are around 2 MPa lower with 66 and 45 MPa respectively (Figure 4-10 b,d).

A detailed view of $S_{1,eff}$ in the vicinity of the lower fault tip is presented in Figure 4-11. The spatial extent for both the minimum and maximum peak values is smaller for approach C9-60. The lower values (<10 MPa) for $S_{1,eff}$ taper towards the fault tip. In contrast, R9-60 has a wider zone of low values (<10 MPa) which seems to expand towards the fault tip. At distances of more than 10 m from the fault zone, both approaches exhibit the same pattern.

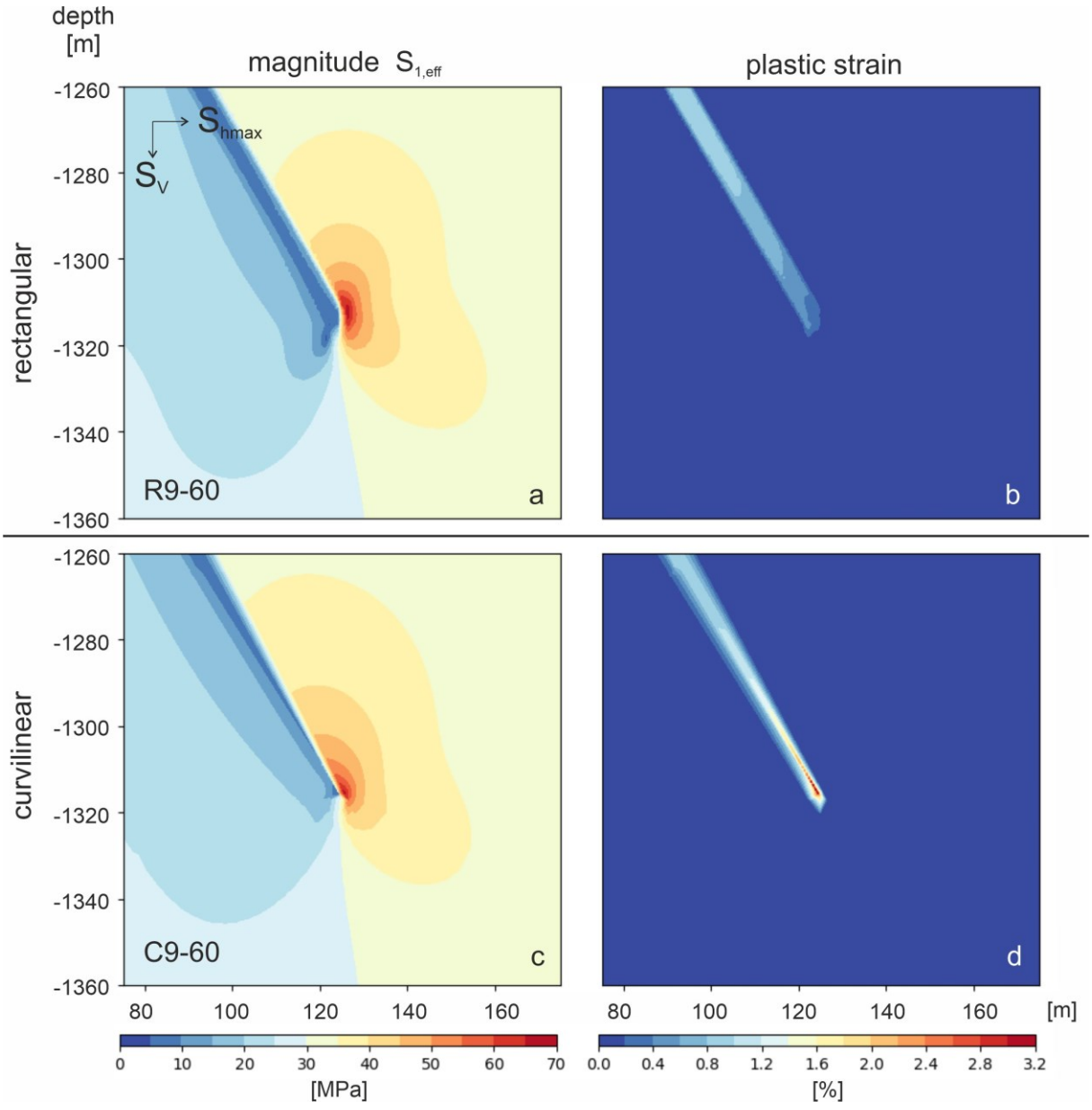

Figure 5-11: Detailed view on the results after the last load step for a 9-element wide fault zone with 60° dip embedded with different grids. Rectangular grid: (a) magnitude $S_{1,eff}$ (b) von Mises plastic strain. Curvilinear grid: (c) magnitude $S_{1,eff}$ (d) von Mises plastic strain.

4.5.3.2. Stress Orientation

The magnitude and orientation of the maximum total principal stress (S_1) is shown in Figure 4-12 for the last load step. The S_1 magnitude distribution shows similar patterns for both grid types. The values range from about 25 MPa at the model top to about 45 MPa at the model bottom. Both models exhibit similar S_1 peaks at the fault tips, which reach 56 and 58 MPa at the upper fault tip and 77 and 78 MPa at the lower fault tip, respectively (Figure 4-12 a,c). Likewise, the orientation of S_1 in the vicinity of the fault tips is very similar. However, there are slight differences in the actual numbers. For the rectangular grid the rotation to the vertical orientation is about 5° counter clockwise on the left and 20°–25° clockwise on the right side of the fault. While left of the fault tip, the rotation is also 5° counter clockwise, the reorientation differs on the right side, where between 25° and 30° clockwise are achieved for the curvilinear approach. From the fault to the sides of the model, the orientation rotates back towards the vertical orientation of S_1 again (Figure 4-12 b,d).

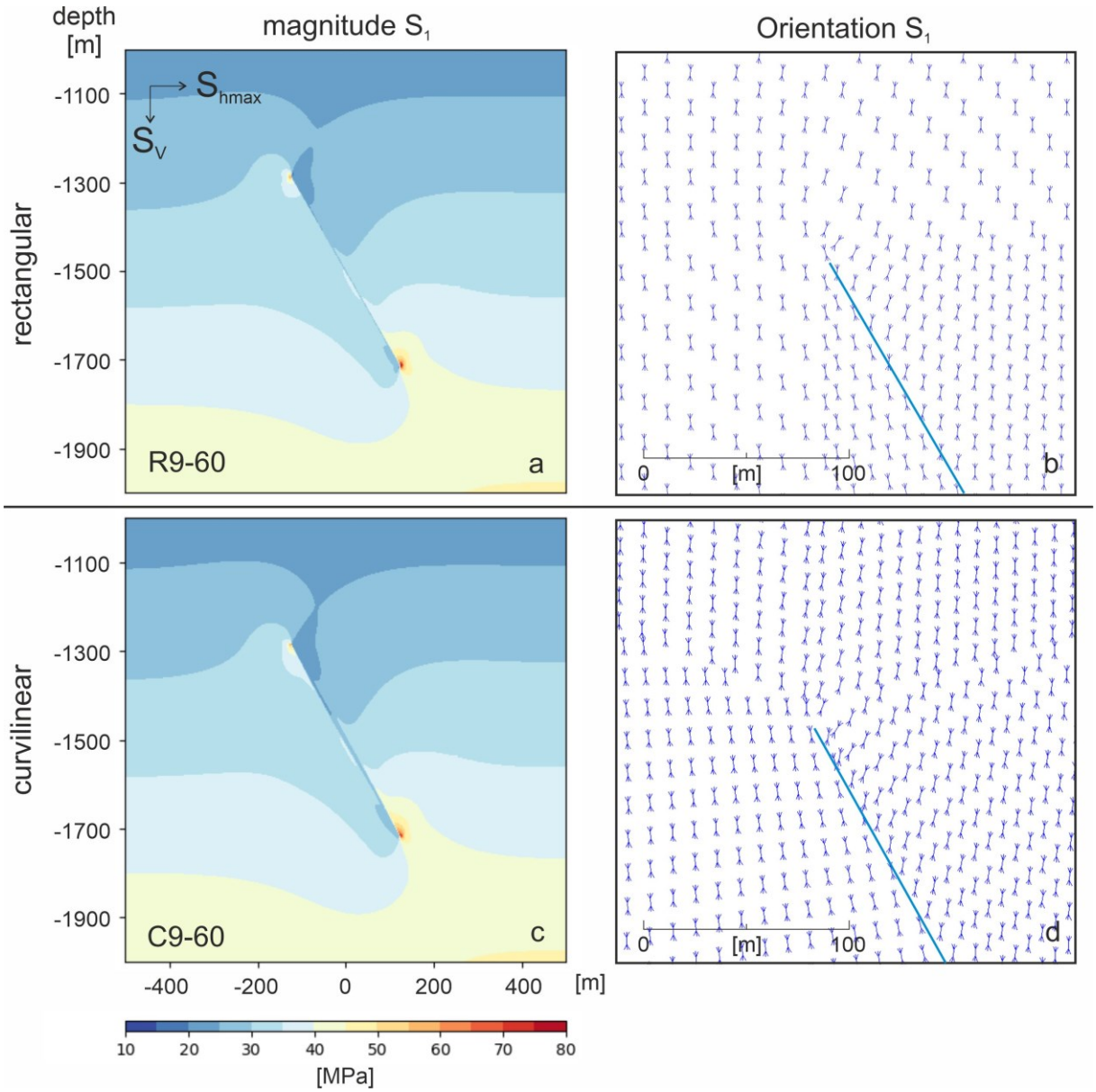

Figure 5-12: Results after the last load step for a 9-element wide fault zone with 60° dip embedded with different grids. Rectangular grid: (a) magnitude of the maximum principal stress (S_1). (b) detailed view of the orientation of S_1. Curvilinear grid: (c) magnitude of S_1. (b) detailed view of the orientation of S_1.

4.5.3.2. Elastic and Plastic Strain

After the last load step, the von Mises elastic strain shows the highest values at the fault tips for both fault grid geometries. At the lower tip, the elastic strain is up to 0.13%. Comparing the elastic strain throughout the fault zone, it is obvious that R9-60 achieves higher values towards the middle of the fault. In contrast, elastic strain in the curvilinear approach decreases strongly from the lower tip towards the middle of the fault and to a lesser extent from the upper tip towards the fault center (Figure 4-13 a,c).

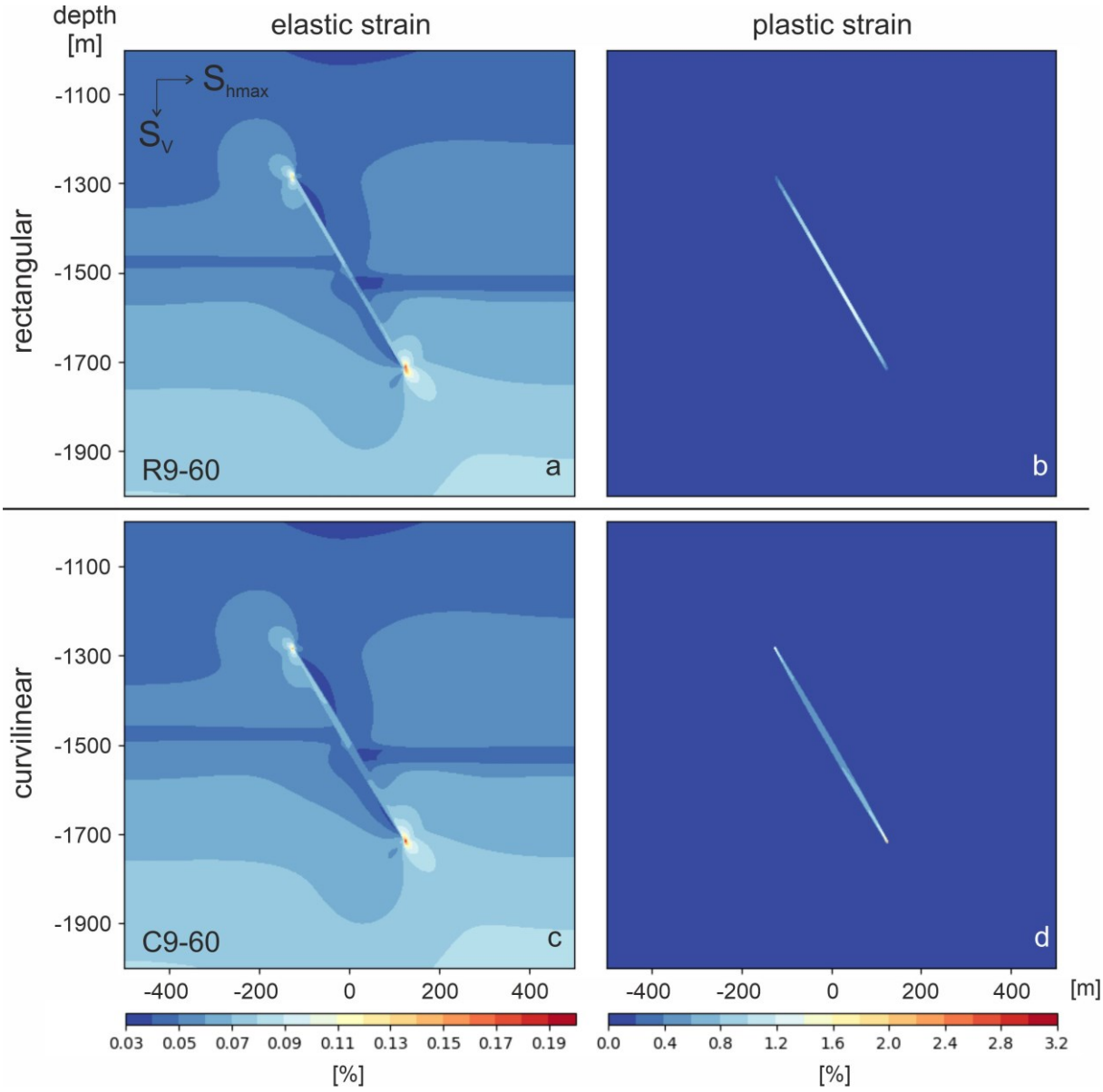

Figure 5-13: Results after the last load step for a 9-element wide fault zone with 60° dip embedded with different grids. Rectangular grid: (a) total von Mises elastic strain (S_1). (b) total von Mises plastic strain. Curvilinear grid: (c) total von Mises elastic strain (S_1). (d) total von Mises plastic strain.

The main difference between both approaches is observed for the von Mises plastic strain. After the last load step, the plastic strain occurs mostly at the fault tips for C9-60. The plastic strain for the curvilinear approach reaches up to 3.2% at the lower fault tip. Towards the middle of the fault, plastic strain decreases to about 0.3%. For R9-60, the plastic strain behaves the other way around. It decreases from the middle of the fault towards the fault tips. The rectangular approach has its highest values of about 1.5% in the middle of the fault and decreases to about 0.4% at the fault tips. Outside the fault

zone no plastic straining occurs (Figure 4-13 b,d). A more detailed view of these plastic strain patterns in the vicinity of the lower fault tip is pictured in Figure 4-11 b,d. This figure shows the von Mises plastic strain for both approaches within 50 m from the fault tip.

5.5.4. Fault Dip

The effect of different fault dips is investigated using the curvilinear approach with a 3-element wide fault zone with 60° (C3-60) and 90° fault dip (C3-90), respectively. Figure 4-14 shows the results for pore pressure, $S_{1,eff}$ and total plastic strain after the last load step. Similar results are achieved for the pore pressure distribution, albeit somewhat higher pore pressures are observed in the upper reservoir section for the vertical fault (Figure 4-14 a,d). For $S_{1,eff}$, approach C3-60 shows peak values of up to 60 MPa for the lower and 50 MPa for the upper fault tip. Those local stress peaks do not occur in case of a vertical fault, i.e., C3-90. Otherwise, the effective stress magnitudes within the fault zone of about 5 MPa are quite similar for both fault dips (Figure 4-14 b,e).

Substantial differences are again observed for plastic straining, as no plastic straining occurs for a vertical fault. In contrast, von Mises plastic strain in case of a fault zone dipping at 60° is 0.6% in the middle of the fault and up to 3.2% at both fault tips (Figure 4-14 c,f).

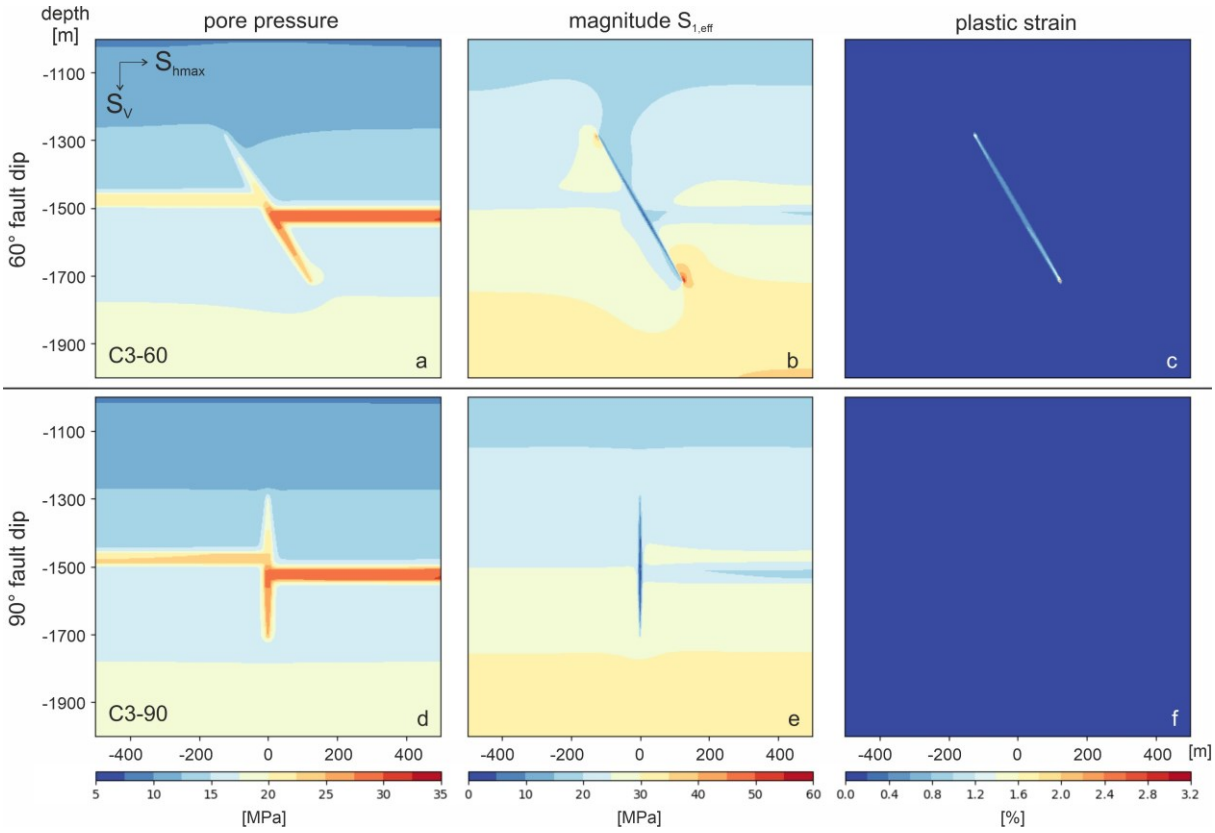

Figure 5-14: Results after the last load step for a 3-element wide fault zone with embedded in a curvilinear grid with different fault dips. 60°-fault dip: (a) pore pressure. (b) magnitude of $S_{1,eff}$. (c) total von Mises plastic strain. 90°-fault dip: (d) pore pressure. (e) magnitude of $S_{1,eff}$. (f) total von Mises plastic strain.

5.6. Discussion

For the initial load step, the expected model behavior is observed. The hydrostatic pressure and the loading result in vertical gradients of both pore pressure and the maximum principal stress ($S_1 = S_v$). Outside the area affected by the predefined fault zone, S_1 is vertical and the stress regime displays normal faulting (Anderson, 1951). No plastic straining is observed after the initial load step which proves that the fault is not already reactivated by the initial and boundary conditions selected. The

results of the last load step, i.e., after 5 years of injection, show higher pore pressure in both reservoir horizons, and therefore, indicates fluid migration through the fault zone. Plastic straining occurs throughout the entire fault zone. Hence, fault reactivation is achieved from pore pressure increase due to fluid injection into the reservoir.

The calculated stress pattern can be compared to other numerical simulations which incorporate faults (Cuisiat et al., 2010; Pereira et al., 2014; Will & Eckardt, 2015). The corresponding stress perturbations derived from such numerical models resemble the results of the base model regarding both spatial extent and magnitude of the stress changes induced by the fault.

5.6.1. Mesh Resolution

A general recommendation is to use a finer mesh in those areas where stress and strain gradients are large. To identify the regions where greater mesh density or local grid refinement is required, preliminary simulations with a coarse mesh appear useful (Ching & Phoon, 2013; Liu, 2013; Sanchez et al., 2015; Ching & Hu, 2016).

In our study, the representation of a fault as 1-element row in a rectangular grid appears to be a special case, but they are not unusual for reservoir simulations. In the last several years, different authors have used this kind of fault zone representation to investigate a multitude of reservoir-related tasks like fault reactivation (De Souza et al., 2014; Deb & Jenny, 2017), CO2-Storage (Olden et al., 2012) and fully-coupled reservoir simulations (De Souza et al., 2012; Deb & Jenny, 2017). However, our modeling results indicate substantial differences compared to fault representations with multiple element rows. For the mechanical part, the stress and strain patterns as well as magnitudes are different and for the hydraulic part, the fault seems to act as barrier for fluid flow in the case of a 1-element representation.

Only minor differences in the resulting stress and strain patterns as well as stress magnitudes exist if the fault is represented as a 3-element or 9-element wide zone. The higher mesh resolution inside the fault zone only increases the maximum values for both stress and strain at the fault tips, but the spatial extent of these differences remains less than 10 m near the fault tips.

Several studies (Ashford & Sitar, 2001; Liu, 2013; Huang & Griffiths, 2015) have evaluated the effects of mesh density on finite element analysis. There are two issues which can be responsible for the punctually higher stress and strain values in the simulations using the higher mesh resolution. First, stress and strain fields have higher gradients in the localization zone, such as the tip of a fault zone, for higher mesh densities (Li & Wierzbicki, 2009). This implies that the finer mesh resolution leads to a more punctually concentrated stress, which in turn, is higher (Liu & Glass, 2013; More & Bindu, 2015). The higher stress values ultimately cause higher plastic strain, which is also observed in the finer mesh resolution. The second issue is that models with a lower mesh resolution, i.e., with less elements, appear to be somewhat stiffer, while increasing the number of elements softens the model slightly and improves the accuracy of the stiffness integration (Liu & Glass, 2013; Ching & Hu, 2016). Therefore, the slightly higher stress and strain values for the models using a higher resolution may originate from the lower effective stiffness at the fault tips.

However, the spatial extent of this variations is very small and the overall stress and strain pattern as well as the hydraulic behavior for the whole model is the same for 3- and 9-element wide fault zones. In order to determine the required mesh resolution inside the fault zone, it is crucial to evaluate the required precision as well as the target location regarding the specific aim of the particular study.

The differences between the one element (R1-60) approach and both multiple row approaches (R3-60 and R9-60) stem from the arrangement of the elements to which the fault zone properties have been assigned. Regarding R1-60, the rectangular grid geometry leads to the fault zone elements being connected by only one common node, i.e., all neighboring elements which share joint edges exhibit the non-permeable and mechanically stronger host rock properties. This subdues the formation of both a

through-going fluid pathway and deformation zone. In contrast, the fault zone with a higher mesh resolution and more element rows has numerous common element faces and, hence, a continuous fluid pathway through the entire fault zone can develop. Likewise, strain can accumulate and form a continuous zone of deformation. The larger amount of fluid flow through the fault zone increases the pore pressure inside the fault zone and leads to reduced effective stresses, which in turn, decreases the shear strength again.

5.6.2. Grid Geometry

Comparing the two fundamental grid geometries studied, the different results in both hydraulic and mechanical simulations can be explained by the special features of the rectangular grid for fluid flow as well as stress and strain propagation.

On the hydraulic part, the rectangular grid induces a spatial restriction in the fluid pathway since some of the elements forming the fault zone are connected by only one node. The reduced fluid migration through the rectangular fault zone also explains the lower pore pressures observed in the upper reservoir section for the rectangular grid geometry (see Figure 4-10 a).

In a coupled simulation the hydraulic behavior directly effects the mechanical response. According to the Mohr–Coulomb criteria (Figure 4-4), a pore pressure increase causes a decrease in the effective stresses, which shifts the Mohr–Coulomb circle towards the shear failure line (Byerlee, 1978; Jaeger et al., 2007; Faulkner et al., 2010). Thus, the higher pore pressures in the curvilinear approach lead to a higher reduction of the effective stresses (Yale, 2003; Gudmundsson, 2011; Shapiro, 2015), which explains the difference between both gird geometries regarding the magnitudes and the spatial extent of $S_{1,eff}$ (Figure 4-10 b,d).

For the rectangular grid, the increase in pore pressure is mainly in the center of the fault which is also the reason for the location of the highest plastic strain values there. However, this does not fully explain the different plastic strain distribution for both grid geometries. Fault geometry may also be partly responsible for this different mechanical response. While the curvilinear approach offers a linear, smooth boundary between the undeformed reservoir rock and the fault zone, the rectangular approach has a stair-stepped geometry (Figure 4-15). This results in some kind of interlocking with the stronger rock properties outside the fault zone, and therefore, constrains strain accumulation compared to the curvilinear approach.

In addition, the grid geometry seems to be responsible for the different results of the plastic strain occurring at the fault tips (Figures 4-11 b,d and 4-13 b,d). The rectangular fault zone ends with a rectangular block of elements. This favors the plastic strain to disperse over multiple elements, which in combination with interlocking of the host rock cells, reduces the plastic strain values at the fault tips even further (Figure 4-15 R). In contrast, the fault in the curvilinear fault converges towards the fault tip (Figure 4-15 C). This causes the strain to accumulate at the fault tips, and thus, exhibits larger plastic strain there.

Particularly the plastic strain pattern of the curvilinear approach seems to be closer to nature. During the development and the growth of a fault, stress concentrations at the fault tips lead to strain localization (Dyskin, 1993; Reches & Lockner, 1994; Hoek & Martin, 2014). Small discontinuities (i.e., Griffith cracks) in the so-called "intact rock" can be stimulated and coalesced by those strain localizations (Brace, 1960; Cowie & Shipton, 1998; Brandes & Tanner, 2019) similar to the ones observed for the curvilinear approach (see Figure 4-13d). This macroscale shear failure of the intact host rock at the fault tips can expend through ongoing strain to extend a continuous fault surface (Lin & Parmentier, 1988). Although the FE method used in our approach cannot model fracturing and consequently, fault propagation, the plastic strain accumulations at the fault tips for curvilinear fault representations seem to mimic the behavior in nature.

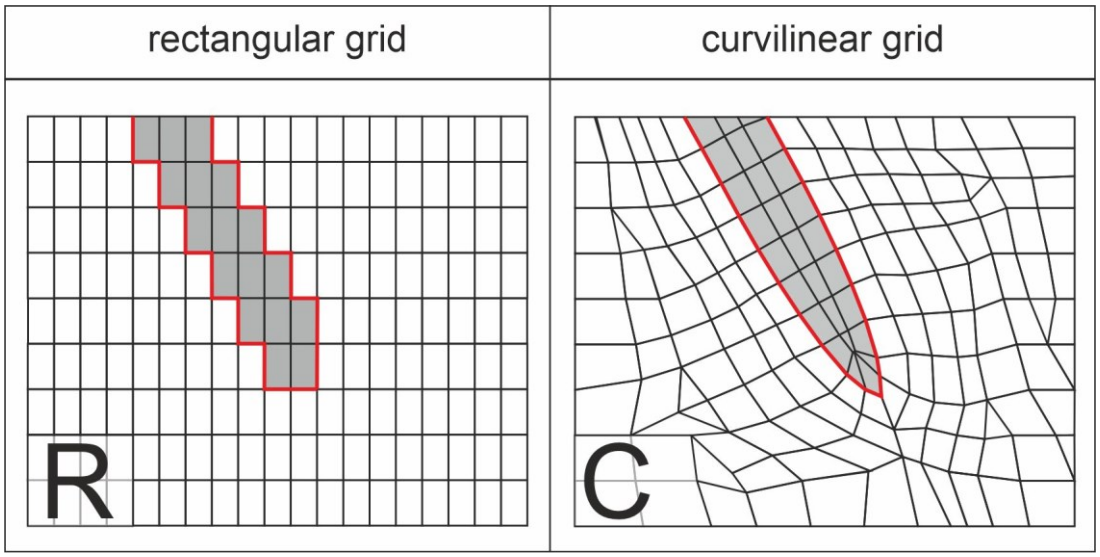

Figure 5-15: Image showing the rectangular (R) and curvilinear (C) grid geometries and their interaction with the surrounding rock mass. While the fault cells in the rectangular approach tend to interlock with the surrounding, stronger host rock, the edges of the fault cells in the curvilinear representation form a surface almost parallel to the fault plane. Furthermore, the curvilinear representation ends in a pointed geometry while the rectangular fault ends in as a block of cells.

5.6.3. Fault Dip

Different fault dip angles do not significantly influence fluid flow. Therefore, the pore pressure distribution is similar for the 60° and 90° dip scenarios. However, the dip of the fault zone has a strong influence on the mechanical behavior. Both stress and strain patterns are reduced for the 90° fault dip compared to the 60° fault dip. Particularly the difference in the plastic strain is striking. There is no plastic straining and, consequently, no fault reactivation for the 90° case. This behavior can be explained according to the Mohr–Coulomb failure criterion (Byerlee, 1978; Faulkner et al., 2010). The stresses acting on the fault plane are divided into the normal stress (σ_n) acting orthogonal to the fault and the shear stress (τ) acting parallel on the fault, which can be calculated according to:

$$\tau = \left(\frac{\sigma_1 - \sigma_3}{2}\right) \cdot \sin(2 \cdot \alpha) \tag{5-8}$$

$$\sigma_n = \left(\frac{\sigma_1 + \sigma_3}{2}\right) + \left(\frac{\sigma_1 - \sigma_3}{2}\right) \cdot \cos(2 \cdot \alpha) \tag{5-9}$$

with maximum (σ_1) and minimum (σ_3) principal stresses and the fault dip (α) (Anderson, 1951; Dutt, 2015). According to the model setup, the initial stress field is the same for both, the 60°- and 90°-fault dip. If σ_1 and σ_3 acting on the fault are the same, the only different variable for the different fault dips in formula (5-8) and (5-9) is the fault dip (α) itself.

The shear stress, calculated by formula (5-8), is zero when the sinus-term is zero, which is the case for a 90° fault dip. Since the shear stress acting on the fault is zero, the shear failure line is not exceeded, and the rock remains intact. Hence, the deformation takes only part of the elastic domain, no plastic strain occurs for the models with a 90° fault dip.

5.6.4. Practical Aspects of Model Building

Between the various approaches there are huge differences due to the amount of work and time needed, i.e., the costs required to incorporate faults into a hydro-mechanical reservoir model. Computing time increases exponentially with the number of elements, so finer mesh resolutions within and near the

fault zone significantly increase the runtime of the simulations. Even if it is not readily available from preceding property modeling or a flow simulation, generating the grid geometry for a regular rectangular model and intersecting it with a fault interpretation is quite straightforward and by far the most rapid technique. Implementing the curvilinear approach for fault representations requires a special grid adapted to the fault geometry. This step can be a rather time-consuming and labor-intensive task, depending on the complexity of the geometry of the fault network being modelled. As shown above, a rectangular grid with the same fault zone resolution can lead to similar results, at least at larger distances from the fault zone.

The rectangular approach can therefore be suitable for a first-order evaluation before more complex models with a curvilinear grid are performed. In addition, for reservoir simulations focusing on the central parts of fault compartments rather than the fault zone itself, the rectangular approach can be reasonable. In contrast, for reservoir simulations focusing on fault zones and their immediate vicinity, better results can be expected by using the curvilinear approach.

5.7. Conclusion

Using a simple generic model setup, different scenarios for the incorporation of faults as volumetric weak zones into hydro-mechanical reservoir models are analyzed. The various scenarios differ regarding the mesh resolution of the fault zone (1-, 3- or 9-element width), the grid geometry (rectangular vs. curvilinear) and the fault dip (60° and 90°). Significant differences in the stress and strain patterns are indicated in the results, which are induced by the fault depending on its incorporation in the numerical model. Based on the numerical simulation results, five general recommendations can be given on how to represent faults in FE reservoir models:

1. The mesh resolution has to be considered very carefully, since it can—combined with a rectangular grid—lead to serious errors. It needs to be ensured that the fault cells do not interlock with the surrounding, stronger and less permeable host rock as this effects both fluid flow through and straining of the fault zone. This interlocking effect mainly occurs for 1-element width fault zones. For grids with multiple element wide fault zones, the only differences are observed in the vicinity of the fault tips. Three element wide fault zones appear to be appropriate for most reservoir-scale models. Only if the aim of the study is within 10 m of the fault zone, a finer resolution should be considered.

2. If the aim of the study is to model the fault zone properly, a curvilinear representation is recommended. In addition to somewhat better fluid migration throughout the whole fault zone, this approach shows higher plastic strain at the fault tips, which appears to be closer to reality.

3. If the aim of the study is at a distance of more than 10 m from the fault, both grid geometries are interchangeable. They show similar stress and strain patterns. In this case, the advantage of the rectangular grid is that it generally takes much less time to generate.

4. Different fault dips produce different mechanical results, i.e., stress and strain patterns. Therefore, care should be taken to consider a realistic fault dip, e.g., from interpretation of depth-converted seismic sections, rather than using a vertical fault dip for simplification.

5. Different fault dips produce similar hydraulic results. If the aim of the study is primarily on hydraulic issues, vertical faults can be an acceptable simplification.

Regarding the upscaling of the material heterogeneity and complex fault zone architecture to a volumetric weak material representing the fault zone, challenges remain. For a more detailed analysis, including architectural and material heterogeneity, a volumetric fault zone description with a grid

adapted to the fault zone geometry seems more appropriate. The possibility of incorporating further details can be presented by local mesh refinement rather than upscaling them to the size of one element.

This research investigates a simple generic fault model in a siliciclastic succession, but the methodology and the findings can be transferred to structurally more complex models as well as other lithologies, e.g., carbonate reservoirs. However, while the general recommendations can be used, the reservoir structure has to be modelled according to the specific geological setting.

Perspectives for future modeling work include sensitivity studies for the material parameters defining the shear strength and the fluid flow of the fault zone as well as the influence of detailed reproduction of the internal fault architecture.

Acknowledgement

Special thanks to Tobias Backers and Dominik Gottron for helpful suggestions and discussions during various parts of this research.

6. Elastic and Frictional Properties of Fault Zones in Reservoir-Scale Hydro-Mechanical Models—A Sensitivity Study

Torben Treffeisen & Andreas Henk

TU Darmstadt, Institut für Angewandte Geowissenschaften, Schnittspahnstraße 9, 64287 Darmstadt, Germany

Published in: Energies 13, Special Issue "Petroleum Geomechanics" (2020): 1-27, (https://doi:10.3390/en13184606)

Abstract

The proper representation of faults in coupled hydro-mechanical reservoir models is challenged, among others, by the difference between the small-scale heterogeneity of fault zones observed in nature and the large size of the calculation cells in numerical simulations. In the present study we use a generic finite element (FE) model with a volumetric fault zone description to examine what effect the corresponding upscaled material parameters have on pore pressures, stresses, and deformation within and surrounding the fault zone. Such a sensitivity study is important as the usually poor data base regarding specific hydro-mechanical fault properties as well as the upscaling process introduces uncertainties, whose impact on the modeling results is otherwise difficult to assess. Altogether, 87 scenarios with different elastic and plastic parameter combinations were studied. Numerical modeling results indicate that Young's modulus and cohesion assigned to the fault zone have the strongest influence on the stress and strain perturbations, both in absolute numbers as well as regarding the spatial extent. Angle of internal friction has only a minor and Poisson's ratio of the fault zone a negligible impact. Finally, some general recommendations concerning the choice of mechanical fault zone properties for reservoir-scale hydro-mechanical models are given.

6.1. Introduction

Hydro-mechanical simulations have developed into a standard tool for various subsurface applications ranging from hydrocarbon and geothermal reservoirs to underground storage sites for CO_2 (Cappa & Rutqvist, 2011; Fachri et al., 2016; Serajian et al., 2016; Schuite et al., 2017). However, challenges exist regarding the proper implementation of faults into such numerical models. Faults not only have a profound impact on fluid flow, but also effect the stress field in their vicinity. In addition, pore pressure changes due to injection or production can induce slippage and fault reactivation, respectively (Pereira et al., 2014; Rueda et al., 2014; Sanchez et al., 2015; Haug et al., 2018). This may cause induced seismicity, land subsidence and well collapse (Segall et al., 1994; Morton et al., 2006; Chan & Zoback, 2007; Vilarrasa et al., 2017). Fault reactivation may also breach the reservoir seal causing up-fault leakage and allowing fluid migration due to enhanced permeability inside the fault zone (Wiprut & Zoback, 2000; Cuisiat et al., 2010; Faulkner et al., 2010). Thus, proper incorporation of faults into hydro-mechanical models is of crucial relevance for various reasons.

In reality, faults are characterized by a complex geometrical structure and a heterogeneous material distribution (Caine et al., 1996; Walsh et al., 2003; Collettini & Holdsworth, 2004; Myers & Aydin, 2004; Childs et al., 2009; Fasching & Vanek, 2011). They should be regarded rather as a fault zone, i.e., a volumetric feature, than as a discrete fault surface (Rawling et al., 2001; Wibberley et al., 2008; Childs et al., 2009; Gudmundsson, 2011). A fault zone typically contains a fault core accompanied by damage zones on either side, but may be structurally more complex including the appearance of multiple fault cores as well as damage zones of variable width and fracture intensity (Caine et al., 1996; Childs et al., 1996; Fasching & Vanek, 2011; Gudmundsson et al., 2013; Bauer et al., 2015). Therefore, the appropriate representation of faults in numerical reservoir models is challenged by two related aspects: (1) the difference in scale between the heterogeneity of the fault zone (centimeters to meters)

and the typical size of the calculation cells of the numerical grid (meters to tens of meters) and (2) the material properties assigned to the fault zone which stem—if available at all—from rock mechanical testing on core samples with a diameter of a few centimeters. Both aspects require upscaling, i.e., merging the heterogeneous material properties of the fault zone (Manzocchi et al., 2008; Olden et al., 2012; Zhang et al., 2015; Qu & Tveranger, 2016), in order to assign reasonable material properties to the fault zone elements of a reservoir-(kilometer)-scale hydro-mechanical model.

In the present study we use a generic finite element (FE) model with a volumetric fault zone description to examine what effect such upscaled parameters have on pore pressures, stresses, and deformation within and surrounding the fault zone. Such a sensitivity study is important as the usually poor data base regarding specific hydro-mechanical fault properties as well as the upscaling process introduces uncertainties, whose impact on the modeling results is otherwise difficult to assess. As the prime focus is on fault reactivation due to pore pressure changes, we explore a parameter range for Young's modulus, Poisson's ratio, cohesion, and angle of internal friction which is typical for fault zone rocks. Modeling results are expected to provide a framework to understand quantitatively how the elastic and frictional-plastic properties assigned to a fault zone in a hydro-mechanical reservoir simulation actually affect the modeling results.

6.2. Elastic and Frictional Fault Zone Properties

Faults are usually not a target for drilling operations. They are rather avoided to reduce well stability problems. Even if coring of a fault zone is attempted, intense fracturing and poor consolidation of fault zone rocks frequently results in very limited core recovery (Paul et al., 2007; Johri et al., 2014). As a consequence, there usually is a lack of fault-specific material parameters to populate a hydro-mechanical model (Zoback, 2007; Hennings et al., 2012). Instead, the material parameters have to be estimated from literature sources considering how faulting and fracturing change the material properties of the intact rock. In the following we review the possible range of mechanical fault rock parameters in the elastic and frictional-plastic domain, which also forms the basis for the subsequent numerical sensitivity study.

6.2.1. Elastic Material Properties

Deformation in the elastic domain can be described by Hooke's Law, which relates stress and strain via an elasticity (or stiffness) matrix (Carmichael, 1988; Jaeger et al., 2007). In case of a linear-elastic and isotropic medium, only two material properties are required: Young's modulus and Poisson's ratio. The Young's modulus or modulus of elasticity of a fault zone can vary by several orders of magnitude between the value of the intact rock and the one of the fault-related rocks in the damage zones and fault core. The Young's modulus for common lithologies (intact rock) ranges from 1 GPa to 100 GPa (Gudmundsson, 2011; Fjær, 2018). It decreases with increasing fracture density, i.e., in the damage zone and tectonic breccias, respectively. Fault gauges which frequently make up the fault core can exhibit Young's modulus values as low as 0.01 GPa (Goodman, 1989; Schön, 2004; Gudmundsson, 2011).

The Young's modulus required for numerical modeling is the static Young's modulus which—ideally—is derived from uniaxial or triaxial testing of cores in the laboratory. Such rock mechanical testing is typically carried out on samples with a diameter of a few centimeters. However, mechanical properties like Young's modulus and unconfined compressive strength (UCS) derived from lab tests are usually significantly larger (1.5×–10×) than the corresponding values of a larger rock mass (Jaeger et al., 2007; Gudmundsson, 2011). This scale-dependence can be accounted for by using empirical correlations, but this inevitably adds uncertainties to the material properties assigned to the fault zone in the numerical model (Eissa & Kazin, 1988; Fjær, 2018; Davarpanah et al., 2020). If no cores are available, an option is to calculate dynamic Young's modulus from well logs (p- and s-wave velocities, density). However, these dynamic Young's modulus values need to be converted to static

ones based on empirical correlations which introduces yet another uncertainty to the upscaled properties.

The second parameter to describe elasticity is Poisson's ratio. It is defined as the negative transversal strain divided by the axial or longitudinal strain (Fjær et al., 2008; Gudmundsson, 2011). Again, determination of static Poisson's ratio requires core samples for laboratory testing, while dynamic values can be derived from borehole logs (p- and s-wave velocities). Poisson's ratios of common lithologies are usually in the range of 0.10–0.35 with most values between 0.2 and 0.3 (Schön, 2004; Fjær et al., 2008; Gudmundsson et al., 2013). If no specific measurements for the Poisson's ratio of a rock unit is available, 0.25 is a value commonly used in numerical simulations.

6.2.2. Frictional Material Properties

In case of most rocks, elastic material behavior is restricted to only a few percent (1–3%) of deformation. If stresses reach the yield point, the subsequent post-failure behavior and irreversible deformation falls into the plastic domain (Brady & Brown, 1993; Jaeger et al., 2007; Gudmundsson, 2011). In case of brittle-plastic material behavior, failure is realized through fracture formation, while in the ductile domain failure occurs as plastic flow (Brace, 1960; Caddell, 1980; Faulkner et al., 2010). Major crustal-scale fault zones include both failure mechanisms with fracturing and a well-defined fault zone in the upper part and plastic flow resulting in a distributed shear zone in the deeper part. However, at typical reservoir depths of a few kilometers, brittle failure is the dominant deformation mechanism in fault zones (Reches & Lockner, 1994; Hoek, 2013; Deb & Jenny, 2017).

A commonly used failure criterion separating the elastic and the plastic domain is the Mohr–Coulomb (MC) failure criterion. The MC criterion defines the maximum shear stress a rock can withstand until shear failure occurs (Byerlee, 1978; Zoback, 2007; Fjær et al., 2008). The corresponding frictional material properties of the MC criterion are cohesion and the angle of internal friction.

Cohesion, also called inherent shear strength, is the shear strength of a rock if the effective normal stress is zero (Goodman, 1989; Bell, 2000; Azarfar et al., 2018). The cohesion of fault zone rocks can vary by several orders of magnitude from completely cohesionless to a few tens of MPa depending on the degree of deformation and healing or recrystallization, e.g., from hydrothermal precipitations (Faulkner et al., 2010; Gudmundsson et al., 2013). For example, a fault zone may contain a fully powdered fault core, which persists of cohesionless rock flour (Caine et al., 1996; Rawling et al., 2001; Holdsworth, 2004; Childs et al., 2009). In contrast, circulation of hydrothermal fluids can cause mineral precipitation (e.g., quartz, barite), which hardens the fault core even more than the surrounding rock mass (Collettini & Holdsworth, 2004; Syversveen et al., 2006; Azarfar et al., 2018). In order to estimate fault zone cohesion, some rules of thumb can be considered:

- The higher the deformation and the strain values during fault zone formation, the more likely the rock mass is highly deformed and powdered. Thus, cohesion decreases with increasing deformation during fault formation (Bell, 2000; Faulkner et al., 2010; Hoek, 2013; Hoek & Martin, 2014).
- Hydrothermal circulation (depending on the chemical content of the circulating fluids) can overprint and cement the fault zone rocks leading to increased cohesion (Bruhn et al., 1994; Faulkner et al., 2010; Gudmundsson et al., 2013).

It should be noted that for sedimentary rocks the intercept of a linear Mohr–Coulomb criterion actually overestimates rock cement strength. In such cases, use of a nonlinear failure envelope would be more appropriate to describe real cohesion at low effective confining stresses.

The second frictional material parameter used in the MC criterion is the angle of internal friction. It describes the increase in shear strength of a rock with respect to an increase in normal stress

(Goodman, 1989; Faulkner et al., 2010; Gudmundsson, 2011). Friction angles of common lithologies range between 5° and 50° (Jaeger et al., 2007; Gudmundsson, 2011). A frequently used average value for rocks is 40.5° equivalent to a coefficient of internal friction of 0.85 (Byerlee, 1978). In general, the friction angle is related to grain size, so coarse-grained rocks tend to have a higher friction angle, while lower friction angles are typical for fine-grained rocks and rocks with a high clay content, respectively (Barton, 1973; Andersson et al., 1991; Faulkner et al., 2006; Chiaraluce et al., 2007; Collettini et al., 2009). Besides grain size, the degree of fracturing also affects the angle of internal friction (Malkowski, 2015). Typically, the friction angle decreases with increasing fracturing of the rock (Sanetra, 2005; Bukowska & Sanetra, 2008).

However, other studies (Sulem et al., 1999; Jafarpour et al., 2012) indicate that during rock degradation in shear and without further weakening due to mineral alteration and clay smearing, the friction angle remains largely unaltered. Thus, weakening in such cases results primarily from cohesion softening.

A fault-specific determination of cohesion and angle of internal friction again requires core samples for triaxial rock mechanical testing in the lab. If the material is not suitable for multistage testing (Bro, 1997; Blümel, 2009; Taheri & Chanda, 2013), at least three samples are required for one triaxial test. Thus, it is very rare that proper rock samples for triaxial testing of fault zone rocks are available to populate a numerical model with specific frictional fault rock properties (Faulkner et al., 2010; Gudmundsson, 2011).

6.3. Modeling Concept

A finite element (FE) model was set up to compare the effect on hydro-mechanical simulation of different elastic and frictional-plastic properties assigned to a fault zone. It consists of over and underburden sections of low permeability with a high-permeability reservoir layer in between and offset by a normal fault. Figure 1a exhibits an elliptical fault zone displacing a reservoir horizon, the geological rationale for this model setup. The reservoir horizon embedded into the 1 km × 1 km × 0.003 km model frame is displaced by a 500 m long normal fault centered in the middle of the model. At the top of the model frame, loading conditions simulate 1 km of overlaying rock material. So the model bottom is adopted to be 2 km beneath the surface. Additionally, the weight of the overburden implemented as pressure acting on the model top, no further mechanical forces, or displacements are assigned to the model. On the hydraulic part, the initial model assumes a hydrostatic pore pressure field. Subsequently, pore pressure at the nodes on the right side of the reservoir unit is increased to simulate fluid injection into the downthrown block. For five years the pore pressure is constantly increased every three months by 0.75 MPa until it finally reaches 15 MPa above hydrostatic.

Starting from a base model which is used as reference for the subsequent sensitivity studies, Young's modulus, Poisson's ratio, cohesion, and angle of internal friction are varied within a range typical for fault zone rocks. At the same time, the model geometry and the material properties for the other model units (reservoir rock and over-/underburden) remain the same in all scenarios. Altogether, 87 FE models with different mechanical parameter combinations assigned to the fault zone have been studied. FE software Ansys 19.2 (Ansys, 2019) is used for the fully coupled hydro-mechanical simulations.

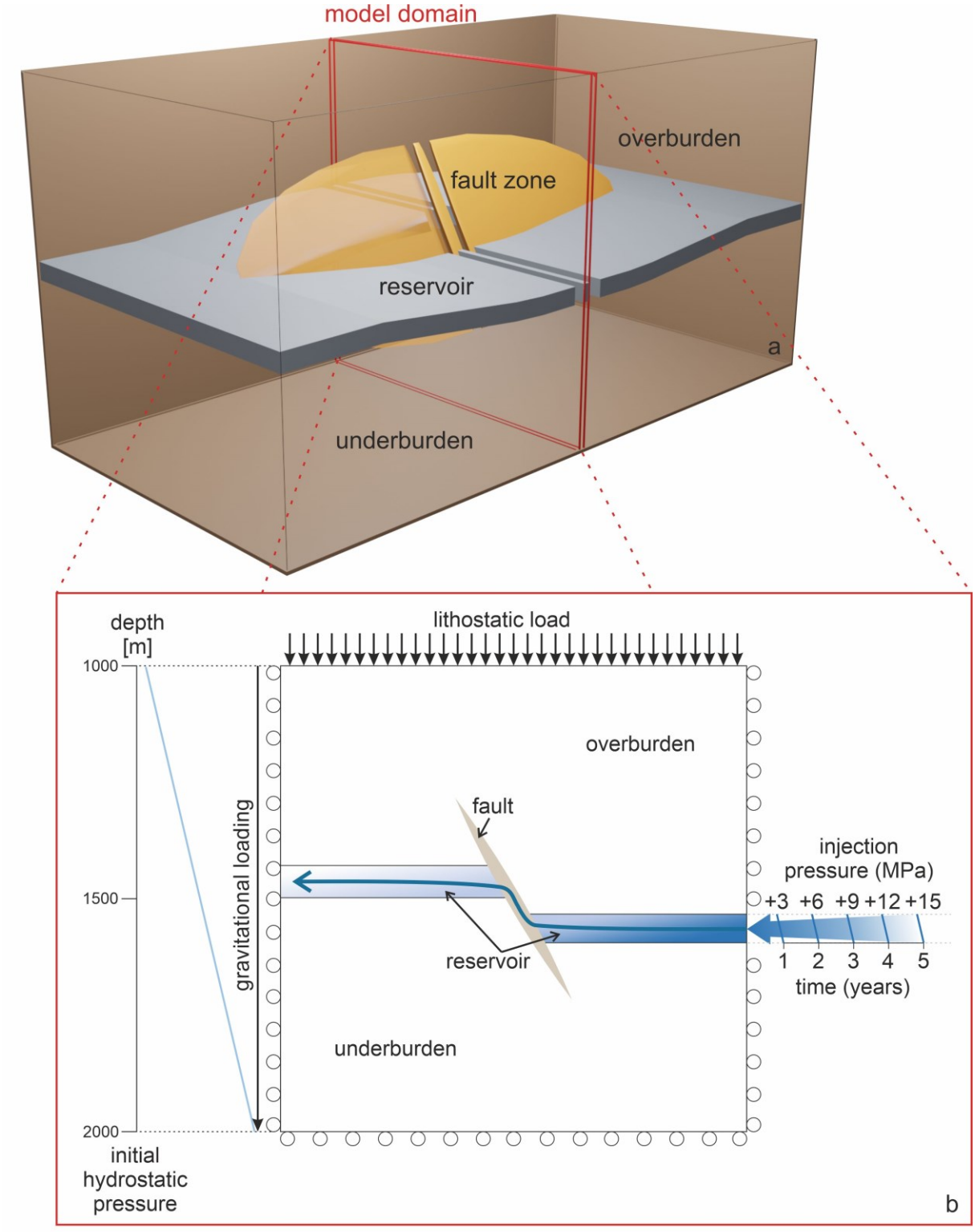

Figure 6-1: (a) A slice through a reservoir horizon displaced by the central part of an elliptical fault zone is the geological rationale for the 3D fault zone model as shown in the cartoon. (b) General model set-up for the hydro-mechanical simulations as well as initial and boundary conditions used.

6.3.1. Model Geometry

The 3D model represents a slice through the central part of a normal fault (Figure 1a). The resulting model domain, the dimensions as well as the initial and boundary conditions are shown in Figure 1b. The model dimensions are 1 km × 1 km × 0.001 km (equivalent to a model slice of one element

thickness) and comprise a fault zone of 500 m height and 60° dip. The fault offsets a 25 m thick reservoir section by 47 m. Using scaling relationships of Johri et al. (2014), the total width of the fault zone including the fault core as well the damage zone is assumed to be 12 m. Treffeisen & Henk (2020b) have shown that in reservoir-scale models discretizing the width of a fault zone into three elements is sufficient to achieve modeling results very similar to a finer discretization. Hence, the size of the elements describing the fault geometry is 4 m × 4 m × 3 m, whereas the whole model domain comprises 45,684 elements.

6.3.2. Constitutive Laws

The hydro-mechanical simulation uses fluid flow through a porous medium and poroelastic-perfectly plastic material behavior. In the following the principle behind such fully coupled hydro-mechanical simulations as well as the assigned boundary conditions are briefly explained. The Modeling utilizes the commercial software program Ansys 19.2 and the reader is referred to the extensive theory and user manuals (Ansys, 2019) for more detailed information.

The mechanical part of the fully coupled simulation is based on the total stresses are reduced by the pore pressure in the rock volume leading to effective stresses. This relationship can be described by (Wang, 2000; Shapiro, 2015; Cheng, 2016):

$$\sigma'_{ij} = \sigma_{ij} - \alpha \cdot p_f \cdot \delta_{ij} \tag{6-2}$$

where the effective stresses (σ'_{ij}) are derived from the total stress tensor (σ_{ij}) by subtracting the pore pressure (p_f), weighted by the Biot coefficient (α) and Kronecker's delta (δ_{ij}).

The hydraulic part of the coupling is defined in Ansys 19.2 with the following mass-balance equation (Ansys, 2019):

$$\nabla q_f + \alpha \cdot \varepsilon_v + \frac{p_f}{Q^*} - S_f = 0 \tag{6-3}$$

where the flux due to Darcy's law q_f (m/s), the volumetric strain ε_v (-), the compressibility parameter Q^* and the degree of fluid saturation S_f (-). Q^* is calculated from the bulk modulus of both the skeleton and the fluid.

These two formulas briefly outline the interaction of the hydraulic and mechanical behavior as changes in pore pressure result in effective stress changes and related volumetric strain. This in turn alters porosity and permeability, which again affect the pore pressure field (Jaeger et al., 2007; Cappa & Rutqvist, 2011).

6.3.3. Initial and Boundary Conditions

Figure 1b shows the mechanical and hydraulic boundary conditions, both for the initial state and the subsequent injection stage. For the mechanical calculations, displacements orthogonal to the model boundaries are not allowed at the base, left, right, front, and back sides of the model (roller boundary conditions). Since the model top is located 1000 m beneath the earth surface, the weight of the overburden is assigned through a pressure boundary condition with an average density of 2300 kg/m3. For the hydraulic calculations, all model boundaries are considered to be impermeable.

During the initial load step, mechanical and hydraulic equilibrium in response to the boundary conditions is achieved. So the whole model domain experiences hydrostatic pore pressure conditions. Concurrently the initial stress field is established through gravitational loading only and no other tectonic (horizontal) stress components are considered in the simulations. Therefore, the tectonic regime is normal faulting with the vertical stress S_v being the maximum principal stress S_1.

Afterwards, fluid injection in the downthrown block is simulated by successively applying higher pore pressures for five years to the boundary nodes of the reservoir layer in the hanging wall of the fault (lower right in Figure 6-1 b). The injection pressure increases for 20 time steps by 0.75 MPa, until the maximum injection pressure of 15 MPa above hydrostatic is reached.

6.3.4. Material Parameters

The hydraulic and mechanical material properties assigned to the fault zone, reservoir and host rock are listed in Table 6-1. Details of the changes in Young's modulus, Poisson's ratio, cohesion, and friction angle assigned to the fault zone in the various sensitivity studies as well as the acronyms dedicated to the corresponding scenarios are shown in Table 6-2. The coding used for each model variant reflects the differences to the base model (BM). For example, BM-c1 implies that the model varies only regarding cohesion of the fault zone rocks and that a value of 1 MPa (instead of 5 MPa as in model BM) is used for the calculations. All other material parameters remain the same.

Table 6-1: Hydraulic and mechanical parameters used for the three model units.

Mechanical	Symbol	Fault Zone	Reservoir	Over-/Underburden
Young's modulus (GPa)	E	0.1–10	30	30
Poissons' ratio (-)	υ	0.1–0.25	0.23	0.23
Friction angle (°)	φ	10–25	40	40
Cohesion (MPa)	c	0.01–5	20	20
Tensile strength (MPa)	T_0	5	20	20
Density (kg/m³)	ρ	2400	2400	2400
Hydraulic				
Biot coefficient (-)	α	0.9	0.5	0.5
Permeability (m²)	k	10^{-14}	5^{-12}	10^{-17}

Table 6-2: Overview of the 87 scenarios studied and the corresponding model names. The scenarios differ regarding the elastic and the frictional properties assigned to the model unit representing the fault zone.

Model Name	Young's Modulus (GPa)	Poisson's Ratio (-)	Cohesion (MPa)	Friction Angle (°)
BM	10	0.25	5	25.0
BM-P0.20	10	0.20	5	25.0
BM-P0.15	10	0.15	5	25.0
BM-P0.10	10	0.10	5	25.0
BM-FA17.5	10	0.25	5	17.5
BM-FA10.0	10	0.25	5	10.0
BM-c1	10	0.25	1	25.0
BM-c1-FA17.5	10	0.25	1	17.5
BM-c1-FA10.0	10	0.25	1	10.0
BM-c0.5	10	0.25	0.5	25.0
BM-c0.5-FA17.5	10	0.25	0.5	17.5
BM-c0.5-FA10.0	10	0.25	0.5	10.0
BM-c0.1	10	0.25	0.1	25.0
BM-c0.1-FA17.5	10	0.25	0.1	17.5
BM-c0.1-FA10.0	10	0.25	0.1	10.0
BM-c0.05	10	0.25	0.05	25.0
BM-c0.05-FA17.5	10	0.25	0.05	17.5
BM-c0.05-FA10.0	10	0.25	0.05	10.0
BM-c0.01	10	0.25	0.01	25.0
BM-c0.01-FA17.5	10	0.25	0.01	17.5
BM-c0.01-FA10.0	10	0.25	0.01	10.0
BM-Y7	7	0.25	5	25.0
BM-Y7-P0.20	7	0.25	5	25.0
BM-Y7-P0.15	7	0.25	5	25.0
BM-Y7-P0.10	7	0.25	5	25.0
BM-Y5	5	0.25	5	25.0

BM-Y5-P0.20	5	0.25	5	25.0
BM-Y5-P0.15	5	0.25	5	25.0
BM-Y5-P0.10	5	0.25	5	25.0
BM-Y3	3	0.25	5	25.0
BM-Y3-P0.20	3	0.25	5	25.0
BM-Y3-P0.15	3	0.25	5	25.0
BM-Y3-P0.10	3	0.25	5	25.0
BM-Y1	1	0.25	5	25.0
BM-Y1-P0.20	1	0.20	5	25.0
BM-Y1-P0.15	1	0.15	5	25.0
BM-Y1-P0.10	1	0.10	5	25.0
BM-Y1-FA17.5	1	0.25	5	17.5
BM-Y1-FA10.0	1	0.25	5	10.0
BM-Y1-c1	1	0.25	1	25.0
BM-Y1-c1-FA17.5	1	0.25	1	17.5
BM-Y1-c1-FA10.0	1	0.25	1	10.0
BM-Y1-c0.5	1	0.25	0.5	25.0
BM-Y1-c0.5-FA17.5	1	0.25	0.5	17.5
BM-Y1-c0.5-FA10.0	1	0.25	0.5	10.0
BM-Y1-c0.1	1	0.25	0.1	25.0
BM-Y1-c0.1-FA17.5	1	0.25	0.1	17.5
BM-Y1-c0.1-FA10.0	1	0.25	0.1	10.0
BM-Y1-c0.05	1	0.25	0.05	25.0
BM-Y1-c0.05-FA17.5	1	0.25	0.05	17.5
BM-Y1-c0.05-FA10.0	1	0.25	0.05	10.0
BM-Y1-c0.01	1	0.25	0.01	25.0
BM-Y1-c0.01-FA17.5	1	0.25	0.01	17.5
BM-Y1-c0.01-FA10.0	1	0.25	0.01	10.0
BM-Y0.7	0.7	0.25	5	25.0
BM-Y0.7-P0.20	0.7	0.25	5	25.0
BM-Y0.7-P0.15	0.7	0.25	5	25.0
BM-Y0.7-P0.10	0.7	0.25	5	25.0
BM-Y0.5	0.5	0.25	5	25.0
BM-Y0.5-P0.20	0.5	0.25	5	25.0
BM-Y0.5-P015	0.5	0.25	5	25.0
BM-Y0.5-P0.10	0.5	0.25	5	25.0
BM-Y0.3	0.3	0.25	5	25.0
BM-Y0.3-P0.20	0.3	0.25	5	25.0
BM-Y0.3-P0.15	0.3	0.25	5	25.0
BM-Y0.3-P0.10	0.3	0.25	5	25.0
BM-Y0.1	0.1	0.25	5	25.0
BM-Y0.1-P0.20	0.1	0.20	5	25.0
BM-Y0.1-P0.15	0.1	0.15	5	25.0
BM-Y0.1-P0.10	0.1	0.10	5	25.0
BM-Y0.1-FA17.5	0.1	0.25	5	17.5
BM-Y0.1-FA10.0	0.1	0.25	5	10.0
BM-Y0.1-c1	0.1	0.25	1	25.0
BM-Y0.1-c1-FA17.5	0.1	0.25	1	17.5
BM-Y0.1-c1-FA10.0	0.1	0.25	1	10.0
BM-Y0.1-c0.5	0.1	0.25	0.5	25.0
BM-Y0.1-c0.5-FA17.5	0.1	0.25	0.5	17.5
BM-Y0.1-c0.5-FA10.0	0.1	0.25	0.5	10.0
BM-Y0.1-c0.1	0.1	0.25	0.1	25.0
BM-Y0.1-c0.1-FA17.5	0.1	0.25	0.1	17.5
BM-Y0.1-c0.1-FA10.0	0.1	0.25	0.1	10.0
BM-Y0.1-c0.05	0.1	0.25	0.05	25.0
BM-Y0.1-c0.05-FA17.5	0.1	0.25	0.05	17.5
BM-Y0.1-c0.05-FA10.0	0.1	0.25	0.05	10.0
BM-Y0.1-c0.01	0.1	0.25	0.01	25.0
BM-Y0.1-c0.01-FA17.5	0.1	0.25	0.01	17.5
BM-Y0.1-c0.01-FA10.0	0.1	0.25	0.01	10.0

The material properties assigned to the fault zone elements cover a range which is typical for fault zones in siliciclastic successions, i.e., Young's modulus was varied between 0.01 GPa and 10 GPa, Poisson's ratio between 0.1 and 0.25, cohesion between 0.01 MPa and 5 MPa and friction angle between 10.0° and 25.0°. For example, the combination of the maximum values from each category, e.g., a Young's modulus of 10 GPa, a Poisson's ratio of 0.25, a cohesion of 5 MPa and a friction angle of 25°, would be typical for a fault zone containing slightly deformed sandstone and re-cemented fault gouge (Goodman, 1989; Faulkner et al., 2010; Gudmundsson, 2011). Combination of the minimum values, i.e., a Young's modulus of 0.01 GPa, a Poisson's ratio of 0.1, a cohesion of 0.01 MPa and a friction angle of 10° would represent a fault rock containing mostly clay and siliciclastic rock flour (Gudmundsson et al., 2013). Between these extremes, various other rock types and, hence, material properties can be imagined, depending on the fraction clay or rock and the fraction of lithified sandstone (Fjær et al., 2008).

The permeability of fault zones in siliciclastic successions is usually controlled by the clay content of the offset rocks. Thus, impermeable faults are more likely in sandstone-shale regimes (Caine et al., 1996; Agosta et al., 2006; Faulkner et al., 2006). However, we decided to choose a semipermeable fault zone since we are particularly interested in how fluid flow effects the mechanical strength of the fault and how this potentially leads to fault reactivation (Faulkner et al., 2010; Fachri et al., 2016). Faults in sandstones with less than 15% clay content show already a slightly reduced permeability in comparison to the host rock (Fisher & Knipe, 2001). For this sensitivity study, we choose a fault zone permeability about two orders of magnitude lower than the reservoir rock to account for some fault damage on hydraulic conductivity. However, modeling techniques are generally applicable and could also be applied to fault zones which act as impermeable barriers or high-permeability conduits for fluid flow.

6.4. Results

The following section presents some of the modeling results. Firstly, the results of the base model (BM) are presented, which provides the baseline for the following comparisons with some of the other 86 scenarios studied (see Table 6-2 for the various models). Afterwards stress and strain patterns for both the whole model area and the fault zone itself are compared between exemplary model setups.

6.4.1. Base Model

The base model (BM) comprises a fault zone with material properties typical for siliciclastic fault zones separating a sandstone reservoir, whereby the fault acts as conduit for fluid flow between different reservoir compartments. The corresponding mechanical material properties for a fault zone in such a setting are inferred from literature (Schön, 2004; Fjær et al., 2008; Gudmundsson, 2011) and set to a Young's modulus of 10 GPa, a Poisson's ratio of 0.25, a cohesion of 10 MPa and an angle of internal friction of 25°. Modeling results are illustrated in Figures 1 and 2 comparing the results for the initial state, i.e., prior to fluid injection (upper row) and after five years of injection with a pore pressure increase in the lower reservoir section of 15 MPa above hydrostatic (bottom row), respectively.

6.4.1.1. Pore Pressure

The initial pore pressure distribution (Figure 6-2 a) shows a hydrostatic gradient resulting from the boundary conditions assigned, i.e., 9.8 MPa at the model top (1000 m depth) and 19.6 MPa at the model base (2000 m). After increasing the injection pressure at a rate of 0.75 MPa every three month over five years to a total of 15 MPa above hydrostatic, the pore pressure inside the reservoir layer has been raised to 30 MPa (Figure 6-2 d). The pressure increase has propagated from the injection point in the down-thrown reservoir section through the fault zone all the way up to the upper fault

compartment on the left side of the model. The increase here is still about 8 MPa above hydrostatic, which results in a pore pressure of about 22 MPa.

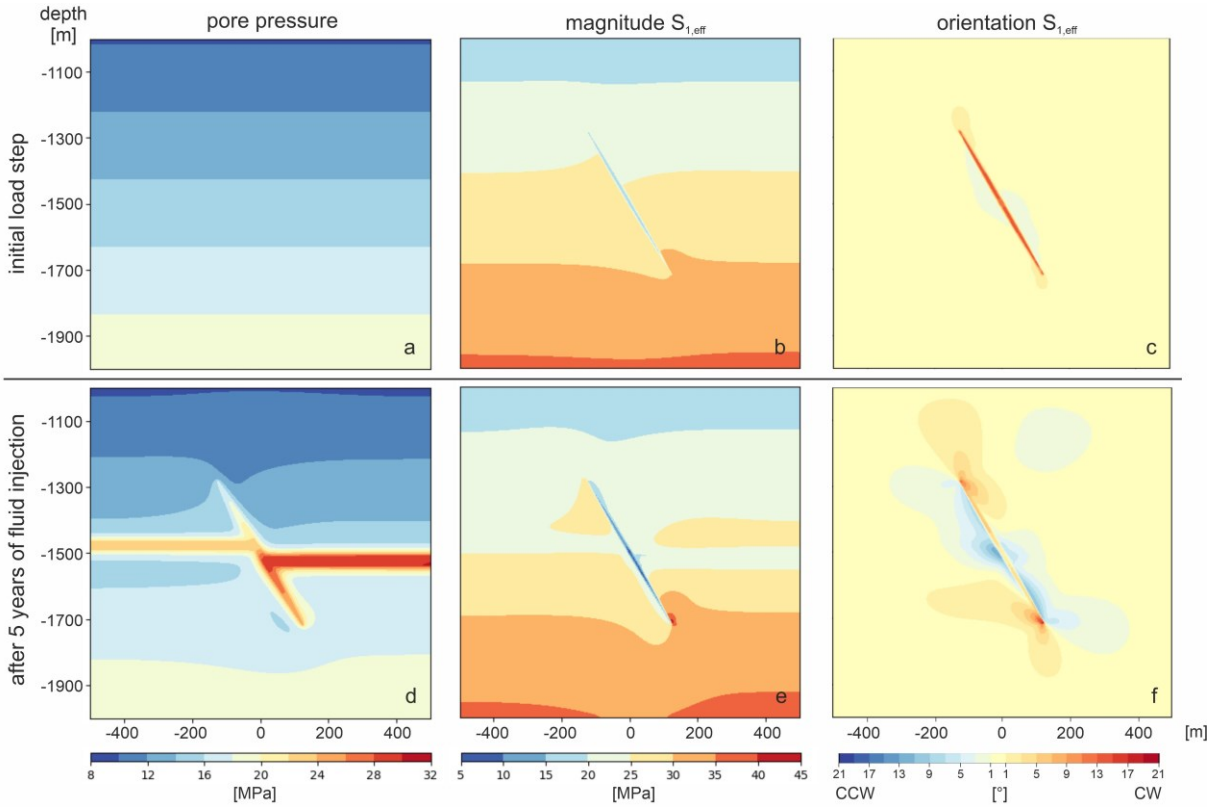

Figure 6-2: Results of the base model (BM) of the spatial variation in pore pressure (a,d), the magnitude of the effective maximum principal stress ($S_{1,eff}$; b,e), and orientation of $S_{1,eff}$ (deviation from vertical; c,f).

6.4.1.2. Magnitude and Orientation of $S_{1,eff}$

The effective maximum principal stress ($S_{1,eff}$) displays 15 MPa at the top and up to 37 MPa at the bottom of the model (Figure 6-2 b). This reflects the combined effects of boundary conditions and gravitational loading and considers poroelastic effects. The fault zone shows the lowest effective stress values due to its higher Biot coefficient in comparison to the surrounding rock mass. Figure 6-2c displays the orientation of $S_{1,eff}$. For ease of visualization, this is presented in form of a contour plot which show the deviations (clockwise (CW) and counterclockwise (CCW)) from the vertical direction, i.e., the undisturbed orientation of $S_{1,eff}$ in a normal faulting regime. As a consequence, outside the model areas affected by the fault hardly any deviation occurs, i.e., $S_{1,eff}$ is vertical. However, inside the fault zone $S_{1,eff}$ has rotated up to 17° CW. In the immediate vicinity of the fault zone and near the fault tips, stress rotations between 5° CCW and 5° CW can be observed.

After five years of fluid injection the pore pressure inside the reservoir (Figure 6-2 d) and the fault zone has increased which directly effects the $S_{1,eff}$ pattern (Figure 6-2 e). The lower, right reservoir section stands out against the surrounding rock mass with $S_{1,eff}$ values about 5–10 MPa lower, while the effective stresses near the fault zone show an increase at the upper left and lower right fault tips as well as a corresponding decrease at the opposing sides. Inside the fault zone, $S_{1,eff}$ has decreased up to less than 10 MPa. Injection does not only modify effective stress magnitudes but also stress orientations (Figure 6-2 f). Significantly larger model areas up to 300 m distance from the fault zone are now showing $S_{1,eff}$ orientations differing from vertical. These stress perturbations follow some kind of a point symmetry with a maximum rotation of 21° CW to the left of the lower and to the right of

the upper fault tip, respectively. On the opposite sides of the fault tips extending to the middle part of the fault zone, the direction of $S_{1,eff}$ deviates between 5° and 15° CW from vertical.

6.4.1.3. Total, Elastic, and Plastic Strain

Figure 6-3 shows the von Mises total strain as well as the corresponding elastic and plastic strain components. For the first load step, total strain ranges from 0 to 0.16% (Figure 6-3 a) and is dominated by elastic straining (compare to Figure 6-3 b,c). After five years of injection, the total strain exhibits values between 0.0 and 1.6% (Figure 6-3 d) and is primarily controlled by plastic straining, which shows significantly higher values than the elastic strain component (compare to Figure 6-3 e,f). Elastic straining only in relation to the initial stress field is shown in Figure 6-3 b. In the vicinity of the fault zone von Mises elastic strain values range from 0.04% at the top to 0.1% at base. Somewhat larger strain values are observed for the weaker fault zone where values range between 0.12% and 0.16%. These lower elastic strains are confined to the fault zone and do not extend into the surrounding rock mass. No von Mises plastic strain is observed for the initial load step (Figure 6-3 c). Thus, it can be excluded that initial loading already causes plastic deformation in and reactivation of the fault zone. For the final load step, i.e., after five years of injection, elastic strain in the fault zone has decreased by about 0.04% compared to the initial load step, ranging now between 0.08% and 0.12% (Figure 6-3 e). The larger elastic strain values extend into the surrounding host rock at the fault tips. While elastic strain has decreased inside the fault zone, plastic strain has increased and occurs throughout the entire fault zone (Figure 6-3 f). Maximum values are about 1.6% at the fault tips, but even within the fault zone plastic straining of at least 0.5% can be observed.

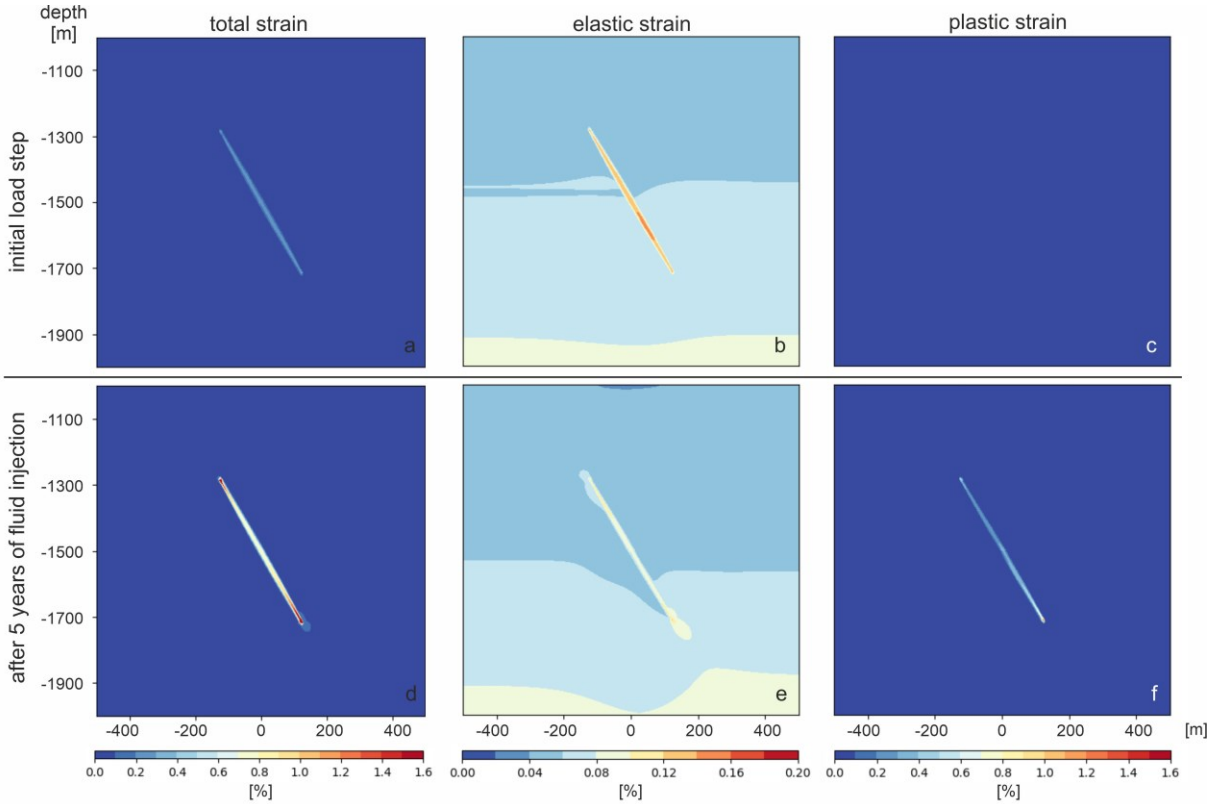

Figure 6-3: Strain simulation results for the base model (BM), i.e., the spatial variation in von Mises total strain (a,d), von Mises elastic strain (b,e), and von Mises plastic strain (c,f).

6.4.2. Influence of Young's Modulus

Comparison of the various sensitivity studies starts with the elastic domain and by varying the Young's modulus assigned to the fault zone elements. Three scenarios differing by an order of magnitude, i.e., 10 GPa, 1 GPa, and 0.1 GPa, are compared. The remaining fault zone properties, i.e., Poisson's ratio, cohesion and friction angle are kept constant at 0.25, 5 MPa, and 25°, respectively.

6.4.2.1. Magnitude and Orientation of $S_{1,eff}$

Figure 6-4 a–c show the magnitude of $S_{1,eff}$ after five years of fluid injection for the three different Young's modulus values of the fault zone. Figure 4a shows the results of the base model (BM). $S_{1,eff}$ magnitudes to the right of the lower and to the left of the upper fault tip are 43.7 MPa and 32.3 MPa, respectively. On the opposite sides, there are local minima of 17.9 MPa and 24.8 MPa. The lowest values for $S_{1,eff}$ of 7.6 MPa can be observed in the central part of the fault zone. A decrease in Young's modulus to 1 GPa (BM-Y1) does not change this overall pattern of $S_{1,eff}$ with minimum and maximum peaks at the fault tips arranged point symmetric to the midpoint of the fault (Figure 6-4 b). However, the maximum values at the lower and upper fault tips are 59.6 MPa and 48.3 MPa, respectively. Thus, the less stiffer fault zone leads to an increase in $S_{1,eff}$ magnitudes by about 16 to 17 MPa in comparison to the base model. The local minima opposite those peaks are 14.2 and 25.6 MPa, respectively. Again, the lowest values of 2.83 MPa can be found in the central part of the fault. A further decrease of the Young's modulus of the fault zone to 0.1 GPa (model BM-Y0.1) intensifies these trends even more (Figure 6-4 c). The maximum values at the fault tips range between 68.6 MPa and 85.7 MPa and the local minimum between 8.7 MPa and 17.4 MPa. The lowest $S_{1,eff}$ magnitudes of 0.3 MPa are again observed in the middle of the fault zone.

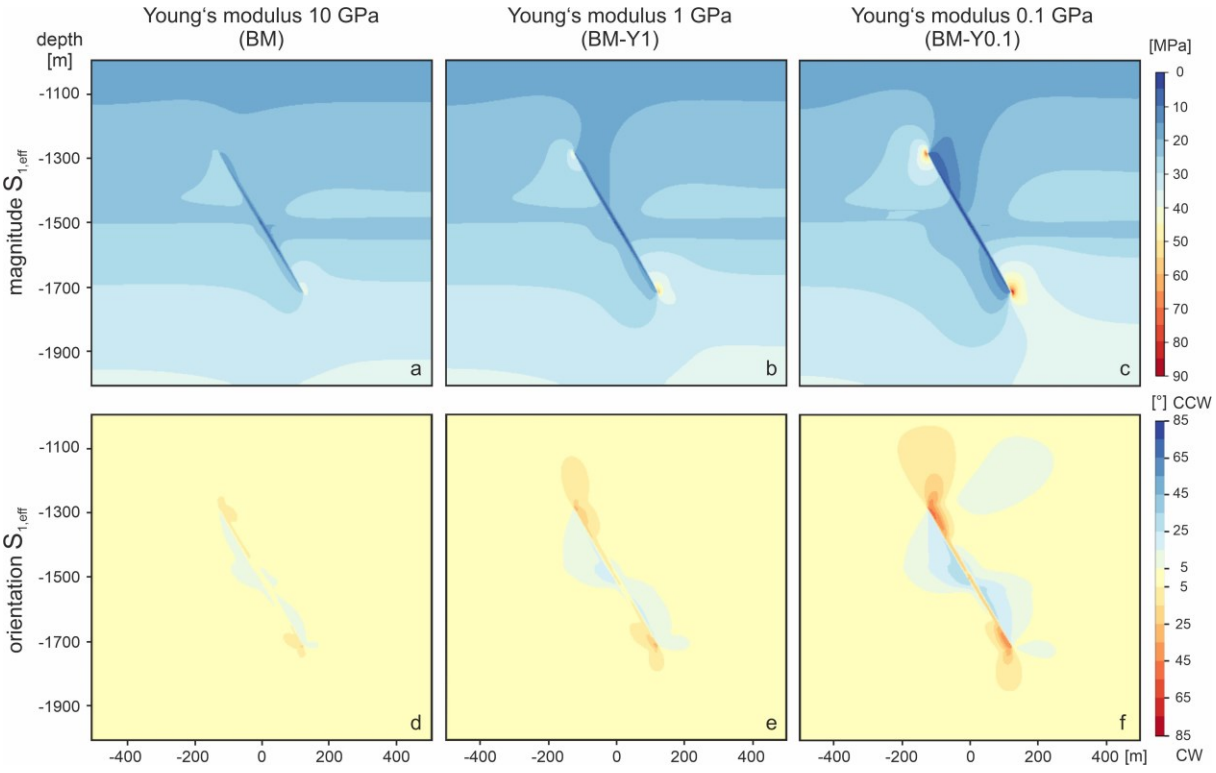

Figure 6-4: Spatial variations in the magnitude (a–c) and orientation (deviation from vertical; d–f) of the effective maximum principal stress (S1,eff) after five years of injection for three different Young's modulus values assigned to the fault zone.

The corresponding orientation of $S_{1,eff}$ for the three scenarios with different fault zone Young's modulus values are presented in Figure 6-4 d–f. After five years of fluid injection, most parts of the

base model (BM) show only minor (5° CCW to 5° CW) deviations from vertical (Figure 6-4 d). Larger values of up to 20° CW occur near the right side at the upper and the left side of the lower fault tip. On the opposing sides and towards the center of the fault zone CCW rotation up to 13.7° is observed. A decrease in Young's modulus to 1 GPa (BM-Y1) increases both the area affected by and the amount of stress rotation (Figure 6-4 e), while the overall pattern remains the same. The maximum rotation of 33.5° CW occurs to the right of the upper and to the left of the lower fault tip, while on the opposing sides a deviation from vertical of up to 21.4° CCW is observed. The further decrease of the Young's modulus to 0.1 GPa (BM-Y0.1, Figure 6-4 f) enhances this pattern leading to stress rotations between 48.4° CW and 32.0° CCW.

6.4.2.2. Elastic, and Plastic Strain

The impact of different fault zone Young's modulus values on elastic and plastic strain patterns after five years of injection is shown in Figure 6-5. Model BM shows a maximum elastic strain of 0.12% in the fault zone elements (Figure 6-5 a; see also Figure 6-3 e which uses a different color scale to visualize details). Decreasing Young's modulus by a factor of 10 (BM-Y1), the maximum values for the elastic strain inside the fault zone is increased to 1.03% (Figure 6-5 b). A further decrease in Young's modulus (BM-Y0.1) leads to larger elastic strain values observed in the fault zone especially at the fault tips, where values can reach up to 7.8% (Figure 6-5 c). Such high elastic strain values can only be achieved because the frictional properties are kept constant in this comparison.

The results for the plastic strain appear to be the other way around (Figure 6-5 d–f). Model BM seems to show plastic straining primarily in the lower part of the fault zone (Figure 6-5 d). However, Figure 6-3 f, which uses a different color contour scheme, shows, that plastic straining actually occurs throughout the entire fault zone with a peak value of 1.5% at the lower fault tip. In model BM-Y1, no through-going plastic strain zone has developed, but the strain peak at the lower fault tip is about twice as much with 3.06% (Figure 6-5 e). For BM-Y0.1 the plastic strain is limited to only a very small area at the lower fault tip, where the maximum value is 1.02% (Figure 6-5 f). The remaining part of the fault zone does not experience any plastic straining.

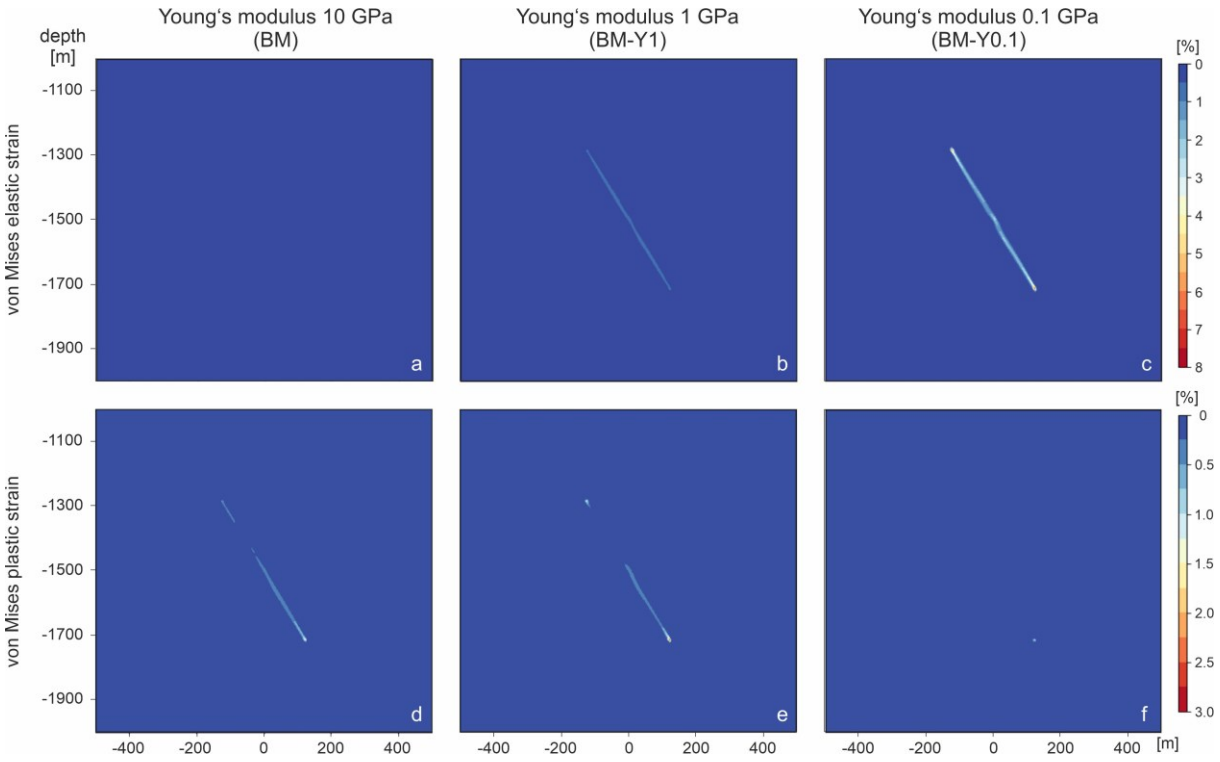

Figure 6-5: Spatial variations in van Mises elastic (a–c) and plastic (d–f) strain after five years of injection for three different Young's modulus values assigned to the fault zone.

6.4.3. Influence of Poisson's Ratio

6.4.3.1. Magnitude and Orientation of $S_{1,eff}$ and $S_{2,eff}$

The effect of different Poisson's ratios of the fault zone rocks on the magnitude of both the vertical ($S_{1,eff}$) and horizontal ($S_{2,eff}$) effective stress is shown in Figure 6-6. The pattern of $S_{1,eff}$ magnitudes after five years of fluid injection is essentially the same for all scenarios i.e., for Poisson's ratios of 0.25 (BM, Figure 6-6 a), 0.15 (BM-P0.15, Figure 6-6 b), and 0.10 (BM-P0.10, Figure 6-6 c). The minimum values inside the fault zone hardly vary for the three models, ranging between 7.4 MPa (BM) and 7.5 MPa (BM-P0.10). Maximum values observed at the lower fault tips vary from 43.7 (BM) to 45.8 (BM-P0.10).

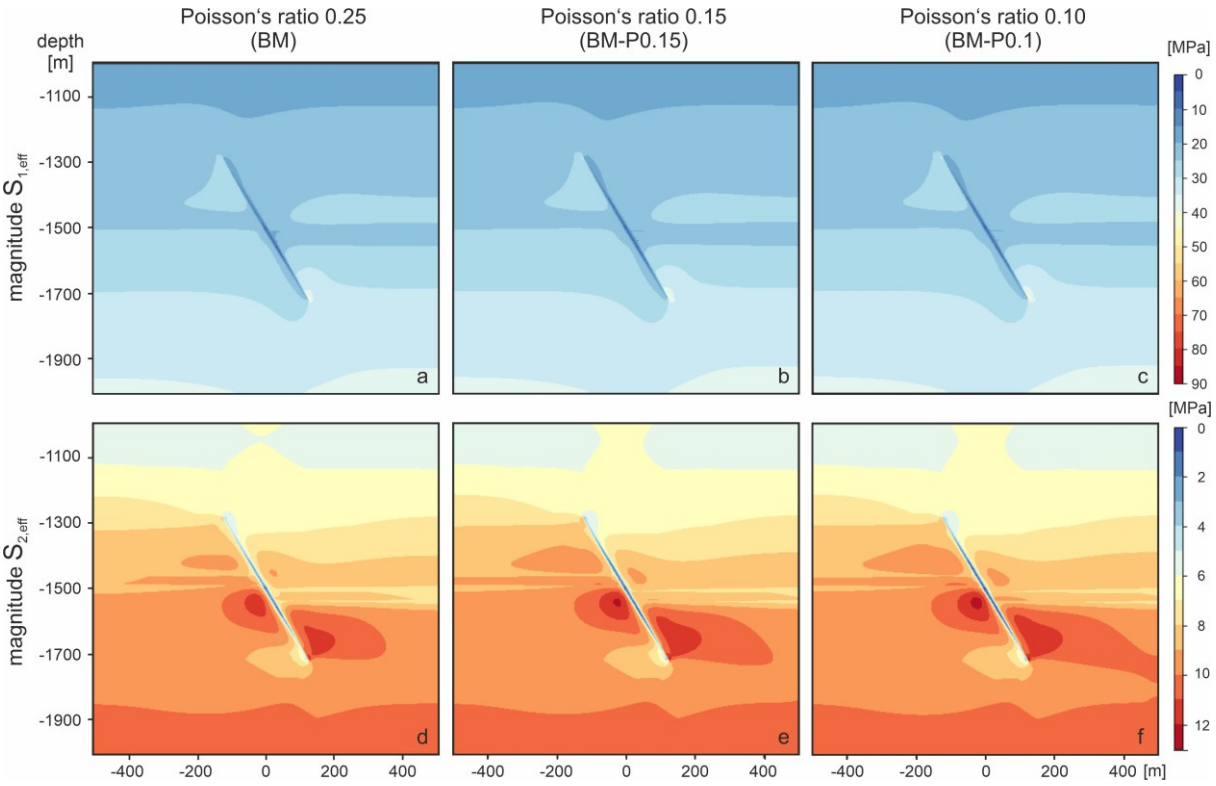

Figure 6-6: Spatial variations in the magnitude of $S_{1,eff}$ (a–c) and the magnitude of $S_{2,eff}$ (d–f) after five years of injection for three different Poisson's ratios assigned to the fault zone.

Comparing the results of $S_{2,eff}$ the overall pattern is again rather similar with peak values in the range of 12 MPa. However, some differences occur inside the fault zone, where minimum $S_{2,eff}$ values are 1.3 MPa (BM, Figure 6-6 d), 0.8 MPa (BM-P0.15, Figure 6-6 e), and 0.5 MPa (BM-P0.10, Figure 6-6 f), respectively.

Regarding the orientation of $S_{1,eff}$ and $S_{2,eff}$, the calculated patterns exhibit no substantial differences depending of the Poisson's ratio assigned to the fault zone unit.

6.4.3.2. Elastic, and Plastic Strain

Figure 6-7 combines elastic and plastic strain results received for the different Poisson's ratio values assigned to the fault zone. The elastic strain pattern and the peak values of 0.13% are essentially the same for all three models (Figure 6-7 a–c). Plastic straining also shows a comparable pattern restricted to the fault zone with maximum values of 1.54%, 1.73%, and 1.76% for models BM, BM-P0.15, and BM-P0.10, respectively (Figure 6-7 d–f).

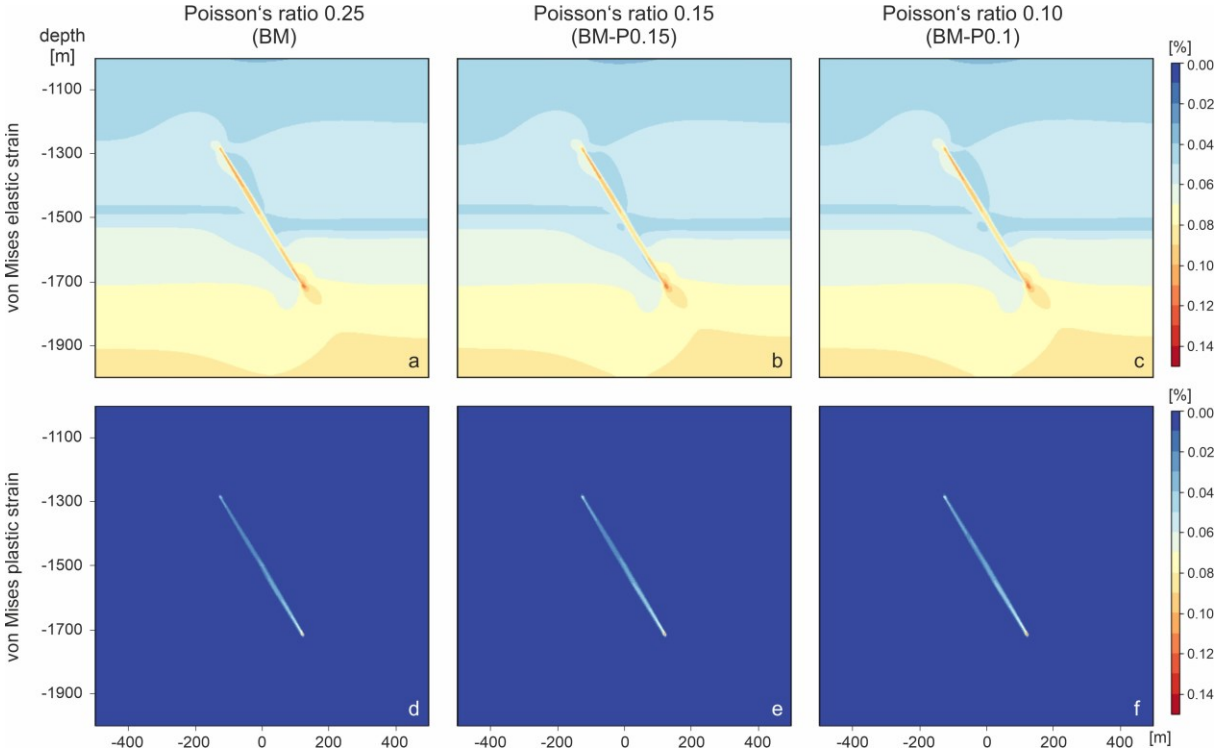

Figure 6-7: Spatial variations in the van Mises elastic (a–c) and plastic strain (d–f) after five years of injection for three different Poisson's ratios assigned to the fault zone.

6.4.4. Influence of Cohesion

6.4.4.1. Magnitude and Orientation of $S_{1,eff}$

Different patterns of $S_{1,eff}$ magnitudes derived after five years of fluid injection are compared in Figure 6-8 a–c for three different cohesion values assigned to the fault zone elements. The values vary from 5 MPa (BM), through 0.5 MPa (BM-c0.5) to 0.01 (BM-c0.01) MPa, while all other fault zone material properties remain the same. Modeling results for BM regarding the magnitude of $S_{1,eff}$ are pictured in Figure 6-8 a, which shows the maximum of 43.7 MPa at the lower fault tip and the minimum of 7.5 MPa inside the fault zone. For a decrease in cohesion to 0.5 MPa (BM-c0.5) the local maximum at the fault tip increases to 59.1 MPa, while the minimum in the middle of the fault decreases to 2.7 MPa (Figure 6-8 b). If the cohesion is decreased even further (BM-c0.01) the corresponding values are 60.5 MPa and 2.7 MPa, respectively (Figure 6-8 c).

Comparing the different results (Figure 6-8 d–f) received for the orientation of $S_{1,eff}$, similar trends can be observed. Model BM exhibits a CW rotation of $S_{1,eff}$ from the vertical orientation of about 20.0° right at the upper left of the lower fault tip extending up to 15 m parallel to the fault into the host rock (Figure 6-8 d). A CCW rotation of 13.7° can be observed on the opposite side of each fault tip, ranging more towards the middle of the fault and extending up to 20 m parallel into the host rock. Changing cohesion to 0.5 MPa (BM-c0.5) enlarges the areas affected by stress rotation as well as the maximum rotation achieved (Figure 8e). $S_{1,eff}$ deviations from vertical in the vicinity of the fault zone range from to 36.5° CW to 22.9° CCW and extent for up to 50 m into the host rock. A further decrease in cohesion to 0.01 MPa (BM-c0.01) only very slight increases the spatial extent of these stress perturbations and the range is now between 37.8° CW and 24.3° CCW (Figure 6-8 f).

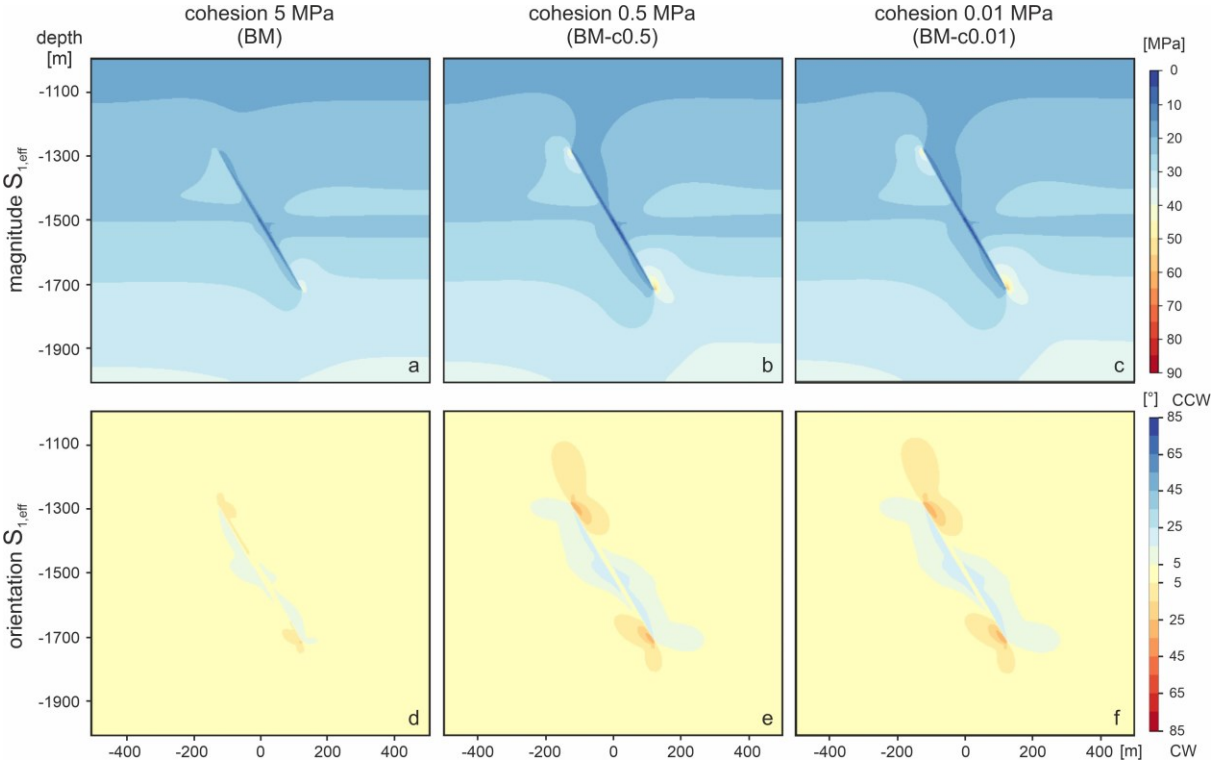

Figure 6-8: Spatial variations in the magnitude (a–c) and orientation (deviation from vertical; d–f) of the effective maximum principal stress ($S_{1,eff}$) after five years of injection for three different cohesion values assigned to the fault zone.

6.4.4.2. Elastic, and Plastic Strain

As has been described above for model BM, elastic strain inside the fault zone ranges between 0.08% and 0.12%, with the maximum being at 0.13% at the lower fault tip (Figure 6-9 a). Decreasing cohesion to 0.5 MPa (BM-c0.5), the elastic strain pattern changes to a certain extent (Figure 6-9 b). Instead of showing the highest values inside the fault zone like in model BM, the values inside the fault zone are the lowest of the whole model domain with a minimum of 0.02%. The maxima remain at the fault tips and increase further to a maximum of 0.16%. A further decrease in cohesion to 0.01 MPa (BM-c0.01) does not change this basic pattern and only slight modifies the values for the minimum within the fault zone and the maximum at the fault tips to 0.01% and 0.17%, respectively (Figure 6-9 c).

The corresponding plastic strain pattern after five years of injection is presented in Figure 6-9 d–f. Due to the color contour scheme required to compare the various simulation results, model BM seems to show plastic strain only in a small area near the base of the fault zone (Figure 6-9 d). However, the detailed analysis shown in Figure 3f reveals that plastic straining actually occurs in the entire fault zone. Plastic strain varies between 0.31% and 0.62% throughout the fault zone and reaches a maximum of 1.54% at the lower fault tip. For a decrease in cohesion to 0.5 MPa (BM-c0.5), the values inside the fault zone increase to 0.81% to 1.61% with a local maximum at the lower fault tip of 4.03% (Figure 6-9 e). A further decrease in cohesion to 0.01 MPa (BM-c0.01) increases the maximum peak to 4.43%, but within the fault zone itself, the values only increase to between 0.89% and 1.77%. However, the basic plastic strain pattern remains the same (Figure 6-9 f).

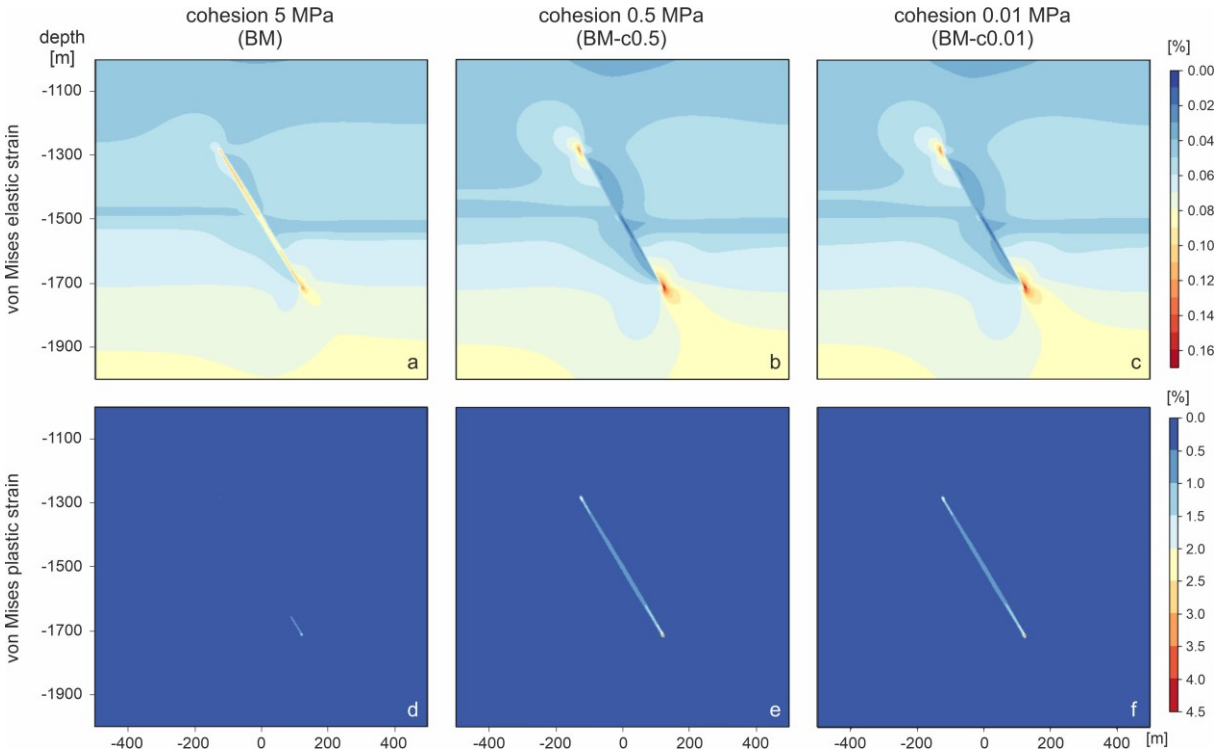

Figure 6-9: Spatial variations in the van Mises elastic (a–c) and plastic strain (d–f) after five years of injection for three different cohesion values assigned to the fault zone.

6.4.5. Influence of Friction Angle

6.4.5.1. Magnitude and Orientation of $S_{1,eff}$

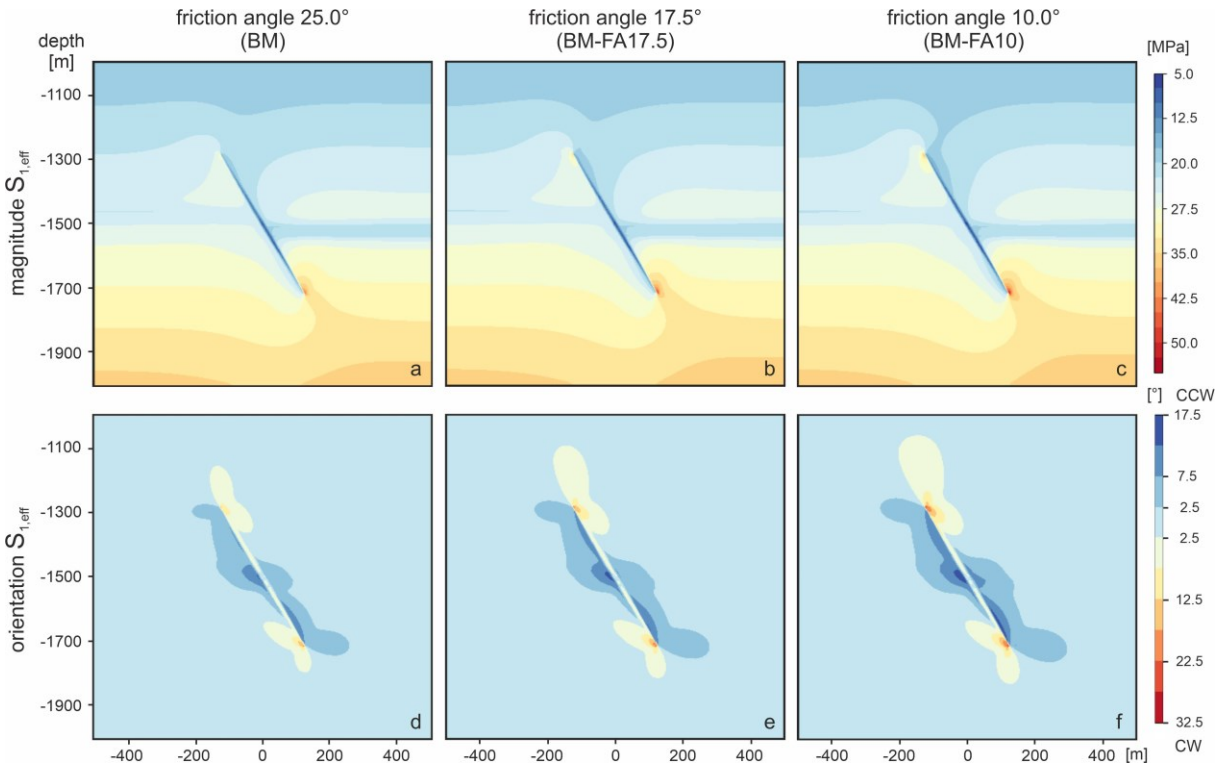

Figure 6-10: Spatial variation in the magnitude (a–c) and the orientation (deviation from vertical; d–f) of the effective maximum principal stress ($S_{1,eff}$) after five years of injection for three different friction angles assigned to the fault zone.

The influence of the angle of internal friction of the fault zone rocks is investigated by comparing the modeling results after five years of injection for scenarios with friction angles of 25.0°, 17.5°, and 10.0°. All other properties are kept constant. The basic pattern regarding the magnitude of $S_{1,eff}$ is similar in all three cases and shows local maxima near the fault tips and minimum values inside the fault zone. For model BM the corresponding values are 43.7 MPa and 7.5 MPa, respectively (Figure 6-10 a). A decrease of the friction angle to 17.5° (BM-FA17.5) increases the difference between these extremes (Figure 6-10 b). The maximum $S_{1,eff}$ magnitude of 48.1 MPa is observed at the lower fault tip, while it is only 7.1 MPa inside the fault zone. A further decrease of the friction angle to 10.0° (BM-FA10) intensifies this difference even more and the corresponding values are 52.3 MPa and 6.6 MPa, respectively (Figure 6-10 c).

Regarding the orientation of $S_{1,eff}$, Figure 6-10 d shows the results of model BM after five years of fluid injection into the reservoir. Orientations deviate from vertical up to 20.0° CW to the right of the upper and to the left of the lower fault tip. The opposing sides of the fault zone show a CCW rotation of 13.7°. Deviations of more than 2.5° from vertical are confined to the immediate vicinity of the fault (up to 70 m). For scenario BM-FA17.5 modeling results show an increase in both the area affected by stress rotations as well as the rotation angles (Figure 6-10 e). The deviations from vertical range between 25.5° CW and 14.4° CCW, extending up to 85 m into the vicinity of the fault. This trend continues if the friction angle of the fault zone is reduced to 10.0° (BM-FA10, Figure 6-10 f). Stress perturbations now extent up to 100 m into the host rock of the fault zone and stress rotations vary between 29.7° CW and 15.6° CCW.

6.4.5.2. Elastic, and Plastic Strain

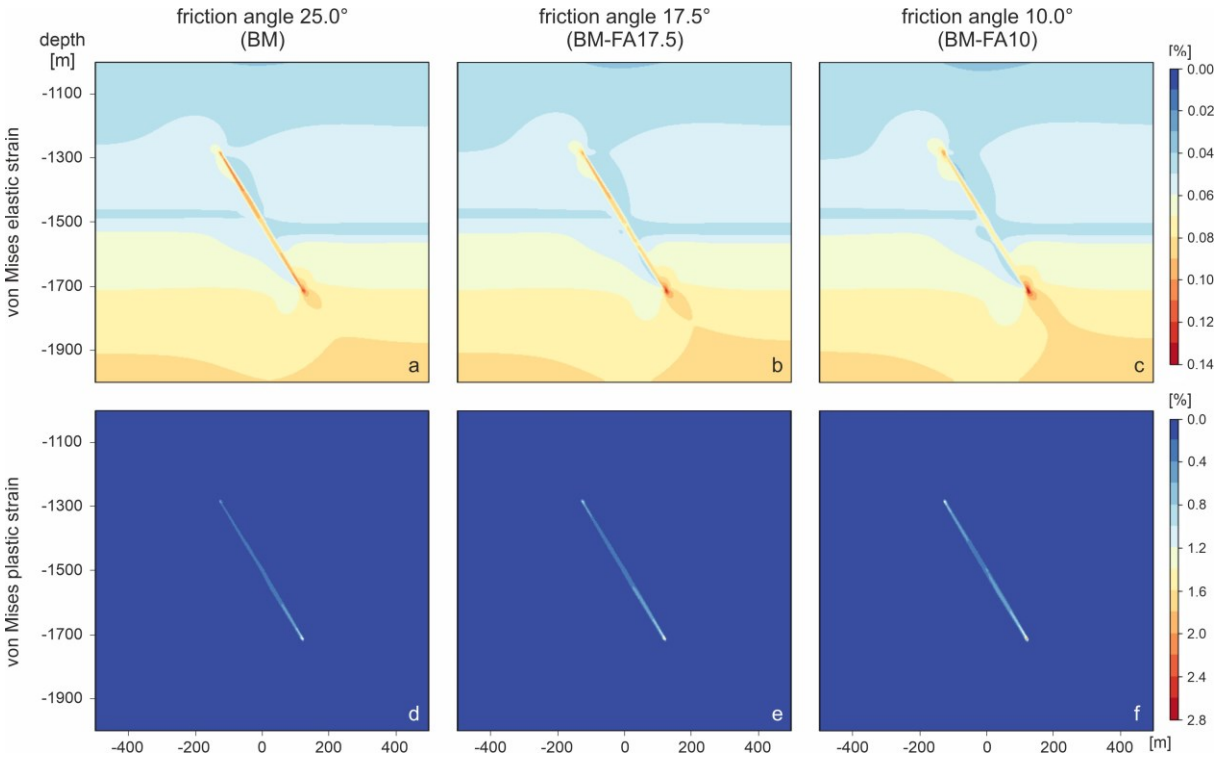

Figure 6-11: Spatial variations in the van Mises elastic (a–c) and plastic (d–f) strain after five years of injection for three different friction angles assigned to the fault zone.

Regarding elastic strain, modeling shows rather similar results for the three different friction angles. There are only minor differences in the strain distribution within the fault zone and the maximum values reached. Model BM model exhibits values up to 0.09%–0.1% in large parts of the fault zone, whereas the peak value of 0.13% is confined to a small area near the lower fault tip (Figure 6-11 a).

For model BM-FA17.5, the elastic strain observed inside the fault zone decreases to 0.08%–0.09% (Figure 6-11 b), but the area affected by higher elastic strains in continuation of the fault both updip and downdip is enlarged. This trend continues for a friction angle to 10.0° (BM-FA10) for which elastic strain within the fault zone is reduced to 0.07%–0.08% (Figure 6-11 c), while the area affected by elastic straining in the vicinity of the fault zone widens.

Considering plastic strain, the trend is reverse. Instead of a decrease in fault zone straining with a decrease in friction angle as was the case for elastic strain, plastic strain within the fault zone increases with decreasing angle of internal friction of the fault rock. Model BM shows plastic strain values of less than 0.4% in most parts of the fault zone (Figure 6-11 d) and a maximum of 1.54% at the lower fault tip. BM-FA17.5 exhibits plastic strain within the fault zone of up to 0.8% (Figure 6-11 e) and to 2.07% at the lower fault tip. Both values increase even further in BM-FA10 to 1.0% plastic strain within the fault zone and 2.61% (Figure 6-11 f).

6.4.6. Interdependence of Parameters

6.4.6.1. Elastic Properties (Young's Modulus vs. Poisson's Ratio)

The impact of different elastic fault zone material properties on the simulation results after five years of fluid injection are examined by analyzing twelve scenarios with different Young's modulus and Poisson's ratios, respectively. Figure 6-12 shows the maximum values calculated for each model regarding the magnitude of $S_{1,eff}$, elastic and plastic strain plotted against the Young's modulus for different Poisson's ratios. All three plots indicate that the different curves, each representing a specific Poisson's ratio, are very close, especially for the magnitude of $S_{1,eff}$ and the elastic strain (Figure 6-12 a, b). Only for plastic strain they differ between 1.0% and 1.75% for a Young's modulus of 0.1 GPa.

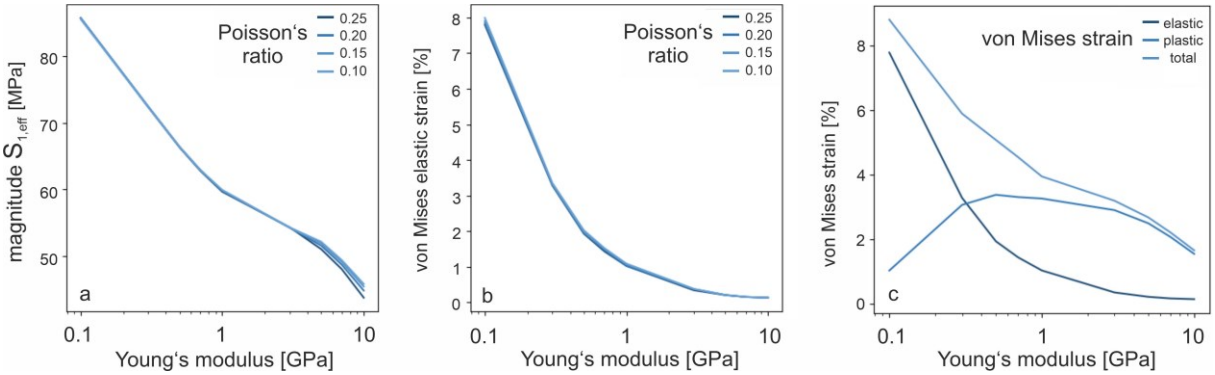

Figure 6-12: Maximum values of the (a) magnitude of the effective maximum principal stress ($S_{1,eff}$), and (b) the von Mises elastic strain for different Young's moduli and Poisson's ratios assigned to the fault zone. (c) Comparison of von Mises elastic, plastic and total strain after five years of injection for different Young's moduli and a Poisson's ratio of 0.25.

A large influence on the modeling results can be observed for Young's modulus. Considering Figure 12a, the magnitude of $S_{1,eff}$ decreases by 20 to 25 MPa if the Young's modulus increases about one order of magnitude. In addition, elastic strain shows decreasing maximum values for increasing Young's moduli (Figure 6-12 b). However, plastic strain results are different as illustrated in Figure 6-12 c. It shows the maximum elastic, plastic, and total strain values for different Young's moduli. At first, plastic strain increases with increasing Young's modulus until a maximum value of about 3.4% is reached for a Young's modulus of 0.5 GPa. From that point on plastic strain decreases with further increasing fault zone Young's modulus until maximum plastic straining is 1.75% for a Young's modulus of 10 GPa (Figure 6-12 c). At the same time, elastic straining reaches its minimum. However, even though the maximum values at the fault tips differ, the general pattern within the fault zone

proper remains the same: increasing Young's modulus lead to larger plastic strain observed in the fault zone.

6.4.6.2. Plastic Properties (Cohesion vs. Internal Friction Angle)

The impact of the plastic properties assigned to the fault is assessed by analyzing 12 scenarios with different parameter combinations of cohesion and angle of internal friction. For this comparison, the maximum values for the magnitude of $S_{1,eff}$ and plastic strain achieved in the model domain are plotted against cohesion for different angles of internal friction (Figure 6-13). Both the magnitude of $S_{1,eff}$ and the plastic strain show only a small reduction with increasing cohesion as long as cohesion is less than 1 MPa. For example, the maximum values of the magnitude of S1,eff achieved for variations in the cohesion of the base model (Figure 6-13 a) are 60.51 MPa (BM-c0.01), 59.14 MPa (BM-c0.5), and 57.84 MPa (BM-c1) until the values for S1,eff drop significantly to 43.72 MPa (BM) for 5 MPa cohesion. The same behavior can be observed for plastic strain (Figure 6-13 b), where the values are 4.43% (BM-c0.01), 4.03% (BM-c0.5) and 3.74% (BM-c1) before decreasing to 1.54% (BM). In both graphs of Figure 13, the distances between the curves derived for various internal friction angles are the same. Thus, for a constant cohesion value, the maximum $S_{1,eff}$ magnitude and the maximum plastic strain decrease linearly with an increase in friction angle.

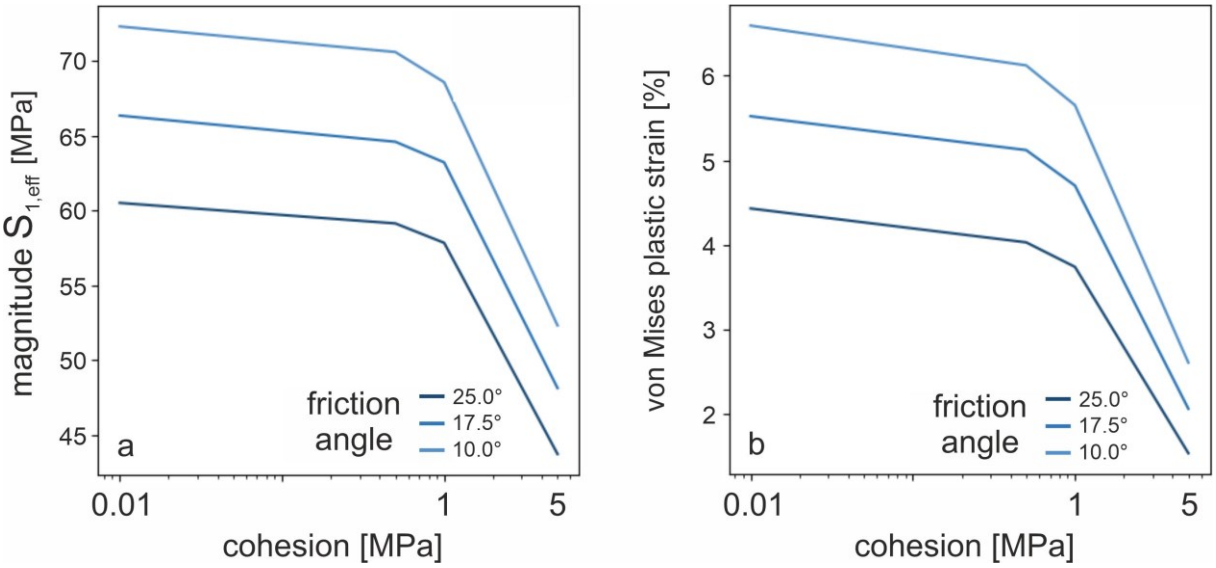

Figure 6-13: Maximum values of the (a) magnitude of the effective maximum principal stress ($S_{1,eff}$) and (b) the von Mises plastic strain after five years of injection for different cohesion values and friction angles assigned to the fault zone.

Although the maximum values partially differ significantly, the general modeling results are rather similar for variations in cohesion and internal friction angle. In Figure 6-14 the stress pattern for the magnitude of $S_{1,eff}$ is shown as an example and similar trends can be observed in orientation plots as well. The base model with its rock properties is displayed in Figure 6-14 a. The rows display the different results achieved for a constant cohesion value by varying the internal friction angle from left (25°) to right (10°) and the columns show the results for one specific friction angle while varying the cohesion from top (5 MPa) to bottom (0.01 MPa). An increase in both the peak magnitude of $S_{1,eff}$ as well as the spatial extent of the stress perturbation can be observed for a decrease in friction angle as well as a decrease in cohesion. Apart from the stress peaks at the fault tips, the effect of varying the internal friction angle on the overall stress pattern is not visible at all and the differences can be only observed at the peak values located at the fault tips.

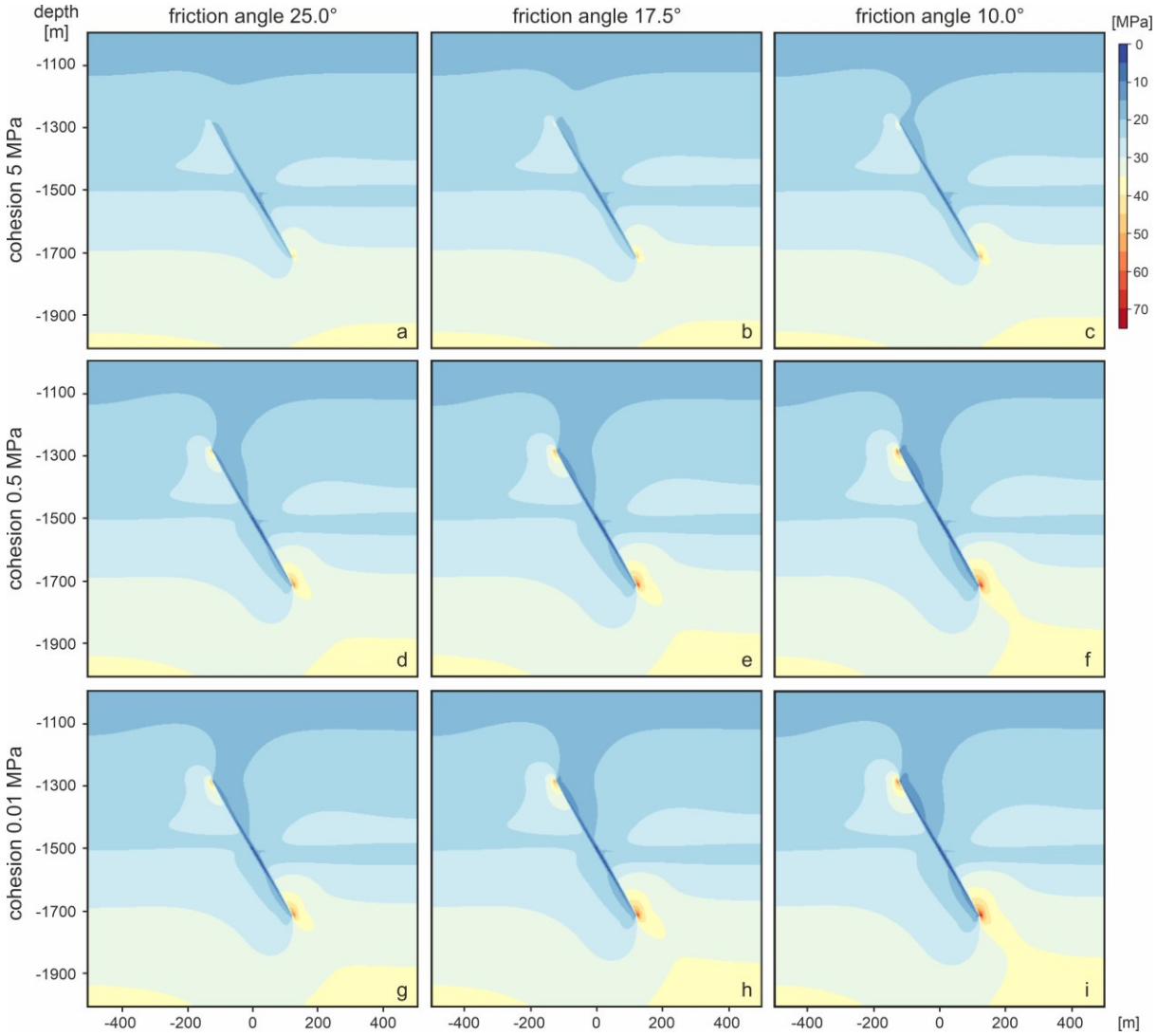

Figure 6-14: Spatial variation in the magnitude of the effective maximum principal stress ($S_{1,eff}$) after five years of injection for three different cohesion values and three different friction angles assigned to the fault zone rocks. The cohesion is varied from top to bottom row (a-d, b-h, c-i) and the friction angle is varied from left to right (a-c, d-f, g-i).

6.5. Discussion

Firstly, the base model (BM) is evaluated to ensure proper model behavior and, building on that, the modeling results for different material properties inside the fault zone are discussed.

6.5.1. Base Model

The BM results for pore pressure (Figure 6-2 a) and $S_{1,eff}$ magnitudes outside the areas affected by the fault zone show the expected increase with depth resulting from the different fluid and rock densities (Figure 6-2 b). The $S_{1,eff}$ orientation in these areas is vertical and thus, in agreement with the normal faulting regime (Anderson, 1951) induced by the prescribed boundary conditions (Figure 6-2 c). The fault zone is not reactivated as a result of initial loading as no plastic straining (Figure 6-3 c) and no differential displacements are observed. After five years of fluid injection into the lower reservoir section, fluid migration through the fault zone has also led to an increase in pore pressure in the upper reservoir part (Figure 6-2 d). More importantly, the pore pressure increase within the fault zone has reduced the effective stresses (Figure 6-2 e), thus, leading to plastic straining (Figure 6-3 f) and reactivation of the fault as well as differential displacements along its entire length. This fault

reactivation has also modified the stress magnitudes (Figure 6-2 e) and orientations (Figure 6-2 f) in the vicinity of the fault zone. Comparable patterns regarding spatial extent and magnitude of the stress changes have also been reported from other numerical simulations of faults (Cuisiat et al., 2010; De Souza et al., 2012; Pereira et al., 2014).

6.5.2. Variations in Elastic Rock Properties

Comparison of the scenarios which differ with respect to Young's modulus shows that a decrease in Young's modulus assigned to the fault zone leads to an increase in the magnitude and re-orientation of $S_{1,eff}$ as well as the spatial extent of the stress perturbations (Figure 6-4). Thus, this relationship follows a negative correlation. For example, the models evaluated in Section 6.4.2.1 show for BM, BM-Y1, and BM-Y0.1 that the magnitude and the rotation angle of $S_{1,eff}$ increases if the Young's modulus of the fault zone is decreased. These trends for Young's modulus can also be observed if combined with other material properties like different Poisson's ratios, cohesions, and internal friction angles. Thus, stiffness contrasts between the fault represented as volumetric weak zone and the host rock lead to magnitude changes as well as stress rotations. Softer rock properties in the fault zone lead to a larger stiffness contrast with respect to the surrounding, which results in broader ranges of between maxima and minima for $S_{1,eff}$ magnitudes and stress reorientations, respectively (Zhang et al., 1994; Bell, 1996). Similarly, the spatial extent of the stress perturbations increases with decreasing stiffness of the fault zone and increasing stiffness contrast, respectively.

The stiffness contrast between the fault zone and the surrounding rock mass also affects the strain values observed in the fault zone. A larger stiffness contrast and therefore a broader ranges of $S_{1,eff}$ magnitudes results in larger values of total strain (Figure 6-12 c). With increasing Young's modulus in the fault zone and, hence, a reduction in stiffness contrast to the country rock, the total strain decreases.

The different Young's moduli imply different slopes of the curves in the stress-strain diagram. Thus, for a given failure stress lower Young's moduli result in larger elastic deformation prior to failure or, in other words, for a given amount of total deformation the share of plastic deformation is less in case of lower Young's modulus. These trends are supported by the modeling results, i.e., peak $S_{1,eff}$ magnitude, elastic strain as well as total strain decrease with increasing Young's modulus of the fault zone rocks. Likewise, the plastic strain should increase with increasing Young's modulus, which is the case for Young's modulus between 0.1 and 0.5 GPa. However, the maximum value is observed for a Young's modulus of 0.5 GPa and the maximum plastic strain decreases between a Young's modulus of 0.5 and 10 GPa (Figure 6-12 c). Thus, the total strain decrease in response to a Young's modulus increase delimits the maximum plastic strain which is achieved in response to respective stress states. The elastic strain component reaches its maximum at a low fault zone stiffness, whereas at high fault zone stiffnesses total strain is dominated by plastic straining.

Contrary to the large influence Young's modulus has on the modeling results, the Poisson's ratio assigned to the fault zone appears to have a negligible impact. This is somewhat surprising as under gravitational loading only Poisson's ratio relates the horizontal stress SH (MPa) to the vertical stress SV (MPa) according to (Jaeger et al., 2007):

$$S_H = S_V \cdot \frac{\nu}{1-\nu} \tag{6-4}$$

Although this relationship holds for the rock units surrounding the fault zone, changing Poisson ratio ν (-) inside the fault zone (while keeping it constant in the rest of the model) has hardly any impact onto the modeling results. The effect of different Poisson's ratios inside the fault zone on the stress and strain pattern is apparently suppressed by the influence the Poisson's ratio of the surrounding rock mass has on the overall stress and strain patterns.

6.5.3. Variations in Plastic Rock Properties

If elastic fault zone properties are kept constant and only frictional-plastic material parameters are varied, modeling results are rather similar as long as cohesion is less than 1 MPa (Figures 6-8 and 6-9). For larger cohesion values, a substantial drop in both the magnitude of $S_{1,eff}$ and plastic strain is observed (Figure 6-13). The increase in pore pressure and the corresponding decrease in effective stresses within the fault zone shifts the Mohr circle in the Mohr–Coulomb diagram towards the failure line and results, in case of lower cohesion values, in larger plastic straining. In turn, larger plastic straining and fault reactivation leads to a stronger loading of the vicinity of the fault and, hence, larger $S_{1,eff}$ magnitudes. For the modeling scenario selected in this study with gravitational loading only, a cohesion of 1 MPa appears to be some kind of a threshold value at larger cohesion values substantially less fault reactivation occurs resulting in reduced stress perturbations concerning both magnitude and spatial extent.

If cohesion is kept constant, the internal friction angle shows a negative correlation for all result parameters. Thus, an increase in the internal friction angle decreases the magnitude and rotation angle of the effective maximum principal stress ($S_{1,eff}$) as well as the values for maximum elastic and plastic strain. This, again, can be explained by the Mohr–Coulomb diagram: the larger the friction angle and, hence, the steeper the slope of the failure line is, the more differential stress the fault zone rock can stand prior to failure. Thus, more stress states are in the plastic domain if the friction angle is lower which in turn results in stronger stress perturbations again.

Differences in the overall pattern for both stress and strain can hardly be detected and the results only seem to differ at the fault tips (Figures 6-10, 6-11, and 6-13). In reality however a fault usually does not end within the reservoir and therefore the area of interest in reservoir modeling, hence the effects of that only occur within a few meters at the fault tips and are not important in reservoir engineering.

6.6. Conclusion

Using a simple generic model setup of a normal fault offsetting a reservoir horizon, the impact of different mechanical fault properties on the stress and strain distribution within a fault zone and its surrounding is analyzed. Thereby, the fault is represented as a volumetric weak zone with uniform properties which inherently implies upscaling of the small-scale heterogeneity of faults observed in nature as well as of the limited size of lab samples available for mechanical testing to the large cell size of the reservoir-scale hydro-mechanical model. This study provides insights on how the elastic and plastic material properties assigned to fault zones of a reservoir-scale model actually affect the results of the numerical simulation. Therefore, it helps to choose proper upscaled fault zone properties by knowing the effect each mechanical parameter has.

Starting with a base model as reference, the mechanical properties assigned to the fault zone are varied within a range typical for faults in sandstone-shale successions, i.e., Young's modulus between 0.1 and 10 GPa, Poisson's ratio between 0.10 and 0.25, cohesion between 0.01 and 5 MPa and angle of internal friction between 10° and 25°. Altogether, 87 different scenarios were studied. Modeling results indicate that these four material properties have substantially different influences on the stress and strain perturbations induced by the fault. The Young's modulus of the fault zone and, more specifically, the contrast in Young's modulus between fault zone and surrounding rocks has by far the strongest impact onto the modeling result. The larger the difference in Young's modulus is, the larger the stress and strain perturbations are, both in absolute numbers as well as regarding the spatial extent. Cohesion turns out to be the second most important material property. In comparison to these two parameters, the impact of the internal friction angle is minor and of the Poisson's ratio assigned to the fault zone essentially negligible.

Consequently, the following guidelines for modeling of faulted reservoirs can be derived from this sensitivity study: If the stress and strain patterns in the vicinity of faults, i.e., within a few hundred meters, are not in the focus of the particular modeling project, the fault zone properties can be determined based on literature data and/or rules of thumb as outlined in Chapter 2. This holds because modeling results indicate that the exact fault properties have no impact on the stress and strain distribution in the far-field of the fault. This, however, changes in the vicinity of a reservoir-scale fault zone, i.e., within a few hundred meters distance to the fault.

If this near-field of a fault is of interest for the modeling study, the reservoir simulation workflow has to start with a first guess of the fault zone parameters based on literature data and experience as usually only very limited or no fault-specific material parameters are available. The initial model run should then be followed by an iterative calibration process by comparing the simulation results to data actually observed. These could be stress orientations (e.g., from borehole breakouts and drilling-induced fractures observed in image logs) and/or stress magnitudes (e.g., from hydraulic tests) observed in wells in the vicinity of the fault. According to the results of the present sensitivity study, during the calibration process the modeler can focus on Young's modulus and cohesion as the most important parameters to achieve a satisfactory fit between model predictions and reality. These two properties are the crucial parameters to assess the reactivation potential of a fault as well as the stress and strain patterns in its vicinity. The angle of internal friction is of less relevance and for Poisson's ratio the standard value of 0.25 can be adopted without concern. This reduction in the number of variables to be tuned during calibration substantially reduces time and computational costs to achieve a validated fault zone description for the hydro-mechanical reservoir model.

This sensitivity studies cannot provide quantitative relationships between the parameters since too many variables besides the four material properties studied influence fault response in hydro-mechanical models. For example, different elastic properties in over and underburden relative to the fault zone would lead to variable stiffness contrast in different sections of the fault zone. This, in turn, would affect the stress and strain patterns in the vicinity of the fault.

However, this sensitivity study provides a guideline which material properties should be of prime interest during upscaling and model calibration. This is also valid, if local mesh refinement in the reservoir-scale model is performed in order to capture the geometrical heterogeneity of the fault zone in greater detail and with smaller elements, respectively. Perspectives for future modeling work include highly detailed fault zone models to provide a sound physical base for upscaling of hydro-mechanical material parameters.

Acknowledgment

We thank Dominik Gottron, Cord-Gerrit Peters and Karsten Reiter for helpful discussions regarding elasto-plastic material properties and modeling results during various parts of this research. Three anonymous reviewers are thanked for their helpful comments and constructive criticism on an earlier version of the manuscript.

7. Synthesis

In this paragraph, the three research articles discussed in this thesis are put into context based on the schematic decision tree (Figure 1-2) modelers have to consider when implementing faults in (hydro-) mechanical finite element simulations. While the research articles are limited to a reservoir-scale only, this synthesis will open the field of view to fault zones in finite element models on all scales. Suggestions on fault representation techniques are made based on the conclusions drawn in the associated research articles. The goal is to gain more realistic simulations and consequently more reliable results regarding fault representation in (hydro-)geomechanical models. Please note that this thesis does not claim to consider all possible fault representations but rather concentrates on the most commonly found.

7.1. Contact Elements vs. Volumetric Weak Zone

The first decision level is on the numerical approach – contact elements or volumetric weak zone – used to implement a fault zone in the numerical model. Both contact elements and volumetric weak zones have led to reasonable values in several studies (Hergert et al., 2011; Fischer & Henk, 2013; Pereira et al., 2014; Rueda et al., 2014; Franceschini et al., 2016; Schlegel, 2016) regarding the aim of each study. Those studies use upscaled and/or merged material properties and are iteratively calibrated through borehole measurements. Thereby the simulation results are compared with stress orientations (e.g. from borehole breakouts and drilling-induced fractures observed in image logs) and/or stress magnitudes (e.g., from hydraulic tests) observed in wells in the vicinity of the fault.

However, Chapter 4 clearly shows different results within a few tens to hundreds of meters distance from the fault for various parameters between both numerical approaches while using the same material input properties. Identifying the more realistic approach in this case is very difficult. Both show similar realistic stress and strain patterns, but clearly differ in the magnitude of each result parameter. In order to figure out which values are closer to reality, comparison and calibration data sets would be needed. Although fault related reservoir data sets exist (e.g. Okada & Matsuda, 1976; Lindsay et al., 1993; Beach et al., 1999; Tamura & Kanaori, 2017), their utility to identify the more realistic approach – contact elements or volumetric weak zone – is limited since they do not provide all necessary values or do not cover a reservoir related environment. To enable such comparison in future studies, drilling arrays of wells through – to determine material properties – and in the vicinity of a fault zone – to determine calibration data e.g. stress magnitudes or orientation – would be necessary as described in chapter 8.1. In conclusion, this thesis cannot settle which numerical approach – contact elements or volumetric weak zone – yields more realistic results in the vicinity of faults concerning the input material properties.

For plate boundary faults and large scale models such as Hergert et al. (2011), where the objective is more on the regional-scale than in the vicinity of the fault, contact elements may be the better choice due to the huge scale difference between the fault zone and the elements of the FE model. Representing the fault zone in models as a 3D volumetric weak zone may overestimate the effect on the simulation results if too large elements are used to represent the fault zone. Concurrently, usage of elements which reflect the actual fault zone width observed in nature could lead to significantly more elements of the model and therefore extreme increase in computing times, even if local grid refinements are possible.

Furthermore, it has to be mentioned that Haug (2019) suggests that some numerical software packages have difficulties representing the fault with contact elements in hydro-mechanical simulations. The models seem to inaccurately calculate the pore pressure along the contact elements and thus the associated effective stress values. This may only concern specific software, but should still be kept in mind when addressing faults in hydro-mechanical models.

On a reservoir-scale a volumetric representation as a weak zone seems to be more appropriate. This enables incorporation of more details, starting with simply subdividing the fault zone into fault core and damage zone. Further subdivisions based on the different material domains found in fault zones are possible (see chapter 8.2). The volumetric representation thereby offers inclusion of – hydraulically - fluid pathways as well as barrier inside the fault zone or – mechanically - weaker and stronger fault rocks, such as shear bands or host rock lenses. Particularly for studies where the vicinity of the fault zone is of interest, incorporation of these fault internal features may be of importance.

Regarding the numerical approach – contact elements vs. volumetric weak zone – results of this thesis indicate that the smaller the scale difference between the model domain and fault, i.e. the difference between the general element size of a model and the element size needed for a volumetric fault zone representation, the more worthwhile is the representation as a volumetric weak zone to incorporate internal details of the fault zone.

In contrast, the larger the scale difference between the model domain and fault, the less is the impact of small-scale structures inside the fault zone, so the simplification of the fault zone to a 2D-surface in 3D models, i.e. using contact elements with zero thickness may also produce accurate modeling results regarding the model scale and the aim of the study.

7.2. Volumetric Weak Zones – Grid Geometry and Mesh Resolution

Choosing a volumetric weak zone, the second decision level is about the grid geometry, explicitly whether the mesh surrounding the fault zone needs to be adjusted to the fault geometry or the fault zone is incorporated into a previously existing – often rectangular – grid by intersecting the grid with the structural model and assigning fault rock properties to the cells cut by fault planes, without any concern about the fault geometry.

If, for instance, the rectangular approach is chosen, the following applies: Since a rectangular grid is already available from preceding property modeling and flow simulations, respectively, it is important to use more than 1-elemt row to represent the fault zone, since a 1-element wide fault zone can lead to serious errors. This combination of grid geometry and mesh resolution almost always leads to interlocking of the fault cells with the surrounding, stronger and less permeable host rock and thereby affects both fluid flow through and straining of the fault zone, which has been clearly shown in this thesis (Chapter 4 and Chapter 5).

For higher mesh resolution occurring interlocking effects for the rectangular grid only lead to very small differences between both grid geometries, which are also only limited to the fault zone itself and its close vicinity up to a few meters away from the fault. The extent of this differences into the surrounding rock may also depend on the fault length and width, so a quantitative number cannot be given.

Since both grid geometries show similar stress and strain patterns at a distance of more than 10 m away from the fault zone, both are interchangeable. Larger, regional-scale reservoir models incorporating many faults normally focus on the overall reservoir behavior instead of the nearfield behavior of a specific fault zone and therefore the rectangular grid may provide appropriate modeling results. This can save much time when generating the model, but also leaves the possibility of modeling the internal fault zone material heterogeneity. Modeling this heterogeneity in turn can have a huge impact on the fluid flow on a reservoir-scale as shown by several recent studies (Syversveen et al., 2006; Fredman et al., 2007; Fredman et al., 2008; Qu et al., 2015; Qu & Tveranger, 2016). The effect modeling the internal mechanical heterogeneity has on the modeling results has to be evaluated with more detailed fault zone models (see chapter 8.2). Adapting the grid to the fault zone and using a curvilinear fault zone representation may only be reasonable if the aim of the study is inside or in the vicinity of the fault zone.

Based on these considerations the modeler may choose a rectangular fault representation when modeling a full-scale reservoir and only using the curvilinear representation, where a fault zone is of special interest or in a smaller-scale model containing a very limited number of fault zones with the goal to investigate the vicinity or the fault zone itself.

7.3. Material Properties and Material Models

After choosing the fault geometry – rectangular or curvilinear – and determining a sufficient mesh resolution, the volumetric weak zone can be incorporated into the model. However, the modeling workflow is not over yet. Upscaling and calibrating of the fault zone properties as well as validation of the hydro-mechanical model are the final decision level needed during the fault zone modeling. General predictions are given in chapter 6-6 about the effect of the elastic and frictional material properties used to simulate poroelasto-plastic material behavior. However, the chosen material properties – Young's modulus, Poisson's ratio, cohesion and internal friction angle – as well as the recommendations derived from this study are limited to the material models used. For the poroelasic domain Hooke's law and the associated stress-strain relationship (see equation 5-5; Wang, 2000; Shapiro, 2015; Cheng, 2016) is used and the Mohr-Coulomb law (see eq. 5-6, Jaeger et al., 2007) is used as failure criterion delimiting the poroelastic range. Still, these material models are only mathematical characterizations and equations of the real behavior of natural rocks, which are only valid for specific conditions.

This has to be kept in mind and considered carefully when choosing the material model in the numerical simulators. For Ansys geomechanical material behavior, besides Mohr-Coulomb, it is possible to use the material models Cam-clay, Drucker-Prager concrete and Jointed Rock. While Drucker-Prager concrete is a modified Drucker-Prager model specifically optimized for the mechanical behavior of brittle construction material like concrete, cement and mortar, and therefore should not be used for modeling natural rock masses, the two others, Cam-clay and Jointed Rock may be sufficient for some fault zone materials.

The Cam-Clay material model is formulated to describe the material behavior of soft soils such as clay. The material model is based on the Critical State theory and the basic assumption that there is a logarithmic relationship between the mean stress and the void ratio (Borja & Lee, 1990; Borja, 1991; Peric, 2006). Due to the huge amount of deformation inside fault zones and associated formation of shear deformation bands, containing large amounts of clay, the Cam-clay material model may also be sufficient for some fault materials.

The Jointed Rock material model is used to model e.g. sedimentary rocks not only by the intact rock properties but also by taking geometric networks of joints or other discontinuities in account (Goodman et al., 1968; Hoek & Brown, 1980; Azami et al., 2012) . The model differs between the rock mass matrix or intact rock, which uses the classic Mohr-Coulomb criterion, and the joint network, which uses an anisotropic Mohr-Coulomb failure model (Ansys, 2019). This enables the input of different frictional properties – cohesion and internal friction angle – for the joint sets but also allows to take the orientation of the joint sets into account. Since damage zones rocks in fault zones and the surrounding rock mass often only differ due to the high amount of fractures and joints in the damage zone, which are also oriented with the fault dip, the Jointed Rock material model may allow to account for this mechanical anisotropy better than the classic Mohr-Coulomb criterion used in this thesis.

Lastly it has to be mentioned that hydro-mechanical models do not account for any temperature effects on the mechanical behavior of the rocks although temperature may act a part in reservoir depths, especially when the geothermal gradient is abnormal, e.g. in geothermal energy applications. To include the effects temperature has on the mechanical behavior of fault zones in reservoir models, a thermo-hydro-mechanical simulation with thermo-mechanical modified Mohr-Coulomb failure criterion (Tian et al., 2013) may model the subsurface behavior more proper.

It has to be stated that the results of this thesis may only apply when using the Mohr-Coulomb failure criterion as material model. However, other material models such as the Cam-Clay or Jointed Rock model may provide more realistic behavior for special fault zone material domains (e.g. clay-rich shear bands or highly fractured damage zones). This should be considered carefully, especially when modeling the internal material heterogeneity of a fault zone such as suggested in the following outlook (Chapter 8.2). Representing the fault zone as one unique upscaled material, as done in this thesis, simply using the Mohr-Coulomb material model could however be sufficient.

8. Outlook

Based on the models used in this thesis, further sensitivity studies can be carried out to investigate more parameters influencing the effect different fault representations have on the results of the hydro-mechanical simulations. After the influence of the elastic and frictional fault zone material properties on the modeling results of hydro-mechanical simulations have been analyzed (chapter 6), the effect of varying hydraulic fault zone material properties on the coupled simulation would be an obvious research objective. Changing the permeability, porosity and Biot's coefficient of the fault zone rocks alters the effective stress magnitude occurring in the fault and therefore should also affect other result parameters like the stress orientation or the elastic and plastic strain observed in the modeling results. A sensitivity study like this could yield guidelines for the upscaling of hydraulic material properties similar to the guidelines provided for mechanical fault zone properties in chapter 6-6.

Another research that may provide valuable insights regarding the different fault representations would be investigating the effect different numerical approaches – contact elements vs. volumetric weak zone – or different grid geometries – rectangular vs. curvilinear grids – as well as the mesh resolution have while intersecting two fault zones. In this case, the generic model should be expanded to a real 3D-model instead of a 3D-slice as used in this thesis in order to model the vertical intersection correctly.

While this possible future research is more or less closely related to this thesis, indications are also given for three grander research topics which will be described in the following sections.

8.1. Complex Analysis of Natural Fault

Validation of the different approaches used in this thesis remains difficult. As previously mentioned, it cannot be determined whether contact elements or volumetric weak zones provide more realistic results based on the material properties assigned. It is always necessary to run the model through a calibration process and adjust the fault zone material properties to validate the model.

Many studies (e.g. Okada & Matsuda, 1976; Lindsay et al., 1993; Beach et al., 1999; Tamura & Kanaori, 2017) on outcrops exist describing a fault zone in detail, including the fault internal material heterogeneities as well as the complex fault geometry. This data can be used to build a very detailed fault zone model, but to validate the hydro-mechanical model experiments are needed which are seldom done on the surface (Morrow & Lockner, 1994). Mechanical validation data could be the stress orientations determined from borehole breakouts and drilling-induced fractures observed in image logs and stress magnitudes e.g. from hydraulic tests.

Validating the fluid flow properties is even more complicated. Core samples are insufficient since they mainly capture microstructural damage; they cannot capture the overall permeability of brittle fault material (Morrow et al., 2014). In-situ characterization of bulk hydraulic properties inside fault zones and their nearby surroundings have been carried out using surface-drilled boreholes (e.g. Le Borgne et al., 2004; Roques et al., 2014), from underground rock laboratories (Klepikova et al., 2020; Jeanne et al., 2018; Abelin et al., 1991a; Abelin et al., 1991b) or single and cross-hole hydraulic packer tests (Brixel et al., 2020). Although such underground laboratories provide almost all required input

data to populate a detailed hydro-mechanical fault zone model, they are insufficient for the validation of reservoir-related fault zones as these laboratories are mainly used to explore nuclear storage sites in crystalline (Brixel et al., 2020) or metamorphic rock (Jeanne et al., 2018).

However, such an underground rock laboratory in a sedimentary context may be necessary to really investigate all required input parameters, i.e. fault zone material heterogeneities and complex internal fault geometry as well as several validation data for both hydraulic and mechanical behavior of the fault zone and its nearby surroundings to build and validate a detailed hydro-mechanical fault zone model.

8.2. Detailed Fault Zone Model

Fault zones in nature have a considerably more complex structure than normally included in reservoir-scale models. Originally present sedimentary facies are deformed and different deformation products lead to the fault zone being based on a degree of deformation at the specific location (Fredman et al., 2008; Braathen et al., 2009; Fachri et al., 2013; Qu et al., 2015; Fachri et al., 2016). However, fault zones are commonly represented with one set of unique, upscaled material properties in reservoir-scale numerical models. In fact, some techniques like transmissibility multipliers (Manzocchi et al., 1999) in hydraulic and contact elements (Hergert et al., 2011; Fischer & Henk, 2013) in mechanical simulations only allow to model the fault zone as one 2D surface with upscaled material, merging the heterogeneous material parameters together and ignoring the three-dimensional nature of fault zone architectures (Qu & Tveranger, 2016). While this reduces computation costs, models with uniform fault material properties cannot calculate fluid flow due to high permeability pathways as well as mechanical interactions triggered by, for instance, stiffness contrasts inside the fault zone (Cappa & Rutqvist, 2011; Fachri et al., 2016; Qu & Tveranger, 2016). The representation of fault zones as volumetric weak zones as zones and thereby as a 3D feature, allows to explicitly model the complex fault structure as well as the internal fault heterogeneity (Fredman et al., 2008; Braathen et al., 2009; Qu et al., 2015). Several reservoir simulation studies focusing on the fluid flow in reservoirs suggest that the internal fluid flow of a fault zone may affect the reservoir behavior during hydrocarbon operations significantly and thereby substantially influences forecasts of field behavior (Al-Busafi et al., 2005; Berg & Skar, 2005; Fachri et al., 2011; Fredman et al., 2007). These studies also suggest that the representation of fault zones as volumetric weak zones and the incorporation of spatial variations of material properties of fault zones yield more accurate hydraulic behavior (Fachri et al., 2013; Fachri et al., 2013b; Qu et al., 2015). However, this leaves the disadvantage that implementing these features requires more elements and a finer mesh resolution inside the fault zone, which in turn means more computing costs for the following simulations (Syversveen et al., 2006). It can be assumed that a similar improvement for the mechanical behavior and for coupled hydro-mechanical reservoir simulation may be achieved through the modeling of spatial variations in the elastic and frictional material parameters (Cappa & Rutqvist, 2011). This may be of interest especially if the aim of the modeling work is in the vicinity of the fault zone. However, because of the lack of information on both material heterogeneities and structural complexity inside fault zones in nature, especially in typical reservoir depths of couple of thousand meters beneath the earth surface alone, modeling completely true to nature may not be possible.

Still, more complex fault zone models can already be developed from more detailed schematic models. A possible workflow is shown in Figure 8-1. The detailed schematic model (Figure 8-1 A) includes lenses, which are e.g. fragments of the undeformed host rock inside the highly deformed fault core, i.e. shear bands. While the shear bands are usually barriers to fluid flow and mechanically weak, the lenses maintain similar hydraulic and mechanical properties as the host rock and therefore can be presumed to be stronger and more permeable (Caine et al., 1996; Faulkner et al., 2010). The fracture density inside related damage zones decreases with increasing distance to the fault core (Johri et al., 2014), which in turn means the permeability as well as the mechanical strength increases in the same

direction. These features can be transferred to numerical models by generating a fault zone featuring a fault core with two material domains – lenses enclosed by shear bands – and surrounded by multiple damage zones with material parameters representing the related fracture density depending on the distance to the fault core (Figure 8-1 B). The exemplary result of such detailed fault zone representation is shown in figure 8-1 C to E for the plastic strain. In this example, the overall fault zone seems to fully experience plastic strain (Figure 8-1 C), but on a smaller scale varying patterns reflecting the material heterogeneity inside the fault zone can be observed (Figure 8-1 D & E).

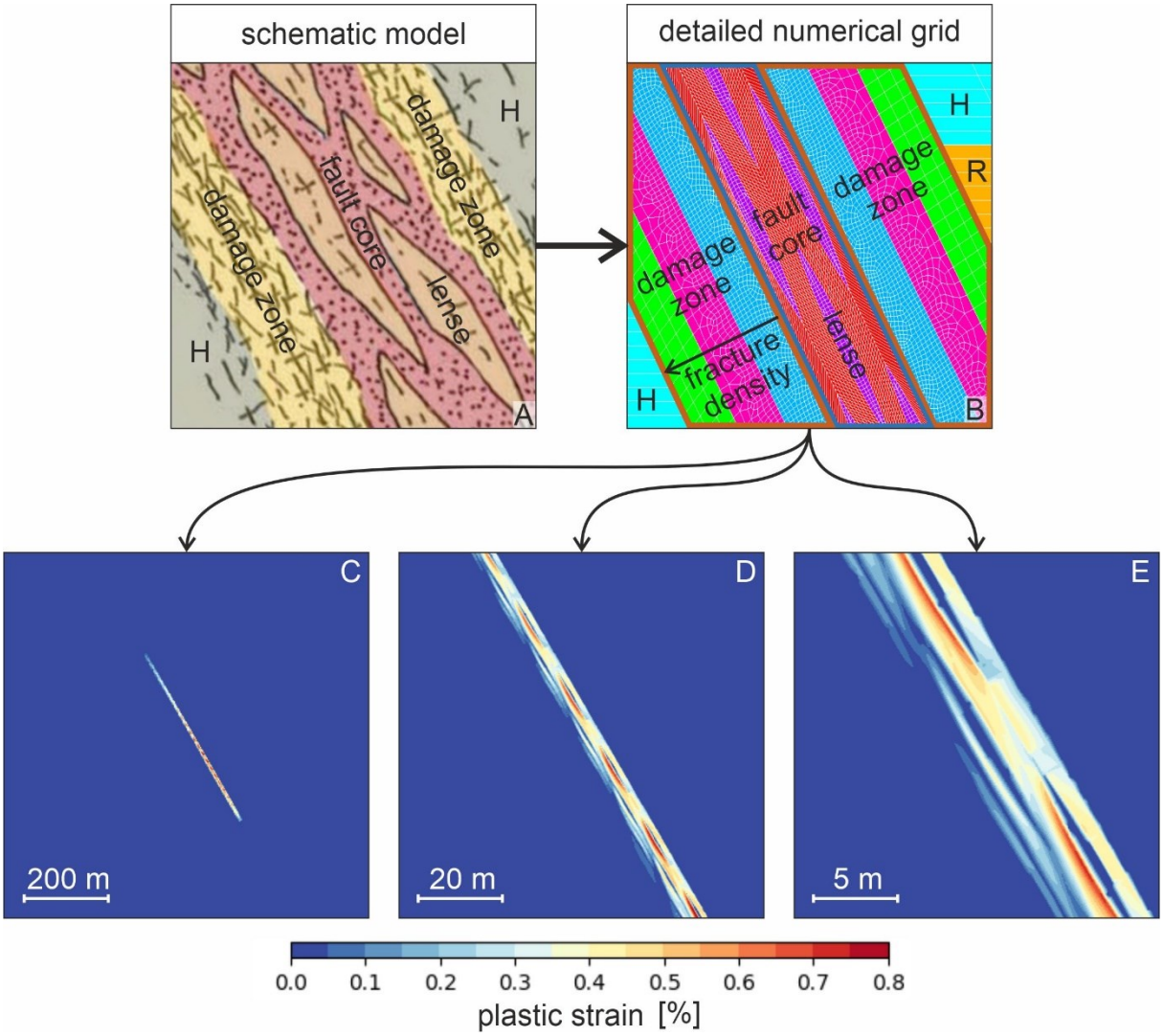

Figure 8-1: Possible workflow from (A) detailed schematic fault model (Fasching & Vanek, 2011) to a more (B) detailed numerical fault representation including fault core with lenses, damage zone with multiple areas of different fracture density, host rock (H) and reservoir (R). Exemplary results for the plastic strain distribution after injection into a reservoir section offset by the fault zone are displayed regarding their scale (C-E).

Future sensitivity studies can compare detailed fault zone models, differing in e.g. the material properties, like permeable or impermeable fault core or different geometrical setups, like lense size and distance or number of damage zone graduation with a model representing the fault zone as uniform weak zone. Thus, effects resulting from a more detailed description of the fault zone on the simulation results can be determined regarding their scale. This may allow recommendations regarding the necessity of modeling the fault zone in detail or sufficient of uniform fault material usage regarding the scope of interest.

If these sensitivity studies show that the usage of such a detailed schematic fault representation has a significant impact on the value of the simulation results in certain cases, implementing such a detailed schematic fault zone into a reservoir model can also be standardized by coding analogue to section 3.1. These studies may also be a starting point for developing upscaling techniques of the detailed fault zone representation to one uniform fault material. This may help in cases where the model dimensions are too large for a detailed implementation and will be further discussed in the next section.

8.3. Workflow for Database-Driven Upscaling of Detailed Fault Zone Models

Incorporating highly detailed fault zones as seen in the previous chapter into reservoir-scale models containing multiple faults will increase the total element number of the model and thereby the computing costs for the simulations significantly. Thus, it may be impossible to incorporate such detailed fault zones into full-field reservoir models, even if detailed mesh generation of fault zones can be highly automated by coding as seen before.

Hence, upscaling and merging of the fault zone properties while still capturing the hydro-mechanical behavior correctly regarding the aim of the simulation before incorporating them into reservoir-scale models is necessary. Developing a workflow to tackle this problem should be a target for future research. A possible approach to model detailed fault zone behavior and incorporate the results into a reservoir model will be outlined in the following.

Based on a regional reservoir model (Figure 8-2 A), a detailed schematic fault zone model (Figure 8-2 B) and associated detailed numerical fault zone model (Figure 8-2 C) are developed with different material domains, as seen in the previous chapter 8-1. Different result parameters, such as stress magnitude and orientation pattern, elastic and plastic strain and/or resulting pore pressure changes and fluid flow are analyzed (Figure 8-2 D).

Concurrently, a database containing many modeling results derived from upscaled fault zone models featuring the same geological setting and overall geometry like the detailed fault models while using only one material domain for the whole fault zone is created (Figure 8-2 F). The models are populated with various hydraulic and mechanical material properties and also property combinations which may not occur in nature – e.g. high cohesion and low friction angle – similar to the sensitivity study carried out on the elastic and frictional fault zone properties (Chapter 6). Although the number of different fault zone material combinations can be reduced by recommendations such as neglecting the Poisson's ration of the fault zone (see Chapter 6-6), the database has to consist of hundreds of modeling results. However, modern storage and compressing techniques as well as the further increasing storage capacity of hard disks make creating such a database possible.

With the results of the detailed fault zone model and the database containing results for multiple material combinations of one unique fault zone material domain, the upscaling process can be started by using modern Data Science and Machine Learning techniques to compare the results of the detailed fault model with the results stored in the database. Once a match is achieved (Figure 8-2 E), regarding the aim of the later full-scale reservoir model, the associated material properties are then assigned with the upscaled fault zone grid (Figure 8-2 F) into the full field reservoir model (Figure 8-2 A).

Albeit the results for the detailed (Figure 8-2 D) and upscaled (Figure 8-2 E) fault zone should be the same, using such a database driven approach to upscale the fault zone properties may lead to completely imaginary fault rock properties assigned to the full-field reservoir. However, such imaginary fault rock properties may represent the fault behavior and the resulting effect on the reservoir behavior more accurately than material properties derived from mathematical upscaling techniques.

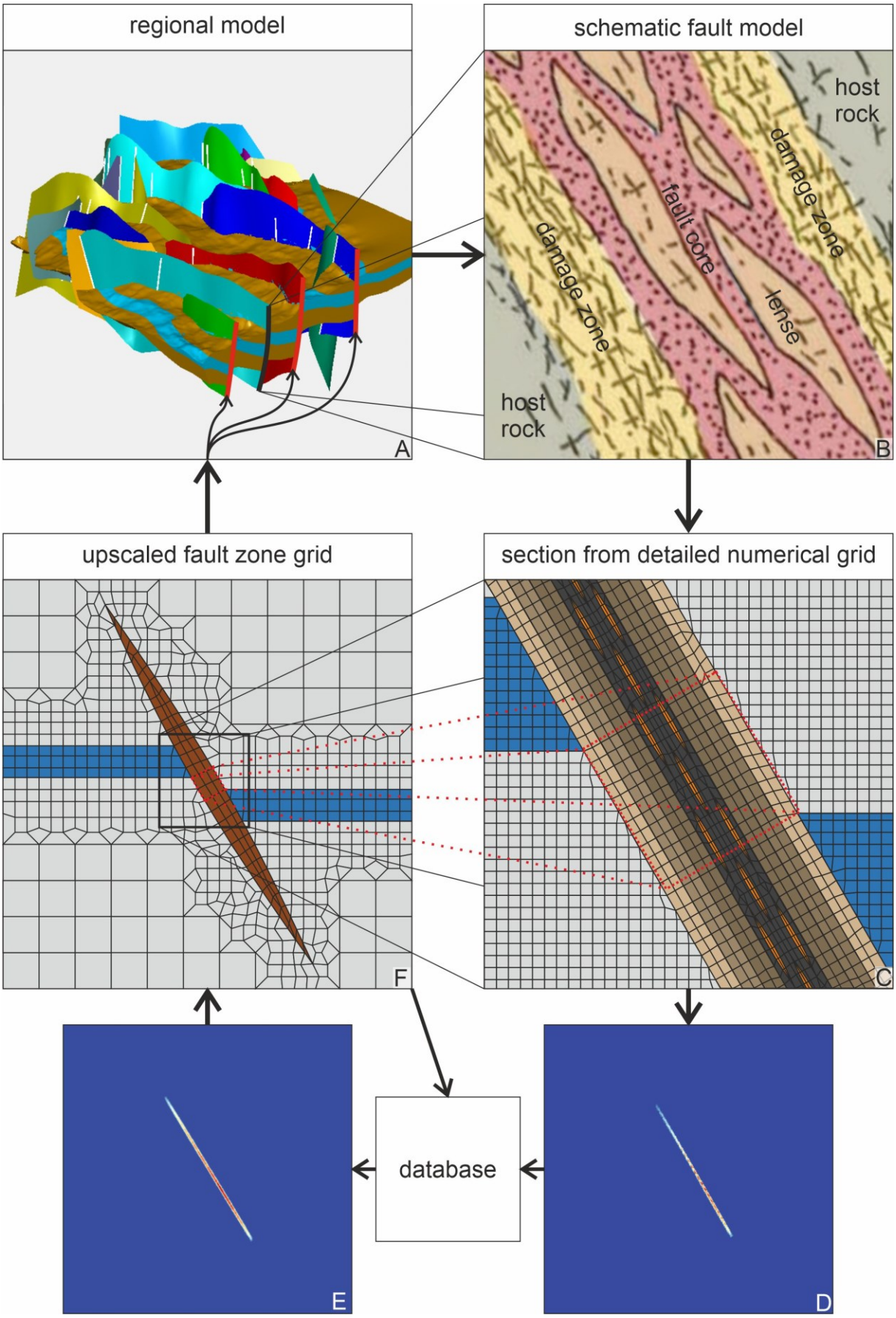

Figure 8-2: Possible schematic workflow for database-driven upscaling of detailed fault zone models to unique fault zone material properties assigned to a regional reservoir model.

References

Abelin, H., Birgersson, L., Gidlund, J., Neretnieks, I. 1991a. A Large-Scale Flow and Tracer Experiment in Granite: 1. Experimental Design and Flow Distribution. *Water Resources research 27*, (12), 3107– 3117.

Abelin, H., Birgersson, L., Moreno, L., Widén, H., Ågren, T. , Neretnieks, I. 1991b. A Large-Scale Flow and Tracer Experiment in Granite: 2. Results and Interpretation. *Water Resources Research 27*, (12), 3119–3135.

Achenbach, J. D., Abo-Zena, A. M. 1973. Analysis of the Dynamics of Strike Slip Faulting. *Journal of Geophysical Research 78*, (5), 866-875.

Aiming, L. & Kazuhiko, Y. 2013. Spatial variations in damage zone width along strike-slip faults. An example from active faults in southwest Japan. *Journal of Structural Geology 57*, 1-15.

Al-Busafi, B., Fisher, Q. J., Harris, S. D. 2005. The importance of incorporating themulti-phase flow properties of fault rocks into production simulation models. *Marine and Petroleum Geology 22*, 365-374

Ansys, 19.2; Ansys Inc. Canonsburg, PA, USA, 2019.

Agosta, F., Prasad, M., Aydin, A. 2006. Physical properties of carbonate fault rocks, Fucino basin (Central Italy): Implications for fault seal in platform carbonates. *Geofluids 7*, (1), 19-32.

Anderson, E. M. 1951. *The Dynamics of Faulting and Dyke Formation with Application to Britain* (2nd Ed.). Oliver and Boyd, Edinburgh, UK.

Anderson, J.-E., Ekman, L., Nordqvist, R., Winberg, A. 1991. Hydraulic testing and modeling of a low-angle fracture zone at Finnsjön, Schweden. *Journal of Hydrology 126*, 45-77

Antonellini, M., Aydin, A. 1994. Effects of faulting on fluid flow in porous sandstone reservoirs: petrophysical properties. *AAPG Bulletin 78*, 355-377

Anyim, K., Gan, Q. 2020. Fault zone exploitation in geothermal reservoirs: Production optimization, permeability evolution and induced seismicity. *Advances in Geo-Energy Research 4*, 1-12

Ashford, S. A., Sitar, N. 2001. Effect of element size on the static finite element analysis of steep slopes. *International Journal for Numerical and Analytical Methods in Geomechanics 25*, (14), 1361-1376.

Azami, A., Yacoub, T., Curran, J. Effects of strength an-isotropy on the stability of slopes. In: (Eds.) *65th Canadian Geotechnical Conference - CGS Geo-Manitoba* 30.-3. September-October 2012. Winnipeg, Manitoba, Canada.

Azarfar, B., Peik, B. , Abbasi, B. A Discussion on Numerical Modeling of Fault for Large Open Pit Mines. In Proceedings of the *52th US Rock Mechanics/Geomechanics Symposium*, 17-20. June 2018. Seattle, Washington, USA.

Backers, T. Stress Alterations in Faulted Reservoirs - A Fracture Mechanical Analysis. In: (Eds.) *77th EAGE Conference and Exhibition* 1.-4. June 2015. Madrid, Spain.

Ballance, P. F. 1976. Evolution of the upper Cenozoic magmatic arc and plate boundary in northern New Zealand. *Earth and Planetary Science Letters 28*, 356-370

Baranova, V., Mustaqeem, A. , Bell, S. 2011. A model for induced seismicity caused by hydrocarbon production in the Western Canada Sedimentary Basin. *Canadian Journal of Earth Sciences 36*, 47-64

Barton, N. 1973. Review of a new shear-strength criterion for rock joints. *Engineering Geology 7*, 287-332

Barton, N. 2013. Shear strength criteria for rock, rock joints, rockfill and rock masses: Problems and some solutions. *Journal of Rock Mechanics and Geotechnical Engineering 5*, (4), 249-261.

Bauer, J. F., Meier, S., Philipp, S. L. 2015. Architecture, fracture system, mechanical properties and permeability structure of a fault zone in Lower Triassic sandstone, Upper Rhine Graben. *Tectonophysics 647*, 132-145

Baysal, E., Kosloff, D., Sherwood, J. W. 1983. Reverse time migration. *Geophysics 48*, 1514-1524.

Beach, A., Welbon, A., Brockbank, P. J., McCallum, J. E. 1999. Reservoir damage around faults; outcrop examples from the Suez Rift. *Petroleum Geoscience 5*, (2), 109-116.

Bell, J. S. 1996. In situ stresses in sedimentary rocks (part 2): Applications of stress measurements. *Geoscience Canada 23*, (3), 135-153.

Bell, F. G. 2000. *Engineering Properties of Soils and Rocks* (4th Ed.). Blackwell, Oxford, UK.

Berg, S. S., Skar, T. 2005. Controls on damage zone asymmetry of a normal fault zone: outcrop analyses of a segment of the Moab fault, SE Utah. *Journal of Structural Geology 27*, (10), 1803-1822.

Billi, A., Salvini, F., Storti, F. 2003. The damage zone-fault core transition in carbonate rocks: implications for fault growth, structure and permeability. *Journal of Structural Geology 25*, 1779-1794.

Blümel, M. Comparison of single and multiple failure triaxial tests. In Proceedings of the *ISRM Regional Symposium - EUROCK 2009*, 29-31. October 2009. Cavtat, Croatia, 239-242.

Bonson, C. G., Childs, C., Walsh, J. J., Schöpfer, M. P., Carboni, V. 2007. Geometric and kinematic controls on the internal structure of a large normal fault in massive limestones: the Maghlaq Fault, Malta. *Journal of Structural Geology 29*, 336-354

Borja, R. I. & Lee, S. R. 1990. Cam-clay plasticity, Part I: implicit integration of elasto-plastic. *Computer Methods in Applied Mechanics and Engineering 78*, (1), 49-72.

Borja, R. I. 1991. Cam-Clay plasticity, Part II: Implicit integration of constitutive equation based on a nonlinear elastic predictor. *Computer Methods in Applied Mechanics and Engineering 88*, 225-240.

Braathen, A., Tveranger, J., Fossen, H., Skar, T., Cardozo, N., Semshaug, S. E., Bastesen, E., Sverdrup, E. 2009. Fault facies and its application to sandstone reservoir. *AAPG Bulletin 93*, (7), 891-917.

Brace, W. F. 1960. An extension of the Griffith theory of fracture to rocks. *Journal of Geophysical Research 65*, (10), 3477-3480.

Brady, B. H., Brown, E. T. 1993. *Rock Mechanics for Underground Mining* (2nd Ed.). Kluwer, London, UK.

Brandes, C., Tanner, D. 2019. Fault mechanics and earthquakes. In: Tanner, D. & Brandes, C. (Eds.), *Understanding Faults - Detection, Dating and Modeling*, Elsevier, Amsterdam, The Netherlands, 11-80.

Brixel, B., Klepikova, M., Jalali, M. R., Lei, Q., Roques, C., Krietsch, H., Loew, S. 2020. Tracking fluid flow in shallow crustal fault zones: 1. Insights from single-hole permeability estimates. *Journal of Geophysical Research: Solid Earth 125, 1-16.*

Bro, A. 1997. Analysis of multistage triaxial test results for a strain-hardening rock. *International Journal of Rock Mechanics and Mining Sciences 34*, 143-145.

Bruhn, R. L., Parry, W. T., Yonkee, W. A., Thompson, T. 1994. Fracturing and hydrothermal alteration in normal fault zones. *Pure and Applied Geophysics 142*, 609-644

Buchmann, T. J., Connolly, P. T. 2007. Contemporary kinematics of the Upper Rhine Graben: A 3D finite element approach. *Global and Planetary Change 58*, (1-4), 287-309.

Buijze, L., van den Bogert, P., Wassing, B., Orlic, B. , ten Veen, J. 2017. Fault reactivation mechanisms and dynamic rupture modelling of depletion-induced seismic events in a Rotliegend gas reservoir. *Netherlands Journal of Geosciences 96*, (5), 131-148.

Bukowska, M., Sanetra, U. 2008. The tests of the conventional triaxial granite and dolomite compression in the aspect of their mechanical properties. *Minearal Resource Management 24*, 345-358.

Burtan, Z., Zorychta, A., Cieslik, J., Chlebowski, D. 2014. Influence of Mining Operating Conditions on Fault Behavior. *Archieves of Mining Sciences 8*, (5), 660-671.

Buske, S., Gutjahr, S., Sick, C. 2009. Fresnel volume migration of single-component seismic data. *Geophysics 74*, (6), 47-55.

Byerlee, J. 1978. Friction of rocks. *PAGEOPH 116*, 615-626.

Caddell, R. M. 1980. *Deformation and Fracture of Solids* Prentice-Hall, Upper Saddle River, NJ, USA.

Caine, J. S., Evans, J. P. , Forster, C. B. 1996. Fault zone architecture and permeability structure. *Geology 24*, (11), 1025-1028.

Cappa, F., Guglielmi, Y. , Virieux, J. 2007. Stress and fluid transfer in a fault zone due to overpressures in the seismogenic crust. *Geophysical Research Letter 34*

Cappa, F., Rutqvist, J. 2011. Modeling of coupled deformation and permeability evolution during fault reactivation induced by deep underground injection of CO_2. *International Journal of Greenhouse Gas Control 5*, (2), 336-346.

Carmichael, R. S. 1988. *Practical Handbook of Physical Properties of Rocks and Minerals*, Informa UK Limited, London, UK.

Chan, A. W., Zoback, M. D. 2007. The role of hydrocarbon production on land subsidence and fault reactivation in the Louisiana coastal zone. *Journal of Coastal Research 24*, 771-786

Cheng, A. H. 2016. *Poroelasticity*, Springer International Publishing, Basel, Schwitzerland.

Chenglong, Y., Wang, H., Fu, X. 2018. The evolution model and sealing of reverse fault in clastic strata. *Natural Gas Geoscience 29*, (4), 529-537.

Chiaraluce, L., Chiarabba, C., Collettini, C., Piccinini, D., Cocco, M. 2007. Architecture and mechanics of an active low-angle normal fault: Alto Tiberiana Fault, northern Alpennines, Italy. *Journal of Geophysical Research 112*, 148-227

Childs, C., Watterson, J., Walsh, J. J. 1996. A model for the structure and development of fault zones. *Journal of the Geological Society 153*, (3), 337-340.

Childs, C., Mazocchi, T., Walsh, J. J., Bonson, C. G., Nicol, A., Schöpfer, M. P. 2009. A geometric model of fault zone and fault rock thickness variations. *Journal of Structural Geology 31*, (2), 117-127.

Ching, J., Phoon, K.-K. 2013. Effect of element sizes in random field finite element simulations of soil shear strength. *Computers & Structures 126*, (1), 120-134.

Ching, J., Hu, Y.-G. 2016. Effect of Element Size in Random Finite Element Analysis for Effective Young's Modulus. *Mathematical Problems in Engineering 1*, 1-10

Chopra, S., Marfurt, K. Seismic Attributes for Prospect Identification and Reservoir Characterization. In: *SEG Geophysical Developments 11*, (1), 2007. Tulsa, OK, USA.

Collettini, C., Holdsworth, R. E. 2004. Fault zone weakening and character of slip along low-angle normal faults: Insights from the Zuccale fault, Elba, Italy. *Journal of the Geological Society 161*, (6), 1039-1051.

Collettini, C., Niemeijer, A., Viti, C., Marone, C. 2009. Fault zone fabric and fault weakness. *Nature 462*, 907-910

Couples, G., Ma, J., Lewis, H., Olden, P., Quijano, J., Fasae, T., Maguire, R. 2007. Geomechanics of faults: impacts on seismic imaging. *First Break 25*, (10), 83-90.

Cowie, P. A., Scholz, C. H. 1992. Displacement-length scaling relationship for faults: data synthesis and discussion. *Journal of Structural Geology 14*, (10), 1149-1156.

Cowie, P. A., Shipton, Z. K. 1998. Fault tip displacement gradients and process zone dimensions. *Journal of Structural Geology 20*, (8), 983-997.

Cox, D. A., Little, J., Oshea, D. 2005. *Using Algebraic Geometry* (2nd Ausg.). Springer-Verlag, New York, New York, USA.

Crawford, B. R., Myers, R. D., Woronow, A., Faulkner, D. R., Rutter, E. H. Porosity-permeability relationships in clay-bearing fault gouge. In Proceedings of the *Society of Petroleum Engineers / International Society of Rock Mechanics Conference*, 20-23. October 2002. Iving, Texas, USA.

Croucher, A. E., O'Sullivan, M. J. 2008. Application of the computer code TOUGH2 to the simulation of supercritical conditions in geothermal systems. *Geothermics 37*, (6), 622-634.

Cuisiat, F., Jostad, H. P., Andresen, L., Skurtveit, E., Skomedal, E., Hettema, M., Lyslo, K. 2010. Geomechanical integrity of sealing faults during depressurisation of the Statfjord Field. *Journal of Structural Geology 32*, (11), 1754-1767.

Davarpanah, S. M., Van, P., Vasarhelyi, B. 2020. Investigation of the relationship between dynamic and static deformation moduli of rocks. *Geomechanics and Geophysics for Geo-Energy and Geo-Resources 6*, 1-14.

De Joussineau, G., Petit, J.-P., Gauthier, B. D. 2003. Photoelastic and numerical investigation of stress distributions around fault models under biaxial compressive loading conditions. *Tectonophysics 363*, (1-2), 19-43.

De Souza, A. L., De Souza, J. A., Meurer, G. B., Naveira, V. P., Chaves, R. A. Reservoir geomechanics study for deepwater field identifies ways to maximize reservoir performance while reducing geomechanics risk. In Proceedings of the *SPE Asia Pacific Oil and Gas Conference*, 22-24. October 2012. Perth, Australia.

De Souza, A. L., De Souza, J. A., Meurer, G. B., Chaves, R. A., Frydman, M., Pastor, J. 2014. Integrated 3D geomechanics and reservoir simulation optimize performance avoid fault reactivation. *World Oil 4*, 55-58

De Waal, H., Muntendam-Bos, A. G., Roest, J. P. 2015. Production induced subsidence and seismicity in the Groningen gas field – can it be managed?, *Proceedings of the International Association of Hydrological Sciences 372*, 129-139

Deb, R., Jenny, P. 2017. Modeling of shear failure in fractured reservoirs with a porous matrix. *Computational Geosciences 21*, 1119-1134

Duda, S. J. 1965. The Stress around a Fault according to a Photoelastic Model Experiment. *Geophysical Journal International 9*, (4), 399-410.

Dutt, A. 2015. Effect of mesh size on finite element analysis of beam. *International Journal of Mechanical Engineering 2*, (12), 8-10.

Duwiquet, H., Arbaret, L., Guillou-Frottier, L., Heap, M. j., Bellanger, M. 2019. On the geothermal potential of crustal fault zones: a case study from the Pontgibaud area (French Massif Central, France). *Geothermal Energy 7*, (33), 1-29.

Dyskin, A. V. 1993. A model of crack growth in microcracked rock. *International Journal of Rock Mechanics and Mining Sciences & Geomechanics Abstracts 30*, (7), 813-820.

Eissa, E. A., Kazin, A. 1988. Relation between static and dynamic Young's moduli of rocks. *International Journal of Rock Mechanics and Mining Sciences & Geomechanics 25*, 479-482.

Engelder, T. 1993. *Stress regimes in the lithosphere*, Princton University Press, Princton , New Jersey, USA.

Eshelby, J. D. 1957. The determination of the elastic field of an ellipsoidal inclusion and related problems. *Proceedings of the Royal Society of London 241*, 376-396

Fachri, M. J., Tveranger, J., Cardozo, N. , Pettersen, Ø. 2011. The impact of fault envelope structures on fluid flow: A screening study using fault facies. *AAPG Bulletin 95*, (4), 619-648.

Fachri, M., Rotevatn, A., Tveranger, J. 2013a. Fluid flow in relay zones revisited: towards an improved representation of small-scale structural Heterogeneities in flow models. *Marine and Petroleum Geology 46*, 144-164.

Fachri, M., Tveranger, J., Braathen, A., Schueller, S. 2013b. Sensitivity of fluid flow to deformation-band damage zone heterogeneity: A study using fault facies and truncated Gaussian simulation. *Journal of Structural Geology 52*, 60-79

Fachri, M., Tveranger, J., Braathen, A., Røe, P. 2016. Volumetric faults in field-sized reservoir simulation models: A first case study. *AAPG Bulletin 100*, (5), 795-817.

Fasching, F., Vanek, R. 2011. Engineering geological characterisation of fault rocks and fault zones. *Geomechanics and Tunnelling 4*, (3), 181-194.

Faulkner, D. R., Lewis, A. C., Rutter, E. H. 2003. Onthe internal structure and mechanics of large strike-slip faults: Field observations from the Carboneras fault, south-eastern Spain. *Tectonophysics 367*, 235-251

Faulkner, D. R. 2004. A model for the variation in permeability of clay-bearing fault gouge with depth in the brittle crust. *Geophysical Research Letters 31*, (19), 1-5.

Faulkner, D. R., Mitchell, T. M., Healy, D., Heap, M. J. 2006. Slip on 'weak' faults by the rotation of regional stress in the fracture damage zone. *Nature 444*, 922-925

Faulkner, D. R., Jackson, C. A., Lunn, R. J., Schlische, R. W., Shipton, Z. K., Wibberley, C. A., Withjack, M. O. 2010. A review of recent developments concerning the structure, mechanics and fluid flow properties of fault zones. *Journal of Structural Geology 32*, (11), 1557-1575.

Feng, Y., Grey, K. E. 2018. Wellbore Strengthening Models. *Lost Circulation and Wellbore Strengthening*, *SpringerBriefs in Petroleum Geoscience & Engineering* 43-72

Ferrill, D., Stamatakos, J., Sims, D. 1999. Normal fault corrugation: Implications for growth and seismicity of active normal faults. *Journal of Structural Geology 21*, (1), 1027-1038.

Ferronato, M., Janna, C., Gambolati, G. 2008. Mixed constraint preconditioning in computational contact mechanics. *Computer Methods in Applied Mechanics and Engineering 197*, (45-48), 3922-3931.

Fisher, Q. J., Harris, S. D., McAllister, E., Knipe, R. J., Bolton, A. J. 2001. Hydrocarbon flow across sealing faults: theoretical constrains. *Marine and Petroleum Geology 18*, 251-257

Fisher, Q. J., Knipe, R. 2001. The permeability of faults within siliclastic petroleum reservoirs of the North Sea and Norwegian Continental Shelf. *Marine Petroleum Geology 18*, 1063-1081

Fisher, Q., Jolley, S. J. 2007. Treatment of faults in production simulation models. In: Jolley, S. J., Barr, D., Walsh, J. J., Knipe, R. J. (Eds.), *Structurally Complex Reservoirs*, 292, Geological Society London Special Publications, London, 219-233.

Fischer, K., Henk, A. A workflow for building and calibrating 3-D geomechanical models-A case study for a gas reservoir in the North German Basin. *Solid Earth 4*, (2), 2013. 347-355.

Fjær, E., Holt, R., Horsrud, P., Raaen, A., Risnes, R. 2008. *Petroleum Related Rock Mechanics* (2nd Ed.). Elsevier, Amsterdam, The Netherlands.

Fjær, E. 2018. Relations between static and dynamic moduli of sedimentary rocks. *Geophysical Prospecting 67*, 128-139

Fontoura, S. A., Lautenschläger, C. E., Righetto, G. L., Inoue, N., Albuquerque, R. A., Gonçalves, C. J. , Alcure, M. Workflow For Wellbore Integrity Analysis During Reservoir Development. In Proceedings of the *Offshore Technology Conference*, 29-31. October 2013. Rio de Janeiro, Brazil.

Fournier, T., Morgan, J. 2012. Insights to slip behavior on rough faults using discrete element modeling. *Geophysical Research Letters 39*, (12).

Foxford, E. A., Walsh, J. J., Watterson, J., Garden, I. R., Guscott, S. C., Burley, S. D. 1998. Structure and content of the Moab Fault zone, Utah, USA. In: Jones, G., Fisher, Q. J. , Knipe, R. J. (Eds.), *Faulting, Fault Sealing and Fluid Flow in Hydrocarbon Reservoirs*, Geological Society, London, UK, 87-103.

Franceschini, A., Ferronato, M., Janna, C., Teatini, P. 2016. A novel Lagrangian approach for the stable numerical simulation of fault and fracture mechanics. *Journal of Computational Physics 314*, 503-521

Fredman, N., Tveranger, J., Semshaug, S., Braathen, A., Sverdrup, E. 2007. Sensitivity of fluid flow to fault core architecture and petrophysical properties of fault rocks in siliciclastic reservoirs: A synthetic fault model study. *Petroleum Geoscience 13*, 305-320

Fredman, N., Tveranger, J., Cardozo, N., Braathen, A., Soleng, H., Røe, P., Skorstad, A., Syversveen, A. 2008. Fault facies modeling: technique and approach for 3-D conditioning and modeling of faulted grids. *AAPG Bulletin 92*, (11), 1457-1478.

Frohlich, C., Deshon, H., Stump, B., Hayward, C., Hornbach, M., Walter, J. 2016. A Historical Review of Induced Earthquakes in Texas. *Seismological Research Letters 87*, (4), 1-17.

Gan, Q., Elsworth, D. 2014. Analysis of Fluid Injection-induced Fault Reactivation and Seismic Slip in Geothermal Reservoirs. *Journal of Geophysical Research: Solid Earth 119*, 3340-3353

Geertsma, J. 1973. Land subsidence above compacting oil and gas reservoirs. *Journal of Petroleum Technology 25*, (6), 734-744.

Geldart, L. P., Sheri, R. E. 1995. *Exploration Seismology* (2nd Ausg.). Cambridge University Press, Cambridge, UK.

Ghavidel, A., Mousavi, S. R., Rashki, M. 2017. The effect of FEM mesh density on the failure probability analysis of structures. *KSCE Journal of Civil Engineering 22*, (2), 1-13.

Ghose, R., Carvalho, J., Loureiro, A. 2013. Signature of fault zone deformation in near-surface soil visible in shear wave seismic reflections. *Geophysical Research Letters 40*, 1074-1078.

Giba, M., Walsh, J. J., Nicol, A. 2012. Segmentation and growth of an obliquely reactivated normal fault. *Journal of Structural Geology 39*, 253-267

Goodman, R. E., Taylor, R. L., Brekke, T. L. 1968. A model for the mechanics of jointed rock. *Journal of the Soil Mechanics and Foundations Division* 637-659.

Goodman, R. E. 1989. *Introduction to Rock Mechanics* (2nd Ausg.). Wiley, New York, NY, USA.

Gudmundsson, A. 1999. Fluid overpressure and stress drop in fault zones. *Journal of Geophysical Research 26*, (1), 115-118.

Gudmundsson, A., Galindo Jiménez, I., Friese, N., Philipp, S. 2008. Dike-induced reverse faulting in a graben. *Geology 36*, (2), 123-126.

Gudmundsson, A. 2011. *Rock Fractures in Geological Processes* Cambridge University Press, Cambridge, UK.

Gudmundsson, A., De Guidi, D., Scudero, S. 2013. Length-displacement scaling and fault growth. *Tectonophysics 608*, 1298-1309

Guglielmi, Y., Cappa, F., Amitrano, D. 2008. High-definition analysis of fluid-induced seismicity related to the mesoscale hydromechanical properties of a fault zone. *Geophysical Research Letters 35*, (6).

Guglielmi, Y., Birkholzer, J., Rutqvist, J., Jeanne, P. , Nussbaum, C. 2017. Can Fault Leakage Occure Before or Without Reactivation? - Results from an in situ Fault Reactivation Experiment at Mont Terri. *Energy Procedia 114*, 3167-3174

Guha-Sapir, D., Vos, F., Below, R., Ponserre, S. 2011. Annual Disaster Statistical Review: The Numbers and Trends. *CRED, Bruessel*

Haug, C., Nüchter, J.-A., Henk, A. 2018. Assessment of geological factors potentially affecting production-induced seismicity in North German gas fields. *Geomechanics for Energy and Environment 16*, 15-31

Henk, A. 2019. Numerical Modeling of Faults. In: Tanner, D. & Brandes, C. (Eds.), *Understanding Faults—Detecting, Dating and Modeling*, 1st Ed., Elsevier, Amsterdam, The Netherlands, 147-164.

Hennings, P., Allwardt, P., Paul, P., Zahm, C., Reid, R., Alley, H., Kirschner, R., Lee, B., Hough, E. 2012. Relationship between fractures, fault zones, stress and reservoir productivity in the Suban gas field, Sumatra, Indonesia. *AAPG Bulletin 96*, 753-772

Hergert, T., Heidbach, O., Bécel, A., Laigle, M. 2011. Geomechanical model of the Marmara Sea region—I. 3-D contemporary kinematics. *Geophysical Journal International 185*, (3), 1073-1089.

Hickman, S., Zoback, M. 2004. Stress orientations and magnitudes in the SAFOD pilot hole. *Geophysical Research Letters 31*, (15), 4.

Hilley, G. E., Mynatt, I., Pollard, D. D. 2010. Structural geometry of Raplee Ridge monocline and thrust fault imaged using inverse Boundary Element Modeling and ALSM data. *Journal of Structural Geology 32*, (1), 45-58.

Hoek, E. & Brown, E. T. 1980. *Underground Excavations in Rock* CRC Press, London, UK.

Hoek, E. 2013. *Practical Rock Engineering* (2nd). Hoek's Corner, North Vancouver, BC, Canada.

Hoek, E., Martin, D. 2014. Fracture initiation and propagation in intact rock – A review. *Journal of Rock Mechanics and Geotechnical Engineering 6*, (4), 287-300.

Holdsworth, R. E. 2004. Weak Faults - Rotten Cores. *Science 303*, (5655), 181-182.

Hollund, K., Mostad, P. , Nielsen, B. 2002. Havana—A fault modeling tool. In: Koestler, A. G. & Hunsdale, R. (Eds.), *Hydrocarbon Seal Quantification*, 11, Norwegian Petroleum Society—Special Publications, Oslo, Norway, 157-171.

Holt, W. E. & Stern, T. A. 1994. Subduction, platform subsidence, and foreland thrust loading; the late Tertiary development of Taranaki Basin, New Zealand. *Tectonics 13*, 1068-1092

Huang, J., Griffiths, D. 2015. Determining an appropriate finite element size for modeling the strength of undrained. *Computers and Geotechnics 69*, 506-513

Jaeger, J. C., Cook, N. G. , Zimmerman, R. W. 2007. *Fundamentals of Rock Mechanics* (4th Ed.). Blackwell Publishing Ltd., Oxford, UK.

Jaeggi, D., Laurich, B., Nussbaum, C., Schuster, K., Connolly, P. 2017. Tectonic structure of the "Main Fault" in the Opalinus Clay, Mont Terri rock laboratory (Switzerland). *Swiss Journal of Geosciences Supplement 110*, 69-86

Jeanne, P., Guglielmi, Y., Rutqvist, J., Nussbaum, C., Birkholzer, J. 2018. Permeability variations associated with fault reactivation in a claystone formation investigated by field experiments and numerical simulations. *Journal of Geophysical Research: Solid Earth 123*, 1694-1710.

Jafarpour, M., Rahmati, H., Azadbakht, S., Nouri, A., Chan, D., Vaziri, H. 2012. Determination of mobilized strength properties of degrading sandstone. *Soils and Foundations 52*, 658-667.

Jayakumar, R., Sahai, V. , Boulis, A. A Better Understanding of Finite Element Simulation for Shale Gas Reservoirs through a Series of Different Case Histories. In Proceedings of the *SPE Middle East Unconventional Gas Conference and Exhibition* 31-02. January-February 2011. Muscat, Oman, 245-262.

Jeon, S., Kim, J., Seo, Y., Hong, C. 2004. Effect of a fault and weak plane on the stability of a tunnel in rock - A scaled model test and numerical analysis. *International Journal of Rock Mechanics and Mining Sciences 41*, 658-663.

Jing, L., Hudson, J. A. 2002. Numerical methods in rock mechanics. *International Journal of Rock Mechanics and Mining Sciences 39*, (4), 409-427.

Johri, M., Zoback, M., Hennings, P. 2014. A scaling law to characterize fault-damage zones at reservoir depths. *AAPG Bulletin 98*, (10), 2057-2079.

Jolley, S. J., Dijk, H., Lamens, J. H., Fisher, Q. J., Manzocchi, T., Eikmans, H., Huang, Y. 2007. Faulting and fault sealing in production simulation models: Brent Province, northern North Sea. *Petroleum Geoscience 13*, (4), 321-340.

Jones, I. F., Ibbotson, K., Grimshaw, M., Plasterie, P. 1998. 3-D prestack depth migration and velocity model building. *Geophysics 17*, (7), 897-906.

King, P. R. & Thrasher, G. P. 1992. Post-eocene development of the Taranaki Basin, New Zealand; convergent overprint of a passive margin. In: Watkins, J. S., Feng, Z., McMillen, K. J. (Eds.), *AAPG Memoir*, *53*, American Association of Petroleum Geologists, 93-118.

Klepikova, M., Brixel, B., Jalali, M. 2020. Transient hydraulic tomography approach to characterize main flowpaths and their connectivity in fractured media. *Advances in Water Resources 136*, *1-14*.

Knai, T. A., Knipe, R. J. 1998. The impact of faults on fluid flow in the Heidrun Field. In: Jones, G., Fisher, Q. J., Knipe, R. J. (Eds.), *Faulting*, *Fault Sealing and Fluid Flow in Hydrocarbon Reservoirs*, 147, Geological Society—Special Publications, London, UK, 269-282.

Knupp, P. M. 2006. Mesh quality improvement for SciDAC applicaitons. *Journal of Physics Conference Series 46*, (1), 458-462.

Kun, M., Onargan, T. 2013. Influence of the fault zone in shallow tunneling: A case study of Izmir Metro Tunnel. *Tunnelling and Underground Space Technology 33*, 34-45.

Kushwaha, A., Bhattacharjee, R., Tewari, S., Mandal, P. K. 2016. Role of geological discontinuities during application of continuous miner technology in underground coal mines. *Journal of Mines*, *Metals and Fuels 64*, (9), 395-405.

Le Borgne, T., Bour, O., de Dreuzy, J. R., Davy, P., Touchard, F. 2004. Equivalent mean flow models for fractured aquifers: Insights from a pumping tests scaling interpretation. *Water Resources Research 40*, *W02512*, *1-10*.

Lin, J., Parmentier, E. M. 1988. Quasistatic propagation of a normal fault: A fracture mechanics model. *Journal of Structural Geology 10*, (3), 249-262.

Lindsay, N. G., Murphy, F. C., Walsh, J. J., Watterson, J. 1993. Outcrop Studies of Shale Smears on Fault Surface. *The Geological Modelling of Hydrocarbon Reservoirs and Outcrop Analogues*, *113-123*.

Liu, Y. 2013. Choose the Best Element Size to Yield Accurate FEA Results While Reduce FE Models's Complixity. *British Journal of Engineering and Technology 1*, (7), 13-28.

Liu, Y., Glass, G. Effects of Mesh Density on Finite Element Analysis. In Proceedings of the *SAE World Congress*, 16-18. April 2013. Detroit, MI, USA.

Liu, E., Martinez A. Seismic Fracture Characterization, Concepts and Practical Applications In: Proceedings of the *EAGE*, 4-7. June 2012. Copenhagen, The Netherlands.

Li, Y., Wierzbicki, T. Mesh-size Effect Study of Ductile Fracture by Non-local Approach. In Proceedings of the *SEM Annual Conference*, 1-4. June 2009. Albuquerque, NM, USA.

Loveless, S., Pluymaekers, M., Lagrou, D., De Boever, E., Doornenbal, H., Laenen, B. 2014. Mapping the Geothermal Potential of Fault Zones in the Belgium-Netherlands Border Region. *Energy Procedia 59*, 351-358

Lund-Snee, J.-E., Zoback, M. 2018. State of stress in the Permian Basin, Texas and New Mexico: Implications for induced seismicity. *The Leading Edge 37*, 127-134

Malkowski, P. 2015. Behaviour of joints in sandstones during the shear test. *Acta Geodynamica et Geomaterialia 12*, (4), 1-12.

Manzocchi, T., Walsh, J. J., Nell, P., Yielding, G. 1999. Fault Transmissibility Multipliers for Flow Simulation Models. *Petroleum Geoscience 5*, 53-63.

Manzocchi, T., Heath, A. E., Palananthakumar, B., Childs, C., Walsh, J. J. 2008. Faults in conventional flow simulation models: A consideration of representational assumptions and geological uncertainties. *Petroleum Geoscience 14*, 91-110

Martin, C. D. & Lanyon, G. W. 2003. Measurement of in-situ stress in weak rocks at Mont Terri Rock Laboratory, Switzerland. *International Journal of Rock Mechanics and Mining Sciences 40*, (7), 1077-1088.

Meier, T. & Backers, T. 2017. Thermo-hydro-mechanische Simulation des Reservoirverhaltens zur Abschätzung des Potential induzierter Seismizität bei Förderung und Injektion. *Erdoel Erdgas Kohle /EKEP 4*, 149-153

Merzer, A. M. & Freund, R. 2007. Equal Spacing of Strike-Slip Faults. *Geophysical Journal of the Royal Astronomical Society 45*, (1), 177-188.

Mitchell, T. M. & Faulkner, D. R. 2009. Experimental measurements of permeability evolution during triaxial compression of initially intact crystalline rocks and implications for fluid flow in fault zones. *Journal of Geophysical Research 113, 1-10.*

Moeck, I., Kwiatek, G., Zimmermann, G. 2009a. Slip tendency analysis, fault reactivation potential and induced seismicity in a deep geothermal reservoir. *Journal of Structural Geology 31*, 1174-1182.

Moek, I., Kwiatek, G., Zimmermann, G., Backers, T., Huenges, E. 2009b. Assessment of fault reactivation potential in a deep geothermal reservoir of the NE-German Basin (Germany). *Transactions - Geothermal Resource Council 33*, 188-192.

More, S. T., Bindu, R. S. 2015. Effect of mesh size on Finite Element Analysis. *International Journal of Engineering Science and Innovative Technology 4*, (3), 1-5.

Morrow, C. A. & Lockner, D. A. 1994. Permeability differences between surface-derived and deep drillhole core samples. *Geophysikal Reserch Letters 21*, 2151-2154

Morrow, C. A., Lockner, D. A., Moore, D. E., Hickman, S. H. 2014. Deep permeability of the San Andreas Fault from San Andreas Fault Observatory at Depth (SAFOD) core samples. *Journal of Structural Geology 64*, 99-114.

Morton, R. A., Bernier, J. C., Barras, J. A. 2006. Evidence of regional subsidence and associated interior wetland loss induced by hydrocarbon production, Gulf Coast region, USA. *Environmental Geology 50*, 261-274

Moser, T. J., Howard, C. 2008. Diffraction imaging in depth. *Geophysical Prospection* 627-641.

Morris, J. P., Hao, Y., Foxall, W., McNab, W. 2011. A study of injection-induced mechanical deformation at the In Salah CO2 storage project. *International Journal of Greenhouse Gas Control 5*, (2), 270-280.

Myers, R., Aydin, A. 2004. The evolution of faults by shearing across joint zones in sandstone. *Journal of Structural Geology 26*, (5), 947-966.

Myers, R., Allgood, A., Hjellbakk, A., Vrolijk, P., Briedis, N. 2007. Testing fault transmissibility predictions in a structurally dominated reservoir: Ringhorn Field, Norway. In: Jolley, S. J., Barr, D., Walsh, J. J. , Knipe, R. J. (Eds.), *Structurally Complex Reservoirs* , Geological Society - Special Publications, London, UK, 271-294.

Nagelhout, A. C., Roest, J. P. 1997. Investigating fault slip in a model of an underground gas storage facility. *International Journal of Rock Mechanics and Mining Sciences 34*, (3), 97-115.

Nasir, O., Fall, M., Nguyen, S. T., Evgin, E. 2015. Modeling of the thermohydromechanical–chemical response of Ontario sedimentary rocks to future glaciations. *Canadian Geotechnical Journal 52*, (7), 836-850.

Nicol, A., Walsh, J. J., Berryman, K., Nodder, S. 2005. Growth of a normal fault by the accumulation of slip over millions of years. *Journal of Structural Geology 27*, 327-342.

Odling, N. E., Harris, S. D., Knipe, R. J. 2004. Permeability scaling properties of fault damage zones in siliclastic rocks. Journal of Structural Geology 26, 1727-1747

Odonne, F., Ménard, I., Massonnat, G., Rolando, J. 1999. Abnormal reverse faulting above a depleting reservoir. *Geology 27*, (2), 1-4.

Okada, A., Matsuda, T. 1976. A Fault Outcrop at the Onosawa Pass and Recent Displacements alone the Atera Fault Central Japan. *Geographical Review of Japan 49*, (9), 632-639.

Olden, P., Pickup, G. E., Jin, M., Mackay, E. J., Hamilton, S. A., Somerville, J., Todd, A. C. 2012. Use of rock mechanics laboratory data in geomechanical modeling to increase confidence in CO_2 geological storage. *International Journal of Greenhouse Gas Control 11*, 304-315

Orlic, B., ter Heege, J., Wassing, B. 2011. Assessing the integrity of fault- and top seals at CO2 storage sites. *Energy Procedia 4*, 4798-4805

Orlic, B., Wassing, B. 2012. A Study of Stress Change and Fault Slip in Producing Gas Reservoirs Overlain by Elastic and Viscoelastic Caprocks. *Rock Mechanics and Rock Engineering 46*, (3), 421-435.

Paltrinieri, E., Sandrone, F., Dudt, J.-P., Zhao, J. 2015. Probabilistic simulations of TBM Tunnelling in highly fractured rocks. *Tunnelling and Underground Space Technology*, 1-12.

Park, J.-W., Guglielmi, Y., Graupner, B., Rutqvist, J., Kim, T., Park, E.-S., Lee, C. 2020. Modeling of fluid injection-induced fault reactivation using coupled fluid flow and mechanical interface model. *International Journal of Rock Mechanics and Mining Sciences 132*, 1-16

Paul, P. K., Zoback, M. D., Hennings, P. H. Fluid Flow in a Fractured Reservoir Using a Geomechanically Constrainer Fault-Zone-Damage Model for Reservoir Simulation. In Proceedings of the *SPE Annual Technical Conference and Exhibition*, 11-14. November 2007. Anaheim, California, USA.

Peacock, D., Knipe, R. J., Sanderson, D. 2000. Glossary of normal faults. *Journal of Structural Geology 22*, (3), 291-305.

Pereira, L. C., Guimarães, L. J., Horowitz, B., Sánchez, M. 2014. Coupled hydromechanical fault reactivation analysis incorporating evidence theory for uncertainty quantification. *Computers and Geotechnics 56*, 202-215

Peric, D. 2006. Analytical solutions for a three-invariant Cam clay model subjected to drained loading histories. *International Journal for Numerical and Analytical Methods in Geomechanics 30*, 363-387.

Pickover, C. 2009. *The Mathbook - From Pythagoras to the 57th Dimension - 250 Milestones in the History of Mathematics* Sterling Publishing Co., New York, New York, USA.

Prevost, J. H., Sukumar, N. 2015. Faults simulations for three-dimensional reservoir-geomechanical Models with the extended finite element method. *Journal of the Mechanics and Physics of Solids 86*, 1-18

Qu, D., Røe, P., Tveranger, J. 2015. A method for generating volumetric fault zone Grids for pillar gridded reservoir Models. *Computers & Geosciences 81*, 28-37

Qu, D., Tveranger, J. 2016. Incorporation of deformation band fault damage zones in reservoir models. *AAPG Bulletin 100*, (3), 423-443.

Rawling, G. C., Goodwin, L. B., Wilson, J. L. 2001. Internal aschitecture, permeability structure, and hydrologic significance of contrasting fault-zone types. *Geology 29*, 43-46

Reches, Z., Lockner, D. A. 1994. Nucleation and growth of faults in brittle rocks. *Journal of Geophysical Research: Solid Earth 99*, (89), 18159-18173.

Rinaldi, A. P., Jeanne, P., Rutqvist, J., Cappa, F. Geomechanical effects during large-scale underground injection. In Proceedings of the *47th US Rock Mechanics - Geomechanics Symposium*, 23-26. June 2013. San Francisco, California, USA.

Rinaldi, A. P., Rutqvist, J., Cappa, F. 2014. Geomechanical effects on CO2 leakage through fault zones during large-scale underground injection. *International Journal of Greenhouse Gas Control 20*, 117-131

Rippon, J. H. 1985. Contoured patterns of the throw and hade of normal faults in Coal Measures (Westphalian) of northwest Derbyshire. *Yorkshire Geological Society 45*, 147-161

Rohr, K., Furlong, K., Riedel, M. 2018. Initiation of strike-slip faults, serpentinization and methane. *Geochemistry, Geophysics, Geosystems 19*, 4290-4312

Roques, C., Bour, O., Aquilina, L., Dewandel, B., Leray, S., Schroetter, J. M., Longuevergne, L., Le Borgne, T., Hochreutener, R., Labasque, T., Lavenant, N., Vergnaud-Ayraud, V. , Mougin, B. 2014. Hydrological behavior of a deep sub-vertical fault in crystalline basement and relationships with surrounding reservoirs. *Journal of Hydrology 509*, 42-54.

Rotevatn, A., Jackson, C., Tvedt, A., Bell, R., Blaekkan, I. 2018. How do normal faults grow?. *Journal of Structural Geology* 1-31

Rueda, J. C., Norena, N., Oliveira, M. F., Roehl, D. Numerical models for detection of fault reactivation in oil and gas fields. In Proceedings of the *48th U.S. Rock Mechanics - Geomechanics Symposium*, 1-4. June 2014. Minneapolis, Minnesota, USA.

Sainoki, A. & Mitri, H. S. 2015. Effect of slip-weaking distance on selected seismic source parameters of mining-induced fault-slip. *International Journal of Rock Mechanics and Mining Sciences 73*, 115-122.

Sanchez, C. M., Zegarra, E. P., Oliveira, M. F., Roehl, D. Application of a 2D equivalent continuum approach to the assessment of geological fault reactivation in reservoirs. In Proceedings of the *XXXVI Ibero-Latin American Congress on Computational Methods in Engineering*, 22-25. November 2015. Rio de Janeiro, Brazil.

Sanetra, U. The change of internal friction angle of intact and jointed rock on different depth. In Proceedings of the *Mining Workshops, Polska Akademia Nauk*, 15-18. June 2005. Krakow, Poland.

Savin, G. N. 1961. *Stress Concentrations around Holes* Pergamon, London, UK.

Schlegel, R. 2016. Neue geomechanische Materialmodelle. *CADFEM Journal 1*, 24-25

Schön, J. H. 2004. *Physical Properties of Rocks - Fundamentals of Petrophysicy* Elsevier, London, Uk.

Schubert, W., Riedmüller, G. 1997. Influence of Faults on Tunnelling. *Felsbau 15*, 483-488

Schubert, W., Riedmüller, G. 2000. Tunnelling in Fault Zones - State of the Art in Investigation and Construction. *Felsbau 2*, 7-15

Schubert, W., Fasching, A., Goricki, A. 2006. Tunneling in Fault zones - State of the Art. *Tunnelling and Underground Space Technology 21*, 376-277

Schubert, W. Design and Construction of Tunnels in Poor and Faulted Rock Masses. In Proceedings of the *ISRM International Symposium - 5th Asian Rock Mechanics Symposium*, 1. January 2009. Tehran, Iran.

Schuite, J., Longuevergne, L., Bour, O., Burbey, T. J., Boudin, F., Lavenant, N., Davy, P. 2017. Understanding the Hydromechanical Behavior of a Fault Zone From Transient Surface Tilt and Fluid Pressure Observations at Hourly Time Scales. *Water Resources Research 53*, 10558-10582

Segall, P., Grasso, J.-R., Mossop, A. 1994. Poroelastic stressing and induced seismicity near the Lacq Gas Field, Southwestern France. *Journal of Geophysical Research Atmospheres 991*, (B8), 15423-15438.

Serajian, V., Diessl, J., Bruno, M. S., Hermansson, L. C., Hatland, J., Risanger, M., Torsvik, M. 3D Geomechanical Modeling and Fault Reactivation Risk Analysis for a Well at Brage Oilfield, Norway. In: (Eds.) *SPE Europec featured at 78th EAGE Conference and Exhibition* 30.-02. May-June 2016. Vienna, Austria.

Shapiro, S. 2015. Fundamentals of Poroelasticity. In: Shapiro, S. (Eds.), *Fluid-Induced Seismicity*, Cambridge University Press, Cambridge, UK, 48-117.

Skoumal, R. J., Barbour, A. J., Brudzinski, M. R., Langenkamp, T., Kaven, J. O. 2020. Induced Seismicity in the Delaware Basin, Texas. *Journal of Geophysical Research: Solid Earth 125*

Soliva, R., Maerten, F., Petit, J.-P., Auzias, V. 2010. Field evidences for the role of static friction on fracture orientation in extensional relays along strike-slip faults: comparison with photoelasticity and 3-D numerical modeling. *Journal of Structural Geology 32*, (11), 1721-1731.

Stagpoole, V. & Nicol, A. 2008. Regional structure and kinematic history of a large subduction back thrust; Taranaki Fault, New Zealand. *Journal of Geophysical Research 113*, 1-19.

Stefanov, Y., Bakeev, R. A. 2014. Deformation and fracture structures in strike-slip faulting. *Engineering Fracture Mechanics 129*, 102-111

Stern, T. A., Davey, F. J. 1989. Crustal structure and origin of basins formed behind the Hikurangi subduction zone, New Zealand. In: Price, R. A. (Eds.), *Geophysical Monograph*, American Geophysical Union, Washington, USA, 73-85.

Stern, T. A. & Nicol, A. 2008. Regional structure and kinematic history of a large subduction back thrust; Taranaki Fault, New Zealand. *Journal of Geophysical Research 113*.

Streit, J. E., Hillis, R. R. 2004. Estimating fault stability and sustainable fluid pressures for underground storage of CO2 in porous rock. *Energy 29*, (9), 1445-1456.

Sulem, J., Vardoulakis, I., Papamichos, E., Oulahna, A., Tronvoll, J. 1999. Elasto-plastic modeling of Red Wildmoor sandstone. *Mechanics of Cohesive-frictional Materials 4*, 215-245.

Syversveen, A., Skorstad, A., Soleng, H., Røe, P., Tveranger, J. Facies modeling in fault zones. In Proceedings of the *10th European Conference on the Mathematics of Oil Recovery*, 4-7. September 2006. Amsterdam, The Netherlands.

Taheri, A., Chanda, E. A new multiple-step loading triaxial test method for brittle rocks. In Proceedings of the *19th NZGS Geotechnical Symposium*, 21-22. November 2013. Queenstown, New Zealand.

Tamura, T., Kanaori, Y. 2017. Active fault Outcrops Concerning the Saigatao Tectonic Line in Central-Southern Part of Yamaguchi Prefecture, Southwest Japan. *Journal of the Japan Society of Engineering Geology 58*, (4), 290-296.

Tanner, D. C., Brandes, C. 2019. Introduction. In: Tanner, D. C. & Brandes, C. (Eds.), *Understanding Faults - Detecting, Dating and Modeling*, 1st, Amsterdam, The Netherlands, 1-9.

Tanner, D., Buness, H., Igel, J., Günther, T., Gabriel, G., Skiba, P., Plenefisch, T., Gestermann, N., Walter, T. 2019. Fault detection. In: Tanner, D. & Brandes, C. (Eds.), *Understanding Faults—Detecting, Dating and Modeling*, 1st Ed., Elsevier, Amsterdam, The Netherlands, 81–146.

Tian, H., Kempa, T., Xu, N., Ziegler, M. 2013. A Modified Mohr-Coulomb Failure Criterion for Intact Granites Exposed to High Temperatures. In: Hou, M., Xie, H., Were, P. (Eds.), *Clean Energy Systems in the Subsurface: Production, Storage and Conversion*, Springer Series in Geomechanics and Geoengineering, Berlin, Germany.

Treffeisen, T. & Henk, A. 2020a. Representation of faults in reservoir-scale geomechanical finite element models – A comparison of different modeling approaches. *Journal of Structural Geology 131*, 1-12

Treffeisen, T. & Henk, A. 2020b. Faults as Volumetric Weak Zones in Reservoir-Scale Hydro-Mechanical Finite Element Models - A Comparison Based on Grid Geometry, Mesh Resolution and Fault Dip. *Energies 13*, (10), 1-28.

Tveranger, J., Aanonsen, S., Braathen, A., Espedal, M., Fossen, H., Hesthammer, J., Howell, J., Pettersen, Ø., Skorstad, A. , Skar, T. The Fault Facies Project. In Proceedings of the *Production Geoscience*, 29-30. May 2004. Stavanger, Norway.

Van Rossum, G. & Drake, F. L. 2009. *Python 3 Reference Manual* CreateSpace, Scotts Valley, CA, USA.

Vermilye, J. M. & Scholz, C. H. 1998. The process zone: a microstructural view of fault growth. *Journal of Geophysical Research 103*, (6), 223-237.

Vidal-Gilbert, S., Nauroy, J.-F., Brosse, E. 2009. 3D geomechanical modelling for CO2 geologic storage in the Dogger carbonates of the Paris Basin. *International Journal of Greenhouse Gas Control 3*, (3), 288-299.

Vidal-Gilbert, S., Tenthorey, E., Dewhurst, D., Ennis-King, J., Van Ruth, P., Hillis, R. 2010. Geomechanical analysis of the Naylor Field, Otway Basin, Australia: Implications for CO2 injection and storage. *International Journal of Greenhouse Gas Control 5*, (2), 827-839.

Vilarrasa, V., Makhnenko, R. Y., Laloui, L. 2017. Potential for Fault Reactivation Due to CO2 Injection in a Semi-Closed Saline Aquifer. *Energy Procedia 114*, 3282-3290

Walcott, R. I. 1987. Geodetic strain and the deformational history of the North Island of New Zealand during the late Cainozoic. In: Oxburgh, E. R., Yardley, B. W., England, P. C. (Eds.), *Philosophical Transactions of the Royal Society of London, Series A: Mathematical and Physical Sciences*, 321, Royal Society of London, London, UK, 163-181.

Walsh, J. B. 1968. Mechanics of Strike-Slip Faulting with Friction. *Journal of Geophysical Research 73*, (2), 761-776.

Walsh, J. J., Watterson, J., Heath, A. E., Childs, C. 1998. Representation and scaling of faults in fluid flow models. *Petroleum Geoscience 4*, 241-251.

Walsh, J. J., Bailey, W. R., Childs, C., Nicol, A., Bonson, C. G. 2003. Formation of segmented normal faults: a 3-D perspective. *Journal of Structural Geology 25*, (8), 1251-1262.

Wang, H. F. 2000. *Theory of Linear Poroelasticity - With Applications to Geomechanics and Hydrogeology* Princton University Press, Princton, NJ, USA.

Wang, H., Jiang, Y., Xue, S., Mao, L., Lin, Z., Deng, D., Zhang, D. 2016. Influence of fault slip on mining-induced pressure and optimization of roadway support design in fault-influenced zone. *Journal of Rock Mechanics and Geotechnical Engineering 8*, (5), 660-671.

Wibberley, C. A., Yielding, G., DiToro, G. 2008. Recent advances in the understanding of fault zone internal structure: A review. In: Wibberley, C. A., Kurz, W., Imber, J., Holdsworth, R. E., Collettini, C. (Eds.), *The Internal Structure of Fault Zones: Implications for Mechanical and Fluid-Flow Properties*, Geological Society - Special Publications, London, UK, 5-33.

Will, J., Eckardt, S. optiRiss - Simulation based optimization and risc evaluation of enhanced geothermal systems. In Proceedings of the *Weimar Optimization and Stochastic Days* 2015. Weimar, Germany.

Will, J., Taixu, B., Eckhard, S., Chang, D., Lake, E. Dynardo technology and applications to well completion optimization for unconventionals. In Proceedings of the *ANSYS Convergence Conference* 2015. Houston, Texas, USA.

Wiprut, D. J., Zoback, M. D. 2000. Fault reactivation and fluid flow along a preciously dormant normal fault in the northern North Sea. *Geology 28*, (7), 595-598.

Wiprut, D., Zoback, M. D. 2002. Fault Reactivation, Leakage Potential, and Hydrocarbon Column Heights in the Northern North Sea. In: Koestler, A. G. & Hunsdale, R. (Eds.), *Norwegian Petroleum Society Special Publications*, 11, Elsevier, 203-219.

Wu, H.-Y., Ma, K.-F., Zoback, M., Boness, N., Ito, H., Hung, J.-H., Hickman, S. H. 2007. Stress orientations of Taiwan Chelungpu-Fault Drilling Project (TCDP) hole-A as observed from geophysical logs. *Geophysical Research Letters 34*, (1).

Yale, D. P. 2003. Fault and stress magnitude controls on variations in the orientation of in situ stress. In: Ameen, M. (Eds.), *Fracture and In-Situ Stress Characterization of Hydrocarbon Reservoirs*, 209, Geological Society - Special Publications, London, UK, 55-64.

Ye, S., Franceschini, A., Zhang, Y., Janna, C., Gong, X., Yu, J., Teatini, P. 2018. A Novel Approach to Model Earth Fissure Caused by Extensive Aquifer Exploitation and its Application to the Wuxi Case, China. *Water Resources Research 54*, (3), 2249-2269.

Zhang, Y.-Z., Dusseault, M. B., Yassir, N. A. 1994. Effects of rock anisotropy and heterogeneity on stress distributions at selected sites in North America. *Engineering Geology 37*, 181-197.

Zhang, Y., Langhi, L., Schaubs, P. M., Delle Piane, C., Dewhurst, D. N., Stalker, L., Michael, K. 2015. Geomechanical stability of CO2 containment at the South West Hub Western Australia: A coupled geomechanical–fluid flow modeling approach. *International Journal of Greenhouse Gas Control 37*, 12-23

Zhang, Z., Chen, F., Li, N., Swoboda, G., Liu, N. 2006. Influence of fault on the surrounding rock stability of a tunnel: Location and thickness. *Tunnelling and Underground Space Technology 61*, 1-11

Zoback, M. D. 2007. *Reservoir Geomechanics* Cambridge University Press, Cambridge, UK.

Resume/CV

Torben Treffeisen

Working experience

TU DARMSTADT – ENGINEERING GEOLOGY 10/2017 – Present

Graduate Research Associate (PhD Candidate)

SAKOSTA GMBH 09/2015 – 10/2017

Engineering Geologist (Student Trainee)

Volunteerism

SV DARMSTADT 98 e.V – BASKETBALL SECTION 07/2011 – 04/2019

Head Basketball Coach 07/2011 – 05/2019

Sports Manager (Basketball Department) 06/2017 – 05/2019

Publications

Treffeisen, T. & Henk, A. 2020-1. Representation of faults in reservoir-scale geomechanical finite element models – A comparison of different modeling approaches. Journal of Structural Geology 131, 1-12

Treffeisen, T. & Henk, A. 2020-2. Faults as Volumetric Weak Zones in Reservoir-Scale Hydro-Mechanical Finite Element Models - A Comparison Based on Grid Geometry, Mesh Resolution and Fault Dip. Energies 13, (10), 1-28.

Treffeisen, T. & Henk, A. 2020-3. Elastic and Frictional Properties of Fault Zones in Reservoir-Scale Hydro-Mechanical Models-A Sensitivity Study. Energies 13, (18), 1-27.

Conference

Treffeisen, T., Henk, A., 2020. Representation of Faults in Reservoir-Scale Hydromechanical Finite Element Models — A Comparison Based on Grid Geometry, Fault Geometry and Model Resolution, AAPG –ACE 2020, online.

Treffeisen, T., 2019. Representation of Faults as Homogenized Continuum in Reservoir-Scale Hydro-Geomechanical Finite Element Models – A Comparison Based on Fault Geometry and Heterogeneity Oral Presentation, SPE – Student Technical Conference, Aachen, Germany.

Software Skills

ANSYS® (experienced) | Python (experienced) | ABAQUS® (basic) | Hyperworks® (basic) | Petrel® geomechanics module (basic)